Integrated Analysis of Diel Cycles, Growth Transitions, and Magnesium Stress in Coccolithophore Metabolism and Calcification

Xiaoxu Ma

Exeter College

University of Oxford

A thesis presented for the degree of

Doctor of Philosophy

Hilary 2025

Declaration

All work presented here is my own and has been conducted over the course of the past six years (2019-2025). Contributions from other individuals are explicitly stated below, and all information derived from other publications is appropriately referenced throughout.

Chapter 2: The study was conceived by Xiaoxu Ma with guidance from Rosalind Rickaby. Xiaoxu Ma conducted the laboratory work. Proteomics measurements and clustering analysis were performed by a commercial company. Xiaoxu Ma carried out the remaining data analysis, interpreted the results, and wrote the manuscript with comments from Craig Dedman -Jones and Samuel Barton.

Chapter 3: The study was conceived by Xiaoxu Ma and Rosalind Rickaby. Xiaoxu Ma conducted the laboratory work, and proteomics measurements were performed by the Department of Biochemistry, University of Oxford. Initial mass spectrometry peak matching was conducted by Craig Dedman-Jones. Xiaoxu Ma carried out all data analysis, interpreted the results, and wrote the manuscript with comments from Craig Dedman-Jones, Samuel Barton, Rosalind Rickaby, El Mahdi Bendif and Qiong Zhang.

Chapter 4: The study was conceived by Xiaoxu Ma and Rosalind Rickaby. Xiaoxu Ma conducted the laboratory work. Metabolomics measurements and primary data analysis were carried out by John Walsby-Tickle from the Department of Chemistry, University of Oxford. Xiaoxu Ma conducted the remaining data analysis, interpreted the results, and wrote the manuscript with comments from Craig Dedman-Jones, Samuel Barton, and Rosalind Rickaby.

Acknowledgements

This thesis marks the completion of several years of research, and I would like to express my sincere gratitude to all those who have contributed to its development.

I would like to thank my supervisor, Professor Rosalind Rickaby, for her supervision. I appreciate her scientific insight, resource coordination, and support throughout the course of this project. Without her support, none of this work would have been possible. I am also grateful for the opportunity to carry out this research within the Department of Earth Sciences, and for the institutional support provided by Exeter College, University of Oxford, as well as the resources that made this work possible.

I am thankful to my collaborators and colleagues, both within and beyond the department, for their valuable input and discussions. Their contributions, through technical assistance, feedback, and shared expertise, have been instrumental to the progress of this work. I would also like to acknowledge the support received from administrative and technical staff, whose help has facilitated many aspects of this research. Specifically, I would like to thank Qiong Zhang for helping me settle into the lab at the start of my PhD and for teaching me key techniques such as seawater preparation and instrument usage, which supported much of my work throughout this project. I thank Qiong Zhang, Jane Barling, and Phil Holdship for their guidance in the clean lab and for teaching me sample preparation and metal analysis using ICP-MS. Although the resulting data were not included in this thesis, the work required considerable time, and I am confident it will be published in the near future. I thank Sofie Gill for generously sharing experimental protocols, including those for chlorophyll extraction, $CaCO_3$ production rates, and sample preparation for PIC: POC measurements, and for personally demonstrating many of these techniques, which formed the foundation of most of my experiments. I thank Samuel Barton for his assistance in modifying chlorophyll measurements and for his guidance on using the Oxylab system, which became an essential part of my research, and for the significant time he invested in addressing technical challenges throughout the project. I thank Craig Dedman-Jones for introducing me to proteomics and for establishing the connections that enabled sample

measurement, which later became a central component of my work. I also thank Marjorie Fournier (Department of Biochemistry, Oxford) for conducting part of the proteomics analysis. I thank John Walsby-Tickle (Department of Biochemistry, Oxford) for sharing sample preparation protocols, conducting my metabolomics measurements, and performing the primary data analysis. I thank Errin Johnson and Charlotte Melia at the William Dunn School of Pathology, Oxford, for accommodating me for SEM and TEM imaging. I thank Christopher Day for conducting isotope measurements, and Luke Williams for managing the lab and ensuring that my experiments could proceed smoothly. I thank El Mahdi Bendif for teaching me DNA extraction, primer design, and the use of various sequence analysis software. I also thank Rowena Stern for accommodating my work on the CPR samples. Although this project was eventually discontinued, I am confident that the skills gained will be valuable in the future. I also thank everyone, named or unnamed, who contributed to solving technical and scientific challenges during the course of this work. Their support and expertise were invaluable at many stages of the project.

I appreciate the broader academic community, whose published research and ongoing dialogue have helped shape the foundation and direction of this thesis. I would also like to thank Samuel Barton, Craig Dedman-Jones, Rosalind Rickaby, El Mahdi Bendif, and Qiong Zhang for their help with proofreading my chapters, their support has been key in bringing this thesis to completion.

I thank all my friends I met from the research group, the department, the university, conferences, and previous collaborations. Their scientific and emotional support has meant a great deal throughout this journey.

Finally, I would like to thank my parents, my brother, and my partner. Their unconditional support, encouragement, and faith in me have been my greatest source of strength. Thank you for always being there.

Abstract

Coccolithophores play a critical role in global biogeochemical cycles through their dual capacities for photosynthesis and intracellular calcification. However, the molecular regulation of these processes across environmental responses, strain- and species-specific patterns, and trait interactions, remains insufficiently understood. This thesis investigates the regulatory mechanisms underlying coccolithophore metabolism across diel cycles, growth phase transitions, magnesium availability, and taxonomic diversity. Time-series proteomics in *Gephyrocapsa huxleyi* reveal extensive diel metabolic reprogramming that tightly couples photosynthesis, carbon metabolism, and cell cycle progression. Growth phase transitions further reshape cellular priorities, with nutrient limitation driving substantial shifts in energy acquisition and utilisation. Notably, proteins previously implicated in calcification display expression patterns decoupled from calcification performance during growth phase transitions, yet remain coordinated with core carbon metabolism. These findings highlight the complexity of calcification regulation and its broader integration with cellular metabolic networks.

Under variable magnesium concentrations, *G. huxleyi* maintains photosynthetic performance while exhibiting substrate-dependent calcification with minimal changes in calcification-related protein expression. The observed decoupling between calcification, photosynthetic efficiency, and protein-level responses underscores the complexity of integrating calcification within the broader cellular regulatory framework, suggesting strong reliance on substrate availability in the absence of clear transcriptional control. These findings reinforce the interpretation of calcification as a secondary process relative to core metabolic functions. Comparative analyses across multiple strains of *G. huxleyi*, *G. oceanica*, *Coccolithus braarudii*, and *Coccolithus pelagicus* under control conditions (Mg-5, unmodified seawater chemistry) reveal size-dependent physiological traits. Metabolic profiling of representative strains confirms size-linked metabolic scaling. Under identical Mg regimes, larger *Coccolithus* species exhibited the lowest sensitivity to Mg variation, whereas *G. huxleyi* and *G. oceanica* showed broadly similar physiological responses, including coordinated variation in cell

size, chlorophyll-a content, and calcification. In both species, calcification again followed a strong linear relationship with magnesium availability, highlighting substrate supply as the primary determinant and further supporting its secondary regulatory status.

Together, these findings provide a multi-scale framework for understanding coccolithophore metabolic regulation, emphasising the dominant role of substrate availability in controlling calcification and the metabolic flexibility that underpins their ecological success and biogeochemical function in a changing ocean.

Table of Contents

List of Figures

List of Tables

Chapter 1 Introduction

1.1 Global significance of coccolithophores

1.1.1 Evolutionary history

Coccolithophores are unicellular marine phytoplankton within the phylum Haptophyta (class Prymnesiophyceae). Their distinctive ability to produce calcareous plates, known as coccoliths, has facilitated their continuous presence in the fossil record since their first appearance in the Upper Triassic (~225 million years ago). Despite undergoing substantial macroevolutionary changes, including multiple extinction events, coccolithophores have steadily diversified and now present a ubiquitous and abundant component of modern phytoplankton communities. Approximately 280 morphologically defined species are currently recognised. *Gephyrocapsa huxleyi* (former *Emiliania huxleyi* (Bendif *et al.*, 2023)), which first emerged ~ 290,000 years ago, has since become one of the most widespread and ecologically dominant coccolithophore species in the present-day ocean (Young *et al.*, 2003).

The taxonomic composition and diversity of coccolithophore assemblages have demonstrated marked sensitivity to environmental change, undergoing significant shifts since their first appearance. Throughout the Mesozoic, coccolithophores exhibited a general trend of increasing diversity, punctuated by extinction events at major geological boundaries such as the Triassic/Jurassic and Cretaceous/Paleogene transitions (Bown *et al.*, 2004; Falkowski *et al.*, 2004). Although background evolutionary rates remained relatively low, brief intervals of elevated speciation occurred during the Late Triassic, Early Jurassic, and Tithonian-Berriasian periods (Bown *et al.*, 2004; Bown, 2005). Notably, intervals of climatic cooling, such as the Neocomian and Late Cretaceous, promoted increased biogeographic differentiation, particularly at high latitudes, further enhancing diversity (Bown, 2005).

In contrast, coccolithophore diversity during the Cenozoic exhibited greater variability, with significantly higher overall rates of speciation, extinction, and turnover compared to the Mesozoic (Bown, 2005). These changes are closely linked to global climate

fluctuations (Bown, 2005). Peak diversity occurred during the Paleocene-Eocene Thermal Maximum (~56 Ma) and declined during subsequent cooling into the Oligocene (Falkowski *et al.*, 2004; Bown, 2005). Continued episodic changes throughout the Eocene and Neogene were closely linked to both global temperature shifts and oceanographic reorganisation (Schneider *et al.*, 2013; Gibbs *et al.*, 2018). Unlike the Mesozoic, Cenozoic cooling was generally associated with reduced diversity, likely due to the expansion of icehouse conditions limiting suitable habitats at higher latitudes (Lorenzo *et al.*, 2019; Müller *et al.*, 2021)(Falkowski *et al.*, 2004; Bown, 2005). However, exceptions to this trend exist, for instance, the Middle Miocene cooling appears to have enhanced both coccolithophore abundance and diversification (Henderiks *et al.*, 2020), highlighting the combined influence of abiotic and biotic factors (Ezard *et al.*, 2011).

Climate-driven selection pressures have not only influenced species turnover but also affected coccolithophore morphology and calcification. Different taxa show varying sensitivities to environmental conditions (Gibbs *et al.*, 2013), and well-preserved fossil records allow reconstruction of trait evolution over time (Henderiks, 2008). The geological coccolithophore morphological and calcification evolutionary trends for different species have been well established, including in the genus *Reticulofenestra* (Hannisdal *et al.*, 2012; O'Dea *et al.*, 2014; Suchéras-Marx & Henderiks, 2014; Imai *et al.*, 2015; Bolton *et al.*, 2016; Guitián *et al.*, 2020; Ma *et al.*, 2023). Due to its cosmopolitan distribution and long geological range, *Reticulofenestra* has been intensively studied, and a general long-term trend of size reduction has been observed over the past 40 million years, although with short-term fluctuations (Suchéras-Marx & Henderiks, 2014; Bolton *et al.*, 2016; Bolton & Stoll, 2024). For instance, size increases are noted during the early Miocene (~20-24 Ma) and mid-Miocene (~15-9 Ma) (Bolton *et al.*, 2016; Guitián *et al.*, 2020, 2022). Additionally, species-specific size responses have been identified; for instance, *Helicosphaera* shows a small decrease in coccolith size over the past 15 million years (Šupraha & Henderiks, 2020), while *Calcidiscus* has exhibited relatively stable coccolith size since the early Miocene, with a maximum in the late Miocene (Knappertsbusch, 2000). These morphological trends have been linked to factors such as atmospheric CO_2 (pCO_2) and nutrient availability, although the precise selective mechanisms remain under investigation. More recent high-resolution records of the

genus *Gephyrocapsa* and its descendant *G. huxleyi* reveal fine-scale diversification and calcification shifts in response to orbital eccentricity and glacial-interglacial cycles during the Pleistocene (Bendif *et al.*, 2019, 2023; Beaufort *et al.*, 2022), further underscoring their sensitivity to climate forcing.

1.1.2 Coccolithophores in Carbon Cycling and Climate Regulation

Although climate change has exerted strong selective pressure on coccolithophore assemblages, species composition, and physiological traits such as cell size and calcification, coccolithophores have also played a critical feedback role in shaping ocean chemistry and the global climate. Their dual role in the carbon cycle, fixing CO_2 through photosynthesis and producing calcium carbonate ($CaCO_3$) through calcification, makes them central to both short-term biological processes and long-term geochemical regulation.

Coccolithophores contribute significantly to the global carbon cycle by influencing both the biological and carbonate pumps. Through photosynthesis, they assimilate CO_2 into organic matter, contributing up to 20% or more of total oceanic primary production in certain regions and seasons (Poulton *et al.*, 2007). Simultaneously, their calcification process produces $CaCO_3$ coccoliths, which account for 40-60% of the $CaCO_3$ flux in tropical and subtropical sediments and nearly half of the total carbonate export in some areas (Broecker & Clark, 2009; Guerreiro *et al.*, 2021). Over geological timescales, their widespread calcification has established a responsive deep-sea $CaCO_3$ sink, enhancing the buffering capacity of the ocean and stabilizing atmospheric CO_2 levels (Ridgwell & Zeebe, 2005). In modern oceans, coccolithophores dominate pelagic $CaCO_3$ production, contributing ~90% of the living calcite pool (Ziveri *et al.*, 2023), and their calcite acts as effective ballast, enhancing organic matter export and regulating the global rain ratio (Armstrong *et al.*, 2001; Klaas & Archer, 2002; Ziveri *et al.*, 2007).

Coccolithophores' contributions, however, are highly variable and sensitive to environmental conditions. Seasonal and spatial changes in coccolithophore primary production and calcification are driven by light, nutrients, and carbonate chemistry. On the Patagonian Shelf, summer blooms of *G. huxleyi* can produce high calcite fluxes, reaching up to 7.3 mmol C m^{-2} d^{-1} (Poulton *et al.*, 2013). In the subpolar North Atlantic,

during late summer non-bloom conditions for coccolithophores, characterised by low cell abundances, they still contribute 10-20% of total primary production in regions such as the central Iceland Basin (Poulton *et al.*, 2010). While calcification and photosynthesis may show parallel trends under certain conditions, their relationship is not fixed and may decouple depending on species composition, depth, and environmental stressors (Poulton *et al.*, 2014; Guerreiro *et al.*, 2017). For example, blooms dominated by low-calcite morphotypes of *G. huxleyi* may exhibit high cell densities but low carbonate export (Poulton *et al.*, 2011). Furthermore, deep-dwelling species such as *Florisphaera profunda* and *Gladiolithus flabellatus* substantially contribute to $CaCO_3$ fluxes from the lower photic zone in stratified tropical waters (Guerreiro *et al.*, 2021), illustrating the complexity of coccolithophore-mediated carbon fluxes across spatial and taxonomic gradients(Poulton *et al.*, 2017).

Future carbon cycle feedback will depend critically on how coccolithophores respond to climate-driven changes such as ocean acidification (OA), warming, and nutrient shifts. These pressures may reduce calcification efficiency, shift morphotype dominance, and lead to divergent responses in photosynthesis and calcification. Earth system models predict a 4-13% reduction in atmospheric CO_2 burden by 3000, contingent on the extent to which coccolithophore calcification is suppressed (Ridgwell *et al.*, 2007). Acidification is expected to reduce particulate inorganic carbon (PIC) production and lower particulate inorganic carbon to particulate organic carbon (PIC: POC) ratios in key species like *G. huxleyi* and *Gephyrocapsa oceanica* (Meyer & Riebesell, 2015; Bach *et al.*, 2015), although heavily calcified forms may still persist under low pH in certain seasons (Smith *et al.*, 2012).

These effects are spatially heterogeneous. Earth system model projections suggest that coccolithophore abundance may increase at high latitudes due to warming and increased dissolved inorganic carbon availability, particularly bicarbonate, while calcification declines globally once CO_2 levels exceed ~600 µatm, especially in low to mid-latitudes (Krumhardt *et al.*, 2017, 2019). Observations from the North Atlantic show a 37% increase in coccolithophore pigment abundance, estimated from haptophyte marker pigments measured in seawater samples and supported by satellite observations of chlorophyll and PIC over the past two decades (Krumhardt *et al.*, 2016). The Southern

Ocean, particularly the Great Calcite Belt (GCB), remains a hotspot of $CaCO_3$ export, where environmental controls like iron availability, temperature, and grazing pressure tightly regulate bloom dynamics (Hopkins *et al.*, 2019; Oliver *et al.*, 2023, 2024). Although PIC increases under optimal conditions (~13-14°C, moderate nutrients), ongoing warming and acidification may drive shifts toward smaller, less calcified forms in many regions, reducing export efficiency (Ziveri *et al.*, 2007; Ridgwell *et al.*, 2009; Rigual Hernández *et al.*, 2020), though recent studies have shown that marine heatwaves may temporarily increase coccolithophore abundance in the North Atlantic (Rivero-Calle *et al.*, 2015; Krumhardt *et al.*, 2016). Importantly, some deep-dwelling, heavily calcified species such as *Coccolithus braarudii* may remain resilient under elevated CO_2 and could become more dominant contributors to future $CaCO_3$ export in polar systems (Krug *et al.*, 2011; Rigual Hernández *et al.*, 2020). Nonetheless, the balance between adaptation, community reorganisation, and environmental forcing remains uncertain.

Given their ecological sensitivity and central role in biogeochemical cycling, even modest changes in coccolithophore physiology, species composition, or export efficiency could lead to significant long-term feedback on atmospheric CO_2. These findings underscore the need for a deeper understanding of coccolithophore biology, especially the regulation of photosynthesis and calcification under changing ocean conditions. Their ability to adapt and maintain these fundamental processes will largely determine their future impact on oceanic carbon cycling and climate regulation.

1.2 Calcification and cellular metabolism

1.2.1 Coccolithophore life cycle

Coccolithophores possess a haplo-diplontic life cycle, alternating between diploid and haploid stages that are often morphologically and ecologically distinct. In many taxa, the diploid (2N) phase produces heterococcoliths, which are intricately structured calcite plates synthesised within the cell. In contrast, the haploid (1N) phase produces simpler holococcoliths composed of rhombohedral calcite crystals that are typically assembled extracellularly or within expanded vesicles (Young *et al.*, 2005; Langer *et al.*, 2021; Ben-Joseph *et al.*, 2023; Meyer & Taylor, 2025). However, this dual-calcifying pattern is not

universal. In several species, including *G. huxleyi*, the haploid phase is entirely non-calcified and often appears as a naked, biflagellate cell (Young *et al.*, 2005; Houdan *et al.*, 2005; Frada *et al.*, 2008; Probert *et al.*, 2014). The expression and morphology of life-cycle phases vary by species, and not all coccolithophores are confirmed to alternate between both forms. Nonetheless, species such as *C. braarudii* and *C. leptoporus* express both phases and exhibit functional trade-offs, with haploids favouring stable, low-nutrient conditions and diploids benefiting from fluctuating nutrient regimes due to greater nitrogen (N) storage capacity (Houdan *et al.*, 2006; de Vries *et al.*, 2024).

These differences in life-cycle expression significantly influence coccolithophore contributions to marine carbon cycling. Diploid heterococcolithophores generally exhibit higher PIC: POC ratios due to their greater calcification capacity, and their heavier coccoliths are more resistant to dissolution and better preserved in sediments, supporting long-term $CaCO_3$ export and burial (Crudeli *et al.*, 2006; Fiorini *et al.*, 2011; Daniels *et al.*, 2016). In contrast, holococcoliths from haploid phases are more fragile and less likely to be preserved, contributing less to the sedimentary carbonate record despite their ecological importance. Field studies show that holococcolithophores dominate in oligotrophic surface waters during stratified conditions, whereas heterococcolithophores prevail in deeper or nutrient-rich layers (Šupraha *et al.*, 2016; D'Amario *et al.*, 2017; Keuter *et al.*, 2019). Physiological experiments further reveal differing sensitivities of the two phases to environmental variables such as light, nutrients, and pCO_2, complicating projections of their respective roles in carbon cycling (Kottmeier *et al.*, 2020a; Langer *et al.*, 2023; de Vries *et al.*, 2024). Although meiosis and syngamy have not been directly observed, sexual reproduction in coccolithophores is strongly inferred from the presence of combination coccospheres, cells bearing both hetero- and holococcoliths, indicating transitions between diploid and haploid phases (Cros *et al.*, 2000; Young *et al.*, 2005). A variety of environmental and physiological triggers have been proposed to mediate these life-cycle transitions, including nutrient limitation, temperature stress, culture ageing, and biotic factors such as viral infection, particularly in bloom-forming species like *G. huxleyi* (Young *et al.*, 2005; Houdan *et al.*, 2005; Frada *et al.*, 2008, 2012, 2019; Šupraha *et al.*, 2016; Bousquet *et al.*, 2025).

The distinct ecological functions and physiological responses of coccolithophore life stages underscore their complex and complementary roles in regulating oceanic carbon flows. This highlights the importance of phase-specific investigations into physiology, calcification, and ecology to better understand coccolithophore contributions to biogeochemical cycles and to improve projections of their responses to ongoing environmental change.

1.2.2 Organic regulation of coccolithogenesis

Coccolith biomineralisation is intricately controlled by a complex interplay of inorganic minerals and an organic matrix, primarily composed of polysaccharides and proteins. This organic component regulates crystal nucleation, morphology, and growth within specialised intracellular compartments known as coccolith vesicles (CVs), which are Golgi-derived vesicles responsible for calcification (Young *et al.*, 1999; Marsh, 2003; Walker *et al.*, 2020). In species such as *Pleurochrysis carterae*, the CV forms directly from the Golgi and contains dense, calcium-rich particles termed coccolithosomes that function as calcium vectors during calcification (Manton & Leedale, 1969; Manton & Peterfi, 1969; Outka & Williams, 1971; van der Wal *et al.*, 1983b; Marsh, 1994). In contrast, in species like *G. huxleyi* and *C. pelagicus*, calcification occurs in a vesicle associated with the nuclear envelope and a distinct structure known as the reticular body (RB), which is morphologically separated from the Golgi but likely derived from it (van der Wal *et al.*, 1983a; Marsh, 1994; Taylor *et al.*, 2007). Despite variation in vesicle architecture, coccolith formation across species follows a common pathway, nucleation begins on an organic base-plate scale, followed by directional crystal growth (Young *et al.*, 1999; Paasche, 2001).

Central to coccolith formation are coccolith-associated polysaccharides (CAPs), acidic macromolecules synthesised in the Golgi and delivered to the CV, where they interact with mineral precursors and organic scaffolds (Marsh *et al.*, 1992; Marsh, 1994). These polysaccharides, rich in uronic acid residues, contain charged carboxyl groups capable of binding calcium ions, thereby modulating crystal nucleation and growth dynamics (Ozaki *et al.*, 2007; Lee *et al.*, 2016; Walker *et al.*, 2018a). Experimental evidence confirms that CAPs directly influence nucleation efficiency and crystal orientation,

essential for proper calcite morphology (de Jong *et al.*, 1976; Marsh & Dickinson, 1997; Kayano & Shiraiwa, 2009; Kayano *et al.*, 2011). The uronic acid content (UAC) of CAPs varies significantly among coccolithophore species, correlating with CV saturation states and potentially reflecting evolutionary adaptations to environmental variability and carbon availability (Lee *et al.*, 2016).

Detailed CAP characterisation has revealed substantial interspecies variation. For example, *G. huxleyi* synthesises a single mannose-rich CAP featuring sulfate esters, xylose, and galacturonic acid sidechains (Fichtinger-Schepman *et al.*, 1981; Walker *et al.*, 2018a). In contrast, species like *P. carterae* produce several distinct CAPs, notably PS-1, PS-2, and PS-3, each with unique structural characteristics and calcification-regulatory functions (Marsh & Dickinson, 1997; Ozaki *et al.*, 2007). PS-2, identified as a glucuronate-tartrate-glyoxylate polymer, exhibits particularly strong calcium-binding affinity and directly influences nucleation and crystal morphology (Marsh *et al.*, 1992; Marsh & Dickinson, 1997; Ozaki *et al.*, 2007). Additionally, another polysaccharide, coccolith matrix acidic polysaccharide (CMAP), structurally similar to PS-2 but differing significantly in anti-calcification activity, emphasises functional diversification among closely related CAPs (Ozaki *et al.*, 2004, 2007). Furthermore, within different *P. carterae* strains (e.g., CCMP 645, 646, 648), co-occurrence of PS-2 and CMAP has been observed, highlighting intra-specific complexity in polysaccharide functionality (Ozaki *et al.*, 2004).

Emerging evidence from cryo-electron microscopy and tomography has clarified the role of the organic base plate in calcification. Initially hypothesised as a stereochemical template directly guiding crystal nucleation (Young *et al.*, 1999; Marsh, 2003), recent investigations suggest a more nuanced function. Detailed structural and chemical analyses have revealed that base plate edges are enriched with positively charged amine groups, which electrostatically attract negatively charged CAP-Ca^{2+} complexes, thus creating a defined spatial and chemical microenvironment for controlled nucleation and crystal elongation, rather than direct molecular templating (Marzec *et al.*, 2019; Walker *et al.*, 2020; Eyal *et al.*, 2022).

Complementing this spatially regulated system, intracellular CAP-rich condensates have been identified as critical reservoirs for calcium ions (Ca^{2+}). Cryo-electron

microscopy and tomography studies have demonstrated that these condensates stabilise and buffer the ionic conditions necessary for controlled biomineralisation within the highly confined coccolith vesicle (Sviben *et al.*, 2016; Gal *et al.*, 2016, 2018; Kadan *et al.*, 2020, 2021; Bino *et al.*, 2025). These compartments act as intermediate storage units, strategically releasing ions to sustain optimal crystallization conditions (Kadan *et al.*, 2021; Bino *et al.*, 2025). Experimental evidence supports this regulatory mechanism, showing that disruptions in CAP composition or function impair calcium condensation processes, resulting in defective coccolith morphology and impaired crystal growth dynamics (Avrahami *et al.*, 2024; Bino *et al.*, 2025)

Upon completion, coccoliths are secreted to the extracellular space coated by CAP-rich organic layers, which facilitate adherence to the cell surface and contribute to coccosphere stability (Marsh, 1994; Walker *et al.*, 2018a). Collectively, the interplay of CAP-driven ion management, spatially organised vesicular structures, and organic scaffolds constitutes a sophisticated macroregulatory network critical for precise, species-specific coccolith formation, laying the foundation for subsequent molecular-level regulation.

1.2.3 Molecular regulation in calcification

The molecular regulation of coccolithophore calcification involves a tightly controlled system of ion transport and protein interactions that manage intracellular Ca^{2+}, DIC, and protons (H^+) to support $CaCO_3$ precipitation within the CV. One of the earliest proteins proposed to contribute to coccolith formation in *G. huxleyi* was glycoprotein A (GPA), a calcium-binding protein associated with coccolith-associated polysaccharides (Corstjens *et al.*, 1998). GPA was shown to influence crystal morphology and orientation during coccolithogenesis (Corstjens *et al.*, 1998), and its localisation around developing coccolith crystals supports a modulatory role. Although its function remains unclear, as GPA is also expressed in the non-calcifying haploid phase (Quinn *et al.*, 2006), suggesting additional roles beyond calcification. Genetic variation in GPA among strains further indicates its potential utility as a population marker rather than a calcification-specific gene (Schroeder *et al.*, 2005). Additionally, transcriptomic analyses have shown GPA expression to be downregulated in calcifying cells, implying that its role, if any, may be

context-dependent (Mackinder *et al.*, 2011). More recently, proteomic studies identified a group of coccolith production-related proteins (COPROs), many of which possess transmembrane domains and signal peptides, suggesting their targeting to the coccolith vesicle is confirmed (Skeffington *et al.*, 2023). However, their exact roles in calcification remain to be confirmed (Skeffington *et al.*, 2023).

Efficient Ca^{2+} transport is vital for coccolithogenesis, necessitating mechanisms that balance the high Ca^{2+} demand for coccolith formation with cytosolic Ca^{2+} homeostasis. Transcriptomic studies in G. *huxleyi* have revealed key ion transporters involved in this process. Comparative analyses between calcifying and non-calcifying strains (von Dassow *et al.*, 2009), as well as transcriptomic responses to calcium-limiting conditions (Mackinder *et al.*, 2011; Nam *et al.*, 2019), identified the upregulation of genes encoding Ca^{2+}/H^{+} exchangers (CAX family), vacuolar-type H^{+}-ATPases (V-ATPases), and solute carrier 4 (SLC4) bicarbonate transporters under calcifying conditions. CAX family transporters facilitate the import of Ca^{2+} into the CV by utilising the proton gradient generated by V-ATPases. Elevated transcription of CAX genes in calcifying strains suggests a direct role in mediating the steep Ca^{2+} influx required for coccolith formation (von Dassow *et al.*, 2009; Mackinder *et al.*, 2011). V-ATPases use ATP to pump protons into the CV, acidifying the compartment and enabling Ca^{2+} import via proton-coupled transport. This role was experimentally confirmed in *P. carterae*, where V-ATPase subunits were localised to the CV membrane during calcification (Corstjens *et al.*, 2001).

Dissolved inorganic carbon (DIC), primarily bicarbonate (HCO_3^-), is crucial for calcification. SLC4 bicarbonate transporters mediate the uptake of HCO_3^- into the CV, providing the inorganic carbon substrate for calcite precipitation. Their differential expression in calcifying versus non-calcifying strains underscores their role in DIC regulation (von Dassow *et al.*, 2009; Mackinder *et al.*, 2011; Nam *et al.*, 2019). Functional characterisation in *G. huxleyi* suggests that SLC4 transporters act primarily as Cl^-/HCO_3^- exchangers, supported by DIDS (4,4'-diisothiocyanatostilbene-2,2'-disulfonic acid) inhibitor studies (Herfort *et al.*, 2002). Complementary ion flux assays in *Coccolithus pelagicus* further confirmed that DIDS inhibits bicarbonate exchange, validating the role of SLC4 proteins in HCO_3^- transport (Taylor & Brownlee, 2003).

Carbonic anhydrases (CAs) contribute to DIC homeostasis by catalysing the reversible hydration of CO_2 to HCO_3^-, enabling efficient substrate supply for calcification. In *G. huxleyi*, two distinct CA isoforms, γ-EhCA2 and δ-EhCA1, have been cloned and characterised, showing differences in expression regulation and structural features suggestive of subcellular specialisation (Soto *et al.*, 2006). Their transcript levels vary under bicarbonate-limiting conditions, indicating distinct roles in partitioning DIC between photosynthesis and calcification (Soto *et al.*, 2006; Richier *et al.*, 2011). Expression analyses show strong upregulation of γ-class CA under calcifying conditions, further linking this isoform to biomineralisation (Quinn *et al.*, 2006). Modelling studies suggest that CA activity near or within the CV enhances local HCO_3^- availability and stabilise carbonate chemistry for efficient calcite precipitation (Holtz *et al.*, 2013). Integrated energy budget and multi-compartment DIC transport models further support the idea that CA activity, in conjunction with bicarbonate transporters and H^+ exporters, is critical in maintaining the chemical gradients necessary for controlled biomineralisation (Holtz *et al.*, 2015a,b, 2017).

ATP-dependent processes, particularly those involving ion transport and pH regulation, account for a substantial portion of the energetic cost of calcification. The active transport of Ca^{2+} and HCO_3^- into the CV requires significant ATP investment, while ATP-driven V-ATPases maintain the proton gradients essential for these transport processes (Corstjens *et al.*, 2001; Holtz *et al.*, 2013). In parallel, plasma membrane H^+-ATPases and voltage-gated proton channels (HVCN1) help extrude excess protons from the cytosol to maintain pH homeostasis, thereby preventing cytoplasmic acidification during rapid $CaCO_3$ precipitation (Suffrian *et al.*, 2011; Taylor *et al.*, 2011).

Voltage-gated proton channels (Hv1-type), first described in *G. huxleyi* and *C. braarudii* (Taylor *et al.*, 2011), represent an ATP-independent mechanism for rapid H^+ export. These channels are activated in response to intracellular acidification and facilitate proton efflux across the plasma membrane, contributing to cytoplasmic pH regulation during active calcification (Taylor *et al.*, 2011). Patch-clamp studies demonstrated their electrophysiological properties, and subsequent experiments showed that pharmacological inhibition or genetic disruption of Hv1 function leads to abnormal

coccolith morphology and impaired pH regulation (Kottmeier *et al.*, 2022), underscoring their essential role in cellular proton dynamics during biomineralisation.

Proteomic studies have advanced our understanding of calcification-related proteins beyond classical ion transporters. The first pan-genomic survey of *G. huxleyi* revealed extensive genome variability across isolates, highlighting the potential for strain-specific metabolic repertoires, including those involved in biomineralisation (Read *et al.*, 2013). Building on this, the recent high-resolution proteomics confirmed the enrichment of calcification-related proteins in the CV membrane of calcifying *G. huxleyi* (Skeffington *et al.*, 2023). These include transmembrane proteins with signal peptides, actin-related cytoskeletal components, and ion exchangers such as $Na^+/Ca^{2+}/K^+$ (SLC24 family) and Mg^{2+} transporters. Many of these proteins are explicitly upregulated under calcifying conditions and localise to vesicular structures, suggesting roles in vesicle maturation, ion transport coordination, and coccolith exocytosis (Skeffington *et al.*, 2023).

The energetic demands of coccolithophore calcification have also been clarified through modelling and physiological studies. Initial hypotheses proposed calcification as a relatively low-cost means of enhancing intracellular CO_2 supply (Anning *et al.*, 1996), but subsequent research emphasised its strong dependence on photosynthetically derived ATP, particularly for sustaining ion transport (Raven & Crawfurd, 2012). More detailed modelling efforts estimated that the combined transport of Ca^{2+}, HCO_3^-, and H^+ accounts for approximately 20-30% of the ATP budget from photosynthesis, with Ca^{2+} transport alone consuming up to 20% (Monteiro *et al.*, 2016). Comparative studies revealed that *G. huxleyi* incurs higher energetic costs for calcification than *C. braarudii*, reflecting species-specific differences in calcification rates and ion transport strategies (Monteiro *et al.*, 2016).

These molecular findings collectively suggest a highly integrated and energy-intensive regulatory framework in coccolithophores. Ion channels, exchangers, proton pumps, carbonic anhydrases, and vesicle-associated proteins work to maintain the intracellular environment required for precise and species-specific calcification. Further molecular-level investigations are needed to elucidate how the expression, localisation, and activity

of calcification-related proteins respond to environmental drivers, and how these responses are linked to broader regulatory pathways and physiological performance.

1.3 Coccolithophore responses to environmental change

Coccolithophores display remarkable physiological plasticity, enabling them to thrive across a broad range of environmental conditions. Key traits such as growth rate, cell size, coccosphere and coccolith morphology, photosynthetic performance, pigment composition, calcification, and elemental stoichiometry (e.g., PIC, POC, PIC: POC ratios) exhibit high variability across species and strains. Their responses to environmental drivers, such as temperature, pCO_2, light, nutrient availability, and salinity, necessitate trait-to-trait analysis that accounts for interspecific differences and cross-trait interactions. Understanding these relationships is essential for predicting their ecological success and contributions to marine carbon cycling under future environmental conditions.

In natural marine environments, these drivers rarely vary independently. Warming often intensifies stratification, simultaneously elevating surface irradiance and suppressing nutrient entrainment from deeper waters. Similarly, rising CO_2 levels contribute not only to acidification but also to warming, while nutrient dynamics frequently co-vary with temperature and light regimes. Although this complex interplay strongly shapes coccolithophore physiology, it also differentially affects individual species and morphotypes, reflecting lineage-specific strategies and ecological niches. Controlled laboratory studies that manipulate single drivers in isolation therefore provide critical mechanistic insights into the independent efforts of each factor and allow the resolution of species-level responses that would otherwise be obscured in mixed communities. The following sections focus on the responses of individual physiological traits to major environmental gradients, integrating evidence across studies to identify both common and divergent patterns of acclimation and adaptation.

1.3.1 Growth rate response

1.3.1.1 Temperature

Growth rate is a fundamental trait that shapes coccolithophore ecological success, bloom dynamics, and contributions to biogeochemical cycles. Many studies confirm that temperature strongly influences growth, typically following an optimum curve beyond which growth declines due to physiological stress (Rosas-Navarro et al., 2016; Tong et al., 2019; Wang et al., 2019; Müller et al., 2021a; Anderson et al., 2021; Bradley & Laws, 2024). For example, *G. huxleyi* generally achieves peak growth within a temperature range of ~ 15-25 °C. Nonetheless, both the thermal optimum and absolute growth capacity vary considerably across strains (Tong et al., 2019; Wang et al., 2019; Krinos et al., 2025), and are further modulated by background factors such as light (Feng et al., 2008) or CO_2 supply (Sett *et al.*, 2014; Schlüter *et al.*, 2014). While moderate warming often enhances growth, cooling below this optimal range or exceeding critical thresholds near 28 °C can substantially inhibit growth in certain strains (Sett *et al.*, 2014; Rosas-Navarro *et al.*, 2016; Matson *et al.*, 2016; Wang *et al.*, 2019; Bradley & Laws, 2024).

Compared with *G. huxleyi*, most other coccolithophore species remain less studied regarding temperature responses. However, available evidence indicates that *G. oceanica* either shares a similar thermal optimum or exhibits a slightly higher one (Gafar & Schulz, 2018; Müller et al., 2021a; von Dassow et al., 2021; Larsen & and Beardall, 2023), though with a somewhat narrower tolerance range (von Dassow et al., 2021). In contrast, larger species such as *C. braarudii* and *C. leptoporus* appear to occupy narrower or cooler thermal niches (Buitenhuis et al., 2008).

1.3.1.2 Ocean acidification

OA (i.e., elevated CO_2 and lowered pH) can alter coccolithophore growth in species- and even strain-specific ways. In some cases, OA alone may moderately decrease or occasionally enhance growth, but interacting factors such as nutrient supply, temperature, and light more often dominate or modulate these effects. For instance, *G. huxleyi* frequently exhibit a bell-shaped growth response to rising CO_2, with an optimum range followed by a decline at higher concentrations. Certain strains show slight growth

enhancement under elevated CO_2, presumably due to improved carbon acquisition (Feng et al., 2008, 2017; Rokitta & Rost, 2012), while other strains display no clear response or even reduced growth (Zhang et al., 2018; Feng et al., 2020).

In contrast, *G. oceanica* generally behaves similarly but can exhibit a higher optimal CO_2 range (Zhang et al., 2015; Gafar & Schulz, 2018). In most studies, the effects of acidification are superseded by changes in light or nutrient regimes (Feng et al., 2017; Zhang et al., 2019, 2020). Reduced nutrient supply can either magnify or mask acidification effects, implying that elevated CO_2 alone is rarely the dominant factor controlling growth (Feng *et al.*, 2020; Zhang & Gao, 2021). Moreover, strain-level genetic variation may play a role, certain *G. huxleyi* populations from highly variable coastal habitats tolerate high pCO_2 and low pH more effectively than those from stable oceanic regions (Zhang et al., 2018).

1.3.1.3 Irradiance

Coccolithophore growth rate typically follows a saturation curve, where growth increases with light intensity up to a species- or strain-specific optimum, after which it may plateau or decline due to photoinhibition. While increasing irradiance generally promotes growth, responses are modulated by species identity, calcification status, nutrient availability, and co-occurring stressors, emphasising the importance of integrated environmental context. In *G. huxleyi*, growth rates consistently rise from low to moderate irradiance (typically between 30 and 300 µmol photons m^{-2} s^{-1}), with light saturation occurring around 300-400 µmol photons m^{-2} s^{-1} under nutrient-replete conditions (Nielsen, 1997; Leonardos & Harris, 2006; Feng *et al.*, 2008, 2017), which is lower than midday surface irradiance but reflects the acclimated growth optima observed experimentally. At very high irradiances, growth may plateau or decline due to excess excitation energy and potential photoinhibition (Trimborn *et al.*, 2007; Ramos *et al.*, 2012; McKew *et al.*, 2013), the latter resulting in part from photodamage to photosystem II.

Dynamic irradiance regimes, simulating vertical mixing, tend to reduce growth compared to constant light, likely due to increased energy demands for photoacclimation (van de Poll et al., 2007). Strain-specific differences are evident, with diploid calcifying *G. huxleyi* cells generally tolerate high light better than haploid non-calcifying counterparts,

reflecting their divergent ecological niches (Houdan et al., 2005; Ruan et al., 2023). Calcifying strains may also experience reduced photoinhibition and maintain higher growth rates under high light, possibly due to enhanced bicarbonate uptake associated with calcification (Grubb *et al.*, 2024). However, calcification is not essential for growth at high irradiance, as non-calcifying strains can display comparable or even higher photosynthetic and growth rates under such conditions (Trimborn *et al.*, 2007).

Compared to *G. huxleyi*, *G. oceanica* shows a similar overall irradiance response but is more sensitive to additional stressors, such as elevated pCO_2 or nutrient limitation, which can exacerbate photoinhibition at high light (Zhang et al., 2015; Gafar & Schulz, 2018). Larger species like *Scyphosphaera apsteinii* are more adapted to low-light conditions and become physiologically stressed under high irradiance and acidification (Gafar et al., 2019), suggesting species-specific light niches.

1.3.1.4 Nutrient (N, P)

Coccolithophore growth rate is highly sensitive to nutrient availability, with macronutrients such as N and phosphorus (P) exerting distinct and often interactive effects. Growth is generally highest under nutrient-replete conditions and markedly suppressed under limitation. N limitation reduces growth and cell division; however, *G. huxleyi* exhibits remarkable endurance by upregulating high-affinity N uptake systems and reorganising metabolic fluxes (Rokitta *et al.*, 2014; McKew *et al.*, 2015). Even under prolonged N-deprivation, *G. huxleyi* maintains photosystem II functionality longer than many diatoms, supporting its ecological success in stratified, N-depleted surface waters (Loebl *et al.*, 2010). Ammonium generally supports faster growth than nitrate (Lecourt *et al.*, 1996), although exceptions exist depending on strain identity and environmental context, particularly under warming or multi-stressor regimes (Lefebvre *et al.*, 2012; Wang *et al.*, 2024). P limitation typically causes more severe growth inhibition than N limitation (McKew *et al.*, 2015; Rokitta *et al.*, 2016), leading to reduced division rates and lower final cell densities (Oviedo *et al.*, 2014). Some *G. huxleyi* strains can persist under low-P by accessing dissolved organic P sources such as phytic acid, albeit with variable efficiency (Li *et al.*, 2023).

Species-level comparisons reveal that, while *G. huxleyi* excels under nutrient stress, larger and less-studied species such as *Calcidiscus leptoporus*, *C. braarudii*, and *Helicosphaera carteri* also display characteristic responses under nutrient depletion, including reduced growth and increased coccolith production during stationary phase (Sheward *et al.*, 2017). Some evidence suggests that *C. braarudii* is particularly sensitive to P limitation relative to N limitation, consistent with its prevalence in P-rich upwelling systems (Sturm *et al.*, 2022). Additionally, studies on *G. oceanica* indicate that nitrate limitation more strongly suppresses growth than ammonium supply (Tong *et al.*, 2016), suggesting that the form of N can significantly shape growth responses.

1.3.1.5 Major and trace elements

Coccolithophore growth responses to changes in major and trace element concentrations vary by species and element. *G. huxleyi* shows broad tolerance to Ca variation, with no significant changes in growth rate across 0-9 mM Ca^{2+}, despite pronounced sensitivity of calcification (Herfort *et al.*, 2004; Trimborn *et al.*, 2007; Leonardos *et al.*, 2009). Even at Cretaceous-like concentrations (up to 40 mM), growth remains stable, suggesting calcification may buffer intracellular Ca^{2+} toxicity (Müller *et al.*, 2015a). In contrast, *G. huxleyi* shows growth inhibition above 25 mM Ca^{2+}, whereas *C. braarudii* maintains growth under similarly high Ca^{2+} levels (Müller *et al.*, 2011).

Fe limitation suppresses growth in *G. huxleyi*, primarily through impaired carbon acquisition and reduced photosynthetic capacity (Muggli *et al.*, 1996; Schulz *et al.*, 2007). Compared to diatoms, *G. huxleyi* shows greater flexibility under Fe stress, including the ability to reduce cell size to maintain metabolic balance (Muggli *et al.*, 1996). Zinc (Zn) limitation reduces growth in *G. huxleyi*, although partial rescue occurs via substitution with cadmium (Cd^{2+}) or cobalt (Co^{2+}), albeit with activation of stress-related proteomic pathways (Shire & Kustka, 2022). Both Zn^{2+} and strontium (Sr^{2+}) can be incorporated into coccoliths without severely impairing growth, suggesting a potential detoxification mechanism through calcification (Santomauro *et al.*, 2016; Sun *et al.*, 2018). However, high Sr^{2+} concentrations reduce calcite production, likely by disrupting mineralogy. In *P. carterae*, Co^{2+} slightly enhances growth up to 10 µM but becomes inhibitory beyond 100 µM, causing reversible arrest of cell division (Blankenship & Wilbur, 1975). These

results highlight *G. huxleyi*'s robust ionic regulation and tolerance relative to other species. Manganese (Mn) is a micronutrient recognised as important for marine phytoplankton productivity (Hawco *et al.*, 2022; Balaguer *et al.*, 2022), although experimental data on the physiological responses of coccolithophores to Mn availability remain limited.

1.3.1.6 Salinity

Coccolithophore growth responses to salinity vary by species and strain, with *G. huxleyi* generally displaying broad tolerance across a salinity range of 20-45 ‰ but displaying strain-specific growth patterns. Most *G. huxleyi* strains show reduced growth at both low and high salinity (Gebühr *et al.*, 2021), although exception exist. For instance, RCC1232, shows enhanced growth at both salinity extremes, while PLYB11 performs better under low salinity conditions (Sheward *et al.*, 2024). Coastal Scandinavian clones tolerate salinities as low as 12-16 ‰, whereas offshore or warm-water strains typically require ≥17 ‰ for sustained growth (Paasche *et al.*, 1996). Arctic strains of *G. huxleyi* tolerate moderate salinity changes (26-35 ‰) with minimal impact on growth (Saruwatari *et al.*, 2016). Growth enhancement under reduced salinity (25 ‰) has also been observed when combined with elevated CO_2 (Xu *et al.*, 2020). In *G. oceanica*, optimal growth is typically observed between 30-35 ‰, with declines occurring outside this range (Larsen & and Beardall, 2023). Overall, growth tends to peak near native salinity conditions, and ecotypic differentiation plays a key role in shaping salinity responses.

1.3.2 Morphological responses (coccosphere, cell, and coccolith size)

1.3.2.1 Temperature

Temperature exerts a significant influence on the coccolithophore morphology, with consistent patterns observed across multiple strains and species. In *G. huxleyi*, cell size, coccosphere volume, and coccolith dimensions typically decrease with increasing temperature, a trend consistently reported across strains (Saruwatari *et al.*, 2016; Matson *et al.*, 2016; Müller *et al.*, 2021a), though the extent of these responses varies among strains (Matson *et al.*, 2016). Enlargement of both cells and chloroplasts at low temperatures has also been documented (Sorrosa *et al.*, 2005; Satoh *et al.*, 2009),

supporting the inverse relationship between temperature and size. Similar size-temperature trends are seen in other species, such as *G. oceanica*, which also shows reduced cell and coccolith size under warming (Sorrosa *et al.*, 2005; Larsen & and Beardall, 2023). Notably, exceptions to the general trend exist. For example, Rosas-Navarro *et al.* (2016) reported that in three *G. huxleyi* strains from the North Pacific, coccolith size, coccolith mass, and tube width all increased from 10°C to 25°C, peaking near the temperature optimum for growth (20-25°C).

1.3.2.2 Ocean acidification

OA generally leads to reductions in coccolith size, coccosphere size, and cell size in many coccolithophore species, although these responses are highly species- and strain-dependent. In *G. huxleyi*, elevated CO_2 and low pH conditions often result in smaller, malformed coccoliths with thinner calcite structures (Bach *et al.*, 2012; Milner *et al.*, 2016; D'Amario *et al.*, 2020). These changes are frequently accompanied by a decrease in coccosphere volume, suggesting a contraction of both cellular and calcified components in response to acidification (Lorenzo *et al.*, 2019; Müller *et al.*, 2021b). Reductions in cell volume are also common, suggesting broader physiological impacts potentially linked to energetic constraints or shifts in carbon allocation strategies (Müller *et al.*, 2021b; Armstrong & Law, 2023).

However, these morphological responses are not universal across taxa. For instance, *H. carteri* appears morphologically resilient to OA, exhibiting minimal changes in coccolith structure and coccosphere integrity (Bianco *et al.*, 2024). Similarly, *Ochrosphaera neapolitana* maintains stable coccolith morphology and calcification-site pH under acidified conditions, reflecting species-specific mechanisms of carbonate chemistry regulation (Liu *et al.*, 2018). Notably, certain *G. huxleyi* strains can maintain or even increase coccolith and coccosphere size under high CO_2 following long-term exposure, suggesting potential for adaptive plasticity or physiological acclimation (Jones *et al.*, 2013; Schlüter *et al.*, 2016).

1.3.2.3 Irradiance

Irradiance significantly influences coccosphere, cell, and coccolith size across coccolithophore species, although species-specific traits and interactions with other environmental factors modulate the magnitude and direction of these responses. In *G. huxleyi*, increasing irradiance generally promotes reductions in coccosphere and cell size, especially under elevated CO_2 levels. These changes are likely driven by photophysiological acclimation and shifts in resource allocation under high-light stress (Feng *et al.*, 2008; Lorenzo *et al.*, 2019). Similar trends of reduced coccolith size and diminished calcification have also been reported, supporting a physiological coupling between coccolith and cell size (Müller *et al.*, 2021b), and indicating that calcification may be constrained under light-saturated or energetically favourable conditions (Moheimani *et al.*, 2012). High irradiance has additionally been associated with smaller coccospheres containing fewer and thinner coccoliths (Leonardos & Harris, 2006; Feng *et al.*, 2008). In contrast, under low-light or nutrient-limiting conditions, cells often grow larger and produce more coccoliths per cell (Sheward *et al.*, 2017). Comparable light-driven morphological patterns have been observed in other species, such as *G. oceanica* and *S apsteinii*, which show reductions in coccolith and coccosphere size and increased calcification sensitivity under high irradiance, albeit with varying degrees of plasticity (Tong *et al.*, 2016; Gafar *et al.*, 2019).

1.3.2.4 Nutrients (N, P)

Coccosphere, cell, and coccolith sizes in coccolithophores respond sensitively to nutrient availability, although the direction and extent of these changes depend on nutrient type and growth phase. Under P-replete conditions, *G. huxleyi* typically exhibits smaller cells and coccospheres with fewer coccoliths per cell, reflecting rapid growth and high division rates (Shiraiwa, 2003; Müller *et al.*, 2008). In contrast, P limitation often leads to increased cell size, larger coccospheres, and elevated calcite content without inducing coccolith malformations, although strain-specific changes such as over-calcification can occur (Oviedo *et al.*, 2014; Aloisi, 2015; Müller *et al.*, 2021b). As cultures transition into the stationary phase due to nutrient depletion, further increases in coccosphere size and coccolith number per cell are commonly observed across species,

including *G. huxleyi*, *G. oceanica*, *C. leptoporus*, *H. carteri*, and *C. braarudii* (Shiraiwa, 2003; Sheward *et al.*, 2017). N limitation, by contrast, generally reduces cell size or volume (Muggli *et al.*, 1996; Müller *et al.*, 2008; Kaffes *et al.*, 2010), though it may also lead to increased cellular calcite content (Müller *et al.*, 2008). Sinking rate responses to N limitation appear growth-phase dependent, with reduced rates during exponential phase and increased rates in stationary phase (Pantorno *et al.*, 2013), Nutrient form further modulates size-related traits, *G. huxleyi* cells grown on ammonium tend to exhibit larger volumes than those grown on nitrate (Lecourt *et al.*, 1996).

1.3.2.5 Major and trace elements

Size responses of coccolithophore coccospheres, cells, and coccoliths to changes in major and trace element concentrations remain less well documented than physiological or geochemical traits. Among the limited examples, Co exposure in *P. carterae* led to marked cell enlargement, with volumes exceeding threefold that of the control at 200 µM Co^{2+}, accompanied by vacuolization and inhibited division (Blankenship & Wilbur, 1975). In *G. huxleyi*, Ca^{2+} limitation eliminated coccosphere formation and produce thin, brittle coccoliths at 1 mM Ca^{2+}, while morphologically intact coccoliths were restored at concentrations ≥5 mM Ca^{2+} (Herfort *et al.*, 2004; Leonardos *et al.*, 2009). Deviations from ambient Mg concentrations similarly induced coccolith malformation in *G. huxleyi*, suggesting reduced or irregular coccolith size (Herfort *et al.*, 2004).

1.3.2.6 Salinity

Under salinity stress, coccosphere, cell, and coccolith sizes show strain- and species-specific trends. Lower salinity generally reduces coccosphere and coccolith sizes, whereas higher salinity often maintains or increases size, particularly in strains adapted to more variable or saline environments (Gebühr *et al.*, 2021; Sheward *et al.*, 2024). In hypersaline conditions (45‰), *G. huxleyi* strain RCC1232 (Mediterranean origin) maintained stable morphologies, while PLYB11 (Norwegian coastal origin) exhibited pronounced enlargement (Sheward *et al.*, 2024). At hyposaline conditions (25‰), both strains showed size reductions, though with strain-specific timing and magnitude (Sheward *et al.*, 2024). Longer-term culture studies further support these findings. In *G.*

huxleyi, coccolith size increased with salinity in several strains, although coccolith thickness often remained constant, decoupling length from mass (Johnsen *et al.*, 2019). Arctic and subarctic strains similarly show size reductions at low salinity (Saruwatari *et al.*, 2016). Strains originating from high-salinity environments tend to better maintain or increase coccolith size under elevated salinity, whereas strains from low-salinity habitats exhibit impaired calcification and reduced coccolith size when salinity declines (Paasche *et al.*, 1996; Gebühr *et al.*, 2021). Morphological changes are often more pronounced in coccosphere size than coccolith size and can occur within 24-48 hours of salinity shifts (Sheward *et al.*, 2024). Despite these changes, coccolith number per cell often remains stable, indicating that morphology is more sensitive to salinity stress than production rate (Paasche *et al.*, 1996). *G. oceanica* exhibits a more integrated morphological response, with an increase in both coccolith length and thickness contributing to higher coccolith mass (Johnsen *et al.*, 2019).

1.3.3 Photosynthetic responses

1.3.3.1 Temperature

Direct measurements of coccolithophore photosynthesis in response to temperature remain limited, but available studies suggest that *G. huxleyi* exhibits an optimal thermal range for carbon fixation. Under nutrient-replete, nitrate-based conditions, photosynthesis and POC production typically increase with temperature up to 20-25 °C (Rosas-Navarro *et al.*, 2016; Bradley & Laws, 2024). Elevated CO_2 can further enhance POC production within this range, particularly under moderate light conditions (Feng *et al.*, 2008; Tong *et al.*, 2019). Beyond the thermal optimum, however, photoinhibition and the accumulation of reactive oxygen species (ROS) impair photosystem function, limiting photosynthetic efficiency (Tong *et al.*, 2019). While both temperature and CO_2 influence chlorophyll *a* content, nitrate availability can exert an even stronger control under certain conditions (Feng *et al.*, 2008, 2017). At high temperatures, thermal variability reduces POC production (Wang *et al.*, 2019), and warming from 20 °C to 24 °C significantly suppresses POC accumulation when ammonium replaces nitrate as the N source (Wang *et al.*, 2024). Over longer timescales, adaptation to elevated temperatures can restore or

even enhance POC production, as demonstrated in experimentally evolved *G. huxleyi* populations (Schlüter *et al.*, 2014).

1.3.3.2 Ocean acidification

OA profoundly affects the photosynthetic physiology and organic carbon dynamics of coccolithophores. Under CO_2-induced acidification, as distinct from direct chemical acidification, key photochemical parameters, such as the maximum quantum yield of photosystem II (Fv/Fm) and electron transport rates, generally remain stable or are slightly stimulated (Iglesias-Rodriguez *et al.*, 2008; Fukuda *et al.*, 2014). As pH declines further, however, coccolithophores tend to shift their inorganic carbon uptake from predominantly HCO_3^- towards greater reliance on dissolved CO_2, altering electron transport efficiency and carbon fixation pathways (Kottmeier *et al.*, 2014, 2016a,b). In coastal environments, reduced salinity can further enhance PSII quantum yield and accelerate photodamage repair (Xu *et al.*, 2020).

Elevated CO_2, particularly when combined with high irradiance, often leads to reduced cellular pigment concentrations (e.g., chlorophyll a, carotenoids) and lowers the saturating light thresholds for maximum electron transport (Zhang & Gao, 2021; Wu *et al.*, 2023). Under such high-light conditions, including ultraviolet exposure, net photosynthetic rates can be maintained or even promoted, leading to elevated POC production (Jin *et al.*, 2017). Although elevated CO_2 may induce metabolic stress and ROS generation, coccolithophores maintain overall photochemical efficiency through robust PSII repair mechanisms (McCarthy *et al.*, 2012; O'Dea *et al.*, 2014).

In addition to these photochemical responses, CO_2 enrichment can modestly stimulate photosynthetic oxygen evolution (Iglesias-Rodriguez *et al.*, 2008) and, in non-calcifying strains under high light and nutrient limitation, enhance CO_2 fixation into organic matter (Leonardos & Harris, 2006). Multi-factorial simulations of future ocean conditions, integrating acidification, warming and stratification, predict a moderate reduction in POC production relative to calcification rates (Müller *et al.*, 2017). Nevertheless, light intensity remains a dominant factor shaping pigment composition, even under acidified conditions (Heidenreich *et al.*, 2019). It is important to note that most of these detailed

photophysiological observations are derived from *G. huxleyi*; comparable data for other coccolithophore species remain limited.

1.3.3.3 Irradiance

Photosynthesis and POC production in coccolithophores are strongly influenced by irradiance, with responses modulated by species identity, nutrient availability, CO_2 concentration, and life-cycle phase. In *G. huxleyi*, photosynthetic rates typically increase with irradiance up to a species- or strain-specific saturation threshold, beyond which photoinhibition often occurs, especially under nutrient-limiting conditions or in haploid cells exhibiting greater light sensitivity than diploids (Houdan *et al.*, 2005; Ruan *et al.*, 2023). At low to moderate irradiance, cells enhance light-harvesting efficiency through elevated chlorophyll content and optimised electron transport (Nielsen, 1997; McKew *et al.*, 2013). At the same time, high-light exposure promotes the expression of photoprotective pigments such as diadinoxanthin and diatoxanthin to mitigate photodamage (McKew *et al.*, 2013; Garrido *et al.*, 2016). Under nutrient-replete conditions, elevated irradiance enhances POC production; however, this stimulation declines or reverses under nitrate or phosphate limitation, often due to impaired Rubisco activity and disrupted carbon allocation (Feng *et al.*, 2017; Zhang & Gao, 2021). In some cases, elevated irradiance exacerbates CO_2-induced suppression of photosynthesis and POC production (Zhang *et al.*, 2015, 2020), while in others, increased light partially mitigates these effects by enhancing photosynthetic energy supply (Feng *et al.*, 2008). Notably, calcified diploid cells often maintain higher photosynthetic performance under strong light, likely due to coccolith-mediated shading and enhanced bicarbonate utilisation (Grubb *et al.*, 2024). In contrast, non-calcifying or haploid cells experience greater photoinhibition and oxidative stress (van de Poll *et al.*, 2007; Ruan *et al.*, 2023).

Other coccolithophore species exhibit comparable but species-specific responses to irradiance. In *G. oceanica*, photosynthetic carbon fixation increases with irradiance up to an optimum, but elevated CO_2 and nutrient limitation reduce light-use efficiency and intensify photoinhibition (Zhang *et al.*, 2015; Tong *et al.*, 2016). The N source also modulates light responses, with ammonium-grown cells generally showing improved tolerance to high light compared to those grown on nitrate (Tong *et al.*, 2016). In *P.*

carterae, OA inhibits POC production, but this effect weakens under high irradiance, suggesting partial compensation by light-driven energy supply (Wu *et al.*, 2023). Conversely, *S. apsteinii*, a low-light-adapted species, reduces its light requirement under elevated CO_2 but exhibits heightened sensitivity to environmental stress under high irradiance (Gafar *et al.*, 2019), reflecting a more constrained ecological niche.

1.3.3.4 Nutrients (N, P)

Photosynthesis and POC production in *G. huxleyi* are highly responsive to nutrient availability. Under N limitation, *G. huxleyi* maintains PSII function for extended periods, showing reduced susceptibility to photoinactivation and sustained PSII repair capacity, thereby enabling prolonged photosynthetic activity under nutrient stress (Loebl *et al.*, 2010). However, nitrate limitation significantly decreases photosynthetic oxygen evolution and HCO_3^- uptake rates, resulting in reduced carbon fixation and lower POC production (Kaffes *et al.*, 2010). N-starved cells also exhibit reduced chlorophyll content and impaired fluorescence parameters, although the accumulation of photoprotective xanthophyll pigments, particularly through the diadinoxanthin-diatoxanthin cycle, helps mitigate photodamage (Zhao *et al.*, 2015).

P limitation also constrains photosynthesis and POC production. In *G. huxleyi*, P limitation triggers phospholipid substitution, cytoplasmic recycling mechanisms, chloroplast structural alterations, and diminished pigment synthesis, all contributing to decreased photosynthetic performance (Shemi *et al.*, 2016). Despite these physiological impairments, P-limitation often increases cellular POC content across multiple strains (Müller *et al.*, 2008; Oviedo *et al.*, 2014), indicating a shift in carbon allocation under nutrient stress. Grown on dissolved organic P (e.g., phytic acid), can enhance photosynthetic carbon fixation and increase carbon accumulation, though excessive DOP may exert adverse effects (Li *et al.*, 2023). These shifts are reflected in strongly elevated cellular C:P and N:P ratios under P-deficient conditions (Sheward *et al.*, 2023), indicating enhanced carbon fixation relative to P assimilation.

Comparatively few studies have examined nutrient effects on other coccolithophores. Under nitrate-limited conditions, *G. oceanica* shows reduced chlorophyll *a* content and maximal relative electron transport rate ($rETR_{max}$), yet maintains relatively stable Fv/Fm

values, indicating sustained photochemical efficiency under N stress (Jiang *et al.*, 2022). Additionally, N source influences POC production and photophysiological traits in *G. oceanica*, with nitrate-grown cells exhibiting higher non-photochemical quenching (NPQ) under medium and high irradiance than ammonium-grown cells (Tong *et al.*, 2016).

1.3.3.5 Major and trace elements

Direct assessments of photosynthetic performance and pigment composition in coccolithophores in response to major and trace element concentrations remain limited and yield mixed results. Under low Ca^{2+} conditions (0-10 mmol L^{-1}), no significant changes in photosynthetic O_2 evolution, chlorophyll-a content, or growth rate were observed in *G. huxleyi* (Leonardos *et al.*, 2009). Similarly, POC production and the maximum photosynthetic rate remained stable across this Ca^{2+} range (Trimborn *et al.*, 2007). However, a contrasting study reported significant reductions in both POC and Fv/Fm at Ca^{2+} concentrations below 2 mmol L^{-1} (Müller *et al.*, 2015a).

At elevated Ca^{2+} levels (>25 mmol L^{-1}), chlorophyll-a content declined in both *G. huxleyi* and *C. braarudii* under normal (50 mmol L^{-1}) and low Mg^{2+} (25 mmol L^{-1}) conditions, whereas a reduction in POC production was observed only in *G. huxleyi* (Müller et al., 2011). Additionally, chlorophyll-a content declined in *G. huxleyi* grown under low Mg^{2+} (Müller et al., 2011). In contrast, another study found that reductions in both POC production and Fv/Fm under elevated Ca^{2+} (>10 mmol L^{-1}) were restricted to a non-calcifying *G. huxleyi* strain, while calcifying strains of *G. huxleyi* and *G. oceanica* maintained stable photosynthetic performance and POC production across a wide Ca^{2+} range (10-40 mmol L^{-1}) (Müller *et al.*, 2015a).

In contrast to the comparatively modest or indirect effects of major ions on photosynthesis, Fe availability exerts a more direct control over carbon acquisition and growth. Fe limitation suppresses active CO_2 and HCO_3^- uptake, resulting in decreased carbon fixation and slower growth in *G. huxleyi* (Schulz *et al.*, 2007). Experimental Fe enrichment stimulates photosynthesis and promotes bloom formation under ambient CO_2 levels, but this enrichment is diminished under OA conditions, suggesting that elevated CO_2 may counteract Fe-driven stimulation of photosynthetic performance

(Rosario Lorenzo *et al.*, 2018). Under Fe stress, reductions in cell volume may also reflect decreased POC production (Muggli *et al.*, 1996).

1.3.3.6 Salinity

Photosynthetic responses to salinity change are less well studied but indicate moderate plasticity. In one study, a small increase in POC production was observed in a larger *G. huxleyi* strain as salinity rose from 25‰ to 45‰, while no significant change occurred in a smaller strain (Sheward *et al.*, 2024). Low salinity (25-30) has been shown to enhance photosynthetic performance under high light by increasing pigment concentrations and, under low light, by boosting effective quantum yield (Xu *et al.*, 2020).

1.3.4 Calcification responses

1.3.4.1 Temperature

Temperature influences coccolithophore calcification and PIC production in a species- and strain-specific manner, with outcomes further shaped by interacting environmental factors. In *G. huxleyi*, warming from 10 °C to 20-25 °C generally enhances PIC production under nutrient-replete conditions, primarily through increased coccolith thickness and mass (Rosas-Navarro *et al.*, 2016). However, supra-optimal temperatures (≥25-28 °C) often lead to declines in PIC production, increased coccolith malformations, and overall physiological stress (Wang *et al.*, 2019; Armstrong & Law, 2023). Long-term exposure to warming and acidification can reduce PIC content and calcification rates by up to 50%, accompanied by decreases in cell and coccolith size (Armstrong & Law, 2023). In contrast, experimental evolution over one year under similar conditions restored both PIC and growth rates, indicating the potential for long-term adaptation (Schlüter *et al.*, 2014).

Calcification responses also occur across strains. Some maintain stable calcification across 10-28 °C (Bradley & Laws, 2024), while others show strain-specific variation in PIC and coccolith shedding, often dependent on growth phase and temperature (Matson *et al.*, 2016). Low temperatures can also stimulate calcification. For instance, cold stress alone at 10 °C increased PIC production despite delayed growth (Sorrosa *et al.*, 2005), and phosphate limitation at 12 °C further enhanced PIC and Ca^{2+} uptake (Satoh *et al.*,

2009). Temperature also interacts with light and CO_2, elevated CO_2 and light at 24 °C reduced PIC and coccolith thickness (Feng *et al.*, 2008), while UVA exposure enhanced calcification at 15-20 °C but not at 24 °C (Tong *et al.*, 2019). Mild warming to 20 °C under high CO_2 also increased coccolith malformations (Milner *et al.*, 2016).

1.3.4.2 Ocean acidification

Calcification in coccolithophores generally decreases under OA, although the extent of response varies by species, strains, and environmental context. In *G. huxleyi*, reduced calcite production and increased coccolith malformation are commonly observed under elevated CO_2 (Riebesell *et al.*, 2000). Notably, the method of acidification influences outcomes. Direct HCl addition, as opposed to CO_2 bubbling, significantly suppresses Ca^{2+} uptake (Fukuda *et al.*, 2014). Comparison between the two methods suggests that chemically lowered pH via HCl triggers more severe reductions in calcification than CO_2-induced acidification at equivalent pH (Kottmeier *et al.*, 2016b). this reduced availability of bicarbonate, by lower pH, appears to be a key factor limiting $CaCO_3$ production (Herfort *et al.*, 2002). Manipulative experiments altering CO_2, HCO_3^-, and pH confirm that reduced bicarbonate availability combined with lower pH increases coccolith malformations and reduces coccolith size and weight (Bach *et al.*, 2011, 2012, 2013; Xie *et al.*, 2021). While HCO_3^- and CO_2 promote calcification, H^+ acts as an inhibitor (Bach *et al.*, 2015). Despite these general trends, exceptions exist. Some studies report insignificant changes in calcification (Richier *et al.*, 2011), while others show enhanced calcification and coccolith mass under high CO_2 (Iglesias-Rodriguez *et al.*, 2008) . Moreover, long-term adaptation can restore calcification rates under elevated CO_2 levels (Schlüter *et al.*, 2016).

Environmental interactions further modulate the calcification response. Nitrate limitation combined with low pH suppresses calcification by restricting substrate supply for $CaCO_3$ precipitation (Zhang *et al.*, 2019; Jiang *et al.*, 2022). OA coupled with warming generally reduces calcite mass and increases coccolith malformations (D'Amario *et al.*, 2020), with responses varying by strain and thermal optimum (Sett *et al.*, 2014). Nutrient limitation often intensifies the inhibitory effects of elevated CO_2 on PIC quotas (Zhang *et*

al., 2019, 2020). Light regime also plays a role. UVB radiation inhibits calcification, whereas UVA can enhance it under elevated CO_2 (Tong *et al.*, 2019).

Species-specific differences are also evident. *O. neapolitana* maintains constant calcification rates by stabilising pH at the calcification site despite external acidification (Liu *et al.*, 2018). In *G. oceanica*, PIC production can increase under nitrate limitation and elevated CO_2 (Zhang *et al.*, 2015; Jiang *et al.*, 2022), and warming may partially mitigate OA-related declines (Gafar & Schulz, 2018). *H. carteri* exhibits relatively low sensitivity of its PIC quota to rising CO_2 (Gafar *et al.*, 2019; Bianco *et al.*, 2024). Additionally, *P. carterae* enhances coccolith production at night when grown under elevated CO_2 but constant pH (Moheimani & Borowitzka, 2011), underscoring the role of diel and chemical context in calcification regulation.

1.3.4.3 Irradiance

Calcification and PIC production in coccolithophores are rarely studied in isolation and are commonly examined alongside additional environmental factors. In *G. huxleyi*, increased irradiance generally leads to decreased calcification under both ambient and elevated pCO_2 levels, particularly when nutrients are limited (Feng *et al.*, 2008; Zhang *et al.*, 2015). The combination of high light and acidification further reduced PIC production in *G. huxleyi* across multiple strains, with light intensifying the negative effects of CO_2 (Zhang & Gao, 2021). Coccolith production peaked at low light, with increased coccolith shedding at higher irradiance, and PIC production saturating at lower light levels than photosynthesis (Moheimani *et al.*, 2012). Increasing irradiance from 40 to 120 µmol photons m^{-2} s^{-1} leads to reduced cell size, coccosphere volume, and PIC production, with calcification being more sensitive than POC production (Grubb *et al.*, 2024). Morphological traits also shift with irradiance, *G. huxleyi* cell, coccosphere, and coccolith sizes decrease under high light, both under nutrient-replete and P-limited conditions (Aloisi, 2015; Müller *et al.*, 2021b).

Similar to *G. huxleyi*, *G. oceanica* exhibits reduced PIC production under elevated light, with this reduction exacerbated by high CO_2 or P limitation (Zhang *et al.*, 2015; Tong *et al.*, 2016). In contrast to the more robust responses seen in *G. huxleyi* and *G. oceanica*, *S. apsteinii* exhibits narrower tolerance to irradiance changes, high light combined with

elevated CO_2 significantly decreases PIC production (Gafar *et al.*, 2019). In *C. braarudii*, physiological responses to irradiance are life-cycle-dependent; the diploid phase suffers calcification defects at high light, while the haploid phase shows greater tolerance, maintaining performance across a broader irradiance range (Langer *et al.*, 2023).

1.3.4.4 Nutrients (N, P)

Calcification in coccolithophores exhibits nutrient-specific responses that are further modulated by interacting environmental drivers. In *G. huxleyi*, P limitation leads to significant increases in cellular calcite content (Shiraiwa, 2003; Müller *et al.*, 2008), and coccolith volume (Müller *et al.*, 2021b), particularly after the transition to stationary phase when cell division slows (Müller *et al.*, 2008). However, the magnitude of this enhancement is strain-specific, with variable PIC and POC increases observed across Mediterranean isolates (Oviedo *et al.*, 2014). P limitation has also been associated with increased coccosphere and coccolith size (Aloisi, 2015). When combined with heat stress, however, P limitation results in reduced calcification and increased coccolith malformation in *G. huxleyi*, *C. braarudii* and *C. pelagicus* (Gerecht *et al.*, 2014, 2018). In contrast, N limitation strongly suppresses PIC production and coccolith volume in both *G. huxleyi* and *G. oceanica* (Müller *et al.*, 2021b; Jiang *et al.*, 2022), significantly reducing calcification rates. These negative effects are further amplified by increased light intensity (Zhang *et al.*, 2019). At the same time, ammonium as the N source leads to greater reductions in PIC compared to nitrate under both low and high CO_2 (Lefebvre *et al.*, 2012) and high light (Tong *et al.*, 2016).

1.3.4.5 Major and trace elements

As the primary substrate for calcification, Ca^{2+} has been the most intensively studied element influencing coccolithophore calcification, whereas the effects of other elements remain comparatively understudied. *G. huxleyi* completely loses its ability to calcify at 0-0.1 mM Ca^{2+} (Herfort *et al.*, 2004; Trimborn *et al.*, 2007; Leonardos *et al.*, 2009; Nam *et al.*, 2019). Increasing Ca^{2+} concentrations from this threshold up to approximately 20-25 mM enhances PIC production (Herfort *et al.*, 2004; Trimborn *et al.*, 2007; Leonardos *et al.*, 2009; Müller *et al.*, 2011), while higher concentrations (e.g., 50 mM) strongly inhibit calcification and cause coccolith malformation (Herfort *et al.*, 2004;

Müller *et al.*, 2011). *G. huxleyi* also respond sensitively to Mg^{2+}, with under-calcification and malformed coccoliths observed at both low and high Mg^{2+}, while optimal morphology is preserved only at ambient seawater Mg concentration (58 mM) (Herfort *et al.*, 2004).

High Sr^{2+} concentrations reduce calcite production in *G. huxleyi* and alter coccolith mineralogy, with transitions from calcite to aragonite and ultimately to strontianite formation under increasing Sr^{2+} stress (Sun *et al.*, 2018). In contrast, larger coccolith-forming species such as *Scyphosphaera* and *Pontosphaera* appear capable of forming well-developed coccoliths even under Sr-enriched conditions (Hermoso *et al.*, 2017). In *P. carterae*, Co^{2+} exhibits a biphasic effect on calcification, enhancing Ca uptake at 100 µM but inhibiting it at 200 µM, accompanied by ultrastructural changes such as vacuolar expansion and dense body accumulation (Blankenship & Wilbur, 1975).

Silicon (Si) plays a crucial structural role in coccolith morphogenesis in certain coccolithophores, particularly those producing complex heterococcoliths (Durak *et al.*, 2016, 2017; Langer *et al.*, 2021). Si deprivation leads to malformed coccoliths without affecting growth or photosynthesis (Durak *et al.*, 2017), although this requirement appears to be species- and life-cycle-specific, as holococcolith formation is generally unaffected by Si availability (Langer *et al.*, 2021).

Lastly, unlike Ca, Mg, Sr, or Si, which exert direct biochemical or structural control over coccolith formation, iron availability primarily influences calcification indirectly by modulating coccolithophore biomass and bloom dynamics. Fe stress alone shows little effect on *G. huxleyi* sinking rates (Muggli *et al.*, 1996). However, under low CO_2 conditions, increased dissolved iron in coastal mesocosms enhances particulate $CaCO_3$ production and bloom formation (Lorenzo et al., 2018).

1.3.4.6 Salinity

Coccolithophore calcification responses to salinity exhibited relatively consistent patterns. In *G. huxleyi*, low salinity conditions (17-26‰) are consistently associated with reduced coccolith size, calcite mass per coccolith, and the appearance of undercalcified morphologies (Paasche *et al.*, 1996; Saruwatari *et al.*, 2016; Sheward *et al.*, 2024). Calcification rates remain relatively stable at moderate salinity (25-35‰) (Xu *et al.*, 2020).

In contrast, high salinity conditions (up to 44-45‰) lead to increased coccolith size and/or enhanced calcification in certain *G. huxleyi* strains (Johnsen *et al.*, 2019; Sheward *et al.*, 2024), although this response is strain-specific (Gebühr *et al.*, 2021). Additionally, *G. oceanica* shows consistent increases in both coccolith length and thickness with rising salinity, resulting in a more pronounced calcification response (Johnsen *et al.*, 2019).

1.3.5 Response of PIC: POC ratio to environmental drivers

In coccolithophores, both PIC and POC production exhibit complex, interactive responses to environmental factors such as temperature, CO_2, nutrients, and irradiance. Generally, increased temperature enhances both PIC and POC production in *G. huxleyi* across a range of 6-26 °C, however, the stimulation varies, resulting in PIC: POC ratios that peak at sub-optimal temperatures (~14-18 °C) and reach a minimum near the optimal growth temperature (~18-22 °C) (Tong *et al.*, 2016; Rosas-Navarro *et al.*, 2016; Bradley & Laws, 2024). When temperature increases from 10°C to 15°C and 20°C, both *G. huxleyi* and *G. oceanica* show increases in both POC and PIC production (Sett *et al.*, 2014). Temperature effects often interact with other environmental factors. Rising temperature from 15°C to 20°C amplifies the negative impact of high pCO_2 on coccolith morphology and reduces PIC:P OC ratios by 40-60% while promoting organic carbon production (Milner *et al.*, 2016). in *C. pelagicus*, 5°C temperature increase (10°C to 15°C) led to a reduction in PIC: POC ratios by 40-60%, regardless of P availability (Gerecht *et al.*, 2014), highlighting the warming impact.

The response to CO_2 gradient (0.5 to 6000 µatm) initially promotes POC and PIC production, with PIC: POC ratios peaking at species-specific CO_2 optima (Sett *et al.*, 2014). Higher CO_2 levels strongly inhibit PIC production more than POC, leading to a decrease in PIC: POC ratios (Sett *et al.*, 2014). Both PIC and POC production exhibit a unimodal response to pCO_2, with strain-specific optima generally occurring between 300 and 600 µatm in *G. huxleyi* and *G. oceanica* (Sett *et al.*, 2014; Zhang *et al.*, 2018), and in *S. apsteinii* (Gafar *et al.*, 2019). Some studies show a monotonic decline in PIC production with increasing CO_2, accompanied by elevated coccolith malformations and reduced PIC: POC ratios in both *G. huxleyi* and *G. oceanica* (Riebesell *et al.*, 2000). A

unimodal response in POC combine with a monotonic decline in both PIC production and PIC: POC ratios in response to pCO_2 under nutrient-replete conditions is also documented (Müller *et al.*, 2017), although such responses are ecotype-specific (Müller *et al.*, 2015b). This discrepancy may be attributed to differences in experimental resolution and sampling density. Exceptions exist where both PIC and POC show a constant increase at elevated CO_2 (up to ~750 µatm), leading to a constant PIC: POC ratio (Iglesias-Rodriguez *et al.*, 2008). Increased H^+, rather than CO_2 itself, led to a significant decline in HCO_3^- uptake (Kottmeier *et al.*, 2016a), which adversely affected calcification (Bach *et al.*, 2011). At the same time, photosynthetic processes remained relatively stable across varying pH levels (Bach *et al.*, 2011; Fukuda *et al.*, 2014), therefore lead t o a low PIC: POC ratios at low pH regardless CO_2 levels (Xie *et al.*, 2021). Notably, over long-term adaptation, *G. huxleyi* shows recovery of PIC production under combined high pCO_2 and elevated temperature, resulting in a stable PIC: POC ratio despite environmental stress (Benner *et al.*, 2013). Similarly, after 2100 generations of evolution under high CO_2, *G. huxleyi* adjusted both PIC and POC production, maintaining an unaffected PIC: POC ratio through coordinated changes, even though absolute calcification declined (Schlüter *et al.*, 2016).

Both PIC and POC production in *G. huxleyi* increased with light, but the PIC: POC ratio shows a unimodal response, rising at low light where PIC increases more than POC, and declining at high light where POC increases more than PIC (van Bleijswijk *et al.*, 1994). Similarly, both *S. apsteinii* (Gafar *et al.*, 2019) and *P. carterae* (Wu *et al.*, 2023) exhibit a unimodal response in both PIC and POC production to light intensity, with optima generally occurring between 50 and 250 μmol photons m^{-2} s^{-1}, although the exact peak intensity varies with ambient CO_2 levels.

In *G. huxleyi*, nutrient limitation (low nitrate and phosphate) increases PIC quotas, while POC production is variably affected depending on the limiting nutrient and light conditions (Zhang *et al.*, 2019). Under nitrate limitation, POC is suppressed whereas maximum PIC production increases, particularly under high light intensity (500 µmol photons m^{-2} s^{-1}), resulting in elevated PIC: POC ratios, regardless of CO_2 level (Zhang *et al.*, 2019; Zhang & Gao, 2021). Nutrient limitation exerts a stronger influence than elevated pCO_2 on both PIC and POC quotas (Zhang *et al.*, 2020). High pCO_2 enhanced

POC quotas particularly under phosphate limitation at low temperature, but does not stimulate calcification unless nutrient stress is also present(Zhang *et al.*, 2020). Consequently, the PIC: POC ratio increases under dual nutrient limitation regardless of CO_2 level (Zhang *et al.*, 2020, 2023). However, the pCO_2 impact on photosynthesis during P limitation shows opposite changes across a broad range of light intensities where P dominants the impact, suppressing photosynthetic rate and leading to increase in PIC: POC ratios (Zhang & Gao, 2021). Another response pattern is evident where N and P limitation reduce both PIC and POC production, along with a decrease in PIC: POC ratios (Müller *et al.*, 2017). The PIC production sensitivity in response to nutrients is strain-specific (Iglesias-Rodriguez *et al.*, 2017). The N form also matters, with nitrate as the N source, high temperature reduces photosynthesis activity; under ammonium conditions, increasing temperature further depresses photosynthetic rates while enhancing PIC, leading to a significant increase in PIC: POC ratios at high temperature (24°C) under ammonium conditions (Wang *et al.*, 2024).

The interactions between environmental factors create complex responses in coccolithophores. An increase in nitrate, P, temperature, and CO_2 all lead to increases in photosynthetic rate, with irradiance showing an optimal range where further increases inhibit photosynthesis (Feng *et al.*, 2017). Calcification is more sensitive, with high irradiance, temperature, and pCO_2 all inhibiting its activity (Feng *et al.*, 2017). Therefore, the calcification to photosynthesis ratio decreases with increases in nitrate, P, irradiance, and pCO_2, increases with temperature rising to its optimum at around 15°C, and further decreases with increasing temperature (Feng *et al.*, 2017). At 24°C, *G. huxleyi* experiences a stronger impact from high irradiance than from temperature and CO_2 on PIC production, significantly reducing PIC: POC ratios by decreasing PIC content (Feng *et al.*, 2008). For *G. huxleyi*, elevated CO_2 increases POC production across light levels, but its negative impact on calcification is mitigated under high light levels, leading to a low PIC: POC ratios under high CO_2 and low light conditions (Jin *et al.*, 2017). Under OA and UV stress, *G. huxleyi* exhibited a drastic decline in PIC production (up to 99%), a moderate reduction in POC (6-15%), and a sharp decrease in the PIC: POC ratio (Gao *et al.*, 2009).

These physiological insights significantly advance our understanding of coccolithophore responses to environmental change; however, most investigations have concentrated on *G. huxleyi*, leaving many other coccolithophore species relatively understudied. Additionally, research efforts have not been evenly distributed across environmental drivers, with extensive exploration of factors like OA and temperature, but limited data on elements such as salinity and trace metals. The considerable discrepancies across studies regarding experimental approaches, strain-specific responses, and trait interactions create uncertainty in synthesising a cohesive understanding. Consequently, future research that encompasses a broader spectrum of environmental conditions and targets representative species diversity is critical, particularly emphasising molecular-level investigations into the regulatory mechanisms underpinning observed physiological responses.

1.4 Aims and objectives of this thesis

This thesis aims to unravel the physiological and molecular mechanisms that govern the regulation of calcification and its integration with broader metabolic processes in coccolithophores, with a particular focus on diel rhythms, growth phase transitions, ionic stress, and interspecific variability. By exploring how calcification is coordinated with cellular metabolism under varying environmental conditions, this work seeks to advance our understanding of coccolithophore functional resilience and their role in the marine carbon cycle.

The specific objectives are to:

1. Investigate diel regulation of cellular physiology and proteome expression, particularly the temporal coordination between photosynthesis and calcification.
2. Characterise metabolic reprogramming during growth phase transitions, with emphasis on changes in carbon allocation and physiological decoupling.
3. Examine the physiological and proteomic responses to Mg availability as a representative ionic stressor, including its effects on calcification, cell size, and metabolic regulation.

4. Compare species- and strain-specific responses across coccolithophores differing in cell size and calcification intensity, to identify size-dependent metabolic strategies and stress responses.

1.5 Thesis outline

Chapter 2 presents diel time-series analyses in *G. huxleyi*, revealing 24-hour rhythmicity in proteome expression and physiological traits including cell size, coccosphere size, chlorophyll-a content, and calcification. It identifies key metabolic pathways underlying temporal coordination and further examines growth phase transitions, focusing on physiological shifts and proteomic reprogramming from exponential to stationary phase. These transitions highlight how nutrient limitation restructures metabolic priorities and constrains calcification capacity.

Chapter 3 investigates the cellular responses of *G. huxleyi* to varying Mg concentrations, integrating physiological and proteomic data to elucidate Mg-dependent control of calcification, growth, and protein expression. The chapter also explores interactions among physiological traits, particularly between photosynthesis and calcification, and examines the molecular underpinnings of these responses.

Chapter 4 expands the analysis to multiple coccolithophore species and strains, comparing cell size, metabolic profiles, and calcification under both non-limiting and stress conditions to assess the generality of regulatory mechanisms. It also synthesises responses under the same experimental framework as Chapter 3 to evaluate coordinated patterns among cell size, pigment content, and calcification across taxa.

Chapter 2 Proteomic and Physiological Adaptations of *Gephyrocapsa huxleyi* to Diel Cycles and Growth-Phase Transitions

Abstract

Like many phytoplankton, coccolithophores grow predominantly during the daytime and divide at night, yet the molecular regulation underlying these diel rhythms remains poorly understood. In particular, how cellular processes are temporally coordinated across the diel cycle, and whether this coordination is reorganised during the transition from exponential to stationary growth, has not been systematically examined. To address this, I investigated the cosmopolitan species *Gephyrocapsa huxleyi* (formerly *Emiliania huxleyi*) grown in batch culture under a 14:10 light: dark cycle. Physiology and proteomic samples were collected every 6 hours, spanning both diel cycles and nutrient depletion leading to a growth phase transition. I found that 43.5% of proteins exhibited a significant 24-hour cycle, highlighting rhythmic DNA replication processes. Moreover, in line with physiological variations, proteins showed distinct diel regulation: gene expression, protein biosynthesis and processing, RNA activities, and metabolite biosynthesis and accumulation primarily took place during the day, whereas DNA replication and cell division were more pronounced at night. During the transition from the late exponential to the early stationary phase of population growth, nutrient assimilation for nitrogen and phosphate was upregulated. I also observed an extended or heightened expression in energy metabolism, alongside a lag in peak expression for glycerolipid biosynthesis, light harvesting, and photosynthetic and respiratory electron transport chain proteins. Calcification occurred predominantly during daylight hours and gradually declined throughout the growth phase transition, presumably because of limited substrate (bicarbonate). No co-expressed proteins linked explicitly to calcification were identified. Collectively, these findings provide molecular evidence for diel regulation of core cellular processes and reveal how nutrient limitation during growth phase transition reshapes metabolic priorities. This chapter highlights the importance of sampling timing in molecular studies and suggests that lagged metabolic processes during stationary

phase may influence the dynamics of organic compound accumulation during coccolithophore blooms, with implications for their role in organic carbon export.

2.1 Introduction

Coccolithophores are unicellular marine algae that play a pivotal role in global carbon cycling, contributing significantly to primary production through photosynthesis and to biogeochemical cycling via calcification (Paasche, 2001; Brownlee *et al.*, 2021). By forming calcium carbonate ($CaCO_3$) coccoliths, these organisms regulate ocean alkalinity and serve as a crucial sink for atmospheric CO_2, directly influencing carbon sequestration and global carbon dynamics (Rost & Riebesell, 2004; Ziveri *et al.*, 2023). Their capacity to thrive under diverse environmental conditions highlights remarkable resilience (Poulton *et al.*, 2007, 2017; O'Brien *et al.*, 2013; Balch, 2018). However, their responses to abiotic factors like light and nutrient availability can profoundly alter their biological activity, geographic distribution, and contribution to the carbon cycle (Poulton et al., 2007; Nissen et al., 2018; Sheward et al., 2023; Zhang et al., 2023). Understanding the cellular mechanisms that regulate their growth and metabolism under dynamic environmental conditions is crucial for predicting their responses to global change.

The cell cycle is a fundamental biological process that drives cell reproduction, ensures accurate DNA replication and chromosome segregation, and preserves genetic integrity across generations (Nyberg *et al.*, 2002; Ambrosio *et al.*, 2015). At the population level, it underpins rapid growth under favourable conditions, resilience through DNA repair, and nutrient recycling, sustaining ecosystems and enabling ecological succession (Lin & Carpenter, 1995; Pascual & Caswell, 1997; Nowak *et al.*, 2023). Extensive research on model species has provided valuable insights into cell cycle regulatory mechanisms, including cyclin-CDK complexes and checkpoints (Barnum & O'Connell, 2014; Huysman *et al.*, 2014; Li *et al.*, 2016; Atkins & Cross, 2018), DNA replication and repair processes (Sclafani & Holzen, 2007), transcriptional and epigenetic regulation (Riba *et al.*, 2022), signalling pathways linking environmental cues to cell cycle progression (Cross & Umen, 2015; Feeney *et al.*, 2016; Cross, 2020), and systems biology approaches to model and predict cell cycle dynamics (Csikász-Nagy, 2009; Guo & Chen, 2024). Together, these studies highlight the complexity and adaptability of cell cycle regulation, revealing how

environmental factors intricately shape cellular processes and offering foundational frameworks to explore cell cycle dynamics in less-studied organisms, such as coccolithophores. In contrast, research on the cell cycles of coccolithophores is limited, with most studies focusing on diel cycle observations and physiological traits (Paasche, 2001; Müller *et al.*, 2008; Kottmeier *et al.*, 2020b), rather than the biological mechanisms controlling cell division and metabolism (Knies *et al.*, 2015; Hernández Limón *et al.*, 2020).

The light-dark cycle is an essential environmental feature resulting from Earth's rotation that creates predictable fluctuations in solar radiation and temperature, shaping physiological processes and gene expression in marine organisms (Ottesen *et al.*, 2013; Becker *et al.*, 2021). While hydrodynamics and nutrient supply are primarily driven by tides, wind and vertical mixing, diel changes in stratification and light penetration can indirectly influence nutrient gradients and availability. Together, these factors ultimately shaping ecosystems (Aylward *et al.*, 2015; Tsakalakis *et al.*, 2022; Muratore *et al.*, 2022). Like many marine phytoplankton (Nelson & Brand, 1979; Chisholm & Brand, 1981; Vaulot *et al.*, 1986; Fujiwara *et al.*, 2020), coccolithophores exhibit phased cell cycles under diel light-dark cycles. Distinct stages, such as cell division during the dark phase and biomass production during the light phase, characterise their diurnal rhythm (Nelson & Brand, 1979; Paasche, 2001; Müller *et al.*, 2008; Kottmeier *et al.*, 2020b). Physiological traits such as cell density, DNA concentration, cell size, particulate organic matter (POC), chlorophyll content, and calcification display diel periodicity. For instance, cell density and DNA concentration double during the night phase, while chlorophyll and calcification accumulate during the light phase (Linschooten *et al.*, 1991; Jochem & Meyerdierks, 1999; Müller *et al.*, 2008; Kottmeier *et al.*, 2020b). Light intensity and day length influence growth, with chlorophyll-a content per unit cell volume negatively correlated with these factors (Paasche, 1967). Calcification is stimulated by light and varies with growth stage (Paasche, 1969, 2001; Müller *et al.*, 2008). While these processes align closely with external light-dark cycles, evidence suggests an internal timer regulating cell division and diel rhythms (Chisholm & Brand, 1981; Price *et al.*, 1998; Sheward *et al.*, 2024), manifested as persistent diel oscillations in in vivo chlorophyll fluorescence (Brand, 1982), and time-dependent changes in photosynthetic capacity

(Pmax) and photosynthesis-irradiance relationships (Harding *et al.*, 1981), alongside diel regulation o carbon assimilation metabolic pathways (Hernández Limón *et al.*, 2020). However, species-specific differences exist. For example, *Pleurochrysis carterae* divides and calcifies irrespective of light-dark cycles (van der Wal. *et al.*, 1987; Godrijan *et al.*, 2022), whereas *Coccolithus pelagicus* ceases cell division in darkness (Langer *et al.*, 2023).

While periodicity in coccolithophore cell cycles and physiological processes like photosynthesis and calcification is well-documented (Paasche, 1967, 1969; Harding *et al.*, 1981; Kottmeier *et al.*, 2020b), the molecular mechanisms underlying these interactions remain poorly understood. Growth phase transitions, such as from the exponential to the stationary phases, significantly influence cell cycle progression and metabolic activity, affecting gene expression and metabolite production to meet the physiological demands of each stage (von Dassow & Montresor, 2011; Rengefors *et al.*, 2017; Olofsson *et al.*, 2022; Diaz *et al.*, 2023). For instance, calcification ceases in the stationary phase (Linschooten *et al.*, 1991), and coccolith detachment rates increase (Sheward *et al.*, 2024). Abiotic factors such as temperature, light and nutrient availability influence cell cycle dynamics in coccolithophores (Olson *et al.*, 1986). Nutrient limitation, for instance, extended the G1 phase under nitrogen (N) limitation (Müller *et al.*, 2008) with reduced protein accumulation (Olson *et al.*, 1986), increased cell size and calcite production under phosphorus (P) limitation (Müller *et al.*, 2008), boosted photosynthesis and calcification with nitrate addition (Balch *et al.*, 1992), and reduced cell cycling and metabolic reprogramming under P and N limitation (Rokitta *et al.*, 2016). However, the broader regulatory networks linking growth stage transitions, cell cycle progression, and metabolic shifts in response to diel cycles and other abiotic factors remain poorly understood in coccolithophores.

This study aims to elucidate how coccolithophores regulate their physiological and molecular processes during natural growth phase transition in response to diel light-dark cycling. To capture these dynamics, I used the model species *Gephyrocapsa huxleyi* in a batch culture setup, maintaining a 14:10 light-dark cycle and sampling every 6 hours to capture fine-scale physiological and proteomic changes. The batch culture setup allows nutrients to become progressively depleted over time and can also lead to additional

changes, including decreasing alkalinity and reduced light penetration as biomass accumulates, enabling us to observe the onset of the stationary phase under multiple resource and environmental constraints. Although simplified, this experimental approach simulates key aspects of natural population development in stratified surface waters, providing insight into how coccolithophores coordinate cellular processes across light-dark phases and evolving resource conditions. This contributes to a better understanding of their temporal regulation under ecologically relevant scenarios.

2.2 Method

2.2.1 Experiment setting

Gephyrocapsa huxleyi (strain OA1), originally isolated from the North Sea in 2011 (Rickaby *et al.*, 2016), was grown in sterile-filtered (0.22 µm) K/2 medium prepared in artificial seawater (Keller *et al.*, 1987). Cultures were grown in batch mode at 17°C under a 14:10 h light: dark cycle (45-75 µmol photons m^{-2} s^{-1}) with light from 6.00 to 20.00 local time. The reported light range (45-75 µmol photons m^{-2} s^{-1}) reflects spatial variation across the incubator shelf measured at the start of the experiment (i.e., distance and angle relative to the side-mounted lamps) rather than temporal changes. Cultures progressed to early stationary phase, during which increased biomass and self-shading likely reduced effective light availability compared to initial conditions. However, cultures were gently mixed prior to each sampling to resuspend settled cells, and the transparent culture flasks permitted light penetration from all sides, helping maintain more uniform exposure relative to stratified shading in natural water columns. Experimental cultures were maintained under the same conditions as the stock cultures. Before sampling, cultures were pre-acclimated for two sequential growth curves to ensure stable and synchronised physiological status across four biological replicates.

To optimise cell density for proteomics and ensure that both individual cell cycle and population growth stages were represented, cell density was monitored daily at 18.00 local time. Upon reaching $1x10^5$ cell ml^{-1} on day 4 at 18.00, samples were collected at 6-hour intervals for measuring key physiological and biochemical traits, including cell density, coccosphere and naked cell size, chlorophyll-a content, $CaCO_3$ content, and

proteomics profiles. The proteomics time series began at Day 4, 24.00, with the final sample collected on Day 7 at 12.00 (Figure 2. 1).

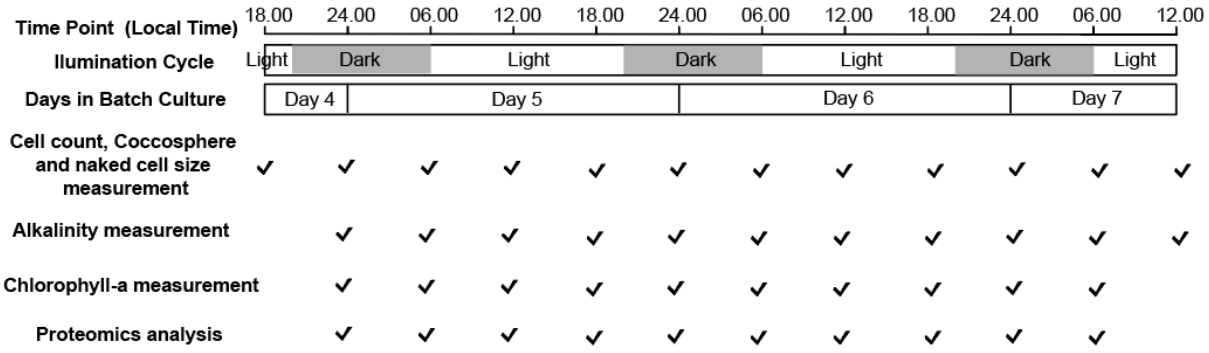

Figure 2. 1: Experimental design and data collection timeline of *Gephyrocapsa huxleyi* batch culture over diel cycle. The timeline begins on Day 4 at 18.00 local time and ends on Day 7 at 12.00 local time; alternating light (white) and dark (grey) shaded regions indicate the 14-hour light and 10-hour dark cycles maintained during the experiment; samples were collected every 6 hours, spanning from the mid-exponential to early stationary growth phases; check marks indicate the time points at which each measurement was taken, specifically, measurements included cell number and size, alkalinity for $CaCO_3$ content, chlorophyll-a concentration, and proteomics analysis. All times are in local time.

2.2.2 Measurement of cell density, size, and carbon content

Cell density, coccosphere size, and naked cell size were measured using a Multisizer 4 Particle Analyser (PN A51387A, Beckman Coulter, Inc., U.S.). For each replicate sample, two parallel preparations were made: one in a 35 ‰ NaCl buffer solution with additional 10 mM $CaCl_2$ to prevent dissolution for coccosphere size measurements, and the other in a 35% NaCl buffer solution with 10mM HCl for naked cell size measurements. A 1:20 ml cell culture dilution was used with each buffer solution.

Growth rates (μ, $6h^{-1}$) were calculated based on changes in cell number across 6-hour intervals throughout the time series:

$$\mu = \frac{lnc_2 - lnc_1}{\Delta t} \quad (2.\ 1)$$

where c_1 and c_2 represent cell numbers at the beginning and end of each 6-hour interval, respectively, and Δt is the time interval (6 hours).

Cellular particulate organic carbon (POC) (pg $cell^{-1}$) was calculated using cell diameters measured with a Coulter Counter (Fan *et al.*, 2022), based on an empirical relationship derived by Montagnes *et al.*, (1994):

$$POC=0.109\ V^{0.991} \quad (2.\ 2)$$

Where V represents the naked cell volume (μm^3) with the diameter measured with the Coulter Counter, assuming a spherical cell shape.

Cellular particulate inorganic carbon (PIC) (pg cell^{-1}) was determined by calculating the volume difference between the coccosphere and acid-dissolved naked cells. This method employed a Coulter Counter, and was explicitly calibrated for coccolithophores (Fan *et al.*, 2022):

$$PIC=0.59 \times (V_1-V_2) \times 2.7 \quad (2.\ 3)$$

Where V_1 is the coccosphere volume(μm^3), V_2 is the naked cell volume(μm^3), 0.59 is the shape factor specific for G. huxleyi, and 2.7 is the calcite density (g cm ^{3}).

2.2.3 Chlorophyll-a extraction

To measure chlorophyll-a content, a 15 ml sub-sample from each triplicate culture at each time point was collected and centrifuged at 4500 rpm for 20 minutes. The supernatant was discarded, and 2 ml of 100% ethanol was added to the cell pellets. Samples were then wrapped in foil and kept a 4°C in the dark for 6 hours to extract pigments. After an additional centrifugation at 4°C at 4500 rpm for 3 minutes, the clarified supernatant was used for measurement. Chlorophyll-a absorbance was determined on the ethanol extracts using UV/VIS Spectroscopy (Unicam Helios Gamma & Delta) and a TECAN Spark® Multimode plate reader. Chlorophyll-a concentration was calculated following Ritchie (2006) as:

$$Chl\ (\mu g\ ml^{-1}) = 12.1551 * A_{665} - 1.4014 * A_{629} \quad (2.\ 4)$$

Where A_{665} is the absorbance of the pigment extract at wavelength 665 nm, and A_{629} is the absorbance of the pigment extract at wavelength 629 nm. Chlorophyll concentrations were subsequently normalised per cell and per naked cell volume (assuming a spherical cell geometry).

2.2.4 Carbon chemistry and determination of calcification

Triplicate sub-samples (>9 mL) of the culture medium were collected at each time point and filtered through 0.22 µm syringe filters. Alkalinity was measured three times per sample using a Gran titration with a Metrohm Ti-touch 916 device. The pH was calibrated daily using NBS pH buffer, and measurement accuracy was verified by performing at least three titrations on certified seawater reference material (Dickson Batch#197; the Certified Reference Materials Laboratory, University of California San Diego), which has a reference total alkalinity concentration of 2256.77 µmol kg^{-1}. Our measured standard alkalinity was 2330.38 ± 15.45µmol kg^{-1}.

Two complementary approaches were employed to estimate calcification rates from alkalinity depletion over 6-hour intervals. The traditional method calculates net calcification or cellular $CaCO_3$ content from the total alkalinity difference normalised to cell number change (Gore *et al.*, 2019):

$$CaCO_3(\text{pg cell}^{-1}) = \left(\frac{\Delta TA}{2\Delta cell\ ml^{-1}}\right) \quad (2.5)$$

where ΔTA represent the total alkalinity difference in the culture medium across each 6-hour interval, and Δcell ml^{-1} denotes the corresponding change in cell number during that interval. The factor of 2 assumes that a decrease of 2 µmol in TA equates to a 1 µmol increase in $CaCO_3$ precipitation (Smith & Key, 1975).

A second method was implemented for comparison:

$$CaCO_3(\text{pg cell}^{-1}) = \left(\frac{\Delta TA}{2\ cell\ ml^{-1}}\right) \quad (2.6)$$

Where cell ml^{-1} represents the total cell number at the end of each 6-hour interval.

The traditional method (equation 2.5) provides valid estimates for long-term population tracking but exhibits limitations in capturing short-term signals, particularly during periods when calcification is active but minimal cell division occurs. During the light period following nighttime division, newly divided cells actively calcify and remove alkalinity from the medium while total cell number remains nearly constant. Under these conditions, calculating per-cell $CaCO_3$ as ΔTA / Δcell ml^{-1} involves division by near-zero values, resulting in artificially inflated or unstable estimates. Equation 2.6 provides population-averaged rates assuming all cells present contributed to alkalinity depletion,

though the approach may not account for heterogeneity in calcification activity among cells of different ages or metabolic states. Unless otherwise specified, the traditional ΔTA / Δcell-based method (equation 2.5) was used to calculate calcification rates throughout the thesis.

To validate alkalinity-derived calcification estimates, these patterns were compared with independently calculated PIC values derived from cell volume measurements using empirically validated equations for *G. huxleyi* (see Methods 2.2.2), providing additional context and robustness to the observed calcification trends across the diel cycle.

The carbon chemistry of seawater was subsequently calculated using the R package "seacarb" (Gattuso et al., 2024), employing the function "carb" with the argument flag = 8, which uses pH and alkalinity as input variables to estimate additional carbonate system parameters.

2.2.5 Shotgun proteomic analysis

At each 6-hour interval, samples containing at least 4 x 10^7 cells were collected from three of the four biological replicates for proteomic analysis. Cells were harvested by centrifugation (3000 rpm for 15 min, at 4°C), resuspended in extraction buffer (20 mM Tris-HCl, pH 8.0), and lysed by sonication on ice (three 10-minute sessions with vortexing) before being stored at -80°C.

S-trap digestion was performed on the 36 samples from project E271. All samples were loaded onto an EvoTip Pure for introduction onto an 8 cm Endurance column with elution using a pre-set 60 SPD gradient on an EvoSep One UPLC system. DIA-PASEF data were acquired using a Bruker timsToF HT MS with a 1.1 s cycle time, between 400-1200 m/z and using 25 m/z DIA windows.

Resulting DIA data in Bruker. d format was searched against the appropriate database (detailed in the result files attached) using DIA-NN. An in-silico predicted spectral library was created with the DIA-NN software, which was then iterated against the DIA data generated for these samples. The search was run at 1% FDR. The DIA-NN. tsv output was compiled, filtered (two-peptide minimum) and pivoted to a normalised protein group-centric output using custom KNIME pipelines, minimum value imputation as applied.

For the investigation of coccolithophore circadian rhythms in E271, statistical comparison of relative abundance between groups was undertaken using CompMS Statistics in Microsoft Excel tool. Thresholds for t-test significance (cells highlighted in yellow) were set to $q < 0.05$. Results in bold were calculated using Welch's t-test, chosen where the data is not normally distributed. Using a label-free quantitative approach, 6925 proteins were identified across all conditions for downstream analysis, following the manual removal of negligible contaminants, including 25 human proteins and trypsin.

Rhythmicity in protein relative abundance over the time series was analysed using the Rhythmic Analysis Incorporating Nonparametric (RAIN) algorithm (Thaben & Westermark, 2014). Log-transformed protein abundance data were arranged as a numeric array with triplicate samples for each time point. The analysis was conducted with a sampling interval of 6 hours and a predefined period of 24 hours. P-values were adjusted using the Benjamini-Hochberg method to control for false discovery rates.

Pairwise t-tests were conducted to identify proteins expressed at different time points under varying growth phases, nutritional conditions, and light cycle (day and night). These tests compared protein expression across sequential time points, the same local time on different days, and every other time point. A significant threshold of $p < 0.05$ was applied, and the log2-fold change (LFC) was used to determine the direction of protein regulation.

Proteins exhibiting significant rhythmic behaviour or different expression were further analysed through functional annotation. Grouping and annotation were conducted using Gene Ontology (GO), Kyoto Encyclopedia of Genes and Genomes (KEGG) and functional annotation clustering analysis via the web server DAVID (Sherman *et al.*, 2022) and the R package "gprofiler2" (Kolberg *et al.*, 2020). For the DAVID analysis, a Benjamini-corrected p-value threshold < 0.05 was applied, with downstream visualisation performed using the "ggplot2" package in R (version 4.4.2).

To elucidate co-expression patterns among the identified proteins, bootstrapped hierarchical clustering was performed using the "pvclust" package (version 2.2-0) (Suzuki & Shimodaira, 2006; Suzuki et al., 2019) in R (version 4.3.3) on an Ubuntu 22.04.4 LTS platform. This analysis incorporated 100,000 bootstrap replications to evaluate clustering stability, employing correlation-based distance metrics and average linkage

clustering. Missing values were managed using pairwise complete observations to maximise data inclusion. Approximately unbiased (AU) p-values were calculated through multiscale bootstrap resampling, with clusters deemed significant at a threshold of AU ≥ 0.95. Computational efficiency was enhanced by parallelising the bootstrap procedure across 96 CPU cores. Final cluster assignments and p-values were extracted using the "pvpick" function, configured to prioritise clusters meeting the AU significance threshold.

2.2.6 Statistical analysis

Averaged values for physiological traits and protein intensities were calculated as the mean ± standard deviation (SD) of four biological replicates for physiological measurements and three biological replicates for proteomic analysis. Significant differences between treatments and the control condition are indicated with asterisks: $p < 0.05$(*), $p < 0.01$(**) and $p < 0.001$(***). All statistical analyses, data processing, and visualisation were conducted using R (version 4.3.2).

2.3 Results and Discussion

2.3.1 General physiological traits across diel cycles and growth phase transitions

All physiological traits exhibited clear diel rhythmicity under the 14:10 light: dark cycle, with statistically significant 24-hour oscillations confirmed by non-parametric RAIN analysis (adjusted p-value < 0.05). This rhythmicity was observed across directly measured traits including cell number ($p<0.001$) (Figure 2. 2a), coccosphere size ($p<0.001$) (Figure 2. 2b), naked cell size ($p<0.001$) (Figure 2. 2b), chlorophyll-a concentration ($p<0.001$) (Figure 2. 2c), medium alkalinity ($p<0.001$) (Figure 2. 2g), cellular chlorophyll-a content ($p<0.001$) (Figure 2. 2e), and cellular $CaCO_3$ content ($p<0.001$) (Figure 2. 2d), as well as derived traits such as POC ($p<0.001$) and PIC ($p<0.001$) (Figure 2. 2f, h). The temporal dynamics revealed a highly coordinated pattern, cell division occurred predominantly during the night, between midnight and dawn (Figure 2. 2a). In contrast, cellular growth processes dominated the light period, with coccosphere and cell size, along with size-derived POC, PIC, and cellular chlorophyll-a and $CaCO_3$ content

following a synchronised diel pattern. These parameters increased steadily during the light period, reached a plateau between 18.00 and midnight, then declined rapidly during the dark phase (Figure 2. 2b, e, f, h). Concurrently, as cell numbers increased through division, in vitro chlorophyll-a concentration increased (Figure 2. 2c), while medium alkalinity declined (Figure 2. 2g), the magnitude of changes in both chlorophyll-a concentration and medium alkalinity between sequential time points peaked during the day and diminished at night, in parallel with the timing of cell division. This consistent diel rhythmicity, observed irrespective of growth stage and environmental conditions, aligns with previous findings on *G. huxleyi* under varying light, temperature, and nutrient conditions (Paasche, 1967, 2001; Linschooten *et al.*, 1991; Jochem & Meyerdierks, 1999; Müller *et al.*, 2008; Kottmeier *et al.*, 2020b) and suggests that the diel cycle of *G. huxleyi* may be endogenously regulated.

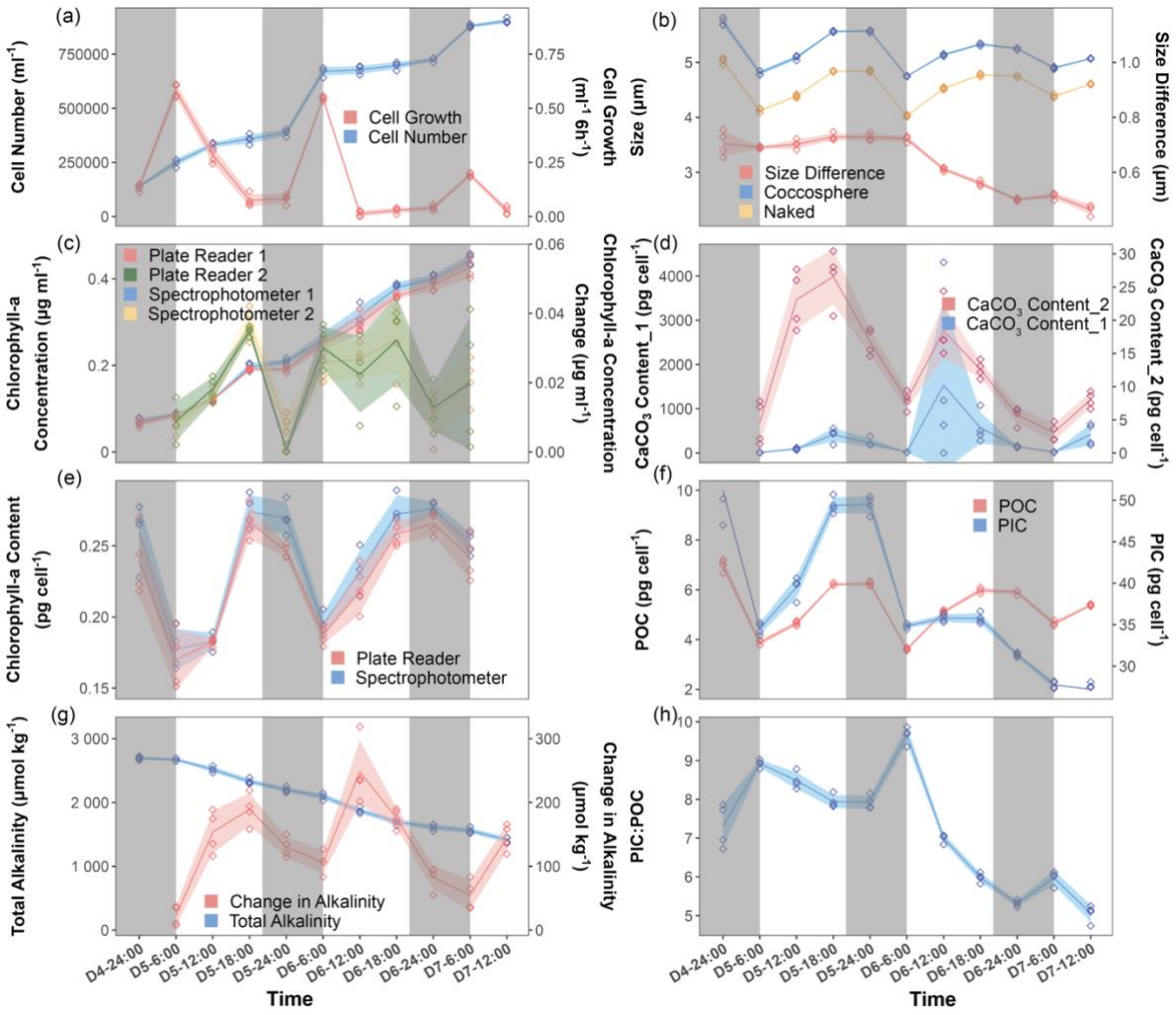

Figure 2. 2: Diel rhythms of physiological traits in *Gephyrocapsa huxleyi* over a 54-hour period. Grey shading indicates dark periods. (a) cell number (blue) and net cell growth (pink) over each

6-hour interval; (b) coccosphere size (blue), naked cell size (yellow), and the size difference between coccosphere and naked cell (pink); (c) chlorophyll-a concentration in the culture medium measured by spectrophotometer (blue) and plate reader (pink), along with 6-hour changes in chlorophyll-a concentration from the same methods (yellow and green, respectively); (d) cellular $CaCO_3$ content estimated using two approaches: blue line shows values calculated by normalising alkalinity change to the change in cell number over each 6-hour interval, pink line shows values normalised to the total cell number at the end of each interval; (f) PIC (blue) and POC (pink) per cell, derived from empirical equations based on naked cell volume and volume differences between coccosphere and naked cells (see Methods 2.2.2); (g) total alkalinity in the medium (blue) and 6-hour change in alkalinity (pink); (h) cellular PIC: POC ratio.

Beyond the well-phased diel cycle, the transition between growth phases introduced notable changes in rhythmicity patterns (Figure 2. 3). As cells entered the stationary phase on Day 6 (Figure A1. 1), cell growth slowed significantly (Figure 2. 3b), accompanied by decreases in both coccosphere and naked cell size (Figure 2. 3a, b). This growth phase transition was characterised by a marked reduction in cellular $CaCO_3$ content (Figure 2. 3f), decreased size differences between coccosphere and naked cells (Figure 2. 3g), and reduced size-based PIC (Figure 2. 3i), particularly at 18:00 and 24:00. Notably, while these calcification-related parameters declined, cellular chlorophyll-a content remained comparable to Day 5 levels (Figure 2. 3e), coinciding with a pH increase on Day 6 (Figure 2. 3h). The timing of cell division also shifted with growth phase progression. During the late exponential phase (Day 5), cell division occurred predominantly at night but extended into daytime hours (Figure 2. 2a), consistent with previous observations (Nelson & Brand, 1979; Kottmeier *et al.*, 2020b). However, as the population transitioned to early stationary phase (Day 6-7), daytime division became increasingly infrequent, with most divisions completing during the night. This pattern highlights that division frequency and timing are closely linked to the physiological states of the population. To identify the growth-limiting factors driving this transition, residual nitrogen and phosphorus concentrations in the seawater medium were calculated (Method A1. 1). The results indicated near-depletion of nitrogen by Day 6, while phosphorus remained available throughout the experiment (Figure A1. 3). These findings align with in situ seawater chemistry observations during *G. huxleyi* growth (Müller *et al.*, 2008). The observed decrease in cell size further supports a nitrogen-limitation response, consistent with previous studies (Müller *et al.*, 2008, 2017).

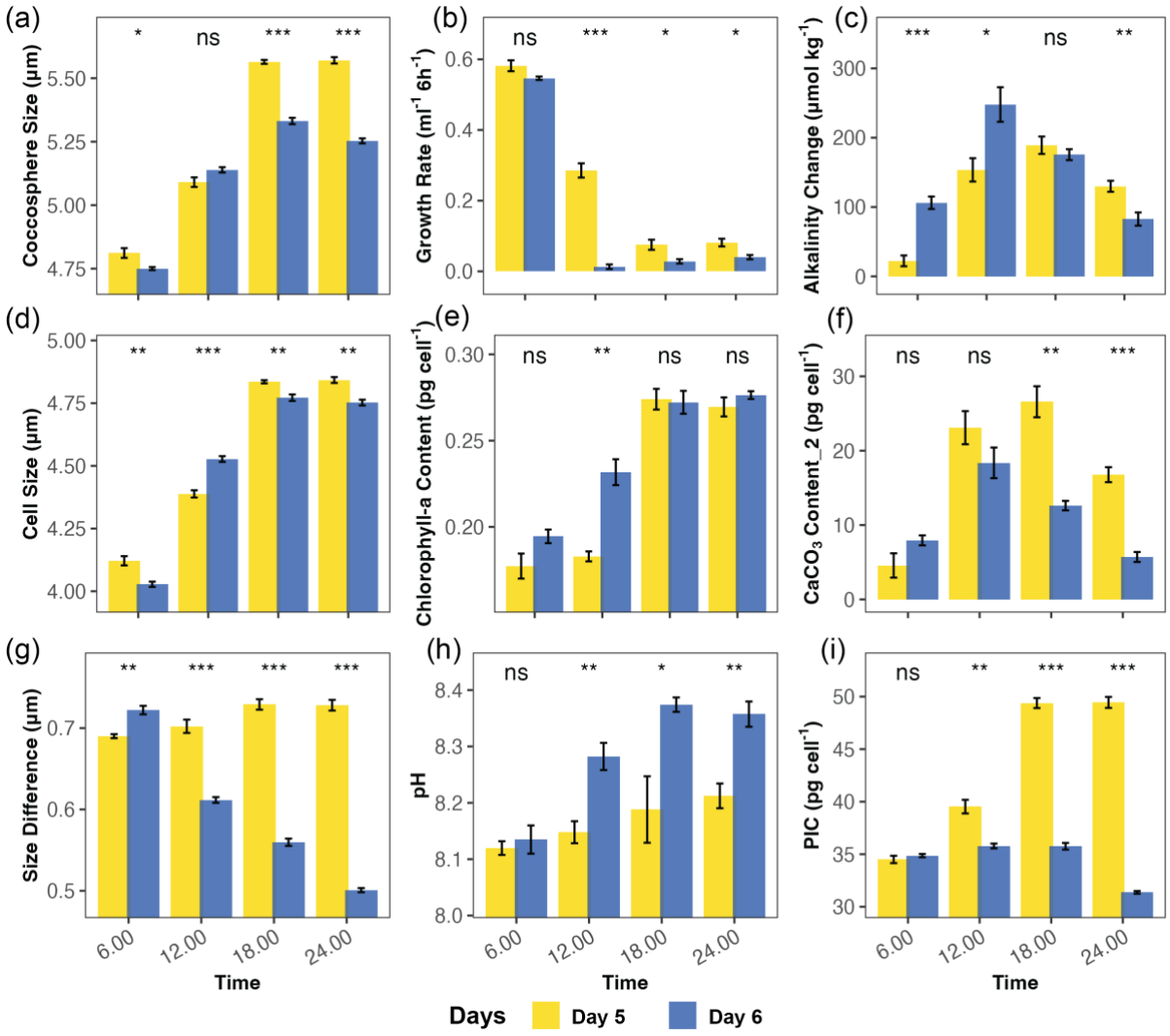

Figure 2. 3: Comparison of physiological traits between Day 5 (late exponential phase) and Day 6 (early stationary phase) in *Gephyrocapsa huxleyi* across the diel cycle. Panels show: (a) coccosphere size; (b) growth rate calculated over 6-hour intervals; for every 6 hours; (c) changes in medium alkalinity over 6-hour intervals; (d) naked cell size; (e) cellular chlorophyll-a content measured with plate reader; (f) cellular $CaCO_3$ content calculated using equation 2.6 (see Methods 2.2.4); (g) size differences between coccosphere and naked cells; (h) pH in culture medium; and (i) cellular PIC content derived from empirical equations based on volume differences between coccosphere and naked cells (see Methods 2.2.2). Asterisks indicate significant differences between Day 5 and Day 6 at each time point, with the number of asterisks denoting the level of significance: *p < 0.05, **p < 0.01, ***p < 0.001. 'ns' indicates no significant difference.

2.3.2 Temporal and growth phase-specific regulation of biological activities

To understand the molecular-level changes in cellular pathways in response to physiological diel cycles, proteomic analysis was conducted with triplicate samples covering 10 timepoints over 54 hours, from Day 4 at 24:00 to Day 7 at 6:00. After filtration, a total of 6,925 proteins were identified as being stably expressed across all timepoints.

Principal component analysis (PCA) revealed that the triplicates were tightly clustered, indicating good reproducibility (Figure 2. 4a). The separation of clusters along the principal component axes (PC1 and PC2 explained 31.6% and 21.8% of the variance, respectively) highlighted significant differences in proteomic profiles between timepoints. The clustering pattern revealed a clear temporal progression, with timepoints from Day 4-5 (early timepoints) positioned in the upper portion of the plot, transitioning through intermediate positions for Day 5-6 timepoints, and culminating with Day 6-7 timepoints in the lower portion. This progression along PC2 appears to primarily reflect the transition from exponential to stationary growth phase rather than diel cycling. While some separation of individual timepoints is evident, the clustering does not show a clear day/night alternating pattern along PC1. Instead, the overall trajectory suggests that growth phase transition is the dominant source of proteomic variation captured by this analysis. Towards Day 6 and Day 7, the clusters became less distinguishable, suggesting reduced proteomic variability as cell entered stationary phase. Differentially expressed proteins were examined by comparing sequential timepoints (Figure 2. 4b). As the timepoints approached the stationary phase, fewer differentially expressed proteins were identified. Enrichment analysis of these differentially expressed proteins revealed similarly reduced numbers of enriched groups (Figure A1. 5).

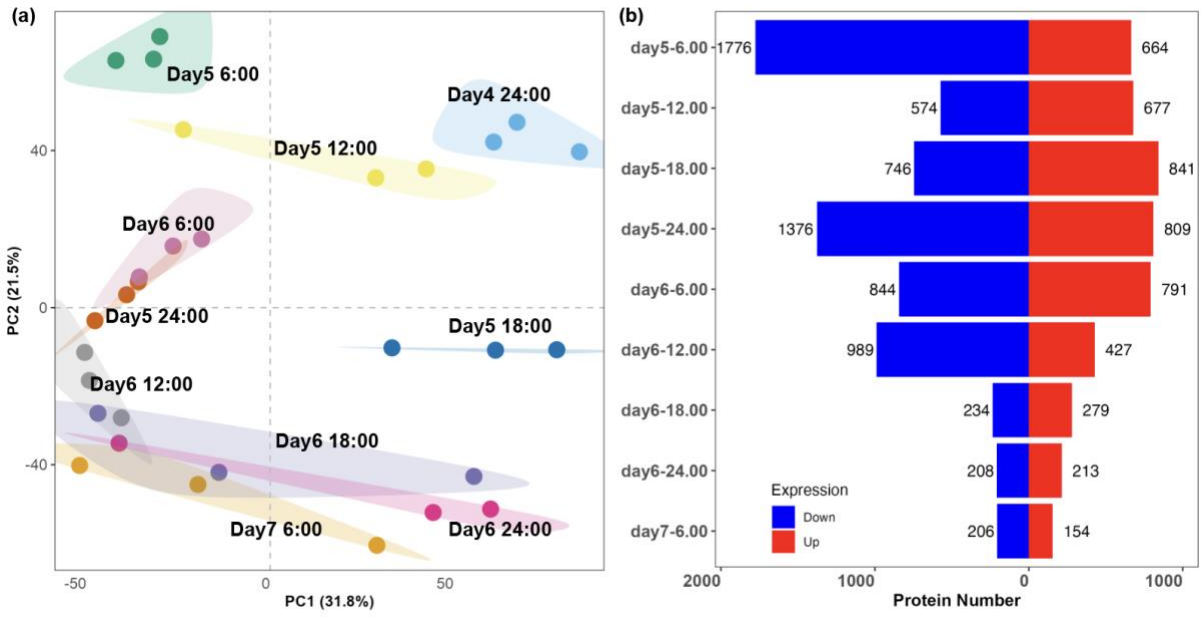

Figure 2. 4: Temporal dynamics of proteomic profiles in *Gephyrocapsa huxleyi*: principal component analysis and differential expression over a 54-hour period.

GO biological process (BP) enrichment analyses were conducted separately for upregulated and downregulated proteins (Figure A1. 7; Figure A1. 8; Figure 2. 5). To avoid redundancy, enrichment groups with identical input gene sets were consolidated, retaining only one representative group per set to streamline the analysis. Temporal dynamics of biological processes were visualised by manually classifying GO terms into functional categories. Upregulated terms comprised 120 unique GO terms across 22 functional categories, while downregulated terms comprised 145 unique GO terms across 24 functional categories. Although some functional categories overlapped, distinct temporal coordination was observed between upregulation and downregulation of individual biological processes. Importantly, when upregulated and downregulated GO terms fell within the same broader functional category at each timepoint, the specific GO terms themselves were non-overlapping. In rare cases where GO terms did overlap, the underlying protein sets were entirely distinct. These overlapping terms included: acetyl-CoA biosynthetic process from pyruvate (GO:0006086) at Day 5 18:00; chlorophyll biosynthetic process (GO:0015995), tricarboxylic acid cycle (GO:0006099), and intracellular protein transport (GO:0006886) at Day 6 12:00; protein folding (GO:0006457) at Day 6 18:00; and regulation of gene expression (GO:0010468) at Day 6 6:00. These overlapping terms demonstrate the fine-tuned temporal coordination of cellular processes, where simultaneous upregulation and downregulation within the same GO terms reflect distinct protein-level dynamics and precise metabolic regulation.

Distinct shifts in biological activity were observed throughout the diel cycle, characterised by alternating regulatory patterns in key processes. Transcription processes, RNA-specific processes, cell cycle and division, and DNA-related processes exhibited periods of downregulation followed by subsequent upregulation, reflecting tight temporal organisation. Processes related to DNA/chromosome processes and DNA repair demonstrated periodic activity, being particularly active at 18:00 and 24:00 but strongly downregulated at 6:00 and 12:00 across both days. For instance, DNA replication (GO:0006260) likely aligns with cell cycle-related timing, coinciding with phases of active division and genome maintenance during the dark phase. In contrast, Photosynthesis-related terms showed peak upregulation at 12:00, likely reflecting periodic responses to light exposure.

Additionally, processes related to energy metabolism, such as glycolytic process (GO:0006096), fatty acid biosynthesis (GO:0006633), and tricarboxylic acid cycle (GO:0006099), exhibited dynamic regulation across timepoints, showing both upregulation and downregulation. This pattern suggests continuous fine-tuning of energy production to meet cellular demands throughout the diel cycle. Notably, coordination was observed between energy metabolism and protein translation processes, likely reflecting the energy requirements of active protein synthesis during growth phases. The alignment of these processes across timepoints underscores their critical role in maintaining cellular homeostasis and supporting essential biological functions.

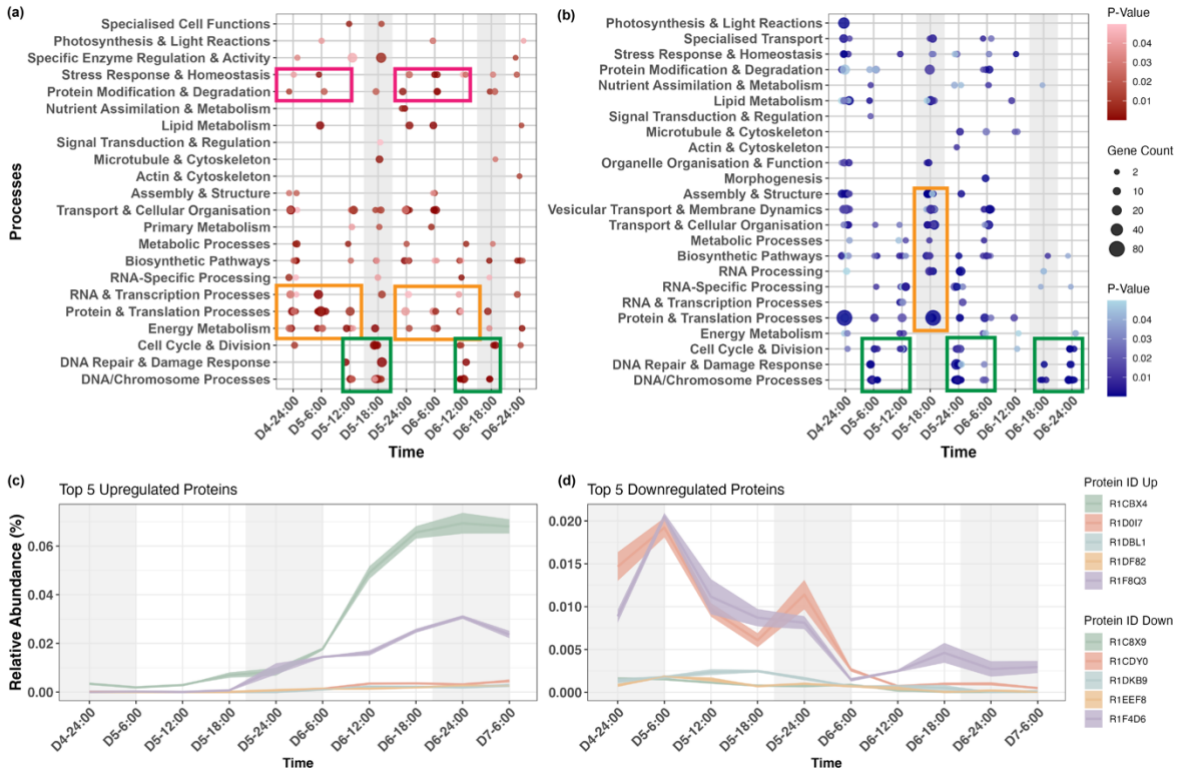

Figure 2. 5: Temporal dynamics of gene ontology biological processes and protein expression across the growth cycle of *Gephyrocapsa huxleyi*.(a) and (b) display the temporal regulation of upregulated and downregulated pathways, respectively. GO terms were manually classified into functional categories, with individual terms and classifications shown in Figure A1.7 and A1.8, respectively. Red bubbles indicate up-regulation, while blue bubbles indicate down-regulation. Bubble size reflects the relative percentage of associated genes for individual GO terms within each comparison, and shading represents p-value significance. (c) and (d) visualise the expression patterns of the top 5 upregulated and downregulated proteins, respectively.

Shifts in timing and magnitude of biological processes between Day 5 and Day 6 highlighted growth phase-dependent regulation. Through the population growth phase transition from the late exponential phase (Day 5) to the early stationary phase (Day 6),

fewer cells were actively dividing (Figure 2. 2a; Figure A1. 1b), leading to desynchronisation among individual cells and their protein expression. Consequently, fewer significantly regulated proteins were identified between timepoints (Figure 2. 4), as individual cells likely occupied different cell cycle stages. On Day 5, processes such as RNA processing (e.g., GO:0006364 rRNA processing) and translation (e.g., GO:0006412 translation and GO:0006413 translational initiation) were more prominent and dynamically regulated to meet the demands of active growth. In contrast, Day 6 showed reduced numbers of significantly regulated proteins with diminished activity for transcription and translation-related terms. However, stress response processes, such as cell redox homeostasis (GO:0045454) and protein modification and degradation, for instance protein peptidyl-prolyl isomerisation (GO:0000413), became more prominent on Day 6. These shifts suggest a cellular transition into a resting or maintenance phase, characterised by increased stress tolerance and reduced biosynthetic activity. The decreased diel regulation due to the growth phase transition from exponential to stationary and nutrient depletion was reported previously (Ashworth *et al.*, 2013).

To better understand changes in protein expression during the growth phase transition, proteins were analysed by comparing corresponding time points on Day 6 (e.g., 6:00, 12:00, 18:00, 24:00) with the same time points on Day 5. Proteins consistently upregulated or downregulated at all time points on Day 6 relative to Day 5 were identified. A total of 89 proteins were consistently upregulated, and 63 proteins were consistently downregulated across all time points on Day 6. The top five proteins exhibiting the highest log2-fold changes in upregulation or downregulation on Day 6 compared to Day 5 were selected and plotted (Figure 2. 5c; Figure 2. 5d), revealing clear regulatory patterns. The up- and down-regulated proteins highlight key cellular adaptations, reflecting a prioritisation of survival and maintenance during the transition from the late exponential phase (Day 5) to the early stationary phase (Day 6). Enhanced energy production and stress management were evidenced by the upregulation of energy metabolism enzymes, such as aconitate hydratase (R1DPH4) in the tricarboxylic acid cycle, alongside increased expression of oxidative stress response proteins, including glutathione peroxidase (R1D0I7), thioredoxin domain-containing protein (R1BL81), and cytochrome c peroxidase (R1D3V0), highlights the cell's efforts to maintain energy

production and mitigate oxidative stress. Conversely, downregulation of ribosome biogenesis, DNA replication (e.g., R1EWX3 DNA polymerase and R1E153 DNA replication licensing factor MCM2), and cell cycle proteins (e.g., R1DUR5 cyclin-dependent kinase regulatory subunit) indicates suppression of growth and proliferation. This helps conserve energy and resources. Additionally, proteins involved in nutrient assimilation, such as R1CBX4 and R1DWQ0 (glutamine synthetase) for nitrogen assimilation and R1CY00 and R1CI06 (alkaline phosphatase) for phosphate utilisation, were upregulated, reflecting a metabolic shift to enhance nutrient acquisition. Enhanced stress tolerance was also observed, with oxidative stress response proteins being upregulated to increase stress resistance, while proteins involved in protein quality control, such as R1DQM3 (heat shock protein 70) and its co-chaperone R1B5X2 (J domain-containing protein) (Kampinga *et al.*, 2019), were downregulated.

In summary, sustained and coordinated expression changes ($p < 0.05$) were observed across multiple timepoints in key metabolic and stress-related proteins (Figure 2. 5a; Figure 2. 5b), with the most significantly changed proteins showing distinct and sharp response patterns over the two days (Figure 2. 5c; Figure 2. 5d). These findings indicate that the transition from Day 5 to Day 6 marks a shift from active growth and division to a survival and maintenance mode, where cellular resources are redirected toward stress resistance and essential upkeep. This shift is most likely driven by the combined effects of progressive nutrient depletion and changes in carbonate chemistry inherent to the batch culture system, though the relative contributions of these factors require further investigation.

2.3.3 Rhythmic proteins exhibit distinct temporal patterns and functional enrichment

To characterise the rhythmic behaviour of proteins, non-parametric RAIN analysis was applied to the 6925 identified proteins. Across all p-value thresholds examined (<0.05, <0.01, <0.001), the majority of rhythmic proteins peaked at 24:00, followed by a smaller proportion peaking at 6:00. While the exact percentages varied slightly between thresholds (e.g., 45.4% at 24:00 for $p<0.05$ and 36.2% for $p<0.001$; Figure 2. 6), the overall trend of peak times remained consistent. To evaluate the robustness of the method, the

top 30 proteins with significant oscillations were visualised (Figure A1. 4). Despite differences in peak timing and involvement in diverse biological processes, all exhibited clear rhythmic patterns, supporting the reliability of the analysis. The percentage of rhythmic proteins observed in this study (~40%) is comparable to other organisms, although significant variation exists across studies. This ranges from 25% RNA genes in *G. huxleyi* (Hernández Limón *et al.*, 2020) to ~90% of expressed protein-coding genes in *Seminavis robusta*, a benthic pennate diatom (Bilcke *et al.*, 2021). This variation may arise from multiple factors. First, methodological differences exist between proteomics and transcriptomics approaches, with most studies focusing on transcriptomics (Ashworth *et al.*, 2013; Zones *et al.*, 2015; Ferrari *et al.*, 2019). Second, analytical methods differ, including the Bayesian clustering method based on Fourier coefficients (Monnier *et al.*, 2010) and JTK cycle (Hughes *et al.*, 2010; Zones *et al.*, 2015; Ferrari *et al.*, 2019). Third, sampling resolution varies considerably, ranging from 12-hour intervals (Ashworth *et al.*, 2013) to 3-hour intervals (Poliner *et al.*, 2015) and even 1-hour intervals (Zones *et al.*, 2015). Finally, biological and experimental factors contribute to observed differences, including environmental conditions (Hernández Limón *et al.*, 2020), culturing conditions (Zones *et al.*, 2015; Ferrari *et al.*, 2019), species-specific periodicity (Chauton *et al.*, 2013; Ferrari *et al.*, 2019; Hernández Limón *et al.*, 2020), and cell division timing (Ashworth *et al.*, 2013).

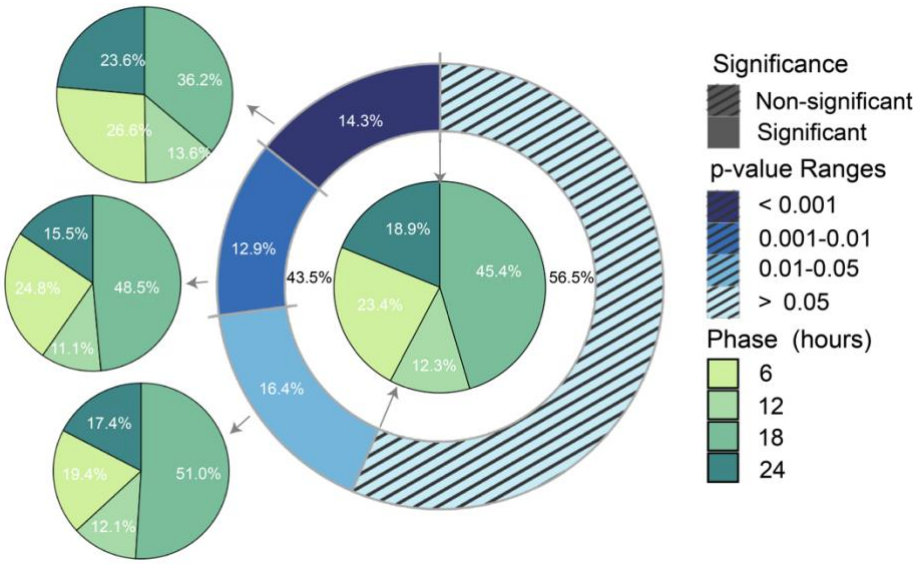

Figure 2. 6: Percentage of proteins in *Gephyrocapsa huxleyi* exhibiting 24-hour rhythmic expression. The outer blue ring displays the overall breakdown of significance levels; the inner green pie chart depicts the distribution of peak expression times for the significant proteins (p-

value <0.05); the outlier green pie chart further breaks down the peak time distributions across the different p-value ranges.

Functional enrichment analysis of significantly rhythmic proteins was conducted separately using g:Profiler and DAVID. For g:Profiler annotation, all significant proteins (p-value < 0.05) were included, while for DAVID, only proteins with a p-value < 0.01 were used due to query capacity limitations. Out of the total 3014 significant proteins ($p < 0.05$), 835 proteins, excluding ambiguous query IDs, were successfully mapped to GO biological processes using g:Profiler, resulting in the identification of six significantly enriched pathways. In DAVID, 1877 proteins meeting the p-value threshold ($p < 0.01$) were analysed, identifying 79 biological processes, of which 52 were significant (p-value < 0.05). Additionally, 171 annotation clusters were enriched, with 86 clusters containing categories that were statistically significant (p-value < 0.05). The significant biological processes enriched by g:Profiler, along with the top 10 enriched terms from DAVID's clusters and biological processes, were visualised (Figure 2. 5).

Distinct but overlapping biological processes were identified using these two enrichment tools. Both analyses consistently highlighted DNA replication processes, such as DNA replication (GO:0006260), emphasising the role of rhythmic proteins in genomic maintenance and cell division (Figure 2. 7). Metabolic processes were enriched in both tools but with different specificities: DAVID identified pathways such as the tricarboxylic acid cycle (GO:0006099) and fatty acid biosynthetic process (GO:0006633), while g:Profiler enriched processes associated with metabolic regulation and small molecule turnover, including the terpenoid metabolic process (GO:0006721), ribose phosphate metabolic process (GO:0019693), and oxoacid metabolic process (GO:0043436). This enrichment of metabolic pathways underscores the involvement of rhythmic proteins in cellular energy production and carbon metabolism. Additionally, DAVID uniquely identified processes related to RNA processing and cell division, such as the U4/U6 x U5 tri-snRNP complex (GO:0046540), mRNA splicing (GO:0000398), cell cycle (KW-0131), and microtubule organisation (GO:0031122), further highlighting critical processes required for transcriptional regulation and genomic stability.

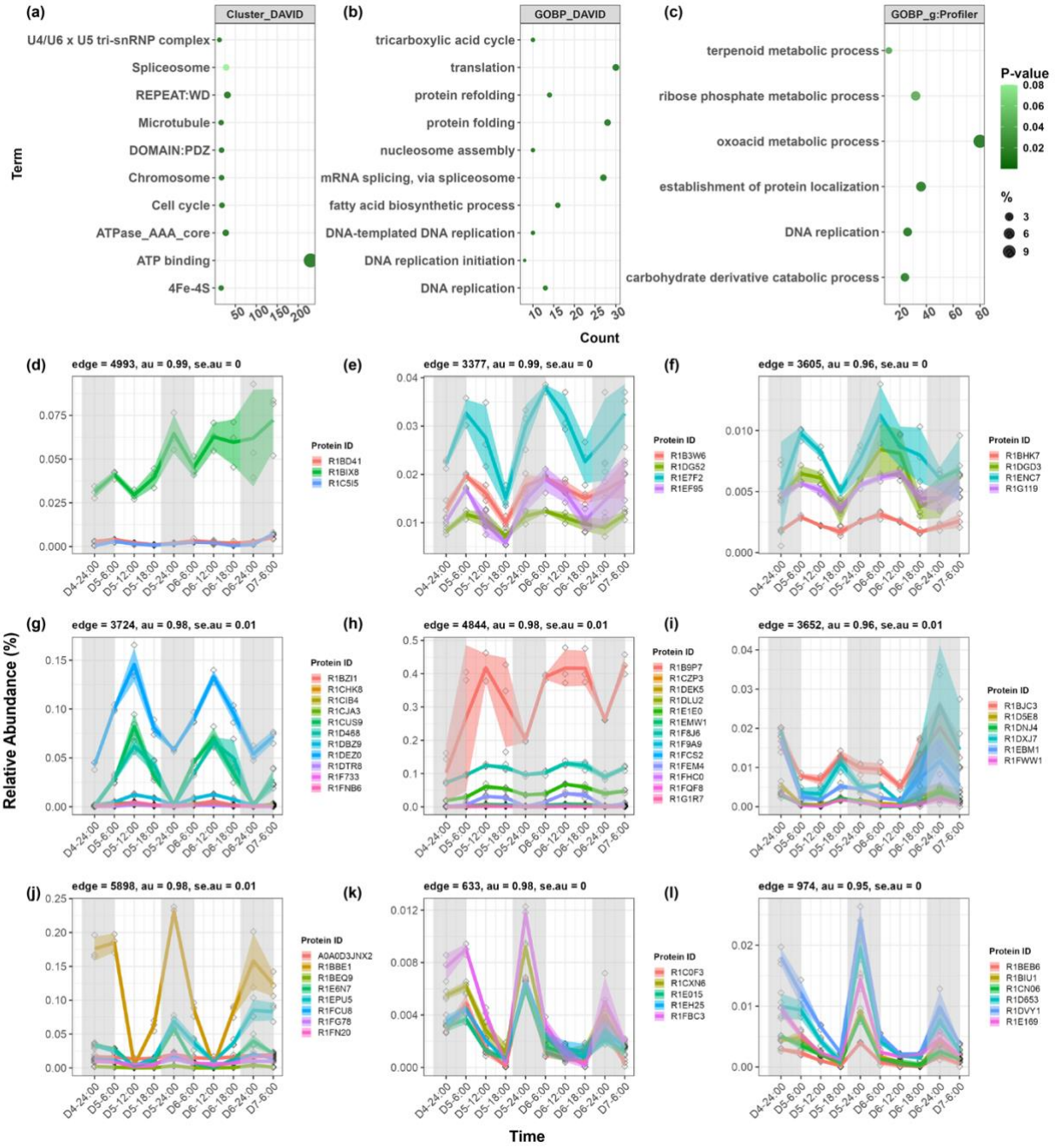

Figure 2. 7: Functional and pathway enrichment analysis of rhythmic proteins in *Gephyrocapsa huxleyi* using DAVID and g:Profiler, and protein expression patterns over day-night transitions. (a-c) Functional enrichment analysis for significantly periodic proteins (p-value < 0.05). Enrichment p-values were calculated using the EASE score in DAVID and the default g:SCS algorithm in g:Profiler. The count represents the number of proteins from the list involved in each annotation category, while the percentage indicates the proportion of involved proteins relative to the total. (d-l) Selected co-expression clusters containing significantly periodic proteins exhibiting distinct peak times throughout the day-night cycle. Cluster characteristics, including average au (approximate unbiased support) and se.au (standard error), are presented in each cluster title. The grey shaded regions indicate dark periods.

Given the high percentage of rhythmic proteins peaking at 24:00, this subset was selected for GO biological process functional analysis, encompassing 569 proteins. The

analysis revealed enrichment in key biological functions, including DNA replication (e.g., GO:0006260: DNA replication, GO:0006270: DNA replication initiation, GO:0006272: leading strand elongation), DNA repair (e.g., GO:0006281: DNA repair), and cell cycle processes (e.g., GO:0000278: mitotic cell cycle, GO:0000076: DNA replication checkpoint signalling). These processes are critical for ensuring the accurate duplication of genetic material (e.g., GO:0006261: DNA-templated DNA replication), maintaining genomic stability through repair mechanisms, and ensuring proper chromosomal segregation (e.g., GO:0007062: sister chromatid cohesion, GO:0051301: cell division) during cell division, thereby preserving overall genomic integrity.

2.3.4 Hierarchical clustering uncovers co-expressed protein modules independent of functional annotation

To obtain an unbiased view of the clustering structure of proteins with similar expression patterns in the 54h time series, independent of prior functional annotations, hierarchical clustering analysis was conducted across all proteins. The analysis combined p-value from RAIN analysis with pvclust analysis to calculate average p-values for each unique cluster, thereby evaluating clusters most likely to exhibit significant rhythmic oscillations. The analysis identified 1290 clusters containing 4782 proteins, of which 2122 exhibited rhythmicity. Among these, 279 clusters (containing 1000 proteins) showed significant rhythmic oscillations across all constituent proteins (p-value < 0.05). The clustering approach revealed coordinated regulation and potential functional relationships among proteins sharing similar expression patterns. The clustering analysis provided complementary insights to the functional enrichment analysis of sequentially changed proteins (Figure 2. 5). Unlike functional enrichment, which groups proteins based on their involvement in specific biological processes, clustering highlights proteins that share similar expression patterns regardless of functional boundaries. This approach suggests potential coordination across multiple biological processes within each cluster, revealing previously unrecognised regulatory networks. For detailed analysis, nine clusters were selected from the top 20 clusters with the lowest average p-values, calculated based on the periodicity of individual proteins within each cluster. These nine

clusters spanned peak expression times from 6:00 to 24:00, each containing sufficient proteins to provide meaningful insights into their broader functional roles.

Proteins peaking at 6:00 (Figure 2. 7a; Figure A1. 8, representative clusters: edge 4993, edge 3377, edge 4660, edge 1494, edge 4720, edge 1352, edge 1243, and others) exhibit diverse but interconnected roles, reflecting cellular transitions at the onset of the light phase. Key metabolic proteins, such as R1DG52 SBPase, likely indicate early activation of the Calvin cycle as light and potentially essential nutrients (Mg^{2+}) become available (Wirtz *et al.*, 1982; Woodrow *et al.*, 1984; Liu *et al.*, 2012). Several proteins support post-division recovery, including R1EF95 dynein light chain and R1DVS3 DJ-1 family protein, which facilitate intracellular transport, organelle positioning (Stuchell-Brereton *et al.*, 2011), and clearance of misfolded proteins via microtubule networks (Kawaguchi *et al.*, 2003; Prasad *et al.*, 2022). Stress management is also prominent, particularly through proteins involved in redox regulation and proteostasis. Antioxidant proteins such as R1F8C0 superoxide dismutase and R1EIK7 glutathione peroxidase mitigate oxidative stress (Wang *et al.*, 2018; Pei *et al.*, 2023), while proteostasis machinery, including R1D9N5 E2 ubiquitin-conjugating enzyme (van Wijk & Timmers, 2010), R1BWL7 Chaperonin 10 (Pareek *et al.*, 2021), and HSF-type DNA-binding domain-containing protein (R1C5I5 and R1D6X0) (Sakurai & Enoki, 2010), maintains protein homeostasis through quality control mechanisms. The potential oxidative stress observed at 6:00 likely results from residual metabolic byproducts of cell division regulation (Patterson *et al.*, 2019; Amponsah *et al.*, 2021), mitochondrial respiration, and adjustment of photosynthetic machinery to the light transition, where imbalances in light absorption and energy utilisation can generate reactive oxygen species (Das & Roychoudhury, 2014; Yu *et al.*, 2019). Together, these proteins ensure proper redox balance and protein integrity, preparing the cell for daytime metabolic activity. Additionally, R1DX49 Importin likely facilitates the import of transcriptional regulators to reset nuclear activities for the upcoming metabolic phase (Lu *et al.*, 2021), while proteins such as R1BH44 Acetoacetyl-CoA synthetase (Bergstrom, 2023) and R1BFE6 Sugar phosphate transporter domain-containing protein contribute to energy production and metabolic transport, ensuring readiness for daytime metabolic demands.

Proteins expressed highly at both 6:00 and 12:00 (edge 3605, Figure 2. 7f) likely function as a continuation of the cellular adaptation from the dark-to-light transition, facilitating energy production and essential cellular processes. These proteins include components involved in stress response, such as R1G119 Putative glutathione-S-transferase (Vaish *et al.*, 2020), metabolic regulation through R1ENC7 SMP-LTD domain-containing protein (Wang *et al.*, 2023) and protein quality control via R1DGD3 Adaptor protein ClpS core domain-containing protein (Torres-Delgado *et al.*, 2020). This temporal overlap suggests coordinated regulation bridging the early light response with peak photosynthetic activity. Proteins peaking at 12:00 (edge 4717, edge 3724, edge 4856, edge 4046, edge 1346, Figure 2. 7; Figure A1. 10) reflect the cellular demand for energy production, transcription, and translation to sustain metabolic output during maximum photosynthetic activity (Harding *et al.*, 1981, 1982). Energy production and regulation dominate this time point, with proteins such as R1FZ52 phosphoglycerate kinase, R1G1H4 pyruvate kinase, and R1CRY1 NADP-dependent glyceraldehyde-3-phosphate dehydrogenase supporting glycolysis and gluconeogenesis to ensure ATP generation and metabolic flexibility. Transport proteins, including ABC transporters (R1DBZ9, R1DEZ0, R1B3W2, and R1CCM6), facilitate the movement of nutrients and ions across membranes, while R1F2Z0 adenosine kinase maintains energy homeostasis by recycling adenosine and supporting ATP pools. Beyond energy production, regulatory processes are well-represented, including transcriptional regulation by Homeobox domain-containing protein (R1CIB4 and R1BZI1) (Calvo *et al.*, 2024) and R1F733 HTH myb-type domain-containing protein (Hirayama & Shinozaki, 2010), as well as signal transduction through R1FUC8 WW domain-containing protein and R1G283 TAZ-type domain-containing protein (Kanai *et al.*, 2000; Ilsley *et al.*, 2002). Chloroplast development and stress response regulation are also represented by R1D4T3 J domain-containing protein, which acts as a co-chaperone of Hsp70, possibly supporting protein folding and quality control (Kampinga *et al.*, 2019a).

Proteins peaking at both 12:00 and 18:00 (edge 4844, edge 1823, Figure 2. 7h; Figure A1. 11) emphasise roles in metabolic production, transportation and stress response, representing the sustained activity during peak photosynthetic hours. Key contributors to cofactor biosynthesis, including R1F8J6 magnesium chelatase, R1E1E0 pyridoxal 5'-

phosphate synthase (Richts *et al.*, 2019), and R1G1R7 cyanocobalamin reductase, likely support essential metabolic and biosynthetic pathways (Fenech, 2012). Their expression patterns are consistent with observations of chlorophyll accumulation during the daytime (Figure 2. 2) and the diel oscillations in cofactor metabolite cycling (Boysen *et al.*, 2021). Proteins involved in stress response and cell growth, such as R1DLU2 AP2/ERF domain-containing protein (Ma *et al.*, 2024), R1FCS2 alkyl hydroperoxide reductase (Seaver & Imlay, 2001), and R1CIB0 peptide-methionine (S)-S-oxide reductase (Weissbach *et al.*, 2002), play critical roles in mitigating oxidative stress. This stress likely results from the imbalance between photosynthetic electron transport and downstream CO_2 fixation under maximal photosynthetic rates (Asada, 2006).

Proteins peaking exclusively at 18:00 (edge 2289, edge 2318, edge 1945, edge 2896, edge 2932, edge 4440, Figure A1. 12) appear to prepare for nighttime processes, marking the transition from daytime photosynthesis to nighttime metabolism. Energy production remains important, as evidenced by Q4G398 ATP synthase subunit delta, while signal transduction is facilitated by R1ERF1 PAS domain-containing protein and R1FP20 SOUL heme-binding protein (Xing *et al.*, 2023). Regulatory activities are prominent, encompassing transcriptional regulation through R1FAR9 Homeobox domain-containing protein and R1C410 Myb-like domain-containing protein (Hirayama & Shinozaki, 2010; Calvo *et al.*, 2024), RNA metabolism via R1DLM9 ATP-dependent RNA helicase, and nucleolar and chromatin regulation through R1CZE3 Nucleolar protein 10, R1E2K4 Chromo domain-containing protein. Furthermore, DNA replication is supported by proteins like R1EAB9 DNA-directed DNA polymerase family A palm domain-containing protein, ensuring efficient cellular division during the night.

Proteins highly expressed at 24:00 (edge 974, edge 633, edge 5898, edge 436, edge 5418, edge 6197, edge 4245, Figure 2. 7j-l; Figure A1. 13) are specialised in cell cycle regulation and chromatin dynamics, ensuring proper chromosome segregation during nighttime cell division (Figure 2. 2). Key proteins supporting these processes include R1BIU1 condensin complex subunit 2, R1CN06 calponin-homology (CH) domain-containing protein, R1D653 structural maintenance of chromosomes protein, R1FBC3 SMC hinge domain-containing protein, R1CGJ9 kinetochore protein Spc24, and R1E015 kinetochore protein SPC25. These proteins are essential for chromatin compaction and chromosome

segregation, while cell cycle regulators such as R1DVY1 cyclin-dependent kinase and R1E169 mitogen-activated protein kinase facilitate signalling and cell cycle progression. Energy and transport-related proteins, including A0A0D3JNX2 acetate-CoA ligase and R1FCU8 ferredoxin-NADP (+) reductase, contribute to energy production and redox balance, supporting the energy-intensive processes of cell division. Additionally, R1BEQ9 PAS domain-containing protein likely senses cellular redox states or other signals to regulate metabolic and transcriptional activities. Intracellular transport and chromosome movement are further supported by motor proteins such as kinesin motor domain-containing protein (R1DVS7 and R1CXP2), R1D7C7 myosin motor domain-containing protein and R1G1U9 TOG domain-containing protein. Proteins highly expressed at both 24:00 and 6:00 (e.g., edge 5621, Figure A1. 13) are predominantly involved in energy metabolism, bridging the nighttime division period with the dawn transition. These include R1C144 isocitrate lyase and R1EG52 phosphoenolpyruvate carboxykinase, which support gluconeogenesis and lipid metabolism, providing energy and carbon skeletons for cellular processes. R1D0K6 acetyl-CoA C-acyltransferase further contributes to fatty acid degradation, ensuring sufficient energy supply during darkness and preparing the cell for metabolic demands as light turns.

2.3.5 Individual proteins and functions highlighted a desynchronised expression corresponding to different growth phases

Through sequential gene expression, functional enrichment analysis, and rhythmic analysis, diel oscillations were observed in broad cellular metabolic pathways, including protein biosynthesis, folding, and DNA replication (Figure 2. 5; Figure 2. 7). By comparing physiological and gene expression patterns over two days, cell division-related proteins were identified as significantly downregulated on Day 6, corresponding to the growth phase transition. However, much information regarding central metabolic processes, such as photosynthesis and respiration, both likely to exhibit diel cycles and to be influenced by growth phase transitions (Ashworth *et al.*, 2013; Hernández Limón *et al.*, 2020) is still lacking. Proteins exhibiting statistically significant diel cycles were primarily associated with basic cellular functions like DNA replication and the cell cycle. Whether energy-regulating pathways and carbon assimilation are similarly governed by diel cycles,

environmental traits, or growth cycle regulation remains to be determined. Additionally, our understanding of fine-tuned cell cycle regulation in *G. huxleyi* is limited compared to other species (Barnum & O'Connell, 2014; Atkins & Cross, 2018).

To begin addressing this knowledge gap, the drivers of the growth phase transition were investigated. In batch culture systems, multiple factors can contribute to growth cessation, including nutrient depletion and changes in carbonate chemistry parameters. Nutrient limitation is the most plausible explanation (Ashworth *et al.*, 2013; Browning & Moore, 2023). The observed reduction in RNA and protein biosynthesis at Day 6 (early stationary phase) (Figure 2. 5) aligns with previous findings of nutrient-limitation-induced growth phase shifts (Rokitta *et al.*, 2014, 2016). The calculated nutrient levels in the culture medium indicated N depletion (Figure A1. 3), and physiological responses such as reduced cell size and calcification also support nitrogen limitation(Riegman *et al.*, 2000) (Figure 2. 3). However, the potential contributions of other factors, including major nutrients such as P and sulphur (S), as well as carbon substrate availability, cannot be ruled out. To identify the primary driver of the growth phase transition, proteins associated with nutrient-assimilation pathways and carbon metabolism and other biological processes that may respond differently under specific nutrient or carbon limitations were grouped and analysed (Rokitta *et al.*, 2014, 2016; McKew *et al.*, 2015).

2.3.5.1 Differential regulation of nitrogen pathways during late exponential and stationary phases

Nitrogen-deletion responsive pathways (Rokitta *et al.*, 2014) (Figure A1. 14) were examined by comparing the protein expression pattern between Day 5 (late exponential) and Day 6 (early stationary). Overall, key steps in nitrogen acquisition and ammonium assimilation were upregulated, while certain downstream branches of amino acid biosynthesis were downregulated. Several enzymes involved in nitrate-to-ammonia assimilation were upregulated, including R1CPI0 Ferredoxin-nitrite reductase (NiR), which catalyses nitrite reduction to ammonia, and R1DEX6 Urease, which hydrolyses urea into ammonia and CO_2 (Witte, 2011). Similarly, glutamine synthetases (R1CBX4 and R1DWQ0), crucial for incorporating ammonium into glutamate to form glutamine, showed increased expression, as did R1D4Y0 Acetylglutamate kinase, an enzyme vital

for arginine biosynthesis. Additionally, R1DNU5 glutamate synthase (GOGAT), part of the GS-GOGAT cycle that drives initial nitrogen assimilation (Balotf *et al.*, 2016), was upregulated. Conversely, enzymes linked to nitrogen-intensive amino acid pathways were downregulated under N-limitation. These included R1E0G9 Aspartate-semialdehyde dehydrogenase, essential for lysine, threonine, and methionine biosynthesis, and R1F6E1 Argininosuccinate synthase, which converts citrulline and aspartate into argininosuccinate, connecting aspartate metabolism to the Ornithine-urea cycle (OUC). Similarly, R1EDI0 Carbamoyl phosphate synthetase, catalysing the first step of the OUC, exhibited reduced expression, consistent with previous observations in the same species under N-limitation (Rokitta *et al.*, 2014). Interestingly, the upregulation of NiR during the stationary phase contrasts with prior observations under N-limitation (Rokitta *et al.*, 2014), where NiR expression was reduced. Although NiR upregulation has been linked to nitric oxide (NO) elevation, such a response is typically accompanied by decreased ammonium assimilation and significant shifts in triacylglycerol (TAG) and monogalactosyldiacylglycerol (MGDG) pools (Dolch *et al.*, 2017), neither of which was observed in this study (Figure A1.15). Most proteins involved in glycerolipid metabolism, including those associated with TAG, phospholipid and galactolipid biosynthesis, displayed delayed peak expression from late afternoon (18:00) to midnight (24:00), with only minimal differences in peak expression levels. Notably, in the TAG biosynthesis pathway, the glycerol-3-phosphate dehydrogenase [NAD (+)] proteins (R1BGY9, R1BJ45, R1DBS0, R1DG23, R1DYC7, R1EE38, R1DHK7), key players in glycerol-3-phosphate metabolism, exhibited unsynchronised expression peaks despite high daytime expression. Similarly, the phospholipid/glycerol acyltransferase domain-containing proteins (R1CES1, R1DEQ8, R1E6C8, R1CES1), associated with acyltransferase reactions, displayed out-of-phase peaks, likely suggesting the presence of isoforms with distinct roles in lipid production (Wendel *et al.*, 2009; Driver *et al.*, 2017). The unchanged TAG and MGDG peak levels indicate that the upregulation of NiR is unlikely to be directly linked to NO signalling. Instead, it may simply reflect an adaptation to enhance nitrogen assimilation under nitrogen-limited conditions. These findings collectively suggest that cells prioritise immediate nitrogen acquisition and assimilation to increase the production of key amino acids, such as glutamate and glutamine, likely enhancing growth and photosynthesis under nitrogen limitation (Fuentes *et al.*, 2001;

Chichkova *et al.*, 2001) (Figure A1. 16), while tempering secondary amino acid biosynthetic pathways in response to nitrogen depletion.

2.3.5.2 Coordinated regulation of photosynthesis and lipid metabolism during growth phase transition

Light harvesting processes in *G. huxleyi* have been reported to exhibit diel cycle in field samples (Hernández Limón *et al.*, 2020), and photosynthesis is generally downregulated under N and P depletion, correlating with growth cessation (Rokitta *et al.*, 2014, 2016). Proteins involved in the photosynthetic light reaction, the Calvin-Benson cycle, and pigment biosynthesis associated with light harvesting were examined (Figure A1. 17). Across the 54-hour sampling period, the expression of most proteins in the electron transport chain (ETC) exhibited strong synchrony, particularly among 3 of the 19 photosystem II (PSII; Q4G395, Q4G3C2, Q4G3F2) proteins, nearly all 46 light harvesting proteins (LHP), Cytochrome b6/f (Q4G3D7), all 4 photosystem I (PSI; R1DIH7, Q4G3B5, Q3G3F5, Q4G3F6) proteins, and 2 of the 6 ATP synthase subunits (Q4G399, Q4G300). These proteins demonstrated responsiveness to both diel cycles and the transition between growth phases. During the late exponential phase on Day 5, expression levels displayed a distinct day-night cycle, characterised by low expression at 6:00, a gradual increase throughout the day, and a peak at 18:00. Upon entering the early stationary phase on Day 6, an extended period of low expression was observed, with a delayed peak time. The rising expression period, initially spanning from 6:00 to 18:00, shifted to 12:00 to 24:00. This shift in expression patterns aligns with the majority of proteins involved in glycerolipid biosynthesis (Figure A1. 15), highlighting coordinated regulatory adjustments during the growth phase transition. Additionally, 13 sugar phosphate transporter domain-containing proteins exhibited an expression pattern aligned with the photosynthetic ETC, consistent with their role in transporting fixed carbon products such as triose phosphates. Notably, previous studies reported transcript-level peaks for photosynthetic ETC elements earlier in the day (Hernández Limón *et al.*, 2020; Becker *et al.*, 2021; Coesel *et al.*, 2021). Differences in timing between transcriptome and protein expression, as well as metabolite accumulation, have been observed (Uchimiya *et al.*, 2022). The afternoon peak of photosynthetic ETC protein expression observed in this study could result from the gradual accumulation of transcripts and proteins over time. Additionally, cell cycle

regulation differed between field samples and this study. In field samples, cell mitosis occurred at the beginning of the dark phase (Hernández Limón *et al.*, 2020), whereas in this study, cell division and its corresponding regulation was observed from midnight to the following morning (Figure 2. 2; Figure A1. 26). These differences in the timing of cell cycle stages may contribute to the variations in protein expression patterns.

Photosynthesis, nutrient cycling, and circadian rhythms are interconnected in multiple ways, influencing cellular metabolism and responses to environmental conditions (Dodd *et al.*, 2015; Haydon *et al.*, 2015). The O_2 evolution rate, which reflects PSII activity, aligns with the circadian rhythm of nitrate reductase (NR), a key nitrogen transporter supporting N assimilation (Joseph & Villareal, 1998). However, its activation time varies between species (Hersey & Swift, 1976; Martinez *et al.*, 1987; Gao *et al.*, 1992; Joseph & Villareal, 1998) and becomes undetectable in the stationary phase (Hersey & Swift, 1976), which may explain the absence of NR activity in our study. Circadian rhythms, driven by the ATP/ADP ratio oscillation between day and night (Pitsawong *et al.*, 2023), regulate photosynthesis. Although photosynthesis is strongly influenced by light (Hennessey & Field, 1991; Hennessey *et al.*, 1993; Diaz *et al.*, 2023), it is also modulated by other factors, including nutrient availability (Salomon *et al.*, 2013; Kharwar & Mishra, 2020; Grettenberger *et al.*, 2024), and changes in pH and CO_2 availability (Dao *et al.*, 2025). For instance, macro-nutrient limitations, such as N, P, and S can lower electron transfer efficiency in PSII (Salomon *et al.*, 2013; Kharwar & Mishra, 2020; Grettenberger *et al.*, 2024). These limitations may contribute to the lag in photosynthetic protein expression observed during the early stationary phase. Additionally, specific proteins linked to the xanthophyll cycle, such as Violaxanthin de-epoxidase (VDE; R1DJ81), were upregulated on Day 6. This response likely reduced PSII efficiency (Rockholm & Yamamoto, 1996), further reinforcing the inhibitory effects of nutrient limitation on photosynthesis (Wykoff *et al.*, 1998).

2.3.5.3 Co-occurring nitrogen and phosphorus limitation drive growth phase transition

P is also a major nutrient, and its depletion can lead cells to enter the stationary phase (Rokitta *et al.*, 2016). *G. huxleyi* exhibits strong P assimilation strategies, utilising two types of alkaline phosphatase (APase) to regulate P uptake under both normal and low P

conditions (Riegman *et al.*, 2000). This contrasts with its low competitiveness for nitrate and provides a significant advantage under P-limitation conditions (Riegman *et al.*, 2000). APase activity is not only induced under P-limitation but also highly active under N-limitation and nutrient replete but acidic conditions (Rouco *et al.*, 2013). In this study, the expression of 2 APases (R1CI06 and R1CY00) increased steadily from Day 5 at 18:00 to the end of the sampling period, showing a 4-5-fold increase in abundance (Figure A1. 18). Additionally, the PhoD-like phosphatase metallophosphatase domain-containing protein (R1C9I0), involved in phosphorus scavenging and recycling, displayed a 25-fold increase in abundance, mirroring the expression patterns of APase. Furthermore, upregulation of the phosphate transporter R1DW77 was observed on Day 6, with expression beginning to increase at 12:00 and peaking at 24:00. The observed APase upregulation is consistent with previous studies reporting its response to P-limitation (McKew *et al.*, 2015; Rokitta *et al.*, 2016). Additionally, the absence of reduced Complex I protein expression (Figure A1. 20), previously reported under N- limitation (Rokitta *et al.*, 2016), supports P-limitation as a factor in this study. However, although P-limitation has previously been associated with increased LHP production (McKew *et al.*, 2015), such an increase was not observed in this study. Instead, evidence for enhanced nitrogen assimilation was observed, suggesting that N limitation may have occurred alongside phosphorus limitation. S limitation, compared to N and P limitation, in coccolithophores remains less studied. A few S-assimilation proteins exhibited diel oscillations, including sulfate adenylyltransferase (R1DAZ7), ferredoxin-sulfite reductase (R1BT40 and R1DP77), cysteine synthase (R1DNF0), and methionine synthase (R1FZW9). These proteins peaked in expression at 6:00 (light onset) and reached their lowest expression at 18:00. However, minimal variation in S-related protein expression was observed during the growth phase transition in our study (Figure A1. 19). Taking these findings together, regarding the nutrient limitations that trigger the transition of growth phase, S limitation is unlikely to be a major factor triggering the transition, while molecular responses point toward N and P limitation playing more prominent roles. Considering the physiological responses and the calculated remaining N and P concentrations in the culture media, it is possible that both N and P limitations, particularly N limitation, contribute to triggering the growth phase transition and delayed photosynthesis. This, in turn, likely leads to a lag in carbon and metabolite accumulation.

In contrast to nutrient limitation, carbon limitation typically induces chlorophyll degradation, Rubisco upregulation, and activation of carbon-concentration mechanisms (CCMs) (Nielsen, 1995; Bach *et al.*, 2011, 2013; Dao *et al.*, 2025). The CO_2 concentration (~6 µmol kg^{-1}) at the onset of Day 6 approached the optimal range for *G. huxleyi* growth reported in some studies (~5-7 µmol kg^{-1}) (Zondervan *et al.*, 2002; Bach *et al.*, 2011) but was lower than in others (~19-23 µmol kg^{-1}) (Sett *et al.*, 2014), and below the optimum for maximal chlorophyll-a and POC production (~24-28 µmol kg^{-1}) (Raven & Johnston, 1991; Bach *et al.*, 2011; Sett *et al.*, 2014). However, the relatively high pH (~8.15) at the onset of Day 6 maintained higher DIC (~1600 µmol kg^{-1}) and HCO_3^- (~1500 µmol kg^{-1}) concentrations (Figure A1. 2) compared to previous studies that typically manipulate CO_2 by fixing either pH or alkalinity. Although Rubscio upregulation observed in this study was consistent with previous studies exposing *G. huxleyi* to lower HCO_3^- and CO_3^{2-} concentrations (Bach *et al.*, 2013), and size-driven POC production was reduced, cellular chlorophyll-a content showed no significant difference across most timepoints on Day 6 compared to Day 5, with a significant increase at 12:00. Furthermore, while ETC proteins expression was delayed on Day 6, diel patterns persisted and photosynthetic proteins recovered in the later afternoon. These mixed signals suggest that further investigation of protein expression related to lipid accumulation and CCMs is needed to fully characterise the carbon limitation response.

2.3.5.4 Mitochondrial electron transport and energy coordination across growth phases

Carbon fixed through photosynthesis serves as a substrate for phosphorylation through the respiratory ETC, which generates ATP to fuel essential cellular activities. To investigate how daily energy regulation adapts to growth phase transitions, proteins associated with various respiratory ETC complexes and related systems were examined (Figure A1. 20). Most proteins involved in different parts of the respiratory ETC exhibited similar expression patterns to the photosynthetic ETC. This includes all 17 complex I proteins, the majority of complex III proteins (10 out of 11), complex IV proteins, and the electron transfer flavoprotein-ubiquinone oxidoreductase (ETF-QO; R1D152). These proteins consistently showed low expression at 6:00 on Day 5, with a gradual increase peaking at 18:00. On Day 6, a delay in expression was observed, with increases starting

only after 12:00 and peaking at 24:00. The coordinated regulation between mitochondrial and chloroplast ETCs likely suggested that both systems operate in parallel to optimise ATP production for biosynthetic processes, ensuring tightly regulated energy metabolism even during the growth phase transition. However, unlike the ATPase in the photosynthetic ETC that exhibited a clear diel cycle, the expression of Complex V showed almost no variation regardless of diel cycle and growth phase transition, which might suggest that the cell prioritises maintaining consistent ATP production to support essential processes, regardless of external or internal metabolic shifts.

Despite this overall synchrony, a few proteins displayed deviations, either with consistent unidirectional expression changes or significant 24-hour rhythmicity. Among these outliers, the two complex II proteins, succinate dehydrogenase (R1EUN2 and R1F8P8), exhibited a moderate increase (~2-fold) in expression on Day 6. As a critical link between the tricarboxylic acid (TCA) cycle and the respiratory ETC, Complex II's increased expression suggests heightened reliance on TCA cycle intermediates for energy production as growth slows and nutrient availability diminishes. This moderate upregulation may reflect a shift toward resource conservation and maintaining energy production during the transition to the stationary phase. Additionally, the ubiquinone biosynthesis protein R1G0W1 exhibited a 2-fold increase in expression on Day 6, potentially indicating an increased demand for ubiquinone production to sustain ETC function. One notable exception within complex III was the Rieske domain-containing protein (R1BIT6), which exhibited a distinct diel cycle, peaking at 6:00 and reaching its lowest expression at 18:00. This protein also showed a slight overall decrease in expression on Day 6. The rhythmic pattern of R1BIT6 may suggest regulation by circadian rhythm proteins or a compensatory mechanism in response to reduced expression of other proteins. The diel peak in Complex III activity at 6:00 could play a role in maintaining a continuous proton gradient during the night, thereby facilitating sustained ATP production for essential maintenance and repair processes.

As the moderate increases in ubiquinone biosynthesis and Complex II activity observed on Day 6 suggest adjustments in energy production pathways in *G. huxleyi*, proteins involved in the TCA cycle, fatty acid biosynthesis, beta-oxidation, lipid oxidation, glycolysis, and gluconeogenesis were examined to understand carbon assimilation and

energy regulation across diel cycles and growth phase transitions. Complex II, which links the TCA cycle to the ETC by transferring electrons from $FADH_2$ to ubiquinone, showed increased expression, indicating greater reliance on TCA cycle intermediates for energy production. This adjustment may compensate for reduced metabolic fluxes in other pathways (e.g., glycolysis or photosynthetic ETC) as nutrient availability declines, and possibly also in response to emerging carbon substrate limitation, helping maintain mitochondrial ATP production to support bicarbonate (HCO_3^-) transport and CCMs (Burlacot *et al.*, 2022; Burlacot, 2023).

2.3.5.5 TCA cycle reprogramming and metabolic shifts during growth phase transition

In the TCA cycle (Figure A1. 21), most proteins exhibited diel oscillations, with lower expression during the day and higher expression at night. Despite this cyclic pattern, many proteins showed increased expression on Day 6 compared to Day 5, particularly those involved in succinyl-CoA biosynthesis. All 4 Succinyl-CoA biosynthesis proteins exhibited moderate increases (1.5- to 2-fold), with sustained higher expression levels on Day 6 when photosynthetic and respiratory ETC proteins both under low expression at 12:00. Notably, pyruvate dehydrogenase (R1FBN4) and citrate synthase (R1DK63 and R1FBN4) constantly increased approximately 1.5-fold, while aconitate hydratase (R1DPH4) maintained its diel cycle peaks at 24:00 and low value at 12:00, with expression increased roughly 1.5 times at 12:00 at Day 6 compared to Day 5. The two isocitrate dehydrogenase proteins (R1CPY1 and R1FDZ3) exhibited distinct trends, with the latter increasing nearly 5-fold on Day 6. Dihydrolipoamide acetyltransferase component of pyruvate dehydrogenase complex (R1DWX5) demonstrated a consistent increase over the sampling period, rising 3-fold from Day 4 (24:00) to Day 7 (6:00). Despite these trends, energy-saving pathways like the glyoxylate shunt were not significantly activated, and the malate-aspartate shuttle, including 2-oxoglutarate/malate translocator (R1F206), previously reported to be downregulated under N-limitation (Rokitta *et al.*, 2014), was not observed in this study. Overall, the TCA cycle exhibited an upward trend in expression during the transition to the stationary phase, aligning with prior observations of TCA responses in stationary phase (Ashworth *et al.*, 2013). This suggests an adaptive shift to sustain energy production and metabolic demands during nutrient limitation.

2.3.5.6 Diel regulation and growth phase adjustments in fatty acid metabolism and β-oxidation

Proteins involved in de novo fatty acid biosynthesis, elongation, desaturation, and hydroxylation were examined (Figure A1. 22). Similar to the glycerolipid and TAG biosynthesis processes (Figure A1. 15), most proteins exhibited diel oscillations, with higher expression during the day and lower expression at night, aligning with the previous study (Poliner *et al.*, 2015). However, in contrast to P assimilations, light harvesting, respiratory ETC, and glycerolipid metabolism, which showed delayed peak expression during the early stationary phase, de novo fatty acid biosynthesis maintained a consistent diel expression pattern without any apparent delay. Moderate changes were observed between growth phases. Key enzymes, such as Acetyl-CoA Carboxylase (R1DJU8 and R1FFT9), 3-oxoacyl-[acyl-carrier-protein] reductase (R1CUW5) and Malonyl CoA-acyl carrier protein transacylase (R1FRD8), showed slight increases, while Fatty acid synthase (R1FQA0), Enoyl-ACP reductase (R1DPI9) and Beta-hydroxyacyl-ACP dehydratase (R1CAN9) were downregulated during the early stationary phase. This suggests a disruption in the fatty acid biosynthesis, potentially leading to malonyl-ACP accumulation due to reduced efficiency in downstream steps. The upregulation of 3-oxoacyl-ACP reductase could reflect a compensatory mechanism to sustain fatty acid elongation. Despite these changes, glycerolipid and TAG biosynthesis remained unaffected, possibly due to sufficient fatty acid reserves. Additionally, Beta-oxidation proteins displayed diel regulation, with upregulation at night and downregulation during the day (Figure A1. 23), aligning with the previous work (Poliner *et al.*, 2015). Among 26 beta-oxidation proteins, only Enoyl-CoA hydratase (R1DW88) and Putative 3-hydroxyacyl-CoA dehydrogenase (R1FG06) showed slight increases during the early stationary phase. Additionally, a small nighttime upregulation of Carnitine O-palmitoyltransferase (R1B2X3) on Day 6, aligning with TCA cycle activity, suggests enhanced energy production to meet growth phase demands.

2.3.5.7 Diel oscillations and growth phase modulation of glycolysis, gluconeogenesis, and pyruvate metabolism

In glycolysis and gluconeogenesis (Figure A1. 25), two glycolysis-specific proteins were identified: phosphofructokinase-1(PFK-1; R1E5W0) and pyruvate kinase (PK; R1DGX4, R1EEU6, R1FQ88, R1G1H4). PFK-1 peaked at 6:00, with lower expression at other time points and minimal differences between the two days. In contrast, PK showed less synchronised expression, except for R1EEU6, which showed increased expression on Day 6. Gluconeogenesis-specific proteins included pyruvate carboxylase (PC; R1D0C2 and R1DFR1), phosphoenolpyruvate carboxykinase (PEPCK; R1EG52), and fructose-1,6-bisphosphatase (FB; R1B8K3, R1DUE0 and R1FII8). PEPCK (R1EG52) and FB (R1B8K3) displayed similar diel regulation patterns, peaking at 24:00 or 6:00, with reduced expression during the day. Proteins shared between glycolysis and gluconeogenesis, such as fructose-bisphosphate aldolase, phosphoglycerate kinase (PGK), phosphoglycerate mutase (PGM), triosephosphate isomerase (TPI), and glyceraldehyde-3-phosphate dehydrogenase, showed either minimal diel variation or peaked in the early morning. An exception was glucose-6-phosphate isomerase (R1DKS4), which peaked at 24:00 or 6:00 and was downregulated during the day. Most proteins, including PGK, PGM and TPI, exhibited increasing trends on Day 6, likely as a response to the growth phase transition. Additionally, pyruvate metabolism was examined (Figure A1. 25), encompassing pathways in the glycolytic cycle (involving PC, PEPCK and PK), and alternative pyruvate-supplying pathways, such as those through alanine, lactate, and malate. Enzymes involved included alanine transaminase (ALT), lactate dehydrogenase (LDH), malic enzyme (ME) and malate dehydrogenase (MDH). Several of these proteins, including PC (R1D0C2 and R1DFR1), ALT (R1EQD8), and ME (R1DNN3), exhibited sustained high expression from 24:00 on Day 5 to 12:00 on Day 6, suggesting upregulation of pyruvate metabolism to meet energy and carbon demands during the early stationary phase, which aligns with previous observations (Ashworth *et al.*, 2013). The diel regulation for both pathways, however, aligns with transcriptome findings in *Phaeodactylum tricornutum* (Su *et al.*, 2024), but differs from *Thalassiosira pseudonana* (Ashworth *et al.*, 2013), highlighting the species-specific metabolic responses.

2.3.5.8 Diel regulation and growth phase-dependent modulation of the cell cycle

Lastly, proteins that likely control cell division and the cell cycle in *G. huxleyi* were examined, focusing on the diel responses and growth phase transitions (Figure A1. 26).

Previous studies indicate that *G. huxleyi* division is not confined strictly to nighttime hours; instead, division may continue for several hours into the light phase (Nelson & Brand, 1979; Kottmeier *et al.*, 2020b). Furthermore, the onset of darkness does not exclusively determine division initiation (Paasche, 1967; Müller *et al.*, 2008). Although most cells within a population typically complete division at night, individual cells are not perfectly synchronised and can exhibit gradual, asynchronous division (Kottmeier *et al.*, 2020b). Under shortened photoperiods, cells may require additional time to prepare before division begins (Paasche, 1967). In this study, *G. huxleyi* continued to divide during the late exponential phase on Day 5, after the onset of the photoperiod (Figure 2. 2). Consequently, not all cells reached the same cell cycle stage by midday, consistent with the observed low cellular chlorophyll-a content measured at 12:00. During the preceding 6-hour morning period, approximately 25% of the population completed division. However, despite not all cells being in the biosynthetic period (G1 phase), likely due to sufficient nutrient levels, high biosynthetic rates persisted in the population, leading to comparable cellular and bulk chlorophyll-a content compared to Day 6 (Figure 2. 2).

To further investigate these observations, proteins involved in cell cycle regulation and associated chromosomal and mitotic processes were examined (Figure A1. 26). Most proteins displayed well-synchronised diel-expression patterns, with distinct day-night peaks. Cyclin-dependent kinases (CDKs) and checkpoint proteins peaked at 24:00, exhibiting lower expression during the day, suggesting late-night mitotic activity or preparation for subsequent cell cycles. Similar patterns were observed for replication factor C (RFC), proliferating cell nuclear antigen (PCNA), minichromosome maintenance proteins (MCM), chromosome condensation and maintenance proteins, regulators of chromosome condensation, ribonucleotide reductase (RNR), the cohesion complex, and histone deacetylases. In contrast, DNA replication licensing factors, histones, and histone methyltransferases peaked at 18:00, likely reflecting active DNA replication during S-phase. Notably, the high abundance of these replication proteins on Day 5, and the mitotic-related proteins observed at both 24:00 (Day 4) and 6:00 (Day 5) align with the extended cell division into the early light period (Figure 2. 2). As cultures transitioned into the early stationary phase (Day 6), key cell cycle proteins (CDKs, checkpoint proteins, DNA replication licensing factors, MCM, RNR, and cohesion complexes) exhibited an

overall decrease in abundance, consistent with a slower division rate under nutrient-limited conditions (Figure 2. 2). Histones remained highly expressed but shifted their peak from 18:00 on Day 5 to 24:00 on Day 6. This delayed peak time aligns with altered energy production pathways (Figure A1. 17; Figure A1. 20), and may suggest a slower chromatin assembly during stationary phase conditions. Together, these diel expression patterns underscore the tight regulation of cell cycle progression in synchrony with light-dark cycles; however, they also reflect modulation by the cells' changing metabolic state, driven by nutrient availability or growth phase transitions in the population.

2.3.6 Calcification patterns and potential regulatory factors

Calcification in *G. huxleyi* is considered phase-specific and primarily restricted to the G1 phase of the cell cycle (Müller *et al.*, 2008; Kottmeier *et al.*, 2020b), during which metabolic activity and biomass accumulation occur. This aligns with our observations that calcification predominantly occurs during the light period, with significantly reduced rates at night, particularly at the period between 24:00 to 6:00, when most cell division occurs (Figure 2. 2). On Day 5 (late exponential phase), calcification increased steadily throughout the photoperiod, peaking at 18:00. By contrast, on Day 6 (early stationary phase), although calcification remained active during the first six hours of the day, its rate plateaued thereafter, maintaining the levels established earlier. These patterns were consistently captured by both alkalinity drift measurements and Coulter Counter analysis (Figure 2. 2; Figure 2. 3), underscoring their robustness. The diel restriction of calcification to the G1 phase is mechanistically plausible, as preparations for cell division, including DNA replication, chromosome condensation, segregation, and organelle duplication, are highly energy-intensive. Moreover, during early mitosis (prophase), membrane-bound organelles such as the Golgi apparatus, where coccolith production occurs (Paasche, 2001), undergo vesiculation (Carlton *et al.*, 2020), likely disrupting coccolith formation and extrusion. This aligns with the general mitotic arrest of secretory pathways (Thyberg & Moskalewski, 1998), further supporting the temporal uncoupling of calcification from active cell division.

As highlighted by previous studies (Anning *et al.*, 1996; Monteiro *et al.*, 2016), calcification in *G. huxleyi* is likely an energy-intensive process. To investigate its

significance in cellular activity and its relationship with other metabolic pathways, the alignment was examined with key energy metabolism processes. While calcification exhibits a diel cycle, its pattern is distinctly desynchronised from energy metabolism pathways such as the TCA cycle (Figure A1. 21), beta-oxidation (Figure A1. 23), and glycolysis (Figure A1. 25), which are typically upregulated during the night or early morning. These pathways primarily support cell cycle regulation and preparation for light-dark transitions rather than directly facilitating calcification. On Day 5, calcification activity corresponded well with photosynthetic pathways (Figure A1. 17), light harvesting, and glycerolipid metabolism (Figure A1. 15). However, on Day 6, these pathways displayed delayed peak times, which did not align with the sustained calcification observed during the morning. While the extended high expression of energy metabolism pathways on Day 6 may have contributed to substrate transport and supported calcification, this does not fully explain why calcification rates did not continue to increase after the recovery of photosynthesis and glycerolipid metabolism later in the day. Therefore, the co-regulation may happen coincidentally; alternatively, the high calcification may be sustained in the afternoon of Day 6, but counterbalanced by dissolution. However, external pH measurements in the culture medium showed a steady increase from 8.1 to ~8.4 over the sampling period, making external dissolution unlikely. The role of intracellular pH, however, remains unclear. Additionally, substrate availability appears to be a critical factor. HCO_3^- concentrations in the culture medium consistently declined, decreasing from 2000 µmol kg^{-1} at the start of the sampling period to below 1000 µmol kg^{-1} by Day 6. This reduction likely restricted calcification, consistent with thresholds reported in earlier studies (Bach *et al.*, 2011, 2013). The relationship between calcification and other cellular processes remains ambiguous, as calcification does not follow the same diel pattern as energy metabolism. During the early stationary phase, reduced calcification is likely attributable to HCO_3^- limitations, although the possibility of active cellular regulation cannot be excluded.

To investigate calcification regulation, proteins that are potentially involved in this process were examined, particularly those associated with substrate availability (Corstjens *et al.*, 2001; Bach *et al.*, 2013). Calcification ability is determined by calcium (Ca) concentration, HCO_3^- concentration, and pH. Proteins possibly related to HCO_3^-

regulation, pH homeostasis and cation transport were analysed. This included several cation transporters, such as those annotated as magnesium transporters with domains for magnesium ion transmembrane transport, based on the rationale that they may also be permeable to Ca^{2+} due to broader substrate specificity (Figure 2. 8). Most exhibited expression patterns similar to the photosynthetic ETC proteins (Figure A1. 17) and glycolipid metabolism (Figure A1. 15), and align with the calcification performance on Day 5. However, on Day 6, the delayed peaking time observed in the photosynthetic ETC proteins (Figure A1. 17) and glycolipid metabolism (Figure A1. 15) was also exhibited in these proteins, but in contrast to the calcification performance. Therefore, these proteins are more likely to participate in the ETC and plastid pH maintenance, rather than facilitating calcification. Notably, V-type ATPase exhibited consistently high expression with minimal variation, potentially highlighting its role in maintaining pH regulation. Conversely, vesicle-fusing ATPase showed expression patterns aligned with cell cycle proteins, peaking between 24:00 and 6:00, suggesting a link to cell division processes. While proteins associated with carbon regulation, such as carbonic anhydrase and HCO_3^- transporters (Figure 2. 8), did not align with calcification patterns, they provide additional context for evaluating potential carbon limitation in this batch culture system. These proteins exhibited the same delayed diel expression patterns observed across multiple metabolic pathways, including photosynthetic components, but showed no clear upregulation in expression magnitude. This suggests a coordinated metabolic timing rather than active induction of CCMs. Despite evidence of reduced size-driven POC on Day 6 and elevated Rubisco and energy metabolic pathways expression, the stable cellular chlorophyll-a content, and lack of strong upregulation of CA and HCO_3^- transporters typically associated with carbon limitation responses suggest that, although HCO_3^- limitation likely constrained calcification, carbon limitation was unlikely to be the dominant driver of the growth phase transition, though a partial contribution cannot be excluded. Overall, no proteins were identified in this study that directly correlated with calcification performance under the conditions tested. Instead, reduced external HCO_3^- availability appears to be the primary factor limiting calcification on Day 6 during the stationary phase. Active regulatory mechanisms to enhance calcification under such conditions were not observed in this study.

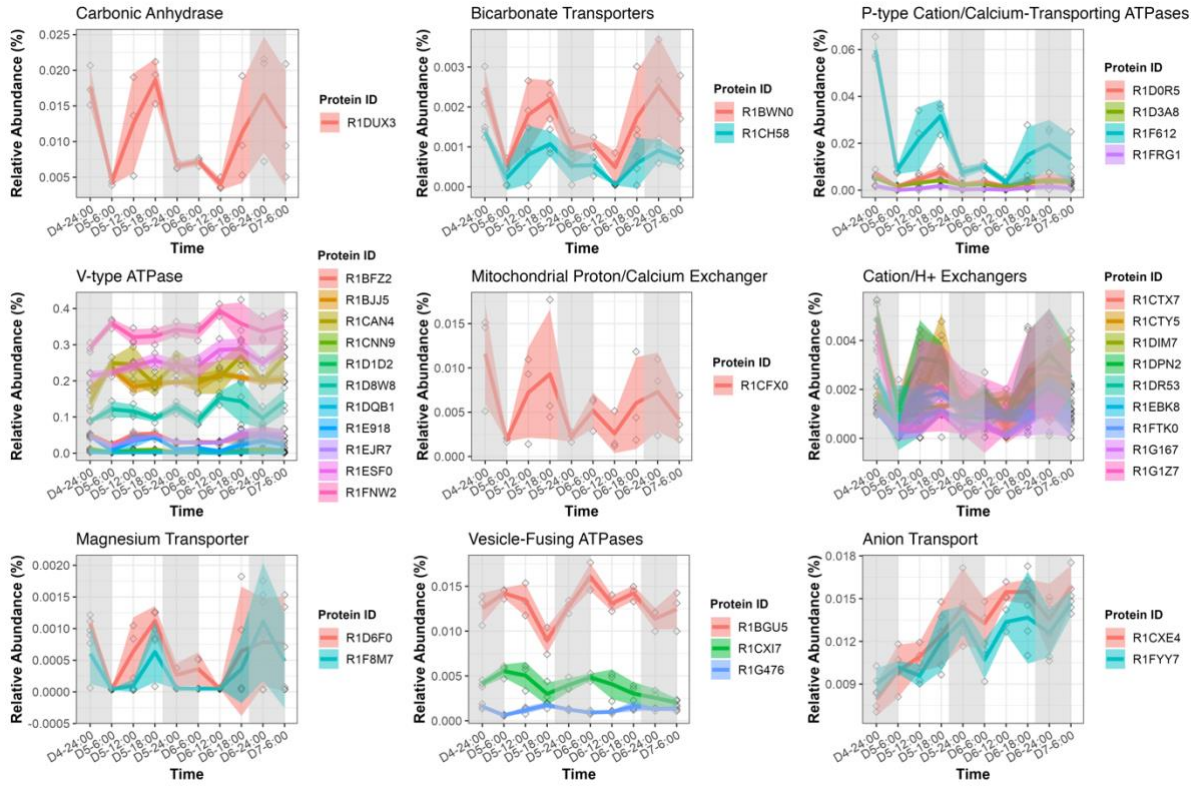

Figure 2. 8: Expression dynamics of proteins involved in ion/pH homeostasis and membrane trafficking in *Gephyrocapsa huxleyi* across day-night cycles.

2.4 Conclusion

The 54-hour time series analysis of *G. huxleyi* physiology and proteomics revealed a detailed molecular-level diel cycle spanning two and a half days, along with the growth phase transition from the late exponential to early stationary phase. Physiologically, cells divide predominantly at night, while pigment accumulation, cell expansion, and calcification occur during the day. Correspondingly, nearly half of the proteins exhibited a 24-hour cycle, with a significant portion involved in gene expression, cell cycle regulation, and ATP-related activities. During the diel cycle, protein and RNA activities were more prominent during the day, while DNA-related activities and cell division were active at night. Pathways such as photosynthesis, de novo fatty acid biosynthesis, pyruvate metabolism, and glycerolipid biosynthesis were upregulated during the day, while the TCA cycle, beta-oxidation, glycolysis and gluconeogenesis peaked at night and early morning. These metabolic rhythms collectively supported a synchronised cell cycle.

Beyond the diel cycle, the growth phase transition also demonstrated significant metabolic shifts. Proteins related to the cell cycle were downregulated during the early

stationary phase, while several other processes, including photosynthesis, respiratory ETC, light harvesting, pyruvate metabolism, and glycerolipid biosynthesis, exhibited delayed peak expression. De novo fatty acid biosynthesis was downregulated, whereas energy metabolism pathways such as the TCA cycle, beta-oxidation, and glycolysis/gluconeogenesis showed upregulation or extended periods of high expression. This metabolic reprogramming was likely driven by nitrogen limitation, although the potential impact of phosphorus limitation cannot be entirely ruled out.

Calcification displayed partial alignment with certain pathways during the late exponential phase but lacked direct evidence of regulation by those pathways. Proteins previously hypothesised to regulate calcification exhibited expression patterns more closely associated with photosynthetic and respiratory ETC processes, suggesting their role in supporting biosynthesis by regulating substrates and pH rather than directly driving calcification. The reduced calcification observed in the stationary phase is most likely attributable to substrate limitation, particularly HCO_3^-.

Some pathway changes, such as TAG biosynthesis, appeared less pronounced in this study compared to previous research on growth phase (Ashworth *et al.*, 2013; Rokitta *et al.*, 2014). This discrepancy may be due to differences in sampling times, as prior studies often sampled during the middle to late stationary phase, where gene expression profiles are more distinct. Additionally, the delayed peak expression observed during the growth phase transition in this study complicates comparisons across time points and may lead to overestimations of metabolic changes. Regarding diel cycles, species-specific responses are expected, as phytoplankton and even strains within a species exhibit diverse cell division patterns. For instance, some divide exclusively at night, others during the day, and some continuously, regardless of light-dark cycles (Nelson & Brand, 1979). Cells in different cell cycle stages express distinct proteins; these variations can reduce the comparability of diel cycles across species.

In natural environments, nutrient availability varies significantly across geological timescales and contemporary spatial gradients, ranging from oligotrophic regions to areas experiencing blooms. These variations, along with growth phase development, predator pressures, and competition (Muratore *et al.*, 2022), drive metabolic

adjustments and often influence cell cycle progression and population growth phase transitions. This study provides a fundamental framework for understanding *G. huxleyi*'s distinct diel cycles and metabolic shifts during growth phase transitions. Given the ecological importance of coccolithophores in carbon fixation and marine carbon cycling, these findings offer a basis for further investigations into how diel rhythms and growth phase transitions are regulated. Such research can elucidate the evolutionary strategies enabling coccolithophores to thrive in diverse oceanic conditions, shaping their long-term contributions to global biogeochemical cycles.

Chapter 3 Changing Magnesium availability reveals feedback between metabolism, physiology and calcification in the coccolithophore *Gephyrocapsa huxleyi*

Abstract

Gephyrocapsa huxleyi is a ubiquitous producer of particulate inorganic carbon (PIC) in the modern ocean. However, its cellular biology and regulation of calcification in response to environmental changes remain poorly understood. Magnesium (Mg) affects photosynthesis and calcification, offering insight into cellular regulation. Herein, a comprehensive physiological, metabolic, and proteomic analysis of *G. huxleyi* was conducted in response to a Mg gradient of 0-210 mM. *G. huxleyi* displayed greater sensitivity to Mg deficiency, characterised by reduced growth rates, enlarged cell size, lower cell densities, and stronger proteomic responses, particularly under Mg-depleted conditions, while fewer changes occurred under excess Mg. Cell size decreased chlorophyll-a per unit volume increased linearly with increasing Mg concentrations, whereas photosynthetic performance remained largely stable across all treatments, with significant disruption only under complete Mg depletion. Both cellular and volume-normalised $CaCO_3$ content were markedly reduced under low and high g availability, with cellular $CaCO_3$ declining linearly with increasing Mg. The findings reveal a hierarchy in cellular priorities: survival is paramount, followed by photosynthetic maintenance, then cell growth and division. Calcification in *G. huxleyi* functions as a secondary metabolic process, non-essential for core cellular functions. Despite significant calcification variation, no associated shifts in overall cell physiology or proteomics were observed. The linear reduction in calcification with increasing Mg-induced Mg/Ca ratios suggests modulation by ion availability or precipitation dynamics, while any molecular regulation appears unresponsive to changes in external Mg concentration, with implications for the global carbon cycle.

3.1 Introduction

Coccolithophores are important single-celled phytoplankton that produce uniquely intracellular low Mg-calcite plates, known as coccoliths. With unique coexisting photosynthetic and calcification abilities, coccolithophores play a significant role in the marine biological pump and carbon cycle by modulating air-sea CO_2 fluxes and altering the export of particulate inorganic and organic carbon (PIC/POC) (Holligan *et al.*, 1993; Ridgwell *et al.*, 2007; Suykens *et al.*, 2010). Coccolithophores are the most productive calcifying organisms, accounting for ~50% of global $CaCO_3$ production, while their photosynthesis contributes to ~20% of surface ocean net primary production (Sikes *et al.*, 1980; Poulton *et al.*, 2007, 2010; Broecker & Clark, 2009). Coccolithophores are found extensively in marine ecosystems, inhabiting a wide range of environments, including coastal and open ocean regions, as well as tropical and polar zones (Gregg & Casey, 2007; Moore *et al.*, 2012). In the modern ocean, the ubiquitous coccolithophore, *Gephyrocapsa huxleyi* (also known as *Emiliania huxleyi* (Bendif *et al.*, 2023)), forms extensive blooms that can extend over hundreds of thousands of square metres (O'Brien *et al.*, 2013; Kondrik *et al.*, 2018).

Given their ecological importance, understanding the molecular machinery underlying coccolithophore calcification and its interplay with photosynthesis is critical. Intracellular calcification within the coccolith vesicle (CV) necessitates meticulous regulation in the transportation of calcification substrates (Ca^{2+}, and dissolved inorganic carbon (DIC, including H^+, OH^-, CO_2, HCO_3^-)), and products (coccolith), across cellular membranes. Photosynthesis utilises CO_2 and light energy for primary carbon assimilation. The complex interaction between calcification and photosynthesis involves possible competition for inorganic carbon or mutual support in substrate supplementation (Brownlee & Davies, 1995; Buitenhuis *et al.*, 1999; Bach *et al.*, 2013). Calcification is thought to be light/energy dependent, with an estimated energetic cost of 19-37% of the energy produced through photosynthetic carbon fixation (Monteiro *et al.*, 2016). This energy is mainly utilised to regulate calcification substrate concentrations at the calcification site (Anning *et al.*, 1996; Raven & Crawfurd, 2012; Monteiro *et al.*, 2016; Brownlee *et al.*, 2021). The presence of ATP-dependent transporters, enzymes and pumps in *G. huxleyi* supports this hypothesis (Mackinder *et al.*, 2011; Bach *et al.*, 2013;

Skeffington *et al.*, 2023). Alternatively, calcification may benefit photosynthesis by providing CO_2 or H^+, alleviating pressure on carbon concentration mechanisms (CCMs) (Raven & Crawfurd, 2012; Monteiro *et al.*, 2016).

The interplay between calcification and photosynthesis has been intensely studied (Brownlee & Davies, 1995; Buitenhuis *et al.*, 1999; Bach *et al.*, 2013). The calcification response has been probed by applying low concentrations of Ca^{2+} or Sr^{2+}, 1-hydroxyethane 1,1-diphosphonic acid (HEDP) in *G. huxleyi* (Asahina & Okazaki, 2004; Walker *et al.*, 2018b). However, no changes in photosynthesis or growth were observed under these conditions despite inhibition of calcification (Asahina & Okazaki, 2004; Walker *et al.*, 2018b). Furthermore, no significant differences in photosynthetic performance were found between calcified and non-calcified *G. huxleyi* cultivated under identical conditions of DIC concentration, Ca^{2+} concentration and light intensity (Herfort *et al.*, 2002; Trimborn *et al.*, 2007). Similarly, manipulating Mg/Ca ratio of growth medium by adjusting Ca^{2+} levels from low to high resulted in severe coccolith malformation or decreased calcification, while photosynthetic performance remained constant (Herfort *et al.*, 2004; Trimborn *et al.*, 2007; Leonardos *et al.*, 2009; Moheimani *et al.*, 2012; Faucher *et al.*, 2020). Thus, currently there is no definitive evidence to support the notion that calcification enhances photosynthesis in coccolithophores.

Photosynthetic performance can be manipulated solely by altering light intensity without changing the availability of ambient calcification substrates. The relationship between calcification and photosynthesis under different light intensities, especially low light, is complex, and influenced by other environmental variables (Balch *et al.*, 1996; Gafar *et al.*, 2019; Zhang *et al.*, 2019; Zhang & Gao, 2021). Calcification exhibits a lower irradiance saturation level compared to photosynthesis, resulting in a delayed inhibition of calcification during decreasing irradiance (Zondervan, 2007). Below the light saturation level, both calcification and PIC/POC significantly decrease (Zondervan, 2007; Perrin *et al.*, 2016). An optimal range of light intensity can be identified, wherein PIC/POC increases with rising light intensity, as do both PIC and POC independently (Feng *et al.*, 2008; Tong *et al.*, 2016). Beyond the optimum light intensity, PIC experiences a pronounced decrease, while POC remains relatively constant (Feng *et al.*, 2008; Tong *et al.*, 2016). Such a decrease in PIC under high irradiance is exacerbated by high pCO_2

levels (Feng *et al.*, 2008; Zhang *et al.*, 2015) in a species-dependent manner (White *et al.*, 2018). Therefore, calcification of coccolithophores is not simply linearly dependent on photosynthesis, and their intertwined relationship remains unclear.

To elucidate the cellular regulation of calcification and its hierarchy amongst other central metabolic functions, i.e., photosynthesis and respiration, it is essential to target variables that impact both energy production and calcite formation, such as DIC. Mg, a relatively understudied variable, has the potential to influence both processes. On the calcification side, Mg is likely to influence calcification via two distinct mechanisms: by interfering with the physicochemical process of calcite precipitation and by disrupting biological calcium transport pathways. As the most abundant divalent metal in the ocean, Mg has exhibited considerable fluctuations over geological timescales, with the Mg/Ca ratio of seawater ranging from 1 mol:mol in the Early Palaeozoic and Jurassic-Cretaceous periods to an average of 5 mol:mol in the modern ocean (Hardie, 1996; Horita *et al.*, 2002; Fantle & DePaolo, 2006; Higgins & Schrag, 2015). In some coastal and river-influenced areas, Mg^{2+} and Ca^{2+} concentrations may be diluted by freshwater to <1 mol:mol (Lebrato *et al.*, 2020). Elevated Mg/Ca ratios or high Mg^{2+} concentrations inhibit inorganic calcite formation (Pan *et al.*, 2021) and are thought to be responsible for the aragonite to calcite oscillation in the primary inorganic carbon mineral precipitation from seawater expressed over the Phanerozoic. Mg^{2+} incorporated into the calcite crystal lattice raises the solubility of the advancing edge, thereby hindering calcite and aragonite nucleation (Morse *et al.*, 1997; Davis *et al.*, 2000; Boon *et al.*, 2020). Consequently, changes in Mg^{2+} concentrations or Mg/Ca ratios can significantly influence natural seawater calcite formation and extracellular biomineralisation through physicochemical pathways (Stanley & Hardie, 1998; Ries, 2010). In addition, high Mg^{2+} levels has been shown to cause severe coccolith malformation during intracellular calcification in coccolithophores (Herfort *et al.*, 2004), potentially through interference with Ca^{2+} uptake or with the nucleation process itself, although the exact mechanisms remain unresolved.

Besides the impact on calcification, Mg^{2+} is also an essential macronutrient for plant growth and development, participating in numerous cellular processes, including DNA and RNA synthesis, enzyme activation, signal transduction and, most importantly, the regulation of photosynthesis and energy production (Verbruggen & Hermans, 2013; Guo

et al., 2016). In the photosynthetic light reaction, Mg^{2+} is inserted into the porphyrin ring of biosynthetic chlorophyll, a process regulated by the enzyme Mg-chelatase in coordination with Mg^{2+} and ATP concentrations (Borah & Bhuyan, 2017). Mg^{2+} is also involved in the formation of pigment-protein complexes in photosystem I (PSI) and photosystem II (PSII), which function in light harvesting and electron transfer for the generation of NADPH and ATP (Renger & Renger, 2007). These products fuel the subsequent dark reaction of photosynthesis (Rochaix, 2011). In the dark reaction, Mg^{2+} serves as a cofactor, stabilising the negatively charged oxygen atoms in the ribulose-1,5-bisphosphate (RuBP) molecule, and facilitating the enzymatic carbon fixation reaction catalysed by ribulose-1,5-bisphosphate carboxylase/oxygenase (Rubisco) during the initial step of the Calvin cycle (Andersson & Backlund, 2008; Bracher *et al.*, 2017). Mg^{2+} is critical for maintaining Rubisco activity and ensuring efficient carbon fixation (Andersson & Backlund, 2008; Bracher *et al.*, 2017). Furthermore, Mg-ATP, serves as a substrate for numerous phosphorylating enzymes and acts as the principal energy source of the cell (Arnold & Kadenbach, 1997; Geigenberger *et al.*, 2010). The rate of Mg-ATP consumption increases with metabolic activity (Arnold & Kadenbach, 1997; Geigenberger *et al.*, 2010). Cytosolic Mg^{2+} and ADP concentrations are key factors regulating cellular respiratory activity to meet the demand for Mg-ATP (Bligny & Gout, 2017), influencing mitochondrial oxidative phosphorylation. Despite its essential role in core intracellular processes, the specific functions of Mg^{2+} in coccolithophore cell biology and calcification remain poorly understood.

Herein, a gradient of Mg availability was employed to elucidate cellular regulation and metabolic processes in the model coccolithophore, *G. huxleyi*, with particular focus on the intricate relationship between photosynthesis and calcification. A comprehensive analysis of *G. huxleyi*'s morphological, physiological, metabolic, and proteomic responses across Mg concentrations ranging from severe deficiency to four times the ambient seawater levels (0 to 210 mM) revealed remarkable adaptability. This adaptability reflects sophisticated regulation of core cellular functions, leading to complex physiological and calcification responses. The use of this chemically disruptive approach provides insight into the molecular mechanisms underlying the relationship between photosynthesis and calcification in coccolithophores, deepening

understanding of their susceptibility to global environmental changes and informing interpretations of the selective pressures shaping coccolithophores' evolution and their calcite production rate.

3.2 Materials and Methods

Gephyrocapsa huxleyi (strain OA1) was isolated from the North Sea in 2011 (Rickaby *et al.*, 2016). Clonal cultures were grown in sterile-filtered (0.22 µm) K/2 medium made up in artificial seawater (Keller *et al.*, 1987) that was modified for Mg concentrations. All experiments were conducted at a temperature of 17°C with a 16:8 h light: dark cycle (45-75 µmol m^{-2} s^{-1}).

3.2.1 Culture experiments

Gephyrocapsa huxleyi was grown across a gradient of seven Mg concentrations that bracket estimates of geological change and extend to more extreme conditions (Table 3. 1). Mg concentrations were adjusted by varying the addition of $MgCl_2$ while balancing NaCl to maintain a constant ionic strength. These adjustments were calculated using Visual MINTEQ 3.1, with a fixed Ca concentration of 10 mmol/kg, representative of modern seawater. Mg treatments were defined as their corresponding Mg/Ca ratio (Table 3. 1). The control condition, with an Mg/Ca of 5 (Mg-5; 54.60 mM), represents ambient seawater (Keller *et al.*, 1987; Lebrato *et al.*, 2020). Low Mg availability was defined as Mg/Ca <5 (<54.6 mM), while high Mg availability referred to Mg/Ca >5 (>54.6 mM). Cells were pre-acclimated to Mg-5 and maintained in exponential growth by weekly sub-culturing to fresh medium. After 28 days, triplicate cultures were transferred from the control to each of the experimental conditions and were subsequently maintained in the exponential growth phase by regular semi-continuous batch transfers to sterile growth medium. As Mg is ubiquitous, trace contamination during artificial seawater preparation in a standard laboratory setting is unavoidable. Any magnesium contamination, including in the Mg-0 condition, is expected to be at trace levels and uniformly distributed across all treatments.

After acclimation, three biological replicates were maintained in each condition for over 100 days with regular subculturing prior to sample collection. Cell number, size

measurements, and growth rate calculations were conducted using the same methodology as detailed in Chapter 2 (Section 2.2.2).

Condition	***Mg-0***	***Mg-0.5***	***Mg-1***	***Mg-5***	***Mg-10***	***Mg-15***	***Mg-20***
Mg/Ca ratio	0	0.5	1	5	10	15	20
[Mg^{2+}] (mM)	0	5.46	10.50	54.60	105.00	157.50	210.00

Table 3. 1: Defined Mg concentration and the corresponding Mg/Ca ratio in the culture media.

3.2.2 Chlorophyll-a extraction

Chlorophyll-a was extracted and quantified following the protocol described in Chapter 2 (Section 2.2.3). Two normalisations were used: (1) chlorophyll-a per cell, calculated based on cell counts, and (2) chlorophyll-a per unit volume, calculated by normalising to cell volume assuming spherical cell geometry.

3.2.3 Scanning electron microscopy and image analysis

During the mid-exponential phase, cells were filtered onto polycarbonate filters (0.8 µm), washed with 100% ethanol and 10 mM $CaCl_2$ solution, and dried overnight in a fume hood. The filtered cells were gold-coated and scanned with a Zeiss Sigma 300 Field Emission Gun Scanning Electron Microscope (FEG-SEM).

Over 200 coccoliths were counted for morphological analysis. Four levels of malformation were defined: i) 'normal' (complete fine structure including visible central area, outer and inner rim, distal and proximal shield elements); ii) 'malformed' (minor incomplete structure, mostly showing gaps or merging of the distal shield elements); iii) 'incomplete' (structure is only partially established with short shield elements and an incomplete central area, sometimes with a proto-coccolith ring observed); and iv) 'malformed and incomplete' (partially established structure with gap between shield elements, causing coccolith not to form a closed oval shape) (Figure 3. 4). For cell and coccolith size analysis, more than 50 coccospheres and 150 coccoliths were measured using ImageJ (https://imagej.nih.gov/ij/).

3.2.4 Carbon chemistry and determination of calcification

Cellular $CaCO_3$ content was calculated using the traditional method described in Chapter 2 (Section 2.2.4, equation 2.5), which estimates $CaCO_3$ productions from total alkalinity depletion normalised to the change in cell number across each sampling interval.

3.2.5 Net Photosynthesis and Dark Respiration Rates

Photosynthesis and dark respiration rates were measured across a range of light intensities (0-1200 $\mu mol\ m^{-2}\ s^{-1}$) with a minimum of three biological replicates per condition. A Liquid-phase Oxygen Electrode System combined with an Oxthem+ Control Unit (Hansatech Ltd, King's Lynn, UK) was used to measure net oxygen evolution in light (net primary production, NP) and oxygen consumption in darkness (dark respiration), both expressed in $\mu mol\ O_2\ ml^{-1}\ s^{-1}$. All biological replicates were sampled from stock cultures grown under corresponding Mg availability conditions. To capture representative physiological responses while reducing bias from growth phase or measurement timing, samples were collected from mid-exponential phase to early stationary phase, with measurements completed within an 8-hour window. Although the number of total replicates per condition varied due to differences in sampling timing and culture availability, each condition included the full range of light intensities, and data from all timepoints were aggregated to generate robust light-response curves. This approach was chosen after preliminary analysis revealed that no single timepoint provided consistent significance across all comparisons. The method was adapted from (Barton *et al.*, 2020). Detailed methodology is provided in the Supplementary Materials.

The Michaelis-Menten model was selected to describe the light dependence of net photosynthesis, as it provided a strong empirical fit across all Mg treatments and enabled consistent estimation of saturation parameters. Although the model does not capture the initial quantum yield or account for photoinhibition, its use was justified by the absence of strong inhibitory trends at high irradiance levels and its comparable performance to linear, logarithmic and exponential fits (Table A2. 5, Table A2. 6). Model fitting was restricted to light-response data only, with dark respiration measurements excluded.

The Michaelis-Menten model was adapted to describe the light dependence of photosynthesis (Ritchie, 2008):

$$P = \frac{Pmax * E}{Ek + E} \quad (3.1)$$

Where P is the photosynthetic rate, E is the light intensity, E_k is the half-saturation constant for irradiance (the light intensity at which the photosynthetic rate is half of its maximum), and P_{max} is the maximum rate of photosynthesis at saturating light intensities.

3.2.6 Shotgun proteomic analysis

At late-exponential growth, triplicate 200 mL sub-samples were collected from the Mg-0 (0 mM), Mg-0.5 (5.46 mM), Mg-5 (control; 54.60 mM) and Mg-20 (210.00 mM) treatments. Cells were collected by centrifugation (3000 rpm for 15 min, at 4°C) and immediately placed at -80°C. Cell pellets were allowed to thaw at room temperature and resuspended in an extraction buffer (20 mM Tris-HCl, pH 8.0) before being lysed by sonication on ice (3 x 10 min with vortexing). Lysates were centrifuged to remove any remaining particulate material, and the protein concentration was quantified using a Bradford assay (Bradford, 1976). Peptides were analysed using nano liquid chromatography (Thermo Fisher Scientific Ultimate RSLC 3000) coupled with a Q Exactive mass spectrometer (Thermo Fisher Scientific) following in-solution trypsin digestion and C18 stage-tip desalting, as described in (Dedman *et al.*, 2023).

Raw spectra were analysed using MaxQuant v2.1.4.0 for protein identification and label-free quantification (LFQ), using the MaxLFQ package (Cox & Mann, 2008; Cox *et al.*, 2014). The reference proteome UP000013827 for *G. huxleyi* was used as a database for protein identification (UniProt Consortium, 2021). Zero values were treated as missing data, and their distribution across conditions was assessed. To stabilise variance between conditions and replicates, a log2 transformation was applied. For proteins with only one missing value in the triplicate samples of each condition, MissForest imputation was performed (ntree=1,000, maxnodes=1,000, with other parameters set to default). Imputation was validated using Kolmogorov-Smirnov tests for each sample, comparing distributions before and after imputation, with no statistically significant differences observed (all p-values > 0.05).

Venn diagrams were generated to visualise protein expression patterns across conditions, and protein lists were compiled for pairs of proteins expressed under stressed conditions (Mg-0, Mg-0.5, Mg-20) and those commonly expressed in all conditions. Proteins were filtered using pairwise t-tests with a p-value cutoff of 0.05. Log2-fold change (LFC) was used to determine the direction of regulation. Significantly differentially expressed proteins were further grouped and annotated using Gene Ontology (GO), Kyoto Encyclopedia of Genes and Genomes (KEGG) and functional annotation clustering analysis via the web server DAVID (Sherman *et al.*, 2022). For the DAVID analysis, a Benjamini-corrected p-value threshold of 0.05 was applied, with downstream visualisation performed using the "ggplot2" package in R (version 4.3.2).

3.2.7 Statistical analysis

Averaged values for physiological traits and protein intensities were calculated as the mean ± standard deviation (SD) of biological replicates. Significant differences between treatments and the control condition are indicated with asterisks: $p \leq 0.05$(*), $p \leq 0.01$(**) and $p \leq 0.001$(***). All statistical analyses, data processing, and visualisation were conducted using R (version 4.3.2).

3.3 Results

3.3.1 Cellular physiology and metabolic performance

3.3.1.1 Trait responses to varying Mg availability

Significant variation in physiological traits was observed across both low and high Mg availability. Growth rates of *G. huxleyi* were markedly suppressed under low-Mg (<Mg-5; 0-54.6 mM), with the lowest rate occurring at Mg-0 (58% lower than Mg-5), and final cell density reduced by half (Figure 3. 1a; Table A2. 1). In contrast, high Mg conditions (≥Mg-5; 54.6-210.0 mM) did not enhance growth significantly, the highest rate was observed at Mg-10 (~5% higher than Mg-5). Cell sizes increased significantly under low Mg and decreased with rising Mg availability (Figure 3. 1b; Figure 3. 4b, c). The largest cells (5.16±0.11 µm) were observed at Mg-0.5 (~11% larger than Mg-5), while the smallest (4.24±0.02 µm) were at Mg-20 (~9% smaller than Mg-5).

Cellular $CaCO_3$ and chlorophyll-a content showed similar trends, both peaking at Mg-1 and decreasing at higher and lower Mg concentrations. Cellular $CaCO_3$ content exhibited greater variability across conditions (Figure 3. 1c), ranging from ~200 pg cell^{-1} at Mg-1 to near zero at Mg-0. A substantial reduction was observed at Mg-20, which was 4-fold lower than at Mg-1 and 3-fold lower than Mg-5. Chlorophyll-a content dropped significantly only at Mg-0 and Mg-20, by ~40% and ~16%, respectively (Figure 3. 1b). When normalised to cell size, chlorophyll-a content increased steadily with rising Mg concentration, reaching more than double the value at Mg-20 compared to Mg-0 (Figure 3. 1e). $CaCO_3$ content per unit volume exhibited a similar unimodal pattern, but the peak shifted from Mg-1 to Mg-5 after normalisation (Figure 3. 1f).

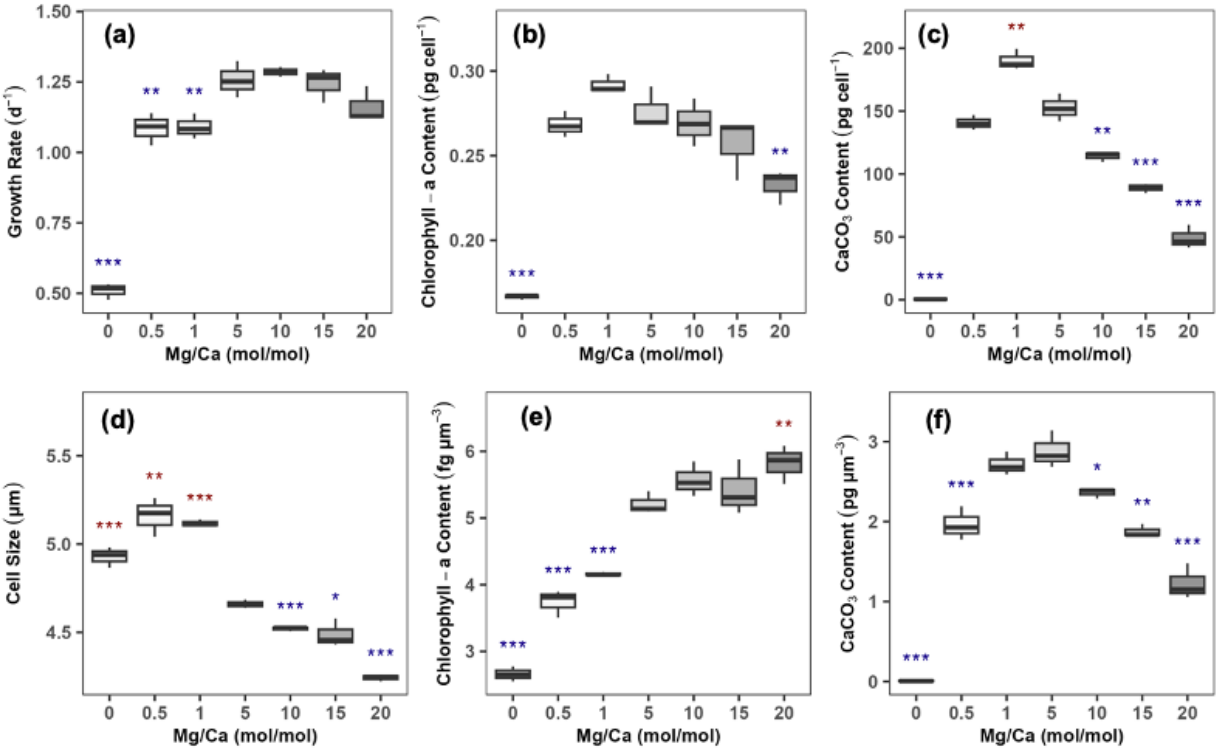

Figure 3. 1: Physiological responses of *Gephyrocapsa huxleyi* to varying seawater Mg availability. (a) Growth rate; (b) Cellular chlorophyll-a content ; (c) Cellular $CaCO_3$ content; (d) Naked cell size; (e) chlorophyll-a content per unit volume; (f) $CaCO_3$ content per unit volume. Experimental conditions (Mg/Ca ratios of 0. 0.5, 1, 10, 15, 20) were compared to the control condition (Mg-5) using paired t-tests. Asterisks indicate significant difference from the control: red asterisks denote significantly higher values and blue indicate significantly lower values than the control. The number of asterisks represents the level of significance: * p<0.05, ** p<0.01, ***p<0.001.

3.1.1.2 Trait Interactions and multivariate analysis

To assess coordinated physiological responses to Mg availability, principal component analysis (PCA) and correlation analysis were performed (Figure 3. 2b; Figure A2. 4). An

initial PCA including all conditions revealed that the extreme Mg-0 treatment dominated the first principal component, obscuring variation among the remaining treatments (Figure A2. 3). After removing the Mg-0 treatment and selecting biologically relevant, non-redundant traits, the PCA revealed two principal axes that together explained 91.8% of total variance (Figure 2b). PC1 (69%) reflected a gradient associated with Mg concentration, with positive loading from growth rate, chlorophyll-a per unit volume, and cell number, and a strong negative loading from cell size, indicating that higher Mg promotes cell division and chlorophyll density while reducing individual cell size. PC2 (22.8%) captured traits including cellular $CaCO_3$ content, chlorophyll per cell, and $CaCO_3$ content per unit volume, which clustered together and peaked at intermediate Mg levels (Mg-1 and Mg-5), suggesting co-regulation of calcification and cellular pigment independent of overall growth.

These PCA patterns were supported by pairwise linear correlations. Cell size was negatively correlated with Mg concentration (R^2 >0.8) (Figure 3. 2c), but showed a weak association with growth rate (R^2 =0.19 with Mg-0 included). A multiple linear regression further confirmed that cell density, Mg concentration, and growth rate together explained 92.43% of the variation in cell size (adjusted R^2 =0.91, $p < 0.001$) (Table A2. 2; Figure A2. 5), with Mg concentration and cell density exerting negative effects, and growth rate having a minor positive contribution.

To investigate the regulation of chlorophyll-a content, two multiple regression models were applied. For cellular chlorophyll-a content, Mg concentration, growth rate, and cell number together explained 82.14% of the variance (adjusted R^2 = 0.79), revealing a significant negative correlation with Mg concentration and a positive correlation with growth rate (Table A2. 3; Figure A2. 6). In contrast, chlorophyll-a content per unit volume increased with both Mg concentration and growth rate (Table A2. 4; Figure A2. 7), reflecting differences in size-normalised versus per-cell pigment accumulation. Consistent with PCA results, cellular $CaCO_3$ content was positively correlated with cellular chlorophyll-a content (R^2 =0.831 with Mg-0 included, Figure 3. 2a). From Mg-1 to Mg-20, cellular $CaCO_3$ content declined linearly with increasing Mg concentrations (R^2 =0.98, Figure 3. 2d).

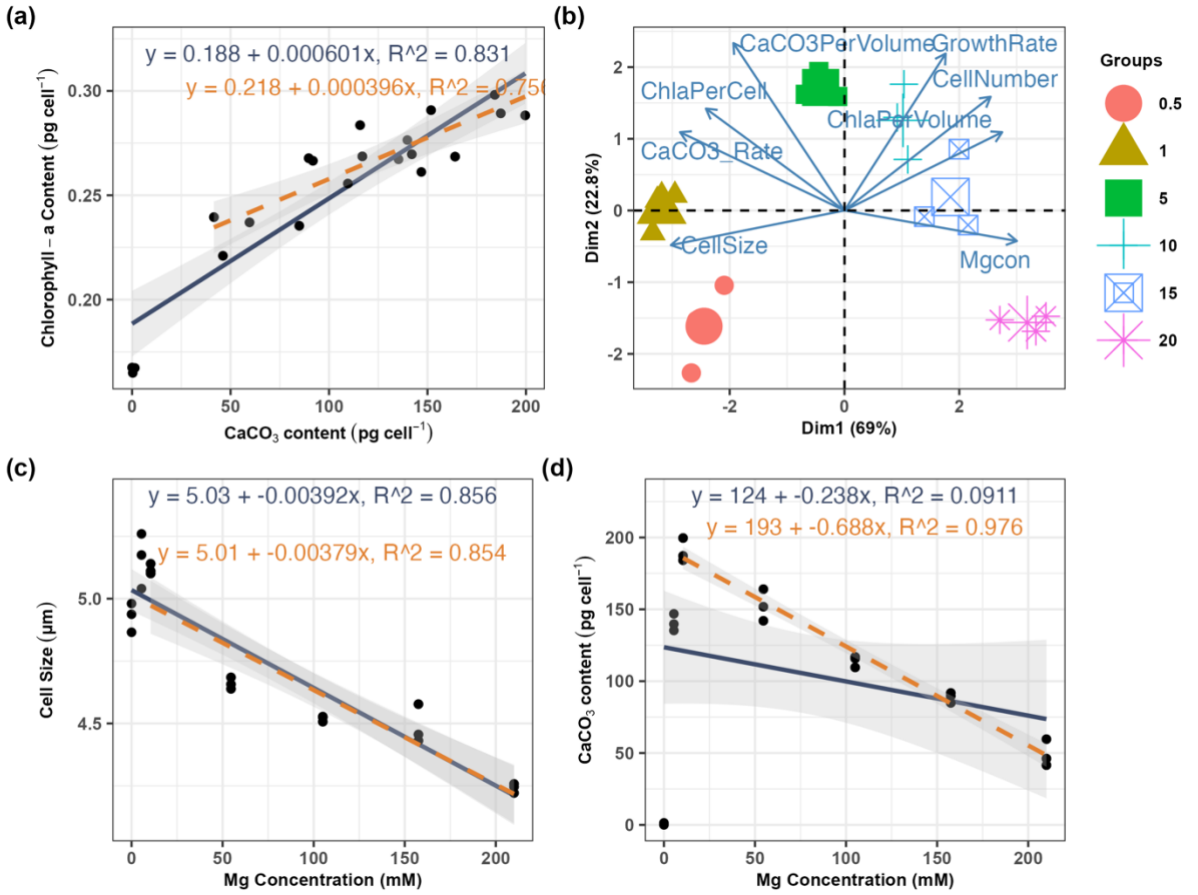

Figure 3. 2: Relationship between seawater Mg availability and *Geophyrocapsa huxleyi* physiological traits. (a) linear regression between cellular chlorophyll-a content and $CaCO_3$ content; (b) principal component analysis of physiological traits across Mg treatments excluding the Mg-0 treatment for all the physiological parameters collected, excluding the calculated carbonate species (Figure A2. 3); (c) linear regression between seawater Mg concentrations and cell size; (d) linear regression between Mg concentrations and cellular $CaCO_3$ content. The Blue solid trendline and equation represent the linear regressions for the full dataset collected across all experimental conditions. The orange dashed trendline and equations in (a) and (c) represent the experimental Mg/Ca ratio range of 0.5 to 20, excluding the Mg-0 condition; in (d) represent the experimental Mg/Ca ratio range of 1 to 20, excluding the Mg-0 and Mg-0.5 condition.

3.1.1.3 Net photosynthesis and dark respiration rates

Metabolic performance was evaluated across selected Mg concentrations (Mg-0, Mg-0.5, Mg-5 (control), and Mg-20), mirroring those used for proteomic analysis. Although total replicate numbers varied across treatments due to differences in sampling timepoints, each condition was evenly represented across all light levels, allowing for robust Michaelis-Menten (M-M) model fitting and reliable comparison of photosynthetic responses. Cellular respiration rates remained consistent across all conditions. Under low to moderate light (45-300 µmol photons m^{-2} s^{-1}), net photosynthesis rates in Mg-0.5 and Mg-20 showed no significant differences from the control. However, at higher light

levels (600-1200 µmol photons m^{-2} s^{-1}), Mg-0.5 displayed significantly higher rates than the control, while Mg-20 showed a significant decrease only at 1200 µmol photons m^{-2} s^{-1}. Notably, net photosynthesis rates in Mg-0 were consistently lower than the control across all light intensities (Figure 3. 3; Figure A2. 8).

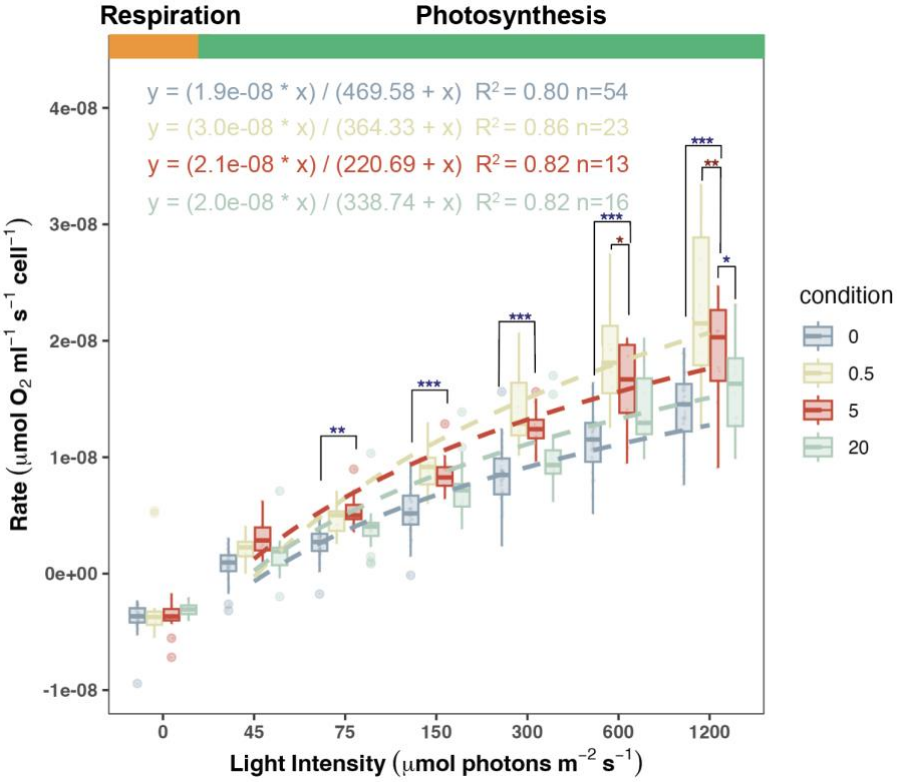

Figure 3. 3: Photosynthetic light-response curves of *Gephyrocapsa huxleyi* under varying magnesium conditions: Mg-0, Mg-0.5, Mg-5 and Mg-20. Rate at 0 µmol photons m^{-2} s^{-1} represent respiration, while rates from 45 to 1200 µmol photons m^{-2} s^{-1} represent net photosynthesis. Saturation points and equations are derived from Michaelis- Menten model with trendlines showing a logarithm fit. Asterisks indicate significant differences from control (red indicates higher values, blue indicates lower values; the number of asterisks corresponds to the significance level: * p<0.05, ** p<0.01, ***p<0.001). Boxplots show median, interquartile range, and extreme values; individual points represent outliers from replicate measurements within each Mg condition. Each light level includes multiple replicate measurements per Mg condition. Dashed lines represent logarithmic fit trends.

Linear fit models were applied, with the logarithmic and Michaelis-Menten (M-M) models standing out, both showing similar R^2 values. Light saturation points, determined via the M-M model, revealed that Mg-0 exhibited the highest saturation irradiance (424.39 µmol photons m^{-2} s^{-1}, R^2 = 0.81), followed by Mg-0.5 (368.37 µmol photons m^{-2} s^{-1}, R^2 = 0.82), Mg-20 (303.04 µmol photons m^{-2} s^{-1}, R^2 = 0.75), and the control (257.87 µmol photons m^{-2} s^{-1}, R^2 = 0.83). Estimated Pmax values from the M-M model were highest in Mg-0.5 (3.01 x 10^{-8} µmol O_2 ml^{-1} s^{-1}), followed by Mg-5 (2.31 x 10^{-8}), Mg-20 (2.06 x 10^{-8}), and Mg-0 (1.94 x

10^{-8}). The dark respiration rates showed comparable magnitudes across treatments, ranging from -3.06 x 10^{-9} µmol photons m^{-2} s^{-1} in Mg-20 to -3.77 x 10^{-9} in Mg-5 (Table A2. 8). Although metabolic rates per unit cell volume showed similar trends, the lower R^2 values likely reflect greater variability due to differences in cell size among conditions (Figure A2. 8).

Overall, metabolic analysis demonstrated remarkable photosynthetic stability of *G. huxleyi* across a wide range of Mg concentrations, particularly under moderate light levels. Mg-0 was notably distinct from the others, exhibiting significantly reduced net photosynthesis and the highest light saturation irradiance.

3.1.1.4 Coccolith morphology

SEM was employed to assess the impact of varying Mg availability on *G. huxleyi* coccolith morphology (Figure 3. 4). A high degree of coccolith morphological regulation was observed between Mg-0.5 to Mg-10, with >90% coccoliths in each condition classified as normal, where the best morphological performance was recorded in the control (Mg-5). In contrast, more incomplete coccoliths were observed in Mg-15, and at Mg-20, whereby >50% were incomplete, while 20% were both severely malformed and incomplete (Figure 3. 4a). This observation aligns with the severe coccosphere malformation in the Mg-15 and Mg-20 treatments (Figure 3. 4b) and the significant reduction in cellular $CaCO_3$ content (Figure 3. 1d). Notably, at Mg-0, *G. huxleyi* reproduced but lost calcification entirely, existing only as naked cells (Figure 3. 4b). Pearson linear regression of coccolith width against length exhibited increasing variability with decreasing Mg availability from Mg-5 to Mg-0.5, in parallel with a small increase in malformation as Mg dropped from Mg-5 to Mg-0.5, whereas the correlation remained high and stable at higher Mg concentrations (Mg-5 to Mg-20) (Figure 3. 4c).

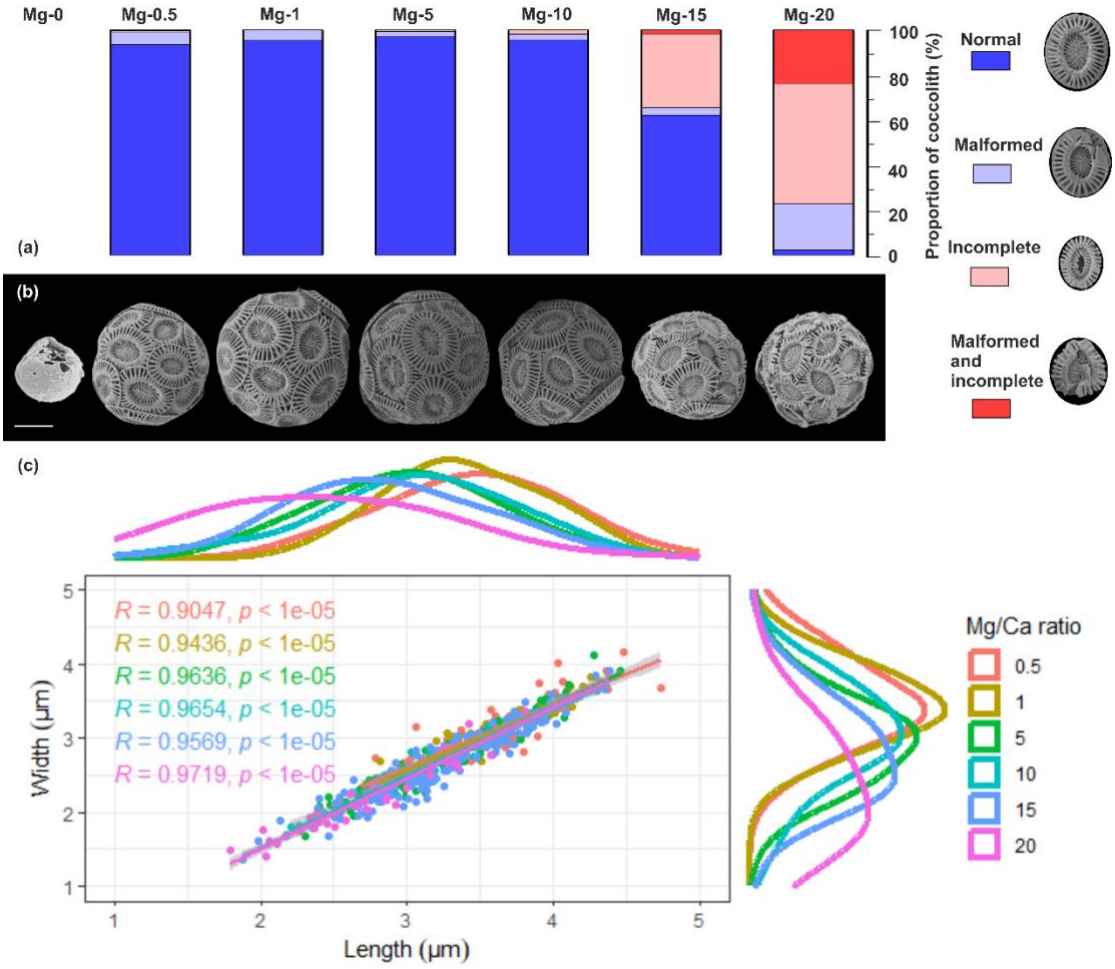

Figure 3. 4: Morphological response of *Gephyrocapsa huxleyi* to varying seawater Mg availability (5.46 to 210 mM). (a) Quantification of coccolith malformation under Mg/Ca ratios of 0.5 to 20 with the standard coccolith morphology presented on the right side; (b) coccosphere morphology response to seawater Mg/Ca ratios of 0 to 20; bar scale = 2 mm (applies to a (legend) and b); (c) coccolith width versus coccolith length. The Pearson linear regression method was applied for each experimental condition.

3.1.2 Shotgun proteomic analysis

Proteomic analysis was performed on selected conditions (Mg-0, Mg-0.5, Mg-5 and Mg-20) to capture the most significant variations in calcification and physiology. Initial data processing yielded 2681 raw protein entries across all treatments. After filtering for potential contaminants, reverse sequences, and proteins only identified by a single peptide, a total of 2614 proteins remained for further analysis. Notable differences in protein identification across conditions were observed: 1474 in Mg-0, 1181 in Mg-0.5, 1091 in Mg-20, and 906 in Mg-5. Of these, 290 in Mg-0, 21 in Mg-0.5, 10 in Mg-5, and 35 in Mg-20 were observed only in their respective conditions, though this may reflect detection thresholds rather than exclusive expression. Additionally, 133 proteins were

common to all stressed conditions (Mg-0, Mg-0.5, Mg-20), 157 were shared between Mg-0 and Mg-0.5, and 49 between Mg-0 and Mg-20. A total of 806 proteins were detected across all treatments (Figure 3. 5a).

3.1.2.2 Condition-specific proteins

Proteins uniquely expressed in the Mg-0 condition were enriched in DNA-related activities, such as DNA replication and repair, as well as ATP binding and ATPase activity. Translation initiation factors and membrane transport proteins were also prominent (Figure 3. 5b). In low-Mg conditions (Mg-0 and Mg-0.5), protein synthesis machinery, ribosomal components, and translation processes showed strong enrichment. RNA-binding proteins, protein transport, and proteasome regulation, are also highlighted, alongside alterations in vesicle trafficking (Figure 3. 5e). Common proteins between Mg-0 and Mg-20 conditions were enriched in oxidative phosphorylation, respiratory chain activities, and proton-transporting ATPase, with a notable representation of membrane-associated processes (Figure 3. 5c). Proteins shared across Mg-0, Mg-0.5, and Mg-20 (excluding Mg-5) conditions displayed enrichment in protein synthesis and turnover, ribosomal functions, translation, and proteasome activity, with cytoplasmic and ribosomal functions being most significant (Figure 3. 5d).

3.1.2.3 Comprehensive analysis of proteins expressed across all conditions

Among the 806 proteins commonly expressed across all conditions, Principal component analysis (PCA) showed clear separation between conditions, with PC1 and PC2 explaining 48.5% and 14% of the variance, respectively (Figure 3. 6b). Notably, Mg-0 samples clustered distinctly from other conditions along PC1, highlighting the substantial impact of Mg depletion on the overall proteome. Pairwise t-tests ($p \leq 0.05$) revealed significant protein expression changes based on the LFC of the LFQ intensity (Figure 3. 6d). Compared to Mg-5, the most pronounced proteomic alterations were observed in Mg-0 (398 proteins; 175 up, 223 down), followed by Mg-0.5 (140 proteins; 63 up, 77 down), while Mg-20 showed the least variability (106 proteins; 48 up, 58 down) (Figure A2. 10; Figure A2. 11; Figure A2. 12).

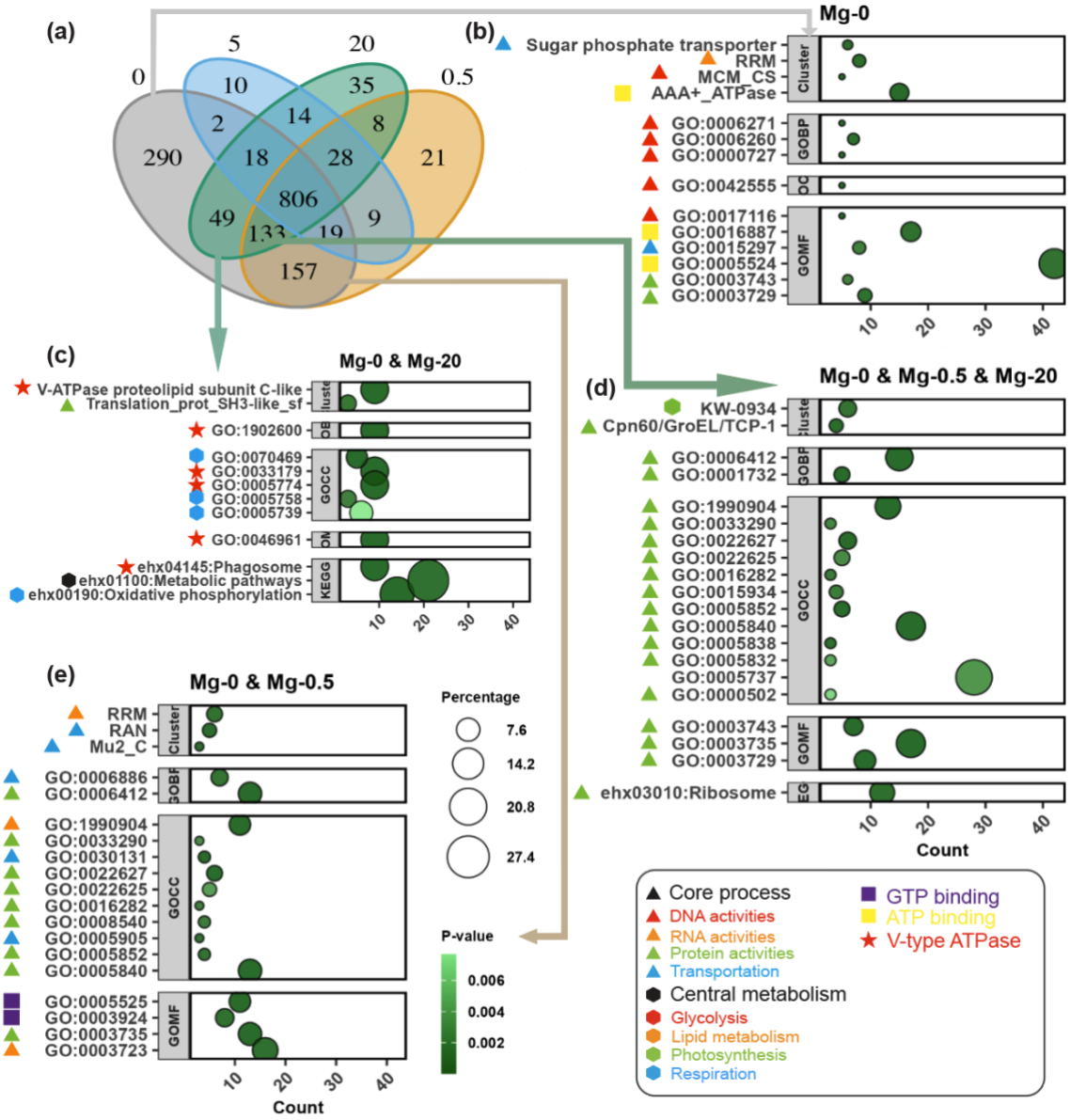

Figure 3. 5: Proteomics analysis of *Gephyrocapsa huxleyi* responses to selected Mg concentrations. (a) Venn diagram showing condition-specific proteins across Mg-0, Mg-0.5, Mg-5, and Mg-20. (b-e) Gene Ontology (GO) enrichment analysis of condition-specific proteins, with circle size representing the percentage of proteins, and colour indicating the Benjamini adjusted p-value. The sections are organised from top to bottom as follows: clusters, Gene Ontology Biological Processes (GOBP), Gene Ontology Cellular Components (GOCC), Gene Ontology Molecular Functions (GOMF), and Kyoto Encyclopedia of Genes and Genomes (KEGG). Protein lists used were derived from (a), with arrows indicating relevant sections. Shapes denote biological functions: triangles mark core processes: DNA-related (red), RNA-binding (orange), protein-related (green), and transport (blue); rectangles highlight ATP- (yellow) and GTP-related (purple) functions; the red start marks V-type ATPase. Polygons represent metabolic processes: glycolysis and gluconeogenesis (red), lipid metabolism (orange), photosynthesis (green), and respiration (blue).

a) Functional enrichment analysis of up- and down- regulated proteins

Functional enrichment analysis of differentially expressed proteins revealed distinct patterns across varying Mg concentrations. In the comparison of Mg-0 vs. Mg-5, proteins upregulated under Mg-0 were predominantly associated with ribosomal and translation processes (e.g., ribosomal subunits, translation initiation factors) as well as photosynthesis (e.g., light response proteins) (Figure 3. 6c). Conversely, proteins downregulated under Mg-0 were involved in metabolic pathways such as glycolysis and fatty acid metabolism, along with cellular components such as the cytosol and chloroplasts. ATP-binding activities and several enzymatic activities were also affected (Figure 3. 6a). In the Mg-0.5 vs. Mg-5 comparison, proteins upregulated in Mg-0.5 were primarily associated with light response, photosynthesis, and cytoskeleton organisation, whereas downregulated proteins did not exhibit significant clustering (Figure 3. 6f). For Mg-20 vs. Mg-5, upregulated proteins in Mg-20 were linked to photosynthesis and ADP-binding domains (Figure 3. 6e), while downregulated proteins were involved in ATP-binding, glycolysis, and cytosolic processes. Notably, a magnesium-related functional cluster (KW-0460 Magnesium) was enriched among downregulated proteins in Mg-20, including magnesium-dependent enzymes such as pyruvate kinase (PK) (R1EEU6) and adenosine kinase (AK) (R1F2Z0) (Figure 3. 6g).

b) Significant downregulation of Mg-binding proteins and high LFC variability in the absence of Mg

Significant changes in Mg-binding proteins and those with high log2-fold variability under experimental conditions (vs. Mg-5, the control treatment), indicate shifts in phosphate homeostasis, membrane remodelling, and nucleotide synthesis. Among the 13 magnesium ion binding [GO:0000287] proteins identified, 10 were downregulated in Mg-0 with LFC from -0.57 to -2.38, including proteins crucial for chlorophyll biosynthesis, glycolysis/gluconeogenesis, and photosynthesis. In Mg-0.5, 4 Mg-binding proteins displayed mixed regulation, while minimal changes were observed in Mg-20 (Figure 3. 6h).

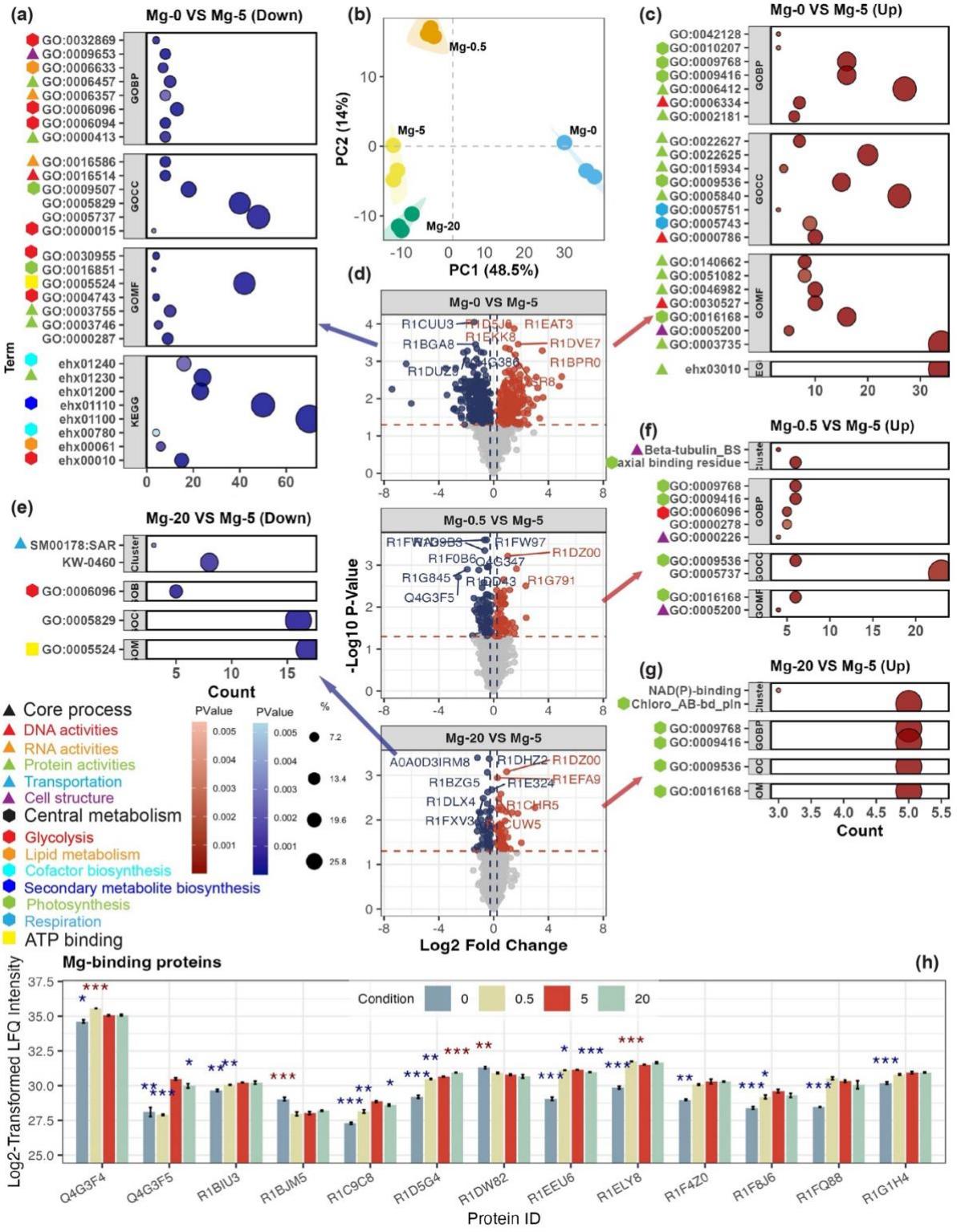

Figure 3. 6: Proteomic responses of *Gephyrocapsa huxleyi* to varying Mg conditions. (b) Principal Component Analysis (PCA) plot showing shared expression profiles across Mg-0, Mg-0.5, Mg-5, and Mg-20; (d) Volcano plots of differentially expressed proteins compared to the control (Mg-5); red and blue dots indicate up- and downregulated proteins, respectively. Dashed line marks significant threshold ($\log_{10}(0.05)$), with the top 10 most significant proteins labelled; (a, c, e, f, g) Gene Ontology (GO) enrichment analysis of significantly expressed proteins (relative to Mg-5). Circle size represents the percentage of proteins; colour indicates Benjamini-adjusted p-value.

Categories are arranged top to bottom as: clusters, Gene Ontology Biological Processes (GOBP), Gene Ontology Cellular Components (GOCC), Gene Ontology Molecular Functions (GOMF), and Kyoto Encyclopedia of Genes and Genomes (KEGG), noting that some groups lack cluster and KEGG annotations. (c, f, g) display GO terms for upregulated proteins (positive Log-fold change (LFC)), while (a, e) shows terms for downregulated proteins (negative LFC); symbols indicate functional categories: triangles represent core processes (DNA replication/repair-red; RNA binding-orange; protein synthesis/folding-green; transport-blue; cytoskeletal functions-purple); polygons represent metabolic and energy pathways (glycolysis/gluconeogenesis-red; lipid metabolism-orange; cofactor biosynthesis-cyan; secondary metabolism-fluorescent blue; photosynthesis-green; respiration-blue); yellow rectangles mark ATP-related processes. (h) Log2-transformed expression levels of Mg-binding proteins across treatments. Asterisks indicate significance (t-test), with colour denoting regulation direction (red: up; blue: down).

The top 10 upregulated proteins across conditions (LFC: 2.88 to 4.97) were predominantly observed at Mg-0, with functions in gene expression /regulation, cytoskeletal structure, biochemical reactions, and central metabolism. The top 10 downregulated proteins were found in Mg-0, participating in lipid metabolism, dephosphorylation, and cellular regulation and signalling. In conditions with less variability, a Photosystem I (PSI) protein (Q4G3F5) was most downregulated in Mg-0.5 (LFC: -2.58), while Histone H2A (R1FF37) was most upregulated (LFC: 2.38). In Mg-20, a Fe/B12 periplasmic-binding domain-containing protein (R1EBU0) was most downregulated (LFC: -1.39). Notable upregulated proteins in Mg-20 included H2A (R1FF37), a Rieske domain-containing protein (R1BIT6; LFC: 2.03), and ATP synthase (R1DTA1; LFC: 1.77).

c) Cellular adaptation to varying Mg availability affects multiple metabolic pathways and cellular processes

Variations in protein expression across experimental conditions revealed distinct cellular adaptations. The Mg-0 treatment exhibited the most variability, significantly affecting ATP-binding proteins (70 proteins, 26 upregulated and 44 downregulated) and membrane-associated proteins (61 proteins, 46 upregulated and 15 downregulated). Ribosomal proteins were notably upregulated in Mg-0, with 23 upregulated versus 3 downregulated.

The key findings for individual metabolic pathways across different Mg concentrations highlight significant changes in cellular processes. In photosynthesis-related pathways, light-harvesting proteins were predominantly upregulated in Mg-0, with more balanced

regulation in Mg-0.5 and Mg-20 (Figure A2. 16). Chlorophyll biosynthesis displayed a compensatory response in Mg-0 (Figure A2. 16). Central carbon metabolism exhibited mixed regulation in the Calvin cycle, with glycolysis /gluconeogenesis pathways significantly downregulated in Mg-0, upregulation in Mg-0.5 and mixed responses in Mg-20 (Figure A2. 16). Lipid metabolism shifted towards catabolism in Mg-0 and Mg-0.5, with fatty acid biosynthesis proteins mostly downregulated in Mg-0 but some upregulation observed in Mg-20. The respiratory ETC and TCA cycle showed varied regulation, with the most changes in Mg-0 and consistent downregulation of Complex I components across all conditions. Ion transport and homeostasis proteins displayed diverse responses: V-type ATPases showed mixed regulation, while Ca^{2+} ATPase (R1FNS5) was notably upregulated in both Mg-0 and Mg-0.5. EF-hand binding proteins were consistently downregulated across all conditions. Various transporters, including those involved in cation, calcium, and proton transport, were predominantly upregulated in Mg-0. ABC transporters showed mixed regulation, with more upregulation in Mg-0 and some downregulation in Mg-20. Cytoskeletal changes were observed, particularly in Mg-0 and partially in Mg-0.5, with CCT complex and tubulin-related proteins predominantly upregulated, while actin-related proteins showed mixed regulation.

3.4 Discussion

Despite the critical role coccolithophores play in the carbon cycle, their physiological response to environmental stresses and the molecular regulation underlying trait interactions remain poorly understood. Unlike many land plants that can experience Mg limitation (Guo *et al.*, 2016), marine systems are typically rich in Mg, with concentrations in the open ocean remaining high and relatively stable (Lebrato *et al.*, 2020). Given the low cellular demand relative to ambient availability, Mg is not considered limiting for marine phytoplankton growth (Ho *et al.*, 2003; Moore *et al.*, 2013). Yet, in this study, *G. huxleyi* displayed substantial physiological and proteomic responses across a wide Mg gradient, particularly under depletion. This capacity to persist under severe Mg scarcity underscores the organism's regulatory flexibility and reveals how metabolic networks are reprogrammed in response to atypical ionic stress. By using Mg availability as a perturbation, not to replicate environmental conditions but to probe regulatory

architecture, this approach offers new insight into coccolithophore trait responses, physiological interconnection, and molecular regulation.

3.4.1 Mg availability decouples cell size and division through metabolic and cell cycle regulation

Cell size is typically maintained through a balance between biosynthetic growth and cell cycle progression (Rhind, 2021). This study demonstrates that Mg availability regulates both cell size and cell division in coccolithophores, but notably through distinct and decoupled mechanisms (Figure 3. 1). Under low Mg conditions (Mg-0 to Mg-1), cell division (growth rate) is significantly suppressed, whereas cell size increases substantially. Conversely, under excess Mg conditions (Mg-10 to Mg-20), cell size decreases without a corresponding change in division rate. This inverse relationship supports that Mg availability may reprogram the cellular balance between biomass accumulation and division, likely through transcriptional, metabolic, and ionic regulatory mechanisms (Walker, 1986; Maier, 2013).

Multiple models have been proposed across different organisms to explain the regulation of cell size and division, where size is carefully regulated and division occurs when size reaches specific checkpoints (Weart *et al.*, 2007; Turner *et al.*, 2012). While classical models of nutrient-driven growth laws posit that nutrient enrichment enhances biosynthetic capacity and leads to larger cell size (Vadia & Levin, 2015), this framework is not applicable to the observed Mg response, where cell size linearly decreased with increasing Mg availability. This pattern suggests that Mg may not solely regulate cell size and division as a conventional nutrient. Alternative models in which size homeostasis results from dynamic feedback between nutrient signalling, growth, size, and cell cycle regulation (Table A2. 2) (Björklund, 2019; Rhind, 2021) may provide better explanation for these observations. While division rate (growth rate) remained mostly stable in high-Mg treatments, cell size declined, suggesting that excess Mg may facilitate bypass of conventional size checkpoints, allowing division to occur at a reduced threshold size (Marshall *et al.*, 2012), or through enhancing DNA replication (Colin *et al.*, 2021). Conversely, under Mg limitation, cells increased in size despite reduced division, indicating a blockade at the G1/S or G2/M phases, consistent with delayed cell cycle

progression due to insufficient nucleotide or protein synthesis capacity (Wolf & Cittadini, 1999; Maier, 2013).

Proteomic data support these interpretations. Under Mg limitation, we detected histones, ribosomal proteins, DNA replication factors, and translation machinery specifically in Mg-0, consistent with an arrested but biosynthetically active G1 phase (Figure 3. 5e). Simultaneously, Mg-binding proteins involved in photosynthesis and nucleotide metabolism were significantly downregulated, indicating functional impairment of Mg-dependent enzymes (Figure 3. 6h). This imbalance likely impairs proper cell cycle progression, reinforcing a model where Mg acts as a cofactor required not only for metabolism but also for the timing and fidelity of cell division (Walker, 1986; Maier, 2013; Pontes *et al.*, 2016; Björklund, 2019).

Chlorophyll-a content trends reinforce this interpretation. Cellular chlorophyll-a content followed cell size trends, increasing under Mg limitation and decreasing under excess Mg, while chlorophyll-a per unit volume showed opposite pattern (Figure 3. 1). This suggests that Mg-limited cells accumulated more biomass per cell but dilute pigment content due to expanded volume, whereas Mg-replete cells maintain compact volumes with dense chloroplast packing, consistent with faster cell cycle turnover.

Taking together, these findings reveal that Mg is not only a structural cofactor in metabolism but also acts as a signalling factor modulating the coupling between biosynthesis and cell division. By altering proteomic profiles, ionic homeostasis, and pigment allocation, Mg availability dynamically reshapes cellular priorities. This supports emerging views that cell size regulation is governed by integrated metabolic and cell cycle control pathways, with Mg playing a central regulatory role (Zhu & Thompson, 2019; Guo & Herman, 2022).

3.4.2 Effects of Mg on photosynthesis and carbon fixation

Mg plays a central role in photosynthesis and plant metabolism, serving as the core of the chlorophyll molecule and an essential cofactor for numerous enzymes involved in carbon assimilation and energy transduction (Parry *et al.*, 2008; Hermans *et al.*, 2013; Guo *et al.*, 2016; Chaudhry *et al.*, 2021). In this study, severe Mg deficiency (Mg-0)

resulted in substantial declines in chlorophyll-a content, photosynthetic rates, and regulation of proteins involved in carbon metabolism (Figure 3. 1; Figure 3. 3; Figure 3. 6). These impairments closely resemble classical Mg-deficiency symptoms reported in higher plants, including chlorophyll loss, inhibited photosynthesis, and disrupted energy metabolism (Guo *et al.*, 2016; Chaudhry *et al.*, 2021). Proteomics data revealed downregulation of Mg-chelatase (R1BIU3, R1F8J6), an enzyme critical for chlorophyll biosynthesis (Figure 3. 6h), likely contributing directly to the observed pigment decline and impaired photochemical capacity (Devi Borah & Bhuyan, 2017). Although PSI/PSII subunits and light-harvesting proteins were upregulated (Figure A2. 16), these compensatory adjustments failed to restore photosynthetic performance, underscoring the fundamental metabolic disruption caused by Mg depletion.

In contrast, across all other conditions (Mg-0.5 to Mg-20), photosynthetic efficiency (Fv/Fm), photosynthetic rates, and respiration remained stable (Figure A2. 1; Figure 3. 3), underscoring the organism's low Mg requirement and high metabolic resilience (Lasa *et al.*, 2000; Tränkner *et al.*, 2016; Jamali Jaghdani *et al.*, 2021).

Chlorophyll-a content displayed divergent trends depending on the normalisation metric. While cellular chlorophyll-a content peaked under Mg-1, it declined under excess Mg, volume-normalised chlorophyll-a increased with Mg availability (Figure 3. 1e, f). These contrasting patterns can be partly attributed to the "package effect", where pigment self-shading increases with cell size, lowering absorption efficiency per chlorophyll molecule (Finkel, 2001; Malerba *et al.*, 2018). This trade-off, in which larger cells accumulate more pigment per cell but exhibit lower chlorophyll-specific efficiency, is widely recognised among phytoplankton (Key *et al.*, 2010; Malerba *et al.*, 2017, 2018).

However, multiple linear regression models revealed that Mg availability also independently influences pigment allocation. Cellular chlorophyll-a content was positively associated with growth rate and negatively with Mg concentration, while volume-normalised chlorophyll-a content responded to both growth rate and Mg concentration, with no effect of cell number (Table A2. 3; Table A2. 4). Additionally, chlorophyll-a remained low in Mg-0 regardless of size scaling (Figure 3. 1). These findings

support that Mg availability exerts an additional regulatory effect on pigment biosynthesis and allocation, beyond the optical constraints imposed by cell volume.

Despite variability in pigment content under both Mg deficiency and excess, photosynthetic efficiency remained remarkably stable (except under Mg-0), indicating a decoupling between chlorophyll levels and photosynthetic capacity (Figure 3. 1; Figure 3. 3). Similar decoupling has been documented in marine phytoplankton under diel and nutrient-limitation conditions, where pigment levels vary while Fv/Fm and carbon fixation remains stable (Harding *et al.*, 1981; Napoléon *et al.*, 2013), and in higher plants, where chlorophyll biosynthesis suppression can be compensated to maintain photosynthetic function (Cho *et al.*, 2024). In this study, this resilience may reflect compensatory regulation to maintain photochemical output, evidenced by moderate upregulation of photosynthetic complexes at Mg-0.5 and Mg-20 (Figure 3. 6). Additionally, modest declines in photosynthetic ETC proteins at Mg-0.5 were likely counterbalanced by upregulation of Rubisco and glycolytic enzymes, supporting carbon metabolism and energy flow. Under high Mg, proteomic stability likely reflects effective vacuolar sequestration and intracellular buffering of excess Mg (Kleczkowski & Igamberdiev, 2021).

The survival of *G. huxleyi* under trace-Mg conditions (Mg-0), despite pronounced suppression of photosynthesis and carbon metabolism, points to a multifaceted survival strategy. One mechanism may involve metal substitution, with divalent cations such as Mn^{2+} potentially replacing Mg^{2+} in critical enzymatic complexes, such as Rubisco and chlorophyll, preserving basic light-harvesting and catalytic function (Bloom & Lancaster, 2018; Selan *et al.*, 2021). The residual photosynthetic activity and high light saturation observed in Mg-0 cells support this interpretation (Figure 3. 3) (Selan *et al.*, 2021). Concurrently, proteomic evidence indicates extensive upregulation of cellular maintenance machinery, including ribosomal proteins, DNA repair machinery, cytoskeletal remodelling, and selective activation of ATP-binding and ion transport proteins (Figure 3. 6; Figure A2. 16). This molecular signature indicates a strategic metabolic shift from growth-oriented biosynthesis toward cellular preservation and survival, enabling persistence under extreme nutrient limitation.

Together, these results demonstrate that *G. huxleyi* employs multifaceted strategies to regulate photosynthesis and pigment allocation through both size-related optical constraints and nutrient-responsive pathways. The observed decoupling between chlorophyll content and photosynthetic efficiency highlights the organism's capacity to sustain chronophysiological function through metabolic flexibility, encompassing compensatory protein regulation, cofactor substitution, and stress-tolerant reorganisation. This adaptive versatility likely underlies the ecological success of coccolithophores across diverse marine environments.

3.4.3 Hinting at the substrate and energy dependence of calcification

Calcification, a process unique to coccolithophores among algae, distinguishes them within marine phytoplankton and underpins their role in biogeochemical cycles and long-term atmospheric carbon sequestration. Despite its ecological significance, the regulatory mechanisms governing calcification in coccolithophores remain poorly understood (Monteiro *et al.*, 2016; Brownlee *et al.*, 2021). This study suggests that calcification in *G. huxleyi* may operate as a secondary process, governed by substrate availability and energetic capacity, but shows limited molecular-level environmental feedback regulation, potentially differing from the sophisticated regulatory systems governing core cellular processes like photosynthesis.

The primary regulatory mechanism governing calcification appears to be substrate availability, particularly Mg/Ca ratios affecting $CaCO_3$ precipitation, rather than active cellular control. Cellular $CaCO_3$ content exhibited a clear linear decline across increasing Mg availability from Mg-1 to Mg-20, with a peak in $CaCO_3$ content at Mg-1 showing only a minor shift from Mg-1 to Mg-5 when normalised to cell volume, indicating strong decreased calcification at both higher and lower concentrations. This unimodal response pattern, largely independent of size-scaling effects, demonstrates that Mg availability serves as the primary driver of calcification performance. The absence of proteins involved in Mg homeostasis (Hermans *et al.*, 2010; Yan *et al.*, 2018), combined with the low selectivity nature of ion transporters in plants and prokaryotes (Hermans *et al.*, 2013; Kobayashi & Tanoi, 2015; Tong *et al.*, 2021), suggests that cells may not actively buffer against external Mg/Ca variations. Consequently, external Mg/Ca ratios may

directly influence internal Mg/Ca composition, including within the CV where calcification occurs. High Mg/Ca ratios are known to inhibit both inorganic and organic mineralisation (Papadakis *et al.*, 2023), explaining the suppression of calcification observed under these conditions.

At low Mg levels (Mg-0.5 and Mg-0), calcification might face additional energy-related constraints. Proteomics revealed downregulation of both photosynthetic and respiratory electron transport proteins under these conditions, consistent with compromised energy production. Since calcification depends on energy-intensive synthesis of organic templates, this likely disrupted the production of key molecules such as coccolith-associated polysaccharides (CAPs) essential for nucleation and base-plate formation (de Jong *et al.*, 1976; Kayano *et al.*, 2011; Walker *et al.*, 2018a). Supporting this, UDP-glucose 6-dehydrogenase (R1F2Z5), a key enzyme in uronic acid biosynthesis, was downregulated at both Mg-0 and Mg-20 (Figure A2. 16), aligning with poor calcification performance and supporting the role of CAP in coccolithogenesis (Marsh *et al.*, 1992; Kayano *et al.*, 2011; Walker *et al.*, 2018a).

Critically, no compensatory upregulation of key calcification components was observed under distinctly different stress conditions (energy limitation at Mg-0 vs. substrate inhibition at Mg-20). While pH, DIC and HCO_3^- are known to influence calcification (Taylor *et al.*, 2011; Bach *et al.*, 2013; Kottmeier *et al.*, 2022), higher final pH and DIC at both Mg-0 and Mg-20 were observed (Figure A2. 2), yet calcification was poor in both conditions. This mismatch indicates that pH and DIC were not the primary determinants in this study, and more importantly, demonstrates the absence of active regulatory responses to favourable geochemical conditions. The expression pattern of H^+ export proteins (R1DD43 and R1FTX7) and V-type proton ATPases was inconsistent with calcification performance, suggesting a generalised stress response (e.g., ion stress) rather than calcification-specific regulation.

If calcification were actively regulated and prioritised, compensatory upregulation of the CAP biosynthetic pathway would be expected under stress conditions. Instead, the consistent downregulation indicates metabolic reallocation away from calcification-related processes. The upregulation of Ca^{2+} ATPase (R1FNS5) at Mg-0 and Mg-0.5, where

Ca^{2+} should not be limiting, likely reflects alternative cellular functions such as Ca^{2+} signalling, osmoregulation, or stress response mechanisms rather than calcification-specific regulation (Shkolnik *et al.*, 2018; Pivato & Ballottari, 2021; Costa *et al.*, 2023). This interpretation is supported by the lack of Ca^{2+} ATPase activity at Mg-20, where calcification was also impaired, suggesting that Ca^{2+} homeostasis operates independently of calcification demand.

The relationship between calcification and photosynthesis demonstrates clear functional independence, contrasting sharply with calcification's passive regulation. Despite similar photosynthetic rates at Mg-5 and Mg-20, $CaCO_3$ content was drastically reduced and coccoliths were malformed at Mg-20 (Figure 3. 4), indicating that calcification is not essential for maintaining photosynthesis under these experimental conditions. Findings in this study also support the view that calcification does not act as a CCM (Bach *et al.*, 2013) nor enhance photosynthesis via light scattering (Paasche & Klaveness, 1970). Photosynthetic rates remained relatively stable between MG-0.5, Mg-5, and Mg-20 (Figure 3. 3), despite significant variation in calcification (Figure 3. 1), implying that coccoliths do not enhance light capture or utilisation within cells through light scattering effects (Mizukawa *et al.*, 2015) and reinforcing the independence of the two processes.

Instead, a more plausible interaction involves a shared internal carbon pool, wherein photosynthesis is prioritised under DIC limitation (Bach *et al.*, 2013; McClelland *et al.*, 2017). Isotopic evidence supports this, coccolith formed at Mg-1 exhibited a threefold negative $\delta^{13}C$ deviation compared to Mg-5 and Mg-15 (Figure A2. 9), despite comparable external DIC and HCO_3^- concentrations between Mg-1 and Mg-5. This $\delta^{13}C$ depletion likely reflects increased cellular $CaCO_3$ content drawing on lighter carbon sources, combined with reduced photosynthetic demand due to lower cell density. Proteomics further revealed upregulation of glycolysis, beta oxidation, and Rubisco at Mg-0.5 (Figure A2. 16), which may supply ^{12}C-enriched substrates for calcification when photosynthetic carbon demand is reduced. However, the exact isotopic flux pathways require further investigation.

The contrast between calcification and photosynthesis regulation is particularly striking at the molecular level. Photosynthesis-related proteins exhibited diverse changes across treatments (Figure 3. 6), consistent with active regulation and prioritisation of photosynthetic function, whereas calcification-related proteins were inconsistently detected, likely due to low abundance, incomplete database annotation, or regulation occurring through post-translational modifications not detectable through this proteomic approach. This differential regulation demonstrates that photosynthesis is actively maintained at stable levels regardless of environmental perturbations or calcification status, whereas calcification appears to lack such active environmental feedback control.

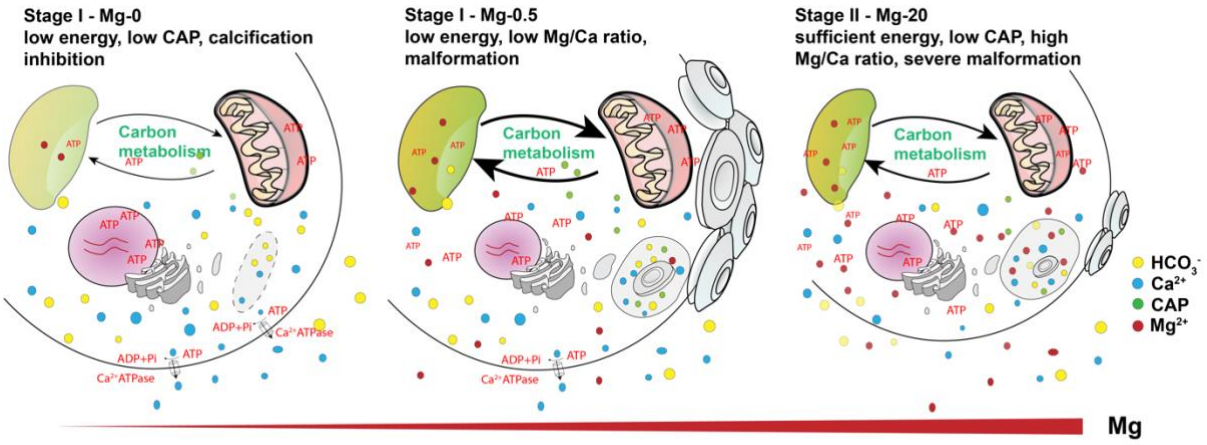

Figure 3. 7: Schematic plot illustrating the proposed cellular response of *Gephyrocapsa huxleyi* to seawater Mg availability based on physiological and proteomic investigation. Stage I represents conditions at Mg-0 and Mg-0.5, where altered carbon metabolism and energy production likely limit the synthesis of calcification-related organic molecules, thus restricting calcification; stage II represents conditions from Mg-1 to Mg-20, particularly at Mg-20, where a high intracellular Mg/Ca ratio is the primary factor inhibiting calcification.

Although cellular $CaCO_3$ content correlated positively with cellular chlorophyll-a content (Figure 3. 2a), this relationship likely reflects shared physiological dependence rather than a functional link, such as compensatory pigment upregulation in response to reduced light availability caused by coccolith shading effects (Price *et al.*, 1998). The absence of consistent protein-level adjustments under distinctly different calcification outcomes (e.g., inhibited calcification at Mg-0, malformations at Mg-20) further supports that calcification and photosynthesis operate as functionally decoupled processes with distinct regulatory mechanisms.

Together, these findings suggests that calcification may function as a secondary cellular process, appearing to be governed primarily by substrate availability (particularly Mg/Ca ratios affecting $CaCO_3$ precipitation) and energetic capacity rather than showing responsive regulation to environmental changes. This substrate-dependent, energy-constrained regulation contrasts with the more responsive control systems observed for core cellular processes like photosynthesis, suggesting calcification may occur when conditions are permissive rather than being actively maintained under stress. The apparent decoupling from photosynthesis, combined with the limited compensatory mechanisms observed under environmental perturbation, suggests that calcification in *G. huxleyi* may represent a process that utilises available resources when substrate conditions are favourable and energy is sufficient, but can be downregulated when cellular resources are prioritised for essential functions.

3.5 Summary

This study demonstrates that the photosynthetic capacity of *G. huxleyi* exhibits remarkable resilience to variations in Mg availability, with significant disruption occurring only under complete Mg depletion. Under stress, cells display notable metabolic adaptability, prioritising functions essential for survival over cell division, photosynthesis and calcification. Calcification operates independently from other cellular processes - despite sufficient substrate availability, calcification is inhibited when energetic demands appear unmet. However, with sufficient energy supply, substrate availability directly controls calcification performance.

Collectively, *G. huxleyi* exhibits a clear cellular hierarchy: cell survival is paramount, followed by resilient photosynthesis, then cell growth and division, with calcification deprioritised under stress conditions. This metabolic hierarchy provides new insights into how coccolithophores adjust to changing ocean chemistry, with significant implications for their role in marine biogeochemical cycles.

Chapter 4 Phenotypic plasticity in coccolithophore species in response to Mg availability

Abstract

Coccolithophores are major contributors to marine carbon cycling through both photosynthesis and calcification, with their physiological responses strongly influenced by environmental conditions. In this study, physiological traits were first examined under non-limiting Mg conditions across six strains representing four coccolithophore species (*Gephyrocapsa huxleyi*, *Gephyrocapsa oceanica*, *Coccolithus braarudii*, and *Coccolithus pelagicus*), revealing strong allometric scaling among cell volume, chlorophyll-a content, and calcification. To explore underlying metabolic strategies, untargeted metabolomic profiling was conducted under non-limiting conditions for three representative strains of different species (*G. huxleyi* OA1, *G. oceanica* RCC1314, and *C. braarudii* RCC1198), revealing species-specific differences in central carbon metabolism and resource partitioning. Building on this, the physiological responses of these species to a gradient of Mg concentrations were assessed. Trait variability was primarily driven by strain-specific responses, while Mg availability served as a secondary modulating factor. Smaller coccolithophores maintained broader Mg tolerance and preserved strong correlations among key traits, such as cell size, chlorophyll-a content, and $CaCO_3$ content, even under moderate Mg stress. In contrast, larger *Coccolithus* species showed narrower tolerance ranges. Calcification decreased linearly with increasing Mg availability, indicating that calcification is not homeostatically maintained but modulated by external Mg levels. Within individual strains, strong linear correlations between cell size, cellular chlorophyll-a content, and $CaCO_3$ content suggest coordinated metabolic control of growth, pigment biosynthesis, and calcification. These findings underscore the fundamental role of cell size in shaping metabolic trade-offs and environmental adaptation in coccolithophores, providing insights into their potential responses to changing ocean chemistry.

4.1 Introduction

Coccolithophores, ubiquitous unicellular calcifying phytoplankton, specialise in intracellular calcification to produce intricately structured platelets of low-Mg calcite, known as coccoliths, which are extruded onto the surface of the cell to produce a coccosphere. These organisms are widespread across marine environments, from coastal to open ocean regions and from the temperate to subpolar waters (Moore *et al.*, 2012; Winter *et al.*, 2014; Hopkins *et al.*, 2015). The ubiquity is exemplified by the cosmopolitan species *Gephyrocapsa huxleyi* (former *Emiliania huxleyi* (Bendif *et al.*, 2023)), which forms massive blooms covering areas of up to hundreds of thousands of square meters (Kondrik *et al.*, 2018; Matson *et al.*, 2019). As coccolithophores possess the dual ability to fix carbon via photosynthesis and to precipitate calcium carbonate through calcification, they play a significant role in the global carbon cycle by modulating air-sea CO_2 fluxes and influencing the export of both particulate inorganic and organic carbon (PIC/POC) (Broecker & Clark, 2009). They contribute up to 50% of pelagic carbonate production and may be preferentially preserved in sediments compared to foraminifera (Poulton *et al.*, 2007; O'Brien *et al.*, 2013), making their carbonate flux a major long-term carbon sink. Over geological time and across spatial scales, the species composition of coccolithophores has evolved, with different species exhibiting distinct calcification capacities and biological responses to environmental conditions (Langer *et al.*, 2006; Poulton *et al.*, 2017). Understanding these species-specific response strategies is essential for predicting their role in the carbon cycle under future climate scenarios (O'Dea *et al.*, 2014; Schlüter *et al.*, 2016; Krumhardt *et al.*, 2019).

Due to its ecological dominance and frequent bloom formation, most research on coccolithophore calcification has focused on *G. huxleyi* (Bach *et al.*, 2013; Benner *et al.*, 2013; Skeffington *et al.*, 2023). However, increasing evidence suggests that less abundant but heavily calcified coccolithophores may have a greater long-term carbon sink potential (Daniels *et al.*, 2014, 2016; Rigual Hernández *et al.*, 2020), yet their biological and calcification strategies remain poorly studied. Cell size is a fundamental trait shaping phytoplankton physiology, influencing metabolic rates, nutrient uptake, and ecological distribution (Glazier, 2022). Larger cells generally exhibit lower surface-area-to-volume (SA/V) ratios, which reduces diffusive nutrient acquisition but allows for

greater storage capacity and metabolic regulation (Finkel *et al.*, 2010). Across most eukaryotic phytoplankton taxa, metabolic processes, such as photosynthesis, respiration, and biomass accumulation, scale positively with cell size, typically following a sublinear ¾ power-law exponent in accordance with metabolic scaling theory (Finkel *et al.*, 2004; Perkins *et al.*, 2019); consequently, mass-specific metabolic rates have been shown to scale negatively with increasing size. This scaling relationship has important implications for growth, carbon fixation, and ecological adaptation, with larger coccolithophores generally requiring higher resource availability and more prevalent in nutrient-rich coastal waters where primary production is elevated (Marañón *et al.*, 2007; Perkins *et al.*, 2019). While cell size strongly influences metabolism, growth, and ecological strategies, $CaCO_3$ production rate does not scale predictably with size (Aloisi, 2015). Coccolithophore species vary in size, and calcification traits such as coccolith size, coccolith volume, and the PIC content per cell generally scale with cell size (Young & Ziveri, 2000; Daniels *et al.*, 2014; Suchéras-Marx *et al.*, 2022). However, calcification sensitivity to environmental change varies widely among species and even within the same species, showing no consistent relationship to cell size (Meyer & Riebesell, 2015; Diner *et al.*, 2015; Rickaby *et al.*, 2016; Faucher *et al.*, 2020). For example, under elevated CO_2 conditions, small species such as *G. huxleyi* and *Gephyrocapsa oceanica* generally show sharp declines in calcification, whereas larger species like *Coccolithus braarudii* exhibit minimal responses (Meyer & Riebesell, 2015). Similarly, calcification responses to changes in nutrient availability, temperature, and carbonate chemistry differ across species, reinforcing that physiological regulation of calcification is species- and strain-specific rather than strictly size-dependent (Diner *et al.*, 2015; Faucher *et al.*, 2017, 2020). This variability highlights the need to move beyond size-based generalisations to understand how coccolithophores regulate calcification under environmental change. Notably, most of these insights derive from laboratory experiments under controlled conditions, and responses in natural environments may differ due to ecological interactions and additional environmental complexity. The interplay between species-specific responses, selection pressures, and ecological shifts determines their role in biogeochemical cycling, particularly in carbon export and ocean alkalinity regulation (Finkel *et al.*, 2010). Expanding research beyond *G. huxleyi* to include a broader range of

species is crucial for improving predictions of coccolithophore contributions to future ocean carbon cycling.

Magnesium (Mg) availability is an underestimated environmental parameter that can potentially influence coccolithophore physiology, yet its role in calcification remains poorly understood. At the same time, Mg/Ca ratios and absolute element concentrations have fluctuated over geological timescales (Ries, 2010; Broecker & Yu, 2011), coccolithophore calcification has persisted, raising questions about whether and to what extent these variations shaped species composition or biomineralisation. Although calcium (Ca) has been extensively studied in coccolithophore biomineralisation (Holtz *et al.*, 2013; Müller *et al.*, 2015a; Faucher *et al.*, 2020), studies suggest that Mg may influence both metabolism and calcification, as indicated by strong correlations between Mg incorporation into coccoliths (DMg) and chlorophyll-a production (Ra *et al.*, 2010a; Müller *et al.*, 2014). This relationship implies that calcite-associated Mg may originate from a shared intracellular Mg pool involved in chlorophyll-a biosynthesis across species (Ra *et al.*, 2010a; Müller *et al.*, 2014). Beyond its metabolic role, Mg availability also affects biomineralisation, as deviations from normal seawater Mg concentrations lead to malformed and undecalcified coccoliths in *G. huxleyi* (Herfort *et al.*, 2004). However, how Mg availability affects both physiology and calcification across different species, and size ranges, remains unclear. First, coccolithophores exhibit species-specific physiological sensitivity to chemical changes (Müller *et al.*, 2011). Second, the relationship between Mg/Ca ratios, temperature, and growth rates varies across species and growth stages (Ra *et al.*, 2010a,b; Müller *et al.*, 2014). Finally, Mg incorporation into coccolith calcite differs among species, as seen in DMg values (Stoll & Ziveri, 2004; Blanco-Ameijeiras *et al.*, 2012; Müller *et al.*, 2014), and Mg isotope fractionation (δ^{26}Mg) (Ra *et al.*, 2010b). These inconsistencies highlight the complexity of Mg regulation in biomineralisation and physiology. Systematic studies on Mg concentration effects across multiple species are needed to clarify its role in both physiological regulation and calcification.

The physiological traits of five coccolithophore strains were examined under non-limiting Mg conditions, including two *G. huxleyi* strains representing different morphotypes, along with one *G. oceanica*, one *Coccolithus pelagicus*, and one *C. braarudii* strain,

representing a range of coccolithophore species with distinct cell sizes and calcification capacities. To investigate interspecies differences not only in physiological performance but also in underlying metabolic strategies, untargeted metabolite profiling was conducted on selected species. This approach allowed identification of potential differences in carbon allocation and energy metabolism that may underpin observed physiological variation. Subsequently, all strains were exposed to a wide range of Mg concentrations, encompassing and exceeding geological variations, to assess their sensitivity and response limits. Together, the integration of physiological and metabolic data enabled evaluation of species-specific response strategies and regulatory mechanisms under changing Mg availability.

4.2 Methods and Materials

Cultures of regular-calcified *G. huxleyi* morphotype A (RCC911), *G. huxleyi* morphotype R (RCC1216), *G. oceanica* (RCC1314), *C. braarudii* (RCC1198) and *C. pelagicus* (RCC3776) were obtained from the Roscoff Culture Collection (Station Biologique de Roscoff, Roscoff, France). All strains were grown in sterile filtered (0.22µm) artificial seawater, enriched with trace metal and vitamin stock at modified K/2 concentration (Keller *et al.*, 1987). Experiments were conducted at 17°C for all strains, except for *G. oceanica*, which was grown at 20°C. A 16:8h light: dark cycle (45-75 µmol m^{-2} s^{-1}) was applied to all strains.

4.2.1 Experimental setup and growth rate measurements

Mg concentration adjustments followed the same procedure as described in Chapter 3 (Section 3.2.1). After a 28-day acclimation in the control condition, all strains were transferred to the full range of Mg concentration media (0 to 210 mM). Three biological replicates were maintained in each condition for over 100 days with regular subculturing prior to sample collection. The *G. oceanica* strain RCC1314 failed to grow during this adaptation period under Mg-0 conditions, while *C. braarudii* RCC1198 and *C. pelagicus* were unable to adapt under Mg-0, Mg-15, and Mg-20 conditions (Table 4. 1). Cell number, size measurements, and growth rate calculations were conducted using the same methodology as detailed in Chapter 2 (Section 2.2.2). All reported cell size

measurements refer to decalcified, naked cells, as measured after acid treatment using the Coulter Counter.

Strain	***Condition***	***Mg-0***	***Mg-0.5***	***Mg-1***	***Mg-5***	***Mg-10***	***Mg-15***	***Mg-20***
	Mg/Ca ratio	0	0.5	1	5	10	15	20
	$[Mg^{2+}]$ (mM)	0	5.46	10.50	54.60	105.0	157.50	210.0
OA1		✓	✓	✓	✓	✓	✓	✓
RCC 911		✓	✓	✓	✓	✓	✓	✓
RCC 1216		✓	✓	✓	✓	✓	✓	✓
RCC 1314			✓	✓	✓	✓	✓	✓
RCC 1198			✓	✓	✓	✓		
RCC 3776			✓	✓	✓	✓		

Table 4. 1: Mg concentrations, corresponding Mg/Ca ratios in the culture media, and experimental conditions for each coccolithophore strain.

4.2.2 Chlorophyll-a extraction

Chlorophyll-a was extracted and quantified following the protocol described in Chapter 2 (Section 2.2.3). Two normalisations were used: (1) chlorophyll-a per cell, calculated based on cell counts, and (2) chlorophyll-a per unit volume, calculated by normalising to cell volume assuming spherical cell geometry.

4.2.3 Scanning electron microscopy and image processing

Sample preparation for SEM, coccosphere size and morphological analyses, followed the same procedures described in Chapter 3 (Section 3.2.3).

4.2.4 Carbon chemistry and calcification measurements

Cellular $CaCO_3$ content was calculated using the traditional method described in Chapter 2 (Section 2.2.4, equation 2.5), which estimates $CaCO_3$ productions from total alkalinity depletion normalised to the change in cell number across each sampling interval.

4.2.5 Metabolomics analysis

Metabolomics analysis was performed on three coccolithophore strains: *G. huxleyi* (OA1), *G. oceanica* (RCC1314), and *C. braarudii* (RCC1198), grown under control conditions (Mg-5), representing species with distinct cell sizes. Metabolites were extracted from mid-exponential cells using ice-cold 80% methanol (aq), following the protocol of Haythorne *et al.* (2022), with slight modifications. Sample volumes were calculated based on cell concentration and estimated cell volume, assuming intracellular metabolite concentrations scale with total cell volume. Cell concentrations were 293956 ±2990 cell ml^{-1} for OA1, 65596 ±2306 cell ml^{-1} for RCC1314 and 12733 ±490 cell ml^{-1} for RCC1198. Cells were pelleted, the supernatant discarded, and 1 ml of solvent was added per sample. Samples were vortexed for 5 minutes, centrifuged at 4000 rpm for 20 minutes, and the supernatant was transferred to autosampler vials to remove cell debris. Metabolite profiling was performed using anion-exchange chromatography coupled with mass spectrometry at the Department of Chemistry, Oxford. Instrument settings followed those described in Haythorne *et al.* (2022). Raw data were processed using MetaboAnalyst 6.0 by collaborators at the Department of Chemistry, University of Oxford, including missing value imputation, data filtering, normalisation, principal component analysis (PCA), and clustering analysis.

4.2.6 Statistical analysis

Physiological measurements were reported as mean ± standard deviation (SD) of biological replicates (n = 3 in all instances). Statistical significance between treatment groups and the control condition was indicated with asterisks: $p \leq 0.05$(*), $p \leq 0.01$(**) and $p \leq 0.001$(***). Two-sided Welch's t-tests were applied to assess differential expression in metabolite data. Two-way ANOVA was used to evaluate the individual and interactive effects of strain and Mg availability on each trait. Multivariate patterns of physiological variation were explored using MANOVA and PCA. Linear Discriminant Analysis (LDA) was applied to assess trait contributions to strain classification. All statistical analyses, data processing, and visualisation were conducted using R (v4.3.2).

4.3 Results and discussion

4.3.1 Size-dependent physiology in coccolithophores

Physiological traits were examined across six coccolithophore strains, ranging in cell size from 4 to 17 µm, representing four species under control conditions (Mg-5) (Figure 4. 1). The strains included two *G. huxleyi* regular-calcified morphotype A strains: (OA1: 4.66±0.02 µm and RCC911: 4.40±0.06 µm), one *G. huxleyi* morphotype R strain (RCC1216: 4.18±0.02 µm), *G. oceanica* (RCC1314: 7.30±0.03 µm), *C. braarudii* (RCC1198: 16.78±0.03 µm), and *C. pelagicus* (RCC3776: 14.94±0.26 µm). Strain OA1 from Chapter 3 was included to facilitate cross-comparison of size-scaling relationships.

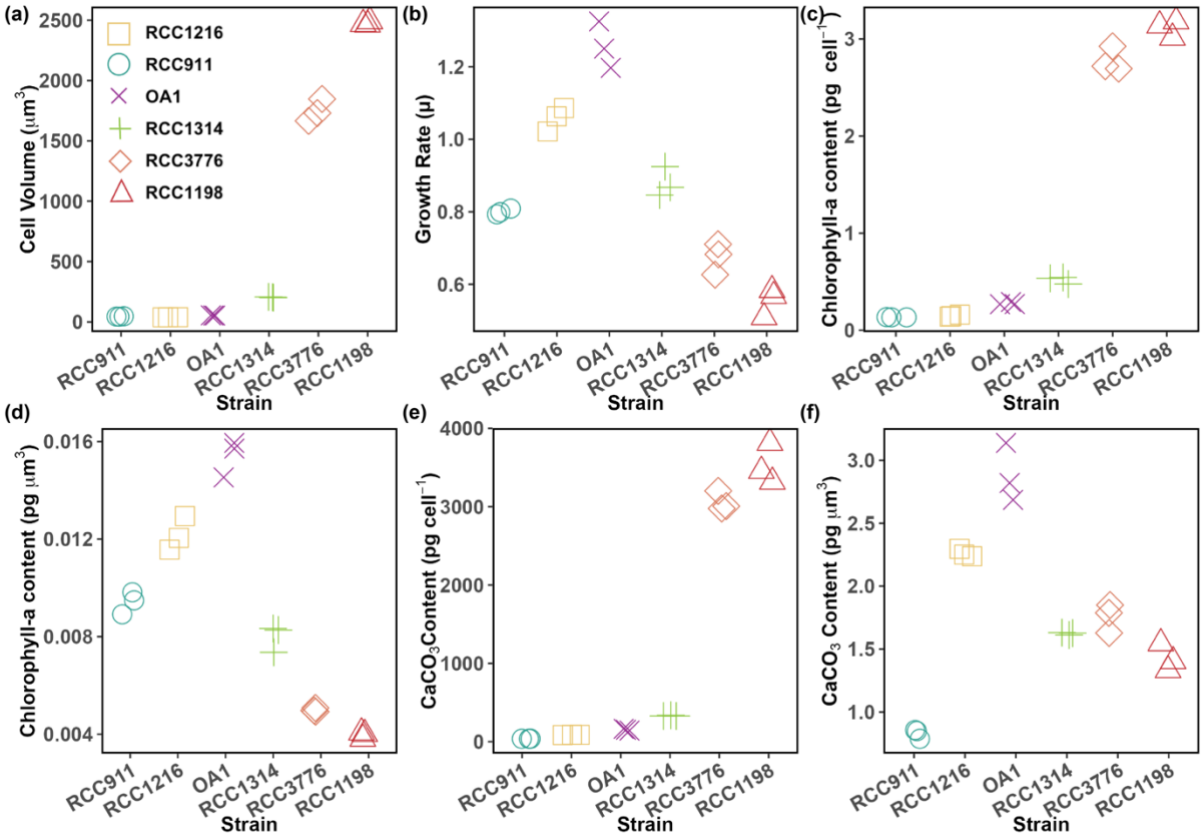

Figure 4. 1: Key physiological traits in four coccolithophore species (*Gephyrocapsa huxleyi* (OA1, RCC911, RCC1216), *Gephyrocapsa oceanica* (RCC1314), *Coccolithus braarudii* (RCC1198), and *Coccolithus pelagicus* (RCC3776)). Panels are (a) cell volume, (b) growth rate, (c) cellular chlorophyll-a content, (d) chlorophyll-a content per unit volume, (e) cellular $CaCO_3$ content, and (f) $CaCO_3$ content per unit volume.

Correlation analysis revealed strong positive allometric scaling between cell volume and both cellular chlorophyll-a content (R^2 =0.98, p< 0.001) and cellular $CaCO_3$ content (R^2

=0.95, p< 0.001) (Figure 4. 2; Figure A3. 2). A similarly strong positive correlation was observed between cellular chlorophyll-a content and cellular $CaCO_3$ content (R^2 =0.98, p < 0.001; Figure 4. 2; Figure A3. 2), suggesting coordinated size-dependent accumulation of pigment and calcite. In contrast, growth rate negatively scaled with cell volume (R^2 =0.70, p< 0.001), with an allometric exponent of -0.134, consistent with previously reported values for coccolithophores (-0.11 to -0.32) (Buitenhuis *et al.*, 2008; Aloisi, 2015; Villiot *et al.*, 2021), and broader phytoplankton taxa (Sarthou *et al.*, 2005; Marañón *et al.*, 2013; Barton & Yvon-Durocher, 2019).

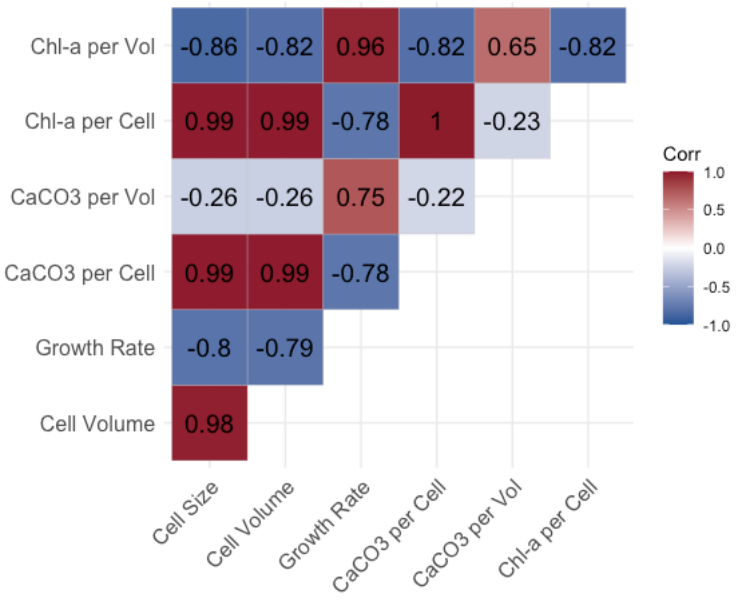

Figure 4. 2: Pairwise correlation matrix of physiological traits in four coccolithophore species (*Gephyrocapsa huxleyi* (OA1, RCC911, RCC1216), *Gephyrocapsa oceanica* (RCC1314), *Coccolithus braarudii* (RCC1198), and *Coccolithus pelagicus* (RCC3776)).

Consistent with the unimodal hypothesis in phytoplankton growth allometry, which posits different scaling relationships above and below 50 μm^3 volume threshold (Marañón *et al.*, 2013), exclusion of the two smallest *G. huxleyi* strains (RCC911 and RCC1216, < 50 μm^3) substantially improved the correlation between cell volume and growth rate (R^2 =0.94, p< 0.001) and yielded a steeper exponent (-0.19; Figure A3. 3). This supports the concept that negative allometry is more consistent across larger size ranges, while smaller nano- and pico-phytoplankton tend to deviate from this pattern (Bec *et al.*, 2008; Marañón *et al.*, 2013).

These findings imply two distinct layers of regulation, absolute chlorophyll-a and $CaCO_3$ content scale predictably with size, consistent with allometric trends (Marañón *et al.*, 2007; Marañón, 2008, 2015; Aloisi, 2015; Álvarez *et al.*, 2017). At the same time, their volume-normalised expressions are shaped by physiological needs and possibly metabolic efficiency. The strong pigment-growth coupling indicates that pigment concentration is tightly regulated to support division, while the weak and complex relationships involving $CaCO_3$ per volume suggest that calcification intensity is influenced by additional constraints. These may include vesicle capacity, ion transport limitations, or strain-specific strategies such as minimal vs. over-calcifying phenotypes.

The strong positive linear correlation between cellular chlorophyll-a and $CaCO_3$ content, consistent across species and maintained under varying Mg conditions (Chapter 3, strain OA1), supports a shared metabolic or regulatory basis. That this coupling persists even when photosynthetic rate is not directly linked to calcification suggests both processes may rely on a shared, size-dependent resource pool, analogous to isometric nutrient uptake scaling in phytoplankton (Litchman *et al.*, 2007; Finkel *et al.*, 2010; Marañón, 2015). Volume-normalised divergence further implies that while larger cells accumulate more pigment and calcite overall, the concentrations of these compounds are actively adjusted to meet functional demands. This layered regulation underscores the interplay between cell structure, biosynthetic allocation, and physiological performance in coccolithophores.

Overall, under control conditions, chlorophyll-a accumulation and $CaCO_3$ content scale predictably with cell size, reflecting size-driven metabolic potential, whereas growth rate is more tightly linked to chlorophyll-a content per unit volume, indicating active physiological regulation. These findings highlight a dual framework of structural scaling and functional adjustment that shapes coccolithophore growth and calcification.

4.3.2 Metabolomic profiling of selected species under control conditions

To explore metabolic differences among coccolithophores of varying species, untargeted metabolomics were performed on three representative strains: *G. huxleyi* (OA1), *G. oceanica* (RCC1314) and *C. braarudii* (RCC1198), grown under standard Mg conditions (Mg-5). These strains span cell diameters from approximately 4.66 µm to 16.78 µm and

exhibit distinct growth rates, with OA1 growing the fastest (1.26 ± 0.07 day^{-1}) and RCC1198 the slowest (0.55 ± 0.04 day^{-1}), while RCC1314 is intermediate in both metrics (Figure 4. 3a, b). Hierarchical clustering (Figure A3. 4) and PCA (Figure 4. 3c) revealed clear metabolic differentiation among the strains, suggesting species-specific metabolic profiles. Among 18,828 detected peaks (m/z/rt), 88 metabolites were annotated, representing various biochemical pathways. Univariate statistical analysis (FDR-corrected p-value < 0.05, fold change > 2) revealed that *G. oceanica* (RCC1314) and *G. huxleyi* (OA1) exhibited fewer metabolic differences between them than either did with *C. braarudii* (RCC1198), indicating greater metabolic similarity between RCC1314 and OA1 (Table 4. 2).

Comparison	***Total Metabolites Detected***	***Significantly Altered Metabolites***	***Up - regulated***	***Down - regulated***	***Annotated Metabolites***
RCC1314 VS OA1	4975	651	158	493	26
RCC1314 VS RCC1198	4996	1300	531	769	36
OA1 VS RCC1198	4995	1104	509	595	29

Table 4. 2: Univariate analysis of untargeted metabolomics data based on FDR-corrected p < 0.05 and fold change > 2. Shown are the total number of detected metabolites, the number of significantly altered metabolites, and counts of up- and down-regulated features in each pairwise comparison.

The relative abundances of 88 annotated metabolites were examined, with a focus on those exhibiting high differential expression (Table 4. 2; Figure 4. 3). Fold-change (FC) values were calculated as the ratio of metabolite abundance in one strain relative to another, with FC >1 indicating higher abundance in the comparison strain, and FC <1 indicating lower abundance relative to the reference strain.

4.3.2.1 Metabolic differences between G. huxleyi (OA1) and G. oceanica (RCC1314)

G. oceanica (RCC1314) exhibited significantly higher levels of glycolytic and gluconeogenic intermediates than *G. huxleyi* (OA1). Notably, Fructose 2,6-diphosphate was 27.5-fold higher (FC = 27.53) and 3-phosphoglyceric acid was 4.34-fold higher in RCC1314, suggesting an upregulation of glycolytic flux in *G. oceanica* (Figure 4. 3d). In contrast, *G. huxleyi* (OA1) exhibited greater enrichment in citric acid cycle (TCA) intermediates (Figure 4. 3e), nucleotide-related compounds (Figure 4. 3f), and amino

acid derivatives (Figure 4. 3g). methylisocitric acid (FC = 0.03) and succinic acid (FC = 0.25) were significantly higher in *G. huxleyi* (OA1), along with nucleotide metabolites such as xanthylic acid (FC = 0.11), uridine (FC = 0.39), and 3'-AMP (FC = 0.40). Amino acid-related metabolites, including O-acetylserine (FC = 0.26) and gamma-delta-dioxovaleric acid (FC = 0.47) were also more abundant in OA1.

4.3.2.2 Metabolic differences between G. oceanica (RCC1314) and C. braarudii (RCC1198)

C. braarudii (RCC1198) displayed higher abundances of key TCA cycle and pentose phosphate pathway (PPP) intermediates than *G. oceanica* (RCC1314). For instance, succinic acid (FC = 0.21) and malic acid (FC = 0.16) were significantly enriched in RCC1198 (Figure 4. 3e). PPP intermediates such as ribulose 5-phosphate (FC = 0.47), gluconate (FC = 0.49), and mannose (FC = 0.42), were also higher in RCC1198. Furthermore, carbohydrate metabolism-related metabolites, including maltitol (FC = 0.26) and methyl beta-D-glucopyranoside (FC = 0.21), were more abundant in RCC1198, alongside several nucleotide metabolites (Uridine, 3'-AMP, adenosine monophosphate, cytidine monophosphate, and uridine 5'-monophosphate; FC values ranging from 0.31 to 0.49). In contrast, *G. oceanica* (RCC1314) exhibited higher glycolytic activity (e.g., fructose 2,6-diphosphate, FC = 4.29) (Figure 4. 3d), amino acid precursors (O-Acetylserine, FC = 2.54), redox balance compounds (NADPH, FC = 11.27), and energy storage metabolites (sorbitol, FC = 16.53; sorbitol-6-phosphate, FC = 291.46).

4.3.2.3 Metabolic differences between C. braarudii *(RCC1198) and* G. huxleyi *(OA1)*

Metabolites related to central carbon metabolism were generally higher in *C. braarudii* (RCC1198) than in *G. huxleyi* (OA1). This included pyruvic acid (FC = 0.22), 3-phosphoglyceric acid (FC = 0.37), malic acid (FC = 0.42), and 4-hydroxy-2-oxoglutarate (FC = 0.17) (Figure 4. 3d, e). Sugars and sugar derivatives, such as UDP-galactose (FC = 0.24), raffinose (FC = 0.28), lactose (FC = 0.43), mannose (FC = 0.43), and glyceric acid (FC = 0.43), were also more abundant in *C. braarudii* (RCC1198). Conversely, *G. huxleyi* (OA1) exhibited higher levels of amino acid derivatives (e.g., aspartate, FC = 3.01; N-acetylglutamate, FC = 5.09; O-acetylserine, FC = 11.50) (Figure 4. 3g) and energy storage compounds (sorbitol, FC = 20.47; sorbitol-6-phosphate, FC = 167.58).

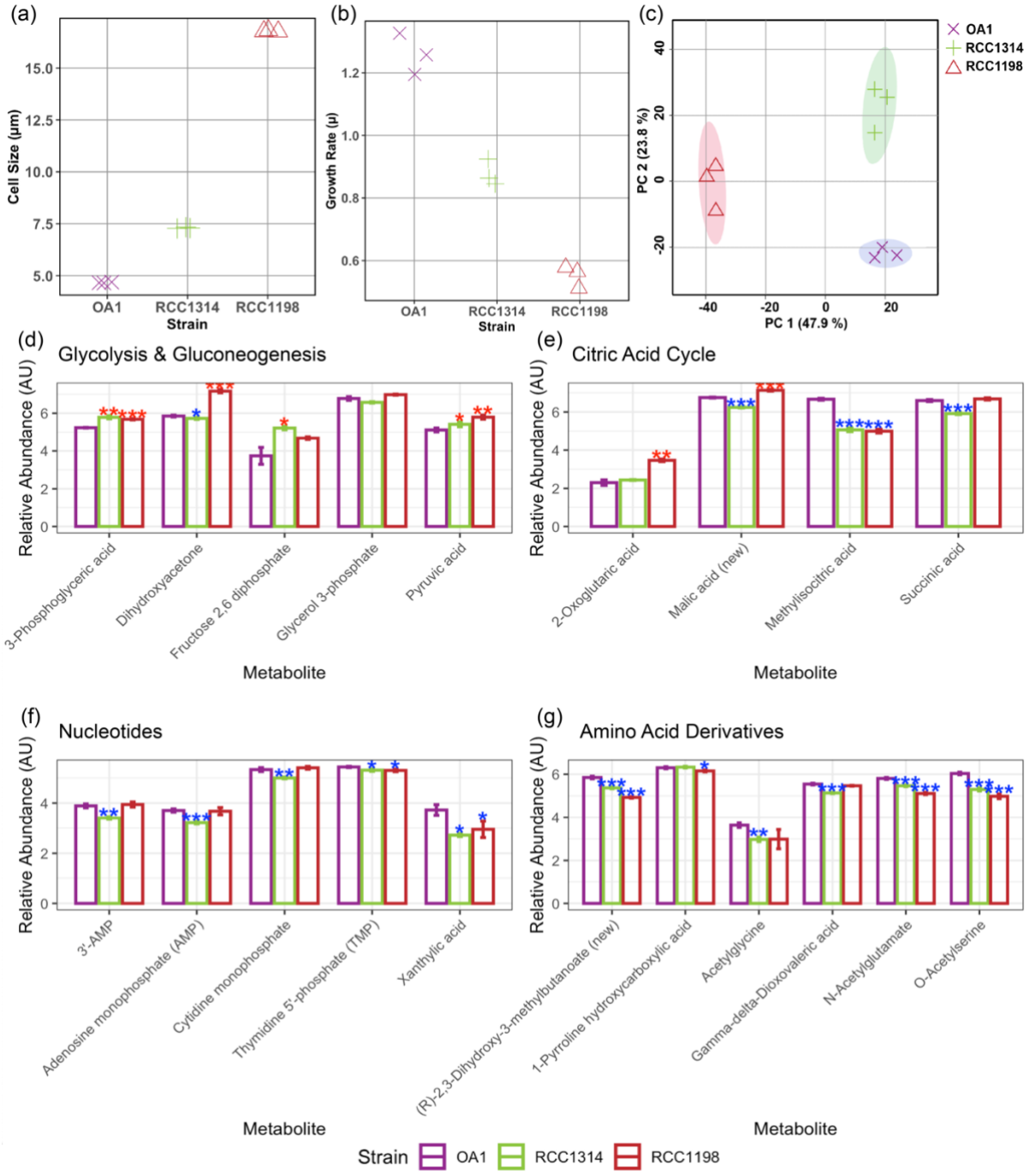

Figure 4. 3: Growth rate (a), cell size (b), and principal component analysis (PCA) (c) of all detected metabolites (c) for *Gephyrocapsa huxleyi* (OA1, RCC911, RCC1216), *Gephyrocapsa oceanica* (RCC1314), *Coccolithus braarudii* (RCC1198), and *Coccolithus pelagicus* (RCC3776). Log-transformed relative abundance of selected metabolites involved in glycolysis and gluconeogenesis (d), the citric acid cycle (e), nucleotide metabolism (f), and amino acid derivatives (g) are shown. Statistical significance for individual metabolites was assessed using t-tests, with G. *huxleyi* (OA1) as the reference. Asterisks denote significance levels (p-values): * $0.01 < p < 0.05$, ** $0.001 < p < 0.01$, *** $p < 0.001$. Metabolites with significantly higher abundance than G. *huxleyi* (OA1) are marked in red, while those with lower abundance are marked in blue.

In summary, the annotated metabolite profiles indicate lower abundances of glycolysis intermediates in *G. huxleyi* compared to both *G. oceanica* and *C. braarudii*, with *G. oceanica* having the lowest TCA intermediate levels overall. The combination of lower glycolysis intermediates but higher TCA cycle intermediates in *G. huxleyi* suggests that alternative carbon sources, such as stored carbohydrates, may fuel the TCA cycle for energy production. This pattern aligns with the growth-dependent depletion of central metabolite pools, previously observed in *Arabidopsis* (Meyer *et al.*, 2007; Sulpice *et al.*, 2009). In contrast, *G. oceanica* shows higher glycolysis intermediates but lower TCA intermediates, suggesting that while glycolysis is active, less carbon enters the TCA cycle. This may indicate a greater diversion of glycolytic products into biosynthetic pathways or mechanisms favouring energy conservation. Meanwhile, *C. braarudii* exhibits higher levels of glycolysis and TCA cycle intermediates, suggesting a more balanced metabolic strategy supporting slower, sustained growth with greater metabolic reserves. These species-specific differences in central carbon metabolism are consistent with the hypothesis that larger protists possess greater mitochondrial capacity and metabolic reserves due to the linear scaling of internal organelles with cell volume (DeLong *et al.*, 2010).

Nucleotide and amino acid derivatives displayed a clearer trend, with greater abundances observed in *G. huxleyi* compared to *G. oceanica* and *C. braarudii*. The elevated nucleotide abundance in *G. huxleyi* may indicate greater ribosomal RNA synthesis, consistent with the Growth Rate Hypothesis (GRH), which predicts a positive correlation between growth rate and RNA content due to increased ribosome production (Flynn *et al.*, 2010; Giordano *et al.*, 2015; Fanesi *et al.*, 2017; Rees & Raven, 2021). The increased amino acid derivatives in *G. huxleyi* may suggest increased precursor availability for protein biosynthesis, aligning with models predicting a linear relationship between biosynthetic protein content and growth rate (Inomura *et al.*, 2020).

While the metabolic differences among *G. huxleyi*, *G. oceanica*, and *C. braarudii* can be attributed to growth rate variations, it remains unclear whether these changes are strictly driven by growth rate, cell size, or species-specific factors. Additionally, the large proportion of non-annotated metabolites may indicate the presence of uncharacterised or incomplete metabolic pathways, limiting the complete interpretation of metabolic

differences. Further studies spanning a broader range of cell sizes, growth rates, and environmental conditions are needed to disentangle size-dependent metabolic trends from species-specific or adaptive responses.

4.3.3 Mg effects and species differences on coccolithophore physiology

In Chapter 3, the physiological responses of a single *G. huxleyi* strain (OA1) to Mg availability were examined, and potential biological mechanisms regulating these responses were explored. This analysis revealed key relationships between physiological traits, including a negative correlation between Mg concentration and both cell size and $CaCO_3$ content, as well as a linear relationship between cellular chlorophyll-a and $CaCO_3$ content (Figure 3. 2). However, whether these trait relationships are conserved across different coccolithophore species remains unclear. The present investigation examines how species with different cell sizes and calcification abilities respond to Mg availability to test if similar physiological patterns occur across taxa.

To address this question, the physiological traits of five coccolithophore strains previously characterised under control conditions (Mg-5) were examined, including two *G. huxleyi* strains of different morphotypes (RCC911, RCC1216), *G. oceanica* (RCC1314), and two *Coccolithus* species (RCC1198, RCC3776), across a gradient of Mg concentrations (Mg-0 to Mg-20, equivalent to 0-210 mM), with results compared to the OA1 strain characterised in Chapter 3. Distinct patterns of Mg tolerance emerged among the tested strains. The *G. huxleyi* strains maintained growth across the full Mg range, showing substantial resilience despite a 37-60% reduction in growth rate at Mg-0 and a doubling of the time required to reach the stationary phase. In contrast, *C. braarudii* (RCC1198) and *C. pelagicus* (RCC3776) exhibited high sensitivity, growing only within a limited Mg range (Mg-0.5 to Mg-10, equivalent to 5.46-105.00 mM). *G. oceanica* (RCC1314) displayed moderate sensitivity, failing to grow under trace Mg (Mg-0) but sustaining growth at moderate to high concentrations (Mg-0.5 to Mg-20, 5.46-210.00 mM) (Figure 4. 4; Figure A3. 5).

4.3.3.1 Growth rate response to Mg availability

Among the newly examined strains, *G. huxleyi* RCC1216 exhibited the highest growth rate, followed by *G. oceanica* RCC1314 and *G. huxleyi* RCC911. The two *Coccolithus* species, RCC1198 and RCC3776, had the lowest growth rates. For comparison, the previously examined *G. huxleyi* OA1grew faster than all five newly analysed strains, with a growth rate more than twice that of RCC1198, the slowest growing strain (Figure A3. 11; Figure A3. 5).

Growth rates across all strains exhibited a dome-shaped physiological pattern in response to Mg availability, with optimal growth around the control condition (Mg-5). Compared to Mg-5, all species showed decreased growth under low Mg availability (Mg-0.5, Mg-1), highlighting a general physiological constraint imposed by Mg limitation (Figure A3. 5). Under high Mg conditions (Mg-10, Mg-15, Mg-20), most strains exhibited stable but slightly reduced growth rates, with the notable exception of RCC911, which showed pronounced reductions at Mg-15 and Mg-20. The inability of *Coccolithus* species (RCC1198, RCC3776) to grow above Mg-10 underscores their narrower physiological tolerance range. These results suggest that there may be a general physiological trade-off at both extremes of Mg availability, with species-specific adaptability appearing to determine the breadth of their Mg tolerance window.

Two-way ANOVA confirmed significant effects of strain identity, Mg availability, and their interaction on growth rates (Table A3. 3). Subsequent analysis revealed that *G. huxleyi* strains exhibited significant strain and Mg interactions, indicating strain-specific responses to Mg availability. In contrast, the *Coccolithus* strains showed non-significant strain and Mg interactions, indicating similar response patterns to Mg availability within this genus. Across all treatments, strain identity exerted a stronger influence on growth rate than Mg availability (Figure A3. 11; Table A3. 3).

4.3.3.2 Cell size response to Mg availability

Cell size exhibited distinct species-specific patterns that contrasted with those of growth rate, with *Coccolithus* species (RCC1198, RCC3776) having the largest cells and *G.*

huxleyi strains the smallest (Figure 4. 4b). The largest cells (RCC1198) were nearly four times larger than the smallest (*G. huxleyi* RCC911) (Figure A3. 6; Figure A3. 11).

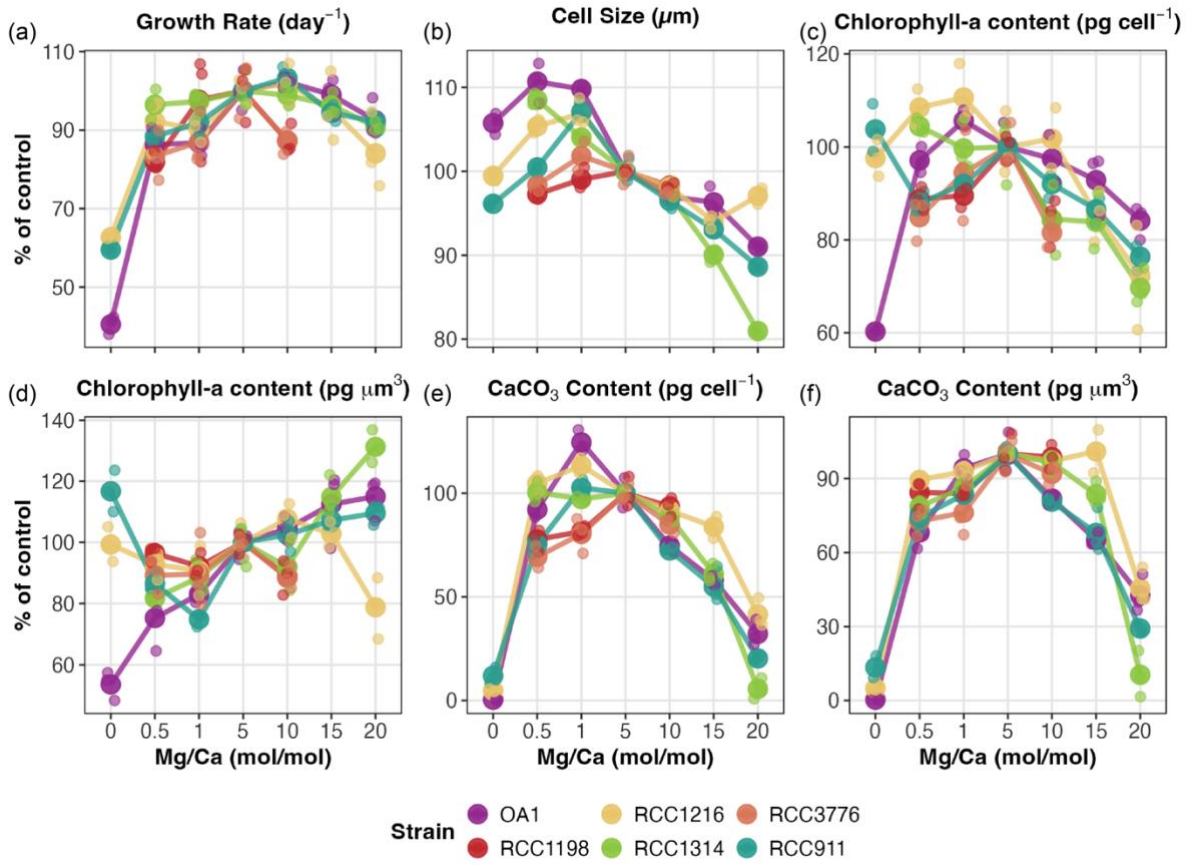

Figure 4. 4: Physiological traits responses of coccolithophore strains to varying seawater Mg availability, expressed as percentage of control conditions (Mg/Ca = 5mol/mol). Species tested: *Gephyrocapsa huxleyi* (OA1, RCC911, RCC1216), *Gephyrocapsa oceanica* (RCC1314), *Coccolithus braarudii* (RCC1198), and *Coccolithus pelagicus* (RCC3776). Traits include (a) growth rate, (b) cell size, (c) cellular chlorophyll-a content, (d) chlorophyll-a content per unit volume, (e) $CaCO_3$ content, and (f) $CaCO_3$ content per unit volume. Lines and larger points represent strain means; smaller scattered points show individual replicate measurements (n-3 per treatment).

Cell size responses to Mg availability showed more variable patterns across strains than growth rates. Under low Mg conditions compared to Mg-5, responses diverged among species. *G. huxleyi* strains (OA1, RCC1216, RCC911) and *G. oceanica* (RCC1314) generally showed increases in cell size, while *Coccolithus* species (particularly RCC1198) showed significant decreases (Figure A3. 6). At higher Mg concentrations, significant cell size reductions were observed across most strains, with a notable exception being an anomalous increase in RCC1216 at Mg-20. ANOVA confirmed that both strains and Mg

availability had strong, independent effects on cell size, with significant strain-by-Mg interactions indicating that strains responded differently to Mg availability (Table A3. 4). The opposing responses between species under low Mg conditions and the abnormal increase in cell size at Mg-20 in RCC1216 may indicate strain-specific strategies for adjusting cell physiology under different Mg stresses, while magnitude variation among *G. huxleyi* species may reflect differential sensitivity.

4.3.3.3 Cellular chlorophyll-a content response to Mg availability

Cellular chlorophyll-a content patterns generally mirrored cell size variations, with *Coccolithus species* exhibiting the highest content and *G. huxleyi* strains the lowest (Figure 4. 4c; Figure A3. 7). Under low Mg conditions, responses varied among strains (Figure A3. 7). Notable reductions occurred in RCC911, RCC1198, and RCC3776, while OA1, RCC1216, and RCC1314 displayed more variable responses that were not statistically significant. At high Mg conditions, significant reductions in chlorophyll-a content were consistently observed across strains, with RCC911 affected across all high Mg conditions, and other strains showing reductions at specific concentrations. The consistent reduction under high Mg conditions suggests that chlorophyll biosynthesis is generally sensitive to elevated Mg levels.

ANOVA revealed that cellular chlorophyll-a content was significantly influenced by strain identity, Mg concentration, and their interaction, with the two *Coccolithus* species (RCC1198, RCC3776) exhibiting similar responses to Mg availability (Table A3. 5).

When normalised to cell volume, chlorophyll-a content revealed an inverse pattern, with *G. huxleyi* strains showing higher concentrations per unit volume than *Coccolithus* species (Figure 4. 4d; Figure A3. 8). This relationship might reflect the general correlation between cell size and pigment across the examined strains and the “package effect” (Finkel, 2001; Malerba *et al.*, 2018).

Under low Mg availability, a general decline in volume-specific chlorophyll-a content occurred, with significant reductions in OA1, RCC911, and RCC1314 at Mg-0.5 (Figure A3. 8). Under elevated Mg conditions, responses diverged notably, OA1 and RCC1314 showed significant increases at Mg-20, while RCC1216 decreased at the same level, and

both *Coccolithus* species declined significantly at Mg-10. The abnormal chlorophyll-a content per unit volume in RCC 1216 is driven by the abnormal size increase at Mg-20 and may indicate additional Mg influence beyond simple size-scaling. These species-specific response differences may result from variations in internal metabolic regulation under Mg stress, potentially including factors such as ion homeostasis, regulatory plasticity, or stress buffering capacity, though further investigation would be needed to confirm these mechanisms.

ANOVA analysis suggested that chlorophyll-a content per unit volume was significantly influenced by strain identity, Mg concentration, and their interaction across all strains. Strain-by-Mg interactions were significant for *G. huxleyi* strains, while *G. oceanica* and two *Coccolithus* species showed minimal interaction effects, reflecting more uniform responses to Mg availability (Table A3. 6).

4.3.3.4 Cellular $CaCO_3$ content response to Mg availability

Cellular $CaCO_3$ content followed a pattern similar to cell size and cellular chlorophyll-a content, with *Coccolithus* species exhibiting the highest content and *G. huxleyi* strains the lowest (Figure 4. 4e; Figure A3. 9). This relationship may suggest either size-scaling effects or underscore an internal correlation between cell size and calcification capacity among coccolithophore species.

Under low Mg conditions compared to Mg-5, species responses diverged markedly, mainly at Mg-1. *Coccolithus* species (RCC1198, RCC3776) showed significant reductions in $CaCO_3$ content (Figure A3. 9), highlighting their sensitivity to Mg limitation. In contrast, *G. huxleyi* strains exhibited less severe and occasionally enhanced calcification (e.g., OA1 and RCC1216 at Mg-1), highlighting species-specific adaptations to environmental change. At high Mg conditions, nearly all strains showed uniform and significant declines in $CaCO_3$ content, except RCC1198 at Mg-10, where the decrease was not statistically significant. This widespread reduction underscores calcification as a particularly Mg-sensitive physiological process, possibly due to impaired Mg/Ca ionic balance essential for coccolith formation. A significant linear decrease in response to rising Mg concentrations was observed in the three *G. huxleyi* strains (OA1, RCC1216, RCC911) and *G. oceanica* (RCC1314) across Mg conditions ranging from 105.0 to 210.0

mM (Mg-1 to Mg-20) (Figure 4. 4e). ANOVA confirmed strong effects of strain identity and significant strain-by-Mg interactions, indicating strain-specific responses to Mg availability. The exception was the *Coccolithus* species, which showed no significant strain effects, indicating uniform responses within this genus (Table A3. 7).

When normalised to cell volume, $CaCO_3$ content per unit volume displayed a unimodal pattern (Figure 4. 4f; Figure A3. 11). Interestingly, values in *Coccolithus* species overlapped with *G. oceanica*, despite their size differences. Within moderate Mg ranges (Mg-0.5 to Mg-10), *G. huxleyi* strains OA1 and RCC1216 exhibited higher volume-specific $CaCO_3$ content than other species, whereas RCC911 had the lowest values. $CaCO_3$ content per unit volume peaked under the control condition (Mg-5), while both lower and higher Mg concentrations led to significant reductions across all species, indicating a unimodal response pattern with strain-specific differences in sensitivity. This independent variation from size changes suggests minimal impact of size-scaling on $CaCO_3$ content.

Two-way ANOVA confirmed significant effects of strain identity, Mg availability, and their interaction on $CaCO_3$ content per unit volume (Table A3. 8). All *G. huxleyi* strains showed significant strain-by-Mg interactions, each responding differently to Mg availability in terms of volume-specific calcification. The *Coccolithus* and *G. oceanica* strains also varied in volume-specific calcification but exhibited similar response patterns across Mg treatments.

Morphological analysis using SEM imaging revealed severe coccolith malformations in *G. huxleyi* (OA1, RCC1216, RCC911) and *G. oceanica* (RCC1314) under high Mg conditions (Figure A3. 18; Figure A3. 19). RCC1314 nearly lost its calcification capability at Mg-20, consistent with the observed reductions in cellular $CaCO_3$ content. A slight increase in coccolith malformations was observed in OA1, RCC1216, and RCC1314 under low Mg conditions, despite variations in their $CaCO_3$ content. Under extreme Mg limitation (Mg-0), coccoliths were not observed for all three *G. huxleyi* strains (OA1, RCC1216, RCC911), as confirmed by SEM examination, though extremely low $CaCO_3$ content was still detected, suggesting minimal calcification activity.

4.3.3.5 Multivariate interactions between species and physiological traits in response to Mg availability

PCA and linear modelling were applied to explore the interactions among physiological traits, identifying clear strain-specific clustering patterns. PCA revealed distinct separation of *Coccolithus* species (RCC1198, RCC3776) from the other strains, with *G. oceanica* (RCC1314) clustering independently but closer to *G. huxleyi* strains (OA1, RCC1216, RCC911). Although *G. huxleyi* strains generally formed well-defined clusters, some overlap was observed primarily under Mg-0 conditions. Excluding Mg-0 data markedly improved strain separation along PC1, whereas samples from different Mg conditions within each strain were separated along PC2 (Figure 4. 5f). ANOVA of PCA scores confirmed that PC1 (71% variance explained) predominantly reflects strain differences, while PC2 (16.1%) strongly associates with Mg concentration (Table A3. 9). MANOVA further supported a significant overall effect of strain on the physiological profile, aligning with the clear separation observed in PCA. Linear discriminant analysis (LDA) reinforced these findings, clearly separating *Coccolithus* species from both *G. oceanica* and *G. huxleyi* and enhancing differentiation among *G. huxleyi* strains upon Mg-0 removal (Figure A3. 15). This highlights that strain-specific variation dominates physiological responses, while Mg-0 conditions override these patterns.

The PCA loading plot revealed strong correlations among traits, particularly between cell size, cellular chlorophyll-a content, and $CaCO_3$ content, as well as between growth rate and chlorophyll-a content per unit cell volume (Figure 4. 5f). However, the growth rate and cell size loaded on opposite sides of PC1, indicating weak correlations under Mg stress conditions, contrasting with the more predictable size-growth relationships observed under control conditions (Figure 4. 2). These correlations were consistently supported by both the trend-dependency network (Figure A3. 16) and individual linear regression analyses (Figure A3. 17; Figure 4. 5a-d). The Mg-0 data were excluded from these analyses due to their pronounced physiological effects, which masked the strain-specific relationship. Excluding Mg-0 not only clarified trait correlations but also strengthened differentiation among *G. huxleyi* strains in LDA (Figure A3. 15), and improved within-strain trait relationships (Figure A3. 17).

Although $CaCO_3$ content per unit volume represents a normalised measure of calcification intensity, it was excluded from the PCA and pairwise correlation analyses due to its weak and inconsistent linear relationships with other traits. Specifically, it showed no significant correlation with cellular pigment content or growth rate and only a moderate negative association with cell volume ($R^2 = 0.34$) (Figure A3. 12). While multiple linear regression suggested that both cell volume and growth rate jointly contribute to variation in $CaCO_3$ per volume ($R^2 = 0.69$, $p < 0.001$) (Table A3. 11), this integrated relationship was not sufficiently reflected in individual trait correlations or PCA loading structure. Excluding it ensures that the PCA captures more coherent axes of covariation among interrelated traits, without being distorted by independently regulated or composite variables (Figure A3. 14).

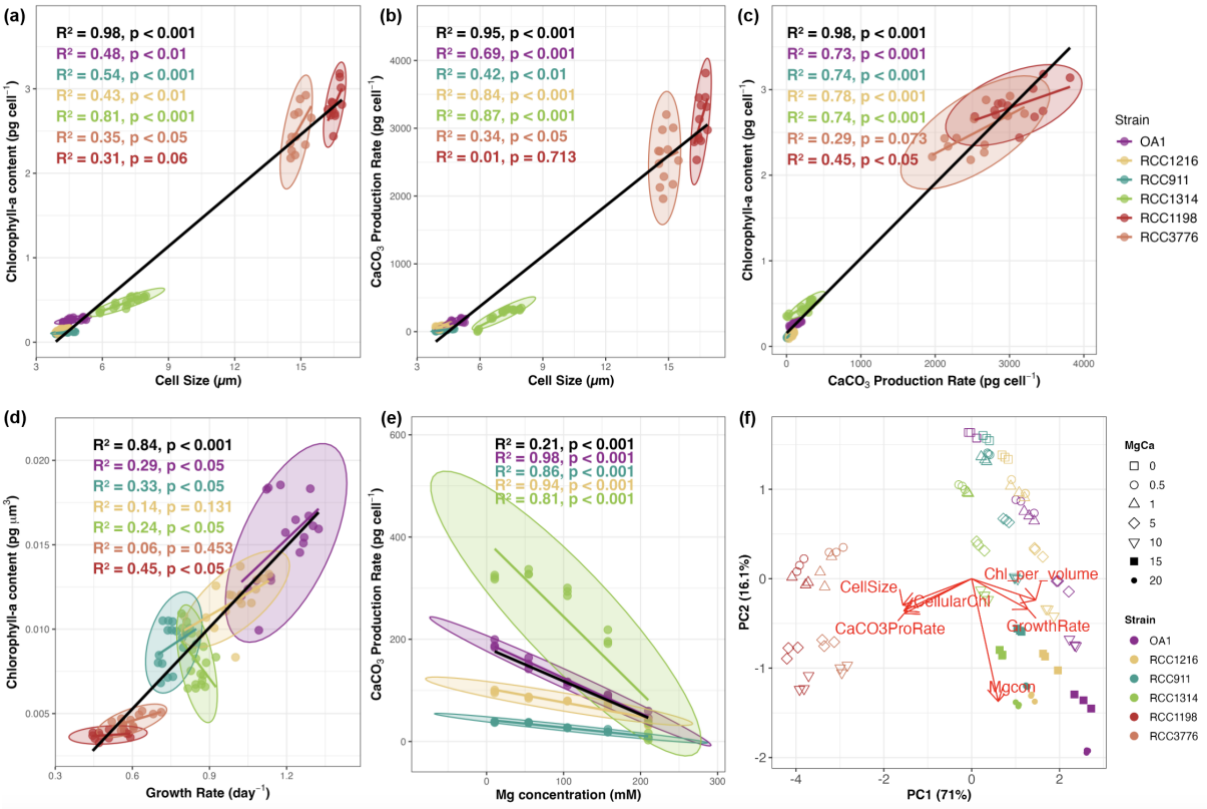

Figure 4. 5: Linear correlations (a-e) and PCA analysis (f) of physiological traits in response to varying seawater Mg availability for four coccolithophore species: *Gephyrocapsa huxleyi* (OA1, RCC911, RCC1216), *Gephyrocapsa oceanica* (RCC1314), *Coccolithus braarudii* (RCC1198), and *Coccolithus pelagicus* (RCC3776). In the linear regression analyses (a-d), data collected under Mg-0 conditions were excluded. In the linear regression analysis (e), data collected under Mg-0 and Mg-0.5 conditions and data from RCC1198 and RCC3776 were excluded.

Comparing overall linear regressions and strain-specific regression suggested that inherent strain differences primarily drive physiological traits, overshadowing direct Mg-

related signals when analysed across all data points. This resulted in strong overall positive linear correlations among traits (R^2 ranged from 0.84 to 0.98, $p<0.001$; Figure 4. 5). In contrast, strain-specific analyses yielded weaker correlations, highlighting that Mg availability significantly modulates trait relationships within individual strains. The three *G. huxleyi* strains (OA1, RCC1216, RCC911) and *G. oceanica* (RCC1314) displayed similarly robust, positive correlations among cell size, cellular chlorophyll-a content and cellular $CaCO_3$ content, indicating potential biologically regulated interactions or coordinated physiological adjustments within constrained ranges (Figure 4. 5). Conversely, the two *Coccolithus* species (RCC1198, RCC3776) consistently showed weak or insignificant trait correlations, underscoring their greater physiological sensitivity and potential vulnerability to Mg-driven environmental variability (Figure 4. 5). However, Growth rate and cell size showed weak overall correlations(R^2=0.38, $p<0.01$) and even weaker strain-level relationships (significant only in *G huxleyi* OA1: R^2 =0.19, $p<0.05$; and *G. oceanica* RCC1314: R2=0.25, $p<0.05$) (Figure A3. 13; Figure A3. 16), consistent with their opposite loading in PCA (Figure 4. 5f). This contrasts with the robust size-growth scaling typically observed across phylogenetically diverse phytoplankton communities and suggests that Mg stress overrides fundamental allometric relationships within coccolithophore groups.

Collectively, these findings demonstrate that both strain identity and Mg availability significantly influence coccolithophore physiological traits, although strain effects dominate overall trait variability, with Mg modulating strain-specific responses (Table A3. 12). Three strains of *G. huxleyi* (OA1, RCC911, RCC1216) exhibited notably distinct physiological patterns in response to Mg conditions, highlighting significant intraspecific variability. This observation aligns with documented strain-specific sensitivities in *G. huxleyi* to various environmental stressors, such as pCO_2 variation (Langer *et al.*, 2009; Hoppe *et al.*, 2011), salinity change (Gebühr *et al.*, 2021), and grazing pressure (Poulson-Ellestad *et al.*, 2016). In contrast, *G. oceanica* (RCC1314) and the two *Coccolithus* species (RCC1198 and RCC3776) showed more uniform responses across traits. Specifically, *G. oceanica* displayed a growth rate response similar to the *Coccolithus* species, while the two *Coccolithus* strains exhibited a parallel pattern in cellular

chlorophyll-a content (Table A3. 5), chlorophyll-a content per unit cell volume (Table A3. 6), and $CaCO_3$ content (Table A3. 7).

The clear differentiation in Mg tolerance ranges across species indicates fundamental physiological plasticity differences, potentially driven by cell size and associated nutrient utilisation strategies. Specifically, smaller cells are generally more efficient at resource acquisition and ionic regulation due to higher surface-area-to-volume ratios (Finkel *et al.*, 2010; Mei *et al.*, 2011; Hillebrand *et al.*, 2022). Consistent with this, metabolite profiling revealed that *G. huxleyi* maintains lower levels of glycolysis and TCA cycle intermediates but elevated nucleotide and amino acid derivatives compared to larger *Coccolithus* species (Figure 4. 3). This pattern may reflect a streamlined metabolic strategy in which carbon is rapidly allocated toward biosynthesis rather than retained in intermediate pools. Such prioritisation could reduce the need to maintain large metabolic reserves, supporting sustained growth across a wide Mg range. In contrast, the larger *Coccolithus* species exhibited higher levels of both glycolysis and TCA intermediates, suggesting a more reserve-oriented metabolic profile, potentially suited for slow, sustained growth (Figure 4. 3). However, this strategy may come at the cost of reduced metabolic turnover and increased resource demands, which, coupled with lower surface-area-to-volume ratios, could constrain ionic homeostasis under stress, and narrow physiological tolerance.

The distinct yet coordinated physiological trait responses to Mg availability reveal potential underlying metabolic trade-offs and cellular regulatory strategies. At low Mg (Mg-0, Mg-0.5, Mg-1), a consistent reduction in growth rates across species highlights Mg's critical roles as a cofactor in ATP synthesis, enzyme activation, and nucleic acid stabilisation, essential for cell-cycle progression and energy metabolism (Romani, 2011; Hermans *et al.*, 2013). At high Mg concentrations (Mg-10 to Mg-20), growth rates in the smaller species, *G. huxleyi* and *G. oceanica*, remained relatively stable, though strain RCC911 exhibited significant reductions at Mg-15 and Mg-20. Despite reductions in cell size (Figure A3. 6), cellular chlorophyll-a content (Figure A3. 7) and chlorophyll-a per unit cell volume (Figure A3. 8), remained relatively constant at moderate Mg levels (Mg-10, Mg-15). This stability likely reflects proportional physiological adjustments, such as concurrent decreases in pigment content and cell volume, that maintain photosynthetic

efficiency under moderate ionic stress. However, these adaptive mechanisms became insufficient at Mg-20, causing significant disruption in pigment-per-volume ratios. Thus, Mg-20 likely represents an upper threshold for ionic stress tolerance in smaller coccolithophores, beyond which fundamental metabolic processes become disrupted (Sunda & Huntsman, 1998).

Calcification in coccolithophores is closely linked to external Mg availability, as demonstrated by the linear correlations observed in both *G. huxleyi* and *G. oceanica* strains across Mg concentrations from Mg-1 to Mg-20 (Figure 4. 5e). Calcification correlated strongly with cell size but appeared decoupled from growth rates (Figure A3. 16), indicating that calcification in these species is a highly Mg-sensitive, independently regulated process under ionic stress conditions. This observation aligns with previous findings that calcification can be substantially reduced without immediately impacting growth or survival in smaller coccolithophore species like *G. huxleyi* and *G. oceanica* (Walker *et al.*, 2018b), reinforcing calcification as a secondary metabolic process.

Consistent with previous studies (Herfort *et al.*, 2004), increased coccolith malformation was observed under both low and high Mg conditions, with more severe malformations at elevated Mg concentrations (Figure A3. 19). However, the findings at Mg-0 diverged notably from previous studies, while earlier work reported that coccolith structure remained relatively complete even under extreme Mg depletion (Herfort *et al.*, 2004), calcification ceased entirely in our experiments. This discrepancy might result from either lower residual Mg concentrations in our experiments or strain-specific differences in ionic regulation capabilities.

The pronounced decrease in calcification under elevated Mg can be explained by disruptions in cellular ionic homeostasis. Elevated extracellular Mg likely partially enters cells via passive diffusion or non-selective ion channels (Beyenbach, 1990; Sunda & Huntsman, 1998), causing excessive intracellular Mg accumulation. Concurrently, high external Mg may competitively inhibit the uptake of essential trace metals and ions, particularly Ca^{2+}, reducing their intracellular availability (Beyenbach, 1990; Sunda & Huntsman, 1998; Romani, 2011; Mellott *et al.*, 2020). Given that coccolithophore calcification strongly depends on intracellular Ca^{2+} concentrations (Herfort *et al.*, 2002,

2004), elevated intracellular Mg, increased Mg/Ca ratios, and reduced Ca^{2+} availability likely mediate the observed calcification inhibition.

The species-specific calcification response, with reduced calcification in *G. huxleyi*, nearly complete loss in *G. oceanica* at Mg-20, and severe limitation of larger *Coccolithus* species at high Mg (>Mg-10) (Figure A3. 9; Figure A3. 18), highlights distinct physiological thresholds across taxa and underscores the role of cell size in determining ionic stress vulnerability. Larger cells, inherently requiring more Ca^{2+} to support their extensive calcification, incur higher metabolic costs to maintain ionic homeostasis, including the active import of Ca^{2+} and extrusion of excess intracellular Mg^{2+} (Finkel *et al.*, 2010; Monteiro *et al.*, 2016). The disruption of elemental homeostasis under high Mg availability likely outweighs any nutritional benefits of Mg enrichment (Mei *et al.*, 2011; Heinrichs *et al.*, 2024), leading to the severe limitation of larger *Coccolithus* species at high Mg (>Mg-10). Additionally, given the essential role of calcification for survival in *Coccolithus* species (Walker *et al.*, 2018b), such impairment may directly constrain their ecological range in Mg-rich environments. Similarly, under extremely low Mg conditions (Mg-0), the complete cessation of calcification in *G. huxleyi* and substantial growth inhibition in larger species likely reflect ionic stress-induced failure of key physiological processes. Smaller cells, with their higher surface-area-to-volume ratios, are more efficient at utilising trace Mg levels and maintaining intracellular ion balance, allowing them to survive even when calcification is halted. In contrast, larger cells may be less able to buffer against ionic perturbations, leading to potentially toxic accumulation of Ca^{2+} or other ions (Müller *et al.*, 2015a). Future work should investigate the molecular and energetic costs of ionic regulation, particularly the mechanisms underlying differential calcification capacity across species. Such understanding will be essential for predicting coccolithophore resilience to environmental change and for refining models of their contribution to carbon cycling.

In the aggregated dataset (including all strains and Mg conditions), strong linear correlations among cell size, cellular chlorophyll-a content, and $CaCO_3$ content were observed (Figure 4. 5). Notably, these robust correlations persisted in *G. huxleyi* and *G. oceanica* when analysing each strain separately and excluding Mg-0 (Figure A3. 17), indicating an inherent metabolic linkage among these traits that remains stable under

moderate ionic stress. One plausible explanation is that cellular chlorophyll-a content reflects overall biosynthetic capacity, which scales with cell size. If both pigment synthesis and calcification draw on shared intracellular carbon pools or are governed by coordinated metabolic regulation, this could explain their strong covariation (Raven & Beardall, 2016; Grubb *et al.*, 2024). However, such regulatory strategies can be limited under extreme conditions such as Mg-0, where core physiological functions become severely impaired, disrupting typical inter-trait linkages. By contrast, *Coccolithus species* lacked such correlations, which may reflect distinct physiological regulation or that the tested Mg range already surpasses their narrower ionic tolerance.

In contrast to these robust linkages, the correlation between growth rate and chlorophyll-a per cell volume was only evident in the aggregated dataset and disappeared in most strain-level analyses (Figure A3. 17), implying that cross-species trends can obscure strain-specific relationships. Environmental stress, ionic homeostasis, or nutrient variability can readily override or mask growth-chlorophyll linkages at finer taxonomic scales (Mei *et al.*, 2011; Hofmann *et al.*, 2019; Heinrichs *et al.*, 2024). Consequently, although general patterns may emerge across multiple species, individual strains exhibit distinct responses under varying Mg concentrations. Future molecular-level studies, such as comparative transcriptomics or metabolomics, are required to clarify the mechanistic basis of these relationships and to reveal how growth and pigment traits are regulated under abiotic stress.

4.4 Conclusion

Due to phytoplankton cell size scaling of metabolic rates and nutrient uptake (Finkel *et al.*, 2010), changes in the marine environment that drive shifts in cell size, such as temperature or nutrient regimes, will in turn affect the structure and dynamics of phytoplankton communities, and thus influence the carbon cycle. Coccolithophores, in particular, exhibit a broad range of cell sizes and make a substantial contribution to marine carbon flux. Consequently, understanding their cellular physiology, the variation within each species, and their response strategies is critically important. By examining species-level physiological traits, conducting metabolomic profiling, and analysing multiple strains of several coccolithophore species under varying Mg concentrations,

this study provides novel insights into the physiological and metabolic responses of coccolithophores to changes in Mg availability. Key relationships between cell size, growth, photosynthesis, and calcification that hold across different species and strains were uncovered.

The findings reveal that distinct cell sizes profoundly affect coccolithophore metabolism under favourable, nutrient-replete conditions, as evidenced by strong allometric scaling between volume, chlorophyll-a content, and $CaCO_3$ content. These relationships align with previously reported coccolithophore and broader phytoplankton allometries. Notably, growth rate correlated most strongly with chlorophyll-a per unit cell volume, suggesting that this trait may serve as a critical metabolic indicator of growth potential. Metabolomic profiles further indicate that differential carbon partitioning and variations in amino acid and nucleotide availability underpin distinct growth strategies among the studied species, with *G. huxleyi* and *G. oceanica* sharing closer metabolic similarities compared to *C. braarudii*. It should be noted that *G. huxleyi* and *G. oceanica* are closely related species within the same genus, so their metabolic similarities may reflect both phylogenetic proximity and size-dependent effects, consistent with the size-dependent growth rate hypothesis.

When examining responses to Mg availability, strain identity dominated overall trait variability, with Mg modulating strain-specific responses. The observed strong linear correlations linking cell size, chlorophyll-a, and calcification were maintained across most Mg treatments (excluding Mg-0) but only in *G. huxleyi* and *G. oceanica*. By contrast, *Coccolithus* species exhibited limited correlations, highlighting potentially narrower ionic tolerance and higher metabolic demands for calcification and ion regulation. Cell size emerged as a critical factor influencing ionic stress vulnerability, with smaller cells maintaining broader Mg tolerance ranges due to more efficient resource acquisition and ionic regulation resulting from higher surface-area-to-volume ratios. The linear reduction of calcification with increasing Mg availability reinforced the secondary nature of calcification in small coccolithophores and the robust linear correlations between cell size, cellular chlorophyll-a content, and $CaCO_3$ content within individual strains suggest inherent metabolic linkages that remain stable under moderate ionic stress but become disrupted under extreme conditions.

Together, these findings advance our understanding of the complex interplay between cell size, metabolic regulation, and environmental adaptation in coccolithophores. The size-dependent physiological responses and species-specific metabolic strategies revealed here provide important insights into the factors shaping coccolithophore ecology and potential responses to changing ocean chemistry. Future molecular-level studies will be crucial for elucidating the regulatory mechanisms underlying these observed patterns and their ecological implications.

Chapter 5 Concluding marks and future directions

Coccolithophores play a central role in global biogeochemical cycles through their unique metabolic capacity to perform both photosynthesis and calcification. Distinct from other phytoplankton, coccolithophores are characterised by their distinctive intracellular calcification process, generating calcium carbonate structures within their cellular matrix. This intracellular biomineralisation mechanism introduces unprecedented complexity to their cellular metabolism. Fundamental questions emerge: How do coccolithophores coordinate the metabolically demanding calcification process with normal cellular activities? What molecular mechanisms regulate the substrate balance between basic cellular processes like carbon fixation and mineral precipitation? How do calcification and other cellular activities respond and adapt to environmental variations such as nutrient availability, temperature fluctuations, and changing ocean chemistry?

These questions are critical because the unique intracellular calcification process represents more than a simple mineralisation mechanism. It reflects a sophisticated cellular strategy potentially involving complex substrate transport, precise biomineralisation control, intricate metabolic coordination, and dynamic environmental responsiveness. This research aims to unravel these complex regulatory processes by answering specific critical questions:

1. Diel regulation: Although many unicellular algae, including coccolithophores, exhibit day-night physiological fluctuations, particularly in calcification, the extent to which protein-level regulation of metabolism follows diel cycles remain unclear.
2. Growth-phase shifts: Transitioning from exponential to stationary phases involves significant changes in resource allocation affecting physiology and calcification. However, the molecular underpinnings (e.g., proteomic shifts) of these transitions in coccolithophores remain understudied.
3. Ionic and nutrient stress: Existing research on coccolithophore responses to macronutrient stress (e.g., nitrogen, phosphate) is more advanced than studies on ionic stressors such as magnesium (Mg). Given Mg's known roles in

photosynthesis and enzyme activation, systematic examination of how varying Mg availability affects coccolithophore physiology, calcification and proteomic profiles is still rare.

4. Species and strain differences: While *Gephyrocapsa huxleyi* serves as a widely used model species, comparative data on larger coccolithophores (e.g., *Gephyrocapsa oceanica*, *Coccolithus braarudii*), which exhibit higher particulate inorganic carbon (PIC) contributions, remain limited. In particular, it is unclear whether species with differing cell sizes possess fundamentally distinct metabolic profiles or environmental stress responses.

By addressing these questions, this thesis provides a comprehensive understanding of coccolithophore biology through integrated temporal (diel), physiological (growth phase), environmental (Mg availability), and taxonomic (cross-species) dimensions. The research uncovers the complex interplay between environmental conditions, cell size regulation, metabolic reprogramming, and calcification, offering a foundation for predicting coccolithophore responses in a changing ocean environment.

This integrated approach yielded several key discoveries that directly address the fundamental questions posted above:

Chapter 2 - Diel regulation and growth phase transitions:

- Nearly half of cellular proteins follow 24-hour cycles, revealing sophisticated temporal coordination of metabolism at the molecular level
- Growth phase transitions reorganise metabolic priorities through nutrient-driven proteomic shifts, with delayed recovery in key biosynthetic pathways
- Calcification declined during the exponential-to-stationary phase transition, controlled by substrate availability rather than protein expression changes

Chapter 3 - Magnesium stress and physiological responses:

- *G. huxleyi* maintained growth across broad Mg concentrations, although growth rate, cell size and pigment content varied significantly with Mg availability
- Photosynthetic performance remained stable across most Mg concentrations, with disruption only under complete depletion

- Calcification was decoupled from photosynthesis, decreasing linearly with increasing Mg availability with minimal changes in calcification-related proteins

Chapter 4 - Species-specific responses and allometric scaling:

- Cell volume, cellular chlorophyll-a content and $CaCO_3$ content showed strong correlations across four coccolithophore species under varying Mg conditions
- *G. huxleyi* and *C. braarudii* exhibit distinct metabolite profiles, with the former enriched in energy metabolism compounds and the latter in nucleotide and amino acid derivatives
- Smaller species (*G. huxleyi*, *G. oceanica*) maintained broader Mg tolerance ranges compared to larger *Coccolithus* species, with all species showing linear with decreases in calcification with increasing Mg availability

These findings collectively demonstrate that coccolithophore metabolism operates through sophisticated regulatory systems that integrate temporal, environmental, and phylogenetic factors to coordinate cellular function and calcification in marine environments.

5.1 Cellular rhythms and growth phase transitions

While diel rhythms in coccolithophores have been examined previously (Paasche, 1967; Müller *et al.*, 2008; Kottmeier *et al.*, 2020b), most studies have focused primarily on physiological traits such as calcification and growth. In Chapter 2, we extended this understanding through a 54-hour time-series analysis of *G. huxleyi*, combining physiological measurements (cell size, pigment concentration, calcification) with untargeted metabolomics and proteomic profiling. This integrative approach revealed intricate diel patterns in cellular processes and showed that nearly half of the proteome exhibited 24-hour oscillation cycles, highlighting a sophisticated temporal coordination of metabolism at the molecular level.

These temporal dynamics go beyond fundamental physiological functions and involve comprehensive metabolic reprogramming. Day-night transitions trigger major shifts in central carbon metabolism, with photosynthesis, de novo fatty acid biosynthesis,

pyruvate metabolism, and glycerolipid biosynthesis upregulated during the day, while the TCA cycle, beta-oxidation, glycolysis, and gluconeogenesis peak at night and early morning. This metabolic partitioning supports the synchronisation of growth and division with light availability.

Growth phase transitions represent another critical temporal dimension of coccolithophore regulation. The shift from exponential to stationary growth phase induces a substantial metabolic reprogramming, characterised by downregulation of cell cycle proteins and altered pathway expression timing. This metabolic shift, likely driven by nitrogen limitation as the primary factor, demonstrates how coccolithophores adapt to resource constraints through coordinated changes in energy acquisition and utilisation pathways.

The divergence of plateaued calcification performance from the delayed recovery seen in photosynthetic and glycerolipid metabolism pathways, coupled with low HCO_3^- and a lack of matching protein-level expression, suggests that substrate supply, rather than protein expression, is the primary constraint on calcification regulation during the transition from exponential to stationary growth phases.

These findings demonstrate that coccolithophores, much like other phytoplankton, align their metabolic activity with diel cycles and adjust carbon allocation at different growth stages, underscoring the tight coupling of cell division timing, photosynthetic capacity, and resource availability. Ecologically, this research provides valuable insights into day-night biosynthetic pathways, which likely influence broader marine food webs and carbon cycling. Additionally, it offers crucial molecular-level understanding of the physiological and proteomic changes characteristic of *G. huxleyi* blooms. However, key questions remain unanswered, such as whether calcification initiation is strictly linked to the G1 cell cycle phase or predominantly triggered by light, and precisely how this process is regulated at the molecular level. Future studies should employ high-temporal-resolution methods to explore these initiation mechanisms. Additionally, comparative investigations into diel and growth-phase responses across coccolithophore species with varying cell sizes and growth rates are needed to determine the generality of these patterns and their implications for marine ecosystems under changing conditions.

5.2 Mg availability and cellular response in *G. huxleyi*

Building on the application of proteomics on diel and growth phase regulation, we next applied this technique to examine how *G. huxleyi* responds to variation in Mg availability in Chapter 3, a previously underexplored environmental factor with the capacity to influence both physiological processes and calcification. This dual role makes Mg a particularly informative probe for dissecting the interaction between metabolic regulation and biomineralisation in coccolithophores. On one hand, Mg acts as an essential cofactor involved in numerous cellular processes, including chlorophyll biosynthesis, ATP stabilisation, and enzymatic function (Verbruggen & Hermans, 2013; Guo *et al.*, 2016; Borah & Bhuyan, 2017). On the other, Mg may influence calcification either indirectly through ionic balance or potentially by interfering with crystal formation at the site of mineralization (Stanley & Hardie, 1998). In contrast to Ca^{2+}, whose role as a direct calcification substrate has been well documented (Herfort *et al.*, 2004; Trimborn *et al.*, 2007; Leonardos *et al.*, 2009; Müller *et al.*, 2011), the impact of Mg on both cellular physiology and calcification remains poorly characterised. Exploring Mg as a modulating rather than a directly incorporated element provides a unique perspective on coccolithophore biology.

Physiologically, *G. huxleyi* demonstrated a remarkable capacity to maintain photosynthetic efficiency across a wide range of Mg concentrations, with notable decline only under complete Mg depletion (Mg-0). This suggests robust homeostatic mechanisms that preserve essential cellular processes under ionic stress. In contrast, cell size, chlorophyll-a content, and calcification showed clear linear responses to Mg availability, implicating Mg as a modulator of carbon allocation and cell cycle regulation.

Proteomic analysis supported these trends, revealing that Mg deficiency triggered upregulation of proteins associated with stress responses, DNA replication, and cell cycle checkpoints, likely buffering the cell against growth arrest. In contrast, excess Mg was associated with upregulation of cell cycle-related proteins, possibly enabling bypass of cell size checkpoints and promoting rapid division. These observations highlight a dual regulatory role of Mg, where limitation activates stress protection, and excess enhances biosynthetic activity.

Interestingly, changes in calcification-related proteins were minimal despite pronounced shifts in $CaCO_3$ content, consistent with findings from Chapter 2. This suggests that calcification is not regulated transcriptionally in response to Mg but is instead governed by substrate availability and energetic thresholds. $CaCO_3$ production closely followed Mg/Ca ratio changes, supporting the model of calcification as a secondary process initiated only when core physiological demands are met. Furthermore, coccolith-associated polysaccharides (CAPs) were not actively upregulated, implying that carbon allocation to calcification is passively adjusted rather than actively promoted under stress.

From an ecological perspective, the ability of *G. huxleyi* to preserve core physiological processes under ionic fluctuations confers a clear adaptive advantage, likely contributing to its wide geographic and ecological distribution. However, the strong modulation of size and pigment traits under Mg variation suggests that organic matter composition and carbon storage may also shift significantly, raising questions about potential impacts on trophic transfer and carbon export. While Mg concentration in the modern ocean remains relatively stable (Lebrato *et al.*, 2020), more dynamic ions such as Ca^{2+} and HCO_3^- show greater spatial and temporal variability and are expected to change further with ocean acidification (Jones *et al.*, 2017; Xue *et al.*, 2021). Given that calcification contributes directly to carbon export and alkalinity balance, improved mechanistic understanding of its substrate-dependence and integration into multi-parameter models will be essential for future biogeochemical predictions.

5.3 Expansion to multiple species and strains

Our current understanding of coccolithophore biology is largely based on *G. huxleyi*, despite the fact that other species such as the larger *Coccolithus* group, may contribute more substantially to carbon export, even if less abundant in surface waters (Guerreiro *et al.*, 2021). The strong Mg-responsiveness of *G. huxleyi* observed in Chapter 3 provided an opportunity to test whether key physiological relationships are shared across strains and species or governed by lineage-specific regulation. To this end, we first assessed fundamental physiological differences among *G. huxleyi* strains and among three species (*G. oceanica*, *C. braarudii*, and *C. pelagicus*) under ambient Mg conditions (Mg-

5), followed by metabolomic profiling on selected species (*G. huxleyi*, *G. oceanica*, *C. braarudii*). Lastly, all strains were exposed to a Mg gradient analogous to Chapter 3 to examine whether the physiological interactions previously observed are conserved or variable across lineages.

As expected, size-dependent physiological characteristics were evident under control conditions: cell volume, chlorophyll-a content, and $CaCO_3$ production were tightly correlated across species, reflecting general allometric scaling principles common in marine phytoplankton (Marañón *et al.*, 2007; Marañón, 2008, 2015; Aloisi, 2015; Álvarez *et al.*, 2017). These relationships provide a mechanistic basis for understanding how metabolic capacity scales with cell size.

Metabolomic profiles revealed clear size- or species-dependent metabolic differentiation, with *G. huxleyi* and *G. oceanica* exhibiting closer metabolic similarities compared to the larger *C. braarudii*. These differences in metabolite composition, particularly in carbon partitioning and amino acid and nucleotide availability, likely underpin the distinct growth strategies employed by species of different sizes.

When exposed to Mg gradients, strain-specific responses emerged as a critical determinant of physiological plasticity. *G. huxleyi* and *G. oceanica* maintained strong physiological coordination and broader Mg tolerance ranges, suggesting efficient resource uptake and ionic regulation likely conferred by their higher surface-area-to-volume ratios. This broad tolerance is consistent with their wide ecological distributions, highlighting metabolic flexibility as a potential trait underpinning ecological success. By contrast, the two *Coccolithus* species shared similar physiological response patterns across traits, including growth rate, pigment content, and $CaCO_3$ production, but displayed narrower tolerance ranges and weaker trait correlations. The breakdown of linear inter-trait relationships under Mg stress suggests distinct regulatory strategies, possibly reflecting higher energetic or structural costs of maintaining homeostasis in larger cells.

These physiological and metabolic differences imply contrasting ecological strategies: smaller, more plastic species may prioritise flexibility and fast response, enabling persistence across dynamic conditions, while larger species may optimise for high

calcification efficiency in narrower environmental windows, potentially enhancing long-term carbon export in more stable niches. The tight linkage between calcification and chlorophyll-a content in *G. huxleyi* and *G. oceanica* further suggests integrated control over pigment biosynthesis and biomineralisation, potentially via shared biosynthetic substrate pools. In contrast, the *Coccolithus* group appears to decouple these processes, indicating alternative regulatory hierarchies. These findings underscore the importance of species- and size-specific metabolic architecture in shaping coccolithophore ecological niches and their contributions to the carbon cycle.

5.4 Integrative understanding of calcification regulation

The research suggests that calcification in coccolithophores functions as a secondary process, primarily driven by substrate availability and contingent upon satisfying baseline energy and carbon demands for cellular survival. Both *G. huxleyi* and *G. oceanica* demonstrated low to no calcification capacity without compromising growth and survival, underscoring the non-essential nature of calcification to fundamental cellular functions.

This substrate dependency is supported by findings from Chapter 2, where *G. huxleyi* exhibited reduced calcification during growth phase transitions when ambient DIC was insufficient. Similarly, in Chapter 3 and Chapter 4, calcification showed a strong linear correlation with Mg availability. These observations emphasise the critical role of substrate availability in regulating calcification. The absence of active regulation is further supported by proteomic data from Chapter 2 and Chapter 3, where proposed calcification-related proteins displayed inconsistent expression patterns relative to calcification changes. In contrast, proteins related to photosynthesis and respiration exhibited clear regulatory responses across both growth phases and Mg treatments. These expression patterns instead point to a possible stress-associated role, rather than direct transcriptional or translational control of calcification. Thus, calcification appears to be responsive rather than proactively regulated at the translational level.

A two-step model is proposed to explain calcification behaviour in *G. huxleyi* and *G. oceanica* under low Mg conditions. Initially, energy limitations may restrict the synthesis

of CAPs, which are essential for nucleation and crystal formation (Marsh, 2003; Kayano *et al.*, 2011; Walker *et al.*, 2018a). We found no evidence for compensatory upregulation of CAPs biosynthetic pathways under conditions of calcification inhibition, suggesting that CAPs production is constrained by stress and energetic limitations. Once sufficient CAPs are present, calcification becomes primarily governed by substrate availability, as indicated by the linear decrease in $CaCO_3$ production with increasing Mg concentration.

In contrast, *Coccolithus* species likely exhibit lower molecular-level adaptability and higher energetic demands for calcification. The lack of Mg-$CaCO_3$ linearity in these species, along with their reduced physiological plasticity, points to potentially distinct calcification mechanisms and a higher vulnerability to environmental fluctuations. This may result in energy undersaturation and subsequent calcification reduction, though molecular confirmation of these hypotheses remains to be established.

Despite the decoupling of calcification and photosynthetic performance, calcification correlated strongly with cellular chlorophyll-a content and cell size across species, particularly within *G. huxleyi* and *G. oceanica*. These correlations suggest a coordinated biosynthetic control linking pigment biosynthesis, cell size, and calcification. Given magnesium's roles in both photosynthesis and calcification, Mg availability may influence this coordination. Further investigation is needed to determine how these relationships manifest across species. A deeper understanding of the pigment-calcification relationship could provide novel methodological opportunities, including potential proxies for estimating PIC production and interpreting coccolithophore productivity in paleoceanographic reconstructions.

5.5 Metabolic flexibility as an evolutionary strategy

A central finding across the experiments is the remarkable metabolic flexibility exhibited by *G. huxleyi* in response to changing conditions. This plasticity enables the species to maintain essential functions despite temporal fluctuations, resource limitations, and environmental stressors. The diel cycling of metabolic pathways, coupled with the ability to reprogram metabolism during growth phase transitions and under Mg stress, demonstrates a sophisticated regulatory network that optimise resource utilisation.

Key metabolic pathways consistently emerged as regulatory hubs across experiments. Carbon metabolism pathways, including photosynthesis, the TCA cycle, glycolysis/gluconeogenesis, and fatty acid metabolism, showed coordinated responses to both temporal cues and environmental perturbations. This suggests that such pathways serve as central nodes in coccolithophore metabolic networks, integrating multiple environmental signals to coordinate cellular responses. Nucleotide and ribosome activity, protein synthesis, and cell cycle regulation demonstrated remarkable adaptability in response to changes across diel cycles, growth phases, and environmental conditions. The maintenance of stable photosynthetic rates across a wide range of Mg concentrations highlights the species' exceptional resilience and physiological adaptability.

The evolutionary significance of this metabolic flexibility cannot be overstated. Coccolithophores have survived multiple oceanic perturbations throughout their evolutionary history, including major changes in ocean chemistry, temperature, and nutrient availability. *G. huxleyi*'s emergence as a cosmopolitan species inhabiting diverse temporal and spatial ranges can be attributed to the adaptive mechanisms revealed in this research.

5.6 Ecological and biogeochemical implications

Beyond individual traits or stress responses, this research offers a systems-level understanding of how coccolithophores integrate environmental signals into ecophysiological outcomes, with implications for their ecological niches and roles in marine biogeochemistry. Rather than focusing solely on trait-level plasticity, the findings from Chapter 2 to Chapter 4 converge on a unifying theme: strain-level metabolic plasticity in *G. huxleyi*, when placed in broader cross-species context (Chapter 4), reveals how divergent regulatory architectures underpin distinct ecological strategies.

Temporal regulation (Chapter 2) demonstrated that diel and growth phase transitions orchestrate broad metabolic reprogramming, allowing *G. huxleyi* to synchronise energy acquisition with cellular demand. This ability to reallocate metabolic fluxes temporally provides a competitive advantage under fluctuating light or nutrient regimes. Coupled

with the Mg-induced reprogramming observed in Chapter 3, these responses highlight how *G. huxleyi* integrates physiological and proteomic changes to buffer variability in environmental fluctuations. Importantly, while photosynthesis remains robust, traits like cell size and pigment content adjust proportionally, indicating energetic prioritisation and carbon storage flexibility.

Cross-species comparisons in Chapter 4 reinforced the significance of these strategies. Smaller taxa like *G. huxleyi* and *G. oceanica* exhibited broader Mg tolerance, more consistent trait correlations, and greater metabolic plasticity, traits that are typically associated with ecological generalism and opportunistic bloom formation. In contrast, larger *Coccolithus* species, while potentially contributing more to long-term carbon export due to higher PIC per cell, exhibited narrower tolerance ranges and weaker physiological coordination, suggesting a strategy optimised for stability rather than flexibility.

These findings imply that future ocean changes may not affect coccolithophore communities uniformly, but instead shift community composition by applying differential selection pressures across species and strains. Such shifts could alter the balance between organic and inorganic carbon fluxes. The demonstrated sensitivity of calcification to both energy and substrate availability suggests that changes in ocean chemistry, including alterations in ion ratios resulting from climate change, could significantly impact coccolithophore calcification rates and thus carbon export. Moreover, the relationship between cell size and calcification intensity implies that shifts in coccolithophore community size structure could alter the efficiency of the carbonate pump independent of species composition changes.

5.7 Future research directions

This research opens several promising avenues for future investigation. One priority is to gain finer-resolution insights into diel regulation by exploring how coccolithophores respond to variations in light regimes. While Chapter 2 established that nearly half of the proteome oscillates on a 24-hour cycle, future work should examine whether these diel expression patterns persist under constant light or varying light intensities. Such studies

would help determine whether diel regulation is endogenously controlled or environmentally entrained. In particular, proteomic profiling at higher temporal resolution under altered photoperiods would offer a clearer picture of how key physiological processes, including calcification, pigment synthesis, and cell division, are temporally coordinated.

Further investigations are also needed to clarify the regulatory mechanisms linking Mg availability to cell cycle control. While proteomic shifts under Mg treatments suggest that Mg modulates biosynthetic activity and may influence checkpoint bypass, direct evidence for molecular regulators remains lacking. Targeted approaches, such as tracking the diel or Mg-responsive expression of cell cycle checkpoint proteins, could help pinpoint how coccolithophores integrate ionic signals with cell cycle progression, especially at the G1/S transition. Although direct gene manipulation in coccolithophores remains technically challenging, combining high-resolution proteomics with emerging single-cell and transcript-level methods may provide new opportunities for mechanistic discovery.

Another key area concerns the energetic and substrate requirements for calcification. Current data indicate that calcification is a substrate-dependent, energetically costly process that only proceeds when basic metabolic needs are met. To refine this model, quantitative studies on in situ energy production, CAP biosynthesis and transport are needed. Dissecting CAP production pathways and their regulation under different stress regimes will help establish whether calcification bottlenecks stem from carbon allocation, energy limitation, or specific regulatory deficits.

In addition, the observed covariation between cell size, chlorophyll-a content, and $CaCO_3$ content raises important questions about whether these traits are functionally coordinated across diverse environmental conditions. Testing whether the linear correlations persist under additional stressors, such as temperature, nutrient availability, and light intensity, will help establish the generality of these relationships. If trait coordination is maintained, future studies could apply approaches such as stable isotope labelling or metabolic flux tracing to assess whether pigment synthesis and calcification draw from shared biosynthetic pools or are co-regulated. Comparative

analyses across species would further clarify whether these linkages are universal strategies or lineage-specific adaptations.

Species-level comparisons also remain underdeveloped. While this study provided foundational insights through metabolite profiling across selected coccolithophore species, additional molecular-level investigations are essential to clarify how interspecific differences in metabolic regulation influence trait expression. Understanding how species-specific regulatory networks govern physiological responses, particularly under stress, will be key to resolving whether observed trait correlations and calcification patterns are conserved or divergent across evolutionary lineages.

Lastly, laboratory findings must be validated in natural settings. Field-based studies incorporating environmental monitoring, community composition analyses, and grazing pressure assessments will provide the necessary ecological context for interpreting cellular-level results. Bridging controlled laboratory experiments with filed-based observation will improve our understanding of coccolithophore contributions to marine biogeochemical cycles across spatial and temporal gradients.

5.8 Concluding remarks

This thesis presents an integrated investigation of coccolithophore physiology and metabolism, revealing how these organisms regulate photosynthesis, growth, and calcification under diel cycles, nutrient dynamics, and ionic stress. Through a combination of time-series proteomics, physiological assays, and cross-species comparisons, the study highlights the metabolic flexibility of small coccolithophores, such as *G. huxleyi*, in coping with environmental variability. In particular, the findings demonstrate how rapid molecular regulation of metabolic pathways, combined with size-dependent physiological responses, enables coccolithophores to maintain cellular function across fluctuating environmental conditions.

Importantly, the research demonstrates that calcification is not a constitutively controlled trait but emerges when metabolic thresholds are met. This finding reframes calcification as a secondary process, tightly coupled to biosynthetic capacity and

resource status. Moreover, species-level comparisons reveal divergent ecological strategies: small, flexible species like *G. huxleyi* exhibit broad environmental tolerance and robust trait integration, while larger species such as *Coccolithus* show narrower ranges and more decoupled physiological coordination. These patterns provide insight into how community composition and trait distributions might shift under future ocean conditions.

Altogether, this thesis advances a systems-level view of coccolithophore biology, linking cellular regulation to ecological and biogeochemical outcomes. By connecting trait responses across temporal, environmental, and taxonomic dimensions, it lays the foundation for more accurate predictions of coccolithophore contributions to ocean productivity and carbon cycling under climate change.

Appendix 1: Supporting information for Chapter 2

Method A1. 1Calculation of daily residual nutrients in the medium and cell division rate

To better understand potential nutrient limitations associated with cell growth, the Nitrogen (N) and Phosphorus (P) concentrations in the seawater media were calculated using the C: N: P stoichiometry relationship of 124C: 16N: 1P for *Gephyrocapsa huxleyi* under control conditions where no nutrient limitations (Sheward *et al.*, 2023). The initial media concentration of N (Ni) and P (Pi) were 1.4 x10^6 pg ml^{-1} and 3.9 x 10^5 pg ml^{-1}, respectively. The calculation equations for the first two sample collection time points are as follows:

$$N1 = \frac{Ni * V - \frac{(POC1) * C1 * 16 * V}{124}}{V} \quad \text{(A1. 1)}$$

$$N2 = \frac{Ni * V - N1 * V1 - \frac{(POC1) * C1 * 16 * V1}{124} - \frac{(POC2) * C2 * 16 * (V - V1)}{124}}{V - V1} \quad \text{(A1. 2)}$$

Here, N1 and N2 represent the N concentration (pg ml^{-1}) in the seawater media at the first and second data collection time points, respectively. V is the initial seawater media volume (ml), and V1 is the removed seawater media volume at the first sample collection time point. POC is the estimated cellular particulate organic carbon content (pg), estimated through cell volume. POC1 and POC2 represent the carbon content at the first and second sample collection time points, respectively. C1 and C2 represent the cell number concentration (cell ml^{-1}) at the first and second sample collection time points, respectively. The N concentration for the remaining time points is calculated successively. The P concentration in the media is calculated similarly, but the relationship between C and P is 124:1 instead of 124:16 for C: N.

To understand the daily cell replication abilities, daily cell division rate is calculated by:

$$cell\ division = \frac{N_{n+1} - N_n}{N_n} \quad \text{(A1. 3)}$$

All datapoint for the cell division calculation are collected at 18 o'clock each day except the last day, where we used the data collected by 12 o'clock. From the previous collected data from this study, the cell is on growing period rather than replicating period therefore the cell number is still considered to be representative for the cell number at 18 o'clock.

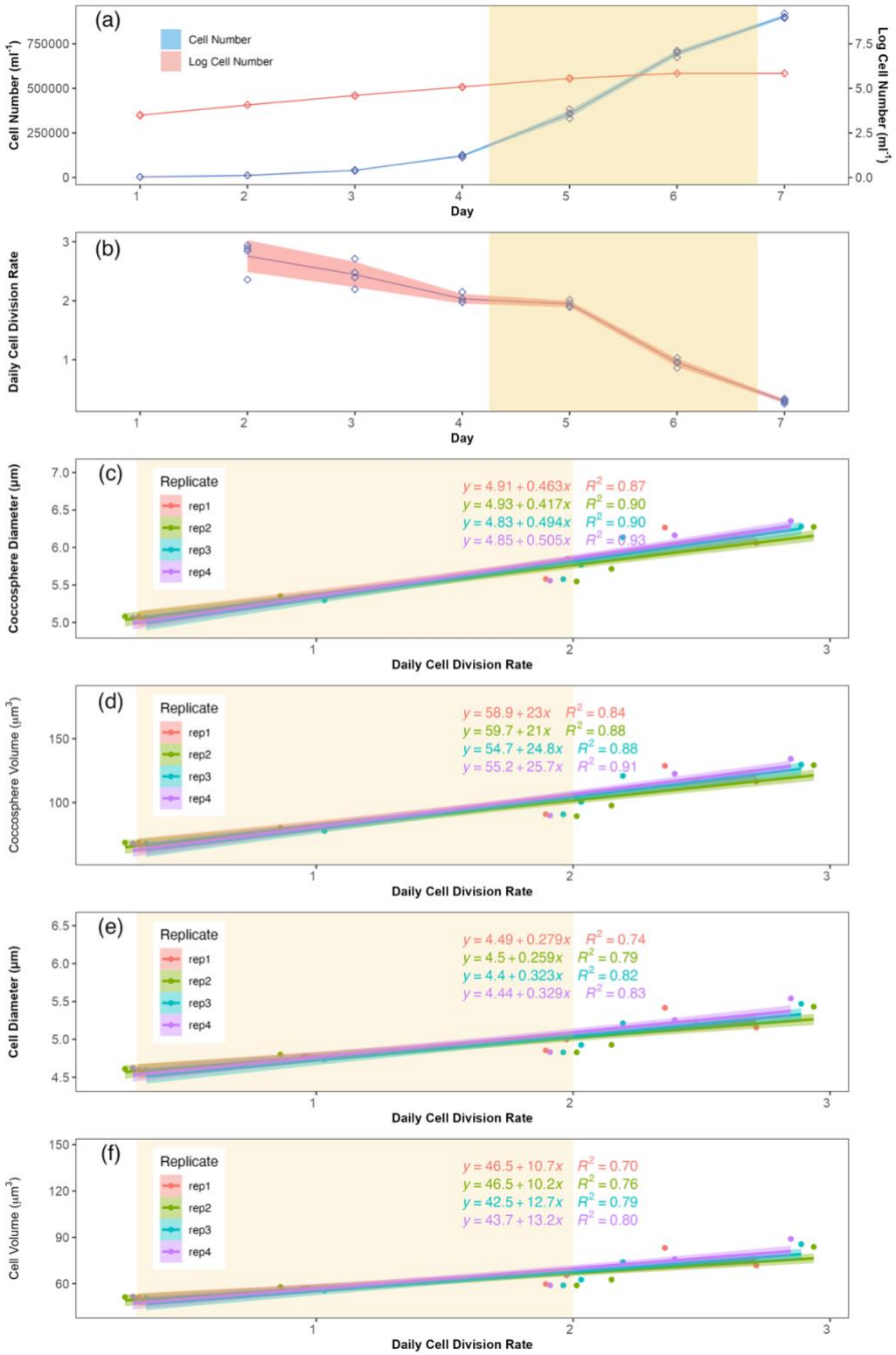

Figure A1. 1: Daily cell number and cell division change. The yellow shadow indicated the sample collection period. (a) absolute cell number and log-transformed cell number change. Blue is the raw cell number, and pink is the log-transformed cell number. (b)daily cell division rate, (c-f) the linear relationship between the daily cell division rate and the coccosphere diameter, coccosphere volume, naked cell diameter and naked cell volume, respectively, the four different colours indicate each replicate sample.

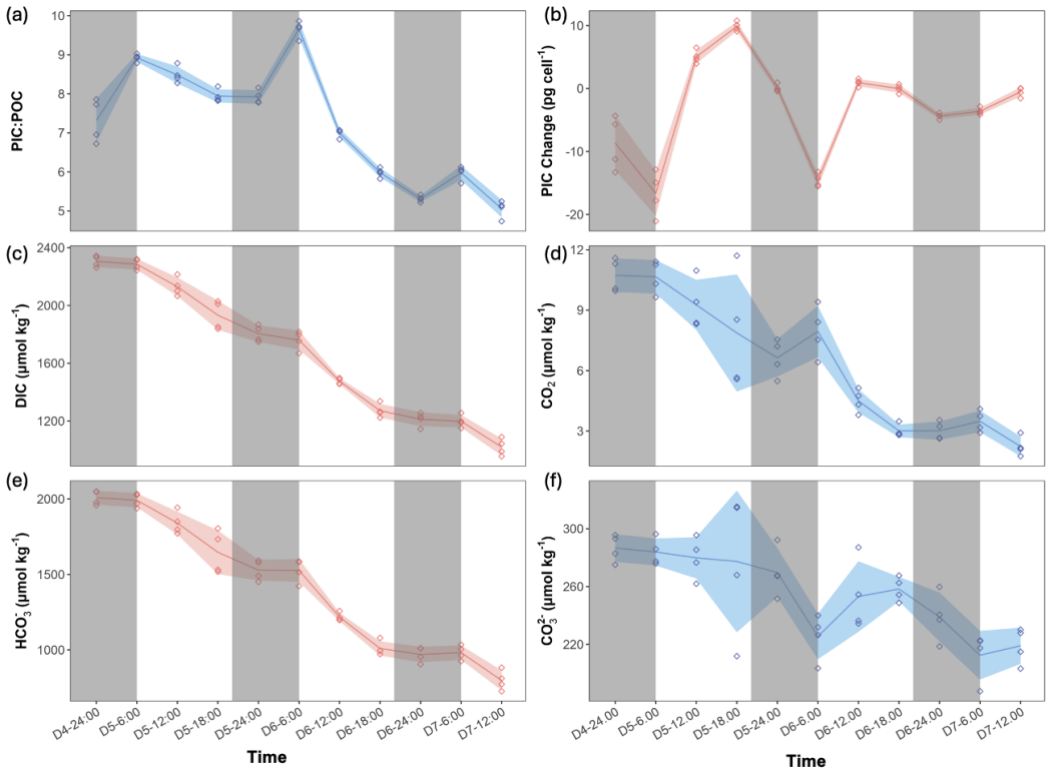

Figure A1. 2 : PIC: POC ratio and cellular PIC content in *Gephyrocapsa huxleyi*, along with changes in seawater carbonate chemistry over time.

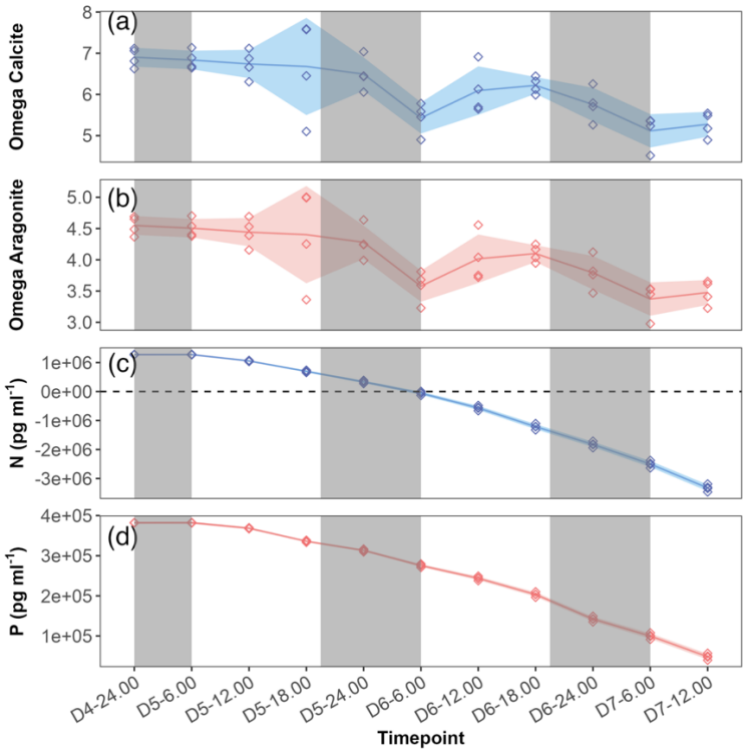

Figure A1. 3: The seawater media chemical condition through time. (a) and (b) represented the saturation status of calcite and aragonite, respectively; (c) and (d) represented the seawater N and P concentration, respectively.

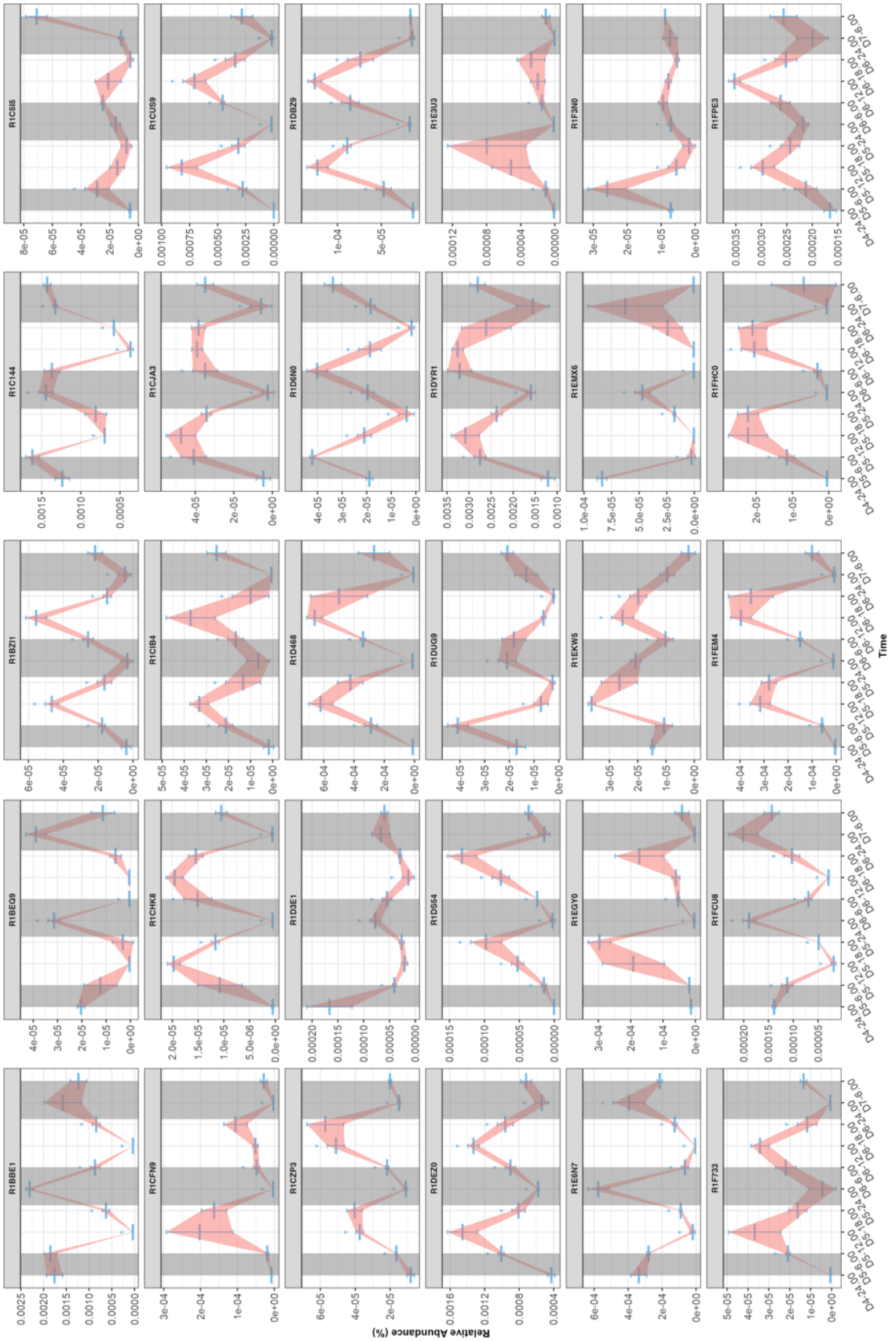

Figure A1. 4: Top 30 rhythmic proteins in *Gephyrocapsa huxleyi* identified by Rhythmicity Analysis Incorporating Nonparametric (RAIN) analysis.

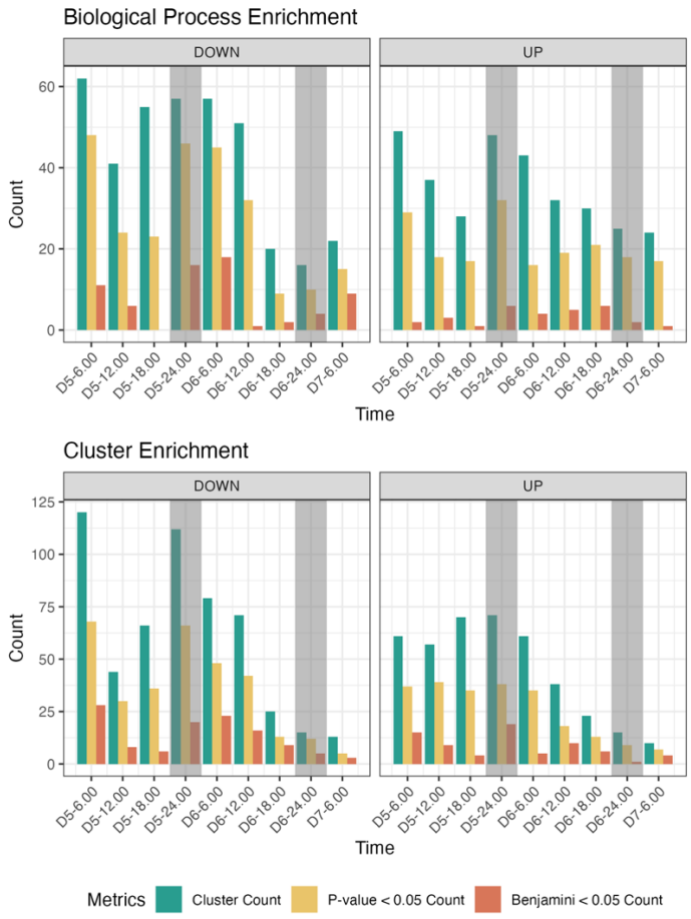

Figure A1. 5: Functional enrichment analysis of differentially expressed proteins in sequential time intervals of *Gephyrocapsa huxleyi*.

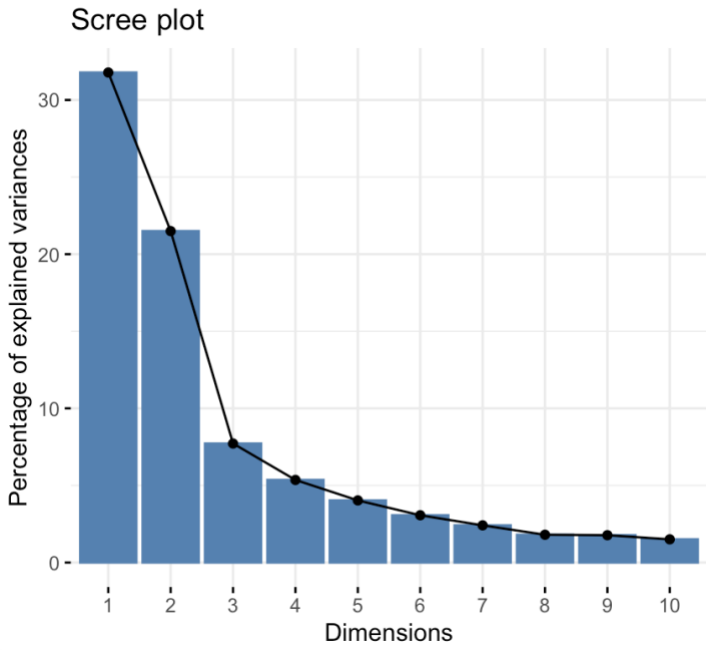

Figure A1. 6: Percentage of explained variance for principal components in *Gephyrocapsa huxleyi* over a 54-hour sampling period.

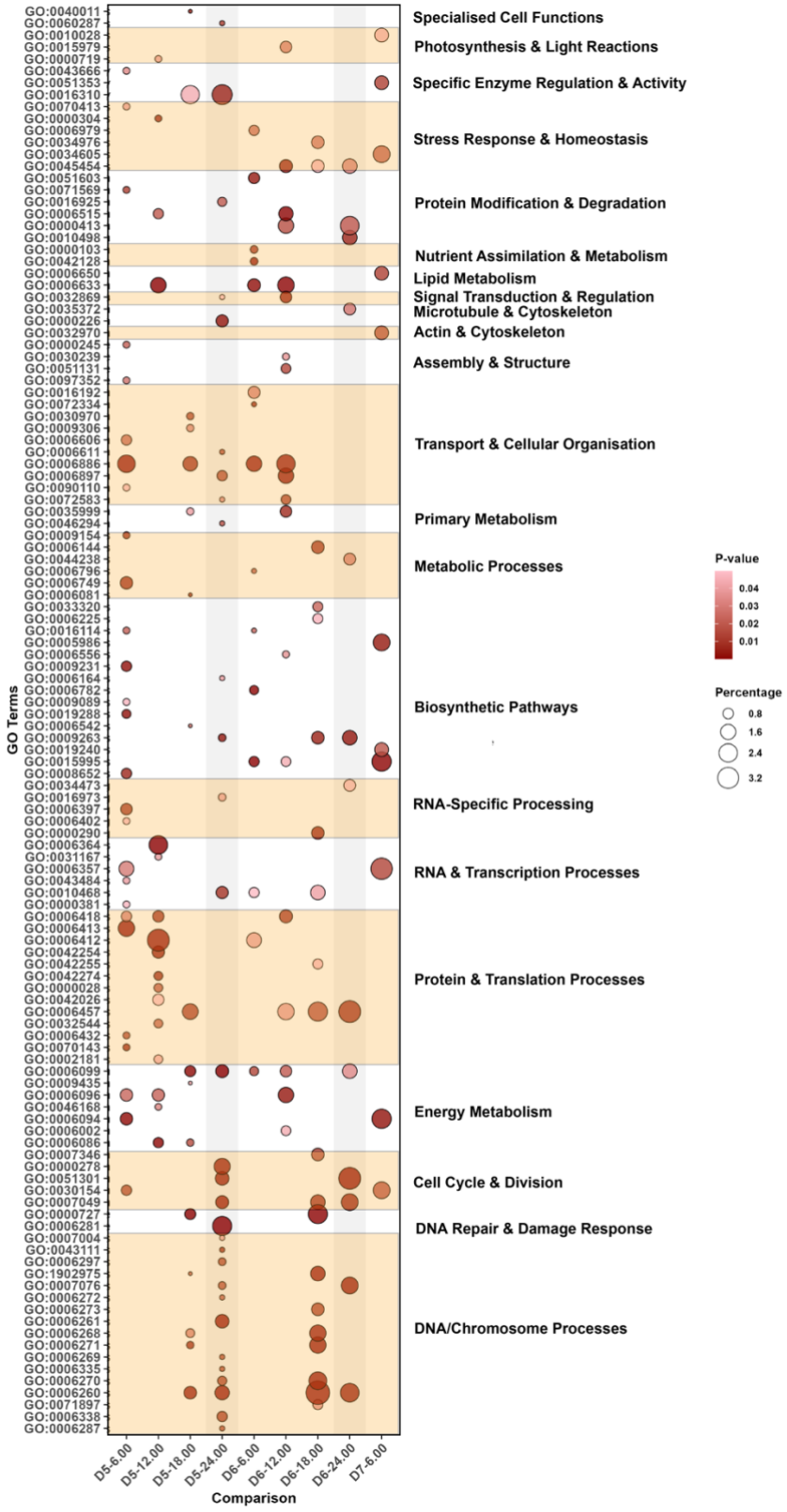

Figure A1. 7: Detailed breakdown of upregulated gene ontology biological process terms in *Gephyrocapsa huxleyi*, grouped under broader functional classifications. Each row represents a specific GO term, with terms organised by their assigned classifications. Bubble size reflects gene count, while colour indicates P-value significance. Temporal dynamics of these processes are displayed across comparisons on the x-axis.

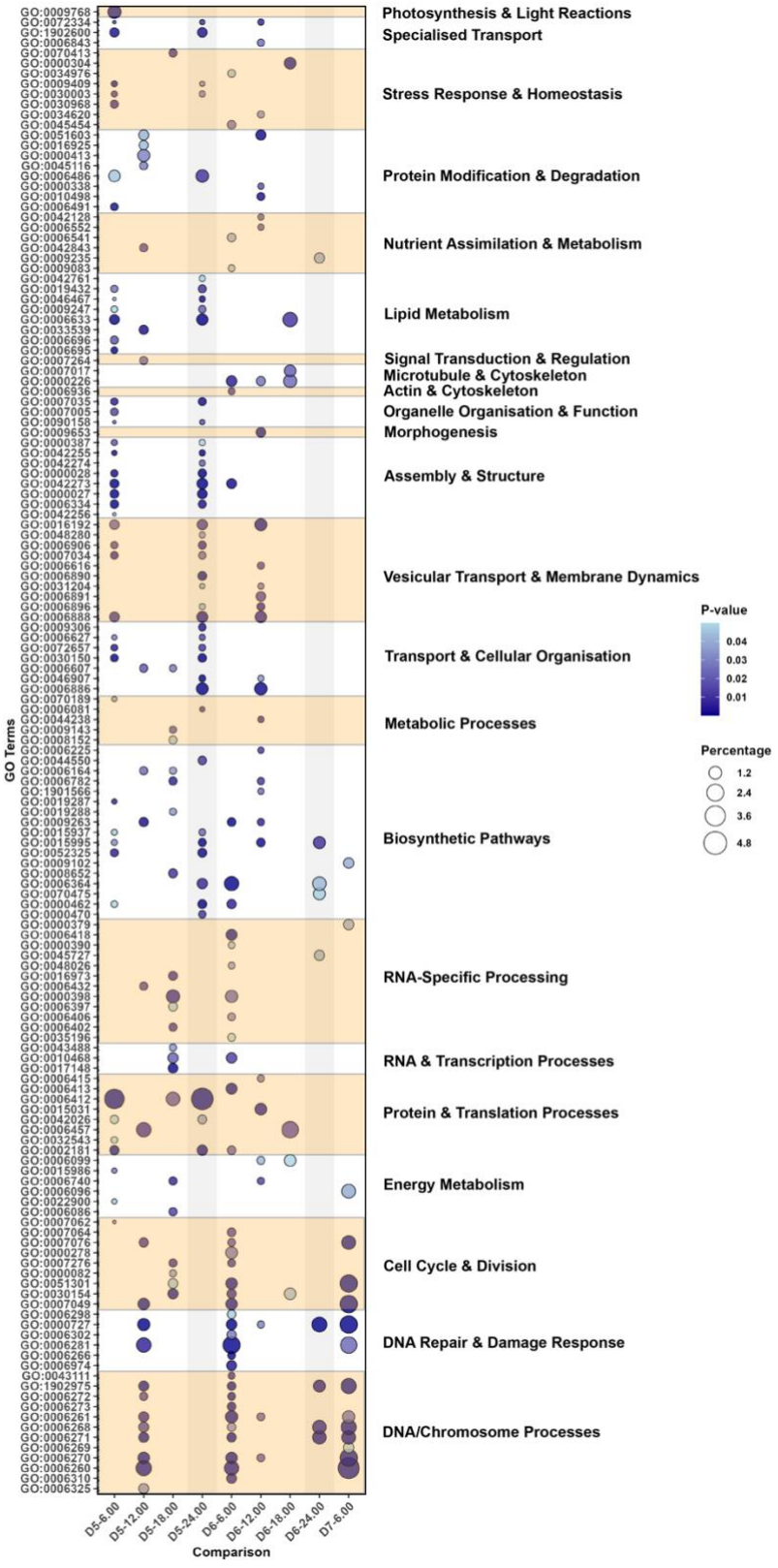

Figure A1. 8: Detailed breakdown of downregulated gene ontology biological process terms in *Gephyrocapsa huxleyi*, grouped under broader functional classifications.Each row represents a specific GO term, with terms organised by their assigned classifications. Bubble size reflects gene count, while colour indicates P-value significance. Temporal dynamics of these processes are displayed across comparisons on the x-axis.

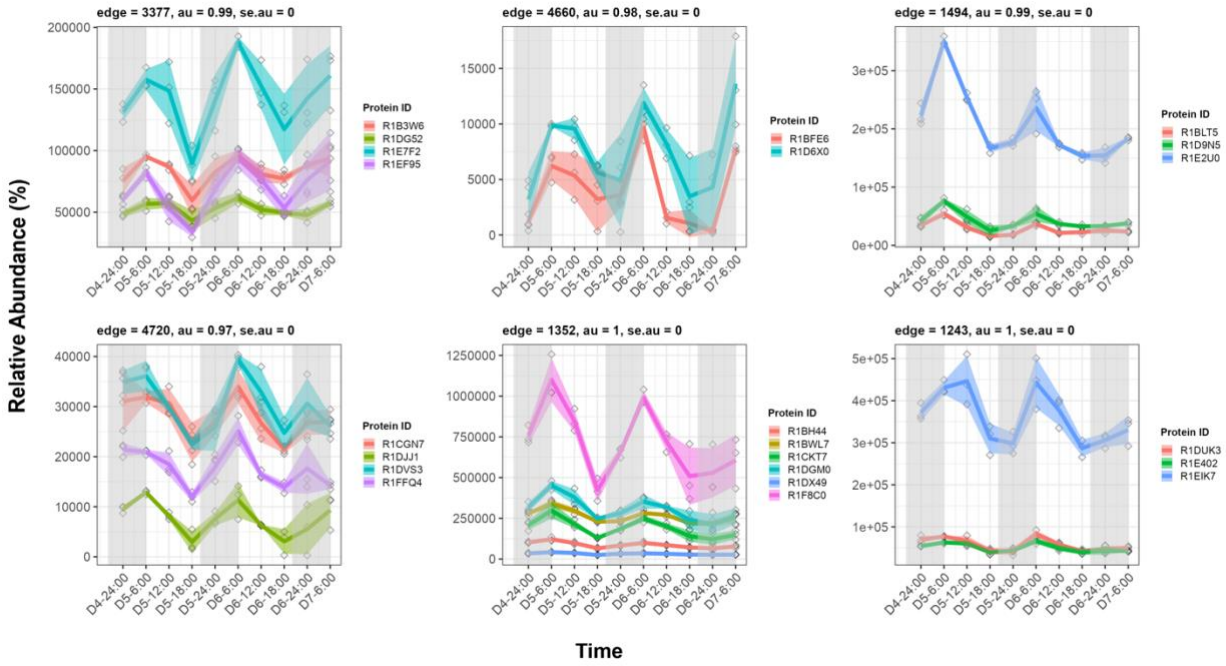

Figure A1. 9: Selected co-expression clusters of proteins in *Gephyrocapsa huxleyi* exhibiting synchronised expression patterns with distinct peaks at 6:00 across day-night transitions.

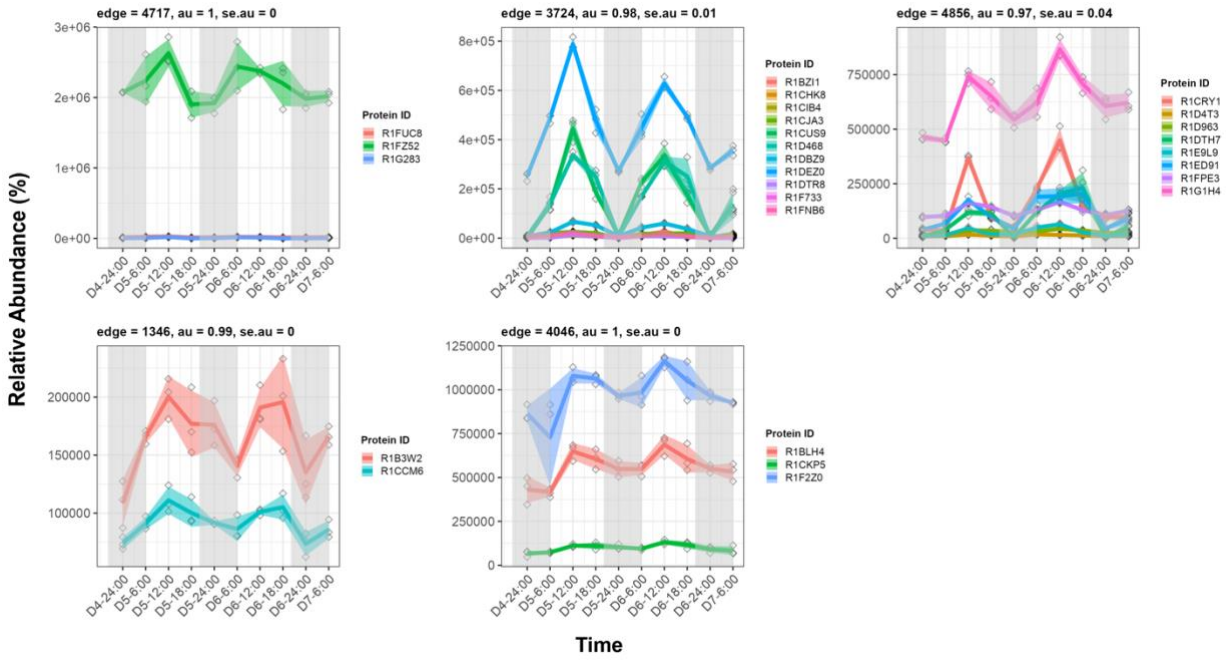

Figure A1. 10: Selected co-expression clusters of proteins in *Gephyrocapsa huxleyi* exhibiting synchronised expression patterns with distinct peaks at 12:00 across day-night transitions.

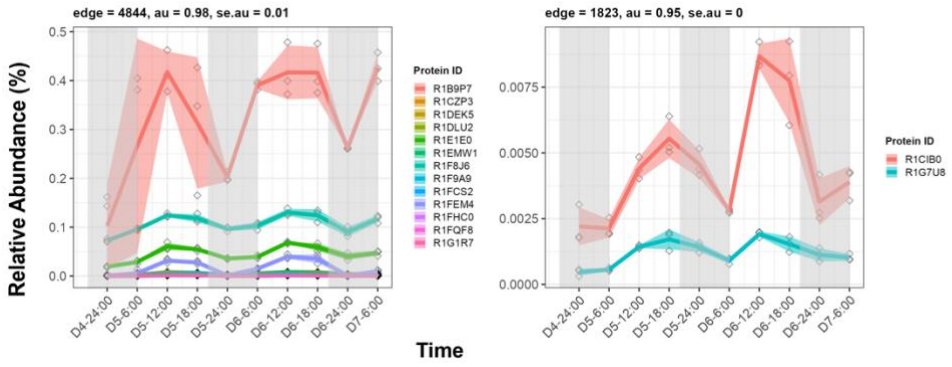

Figure A1. 11: Selected co-expression clusters of proteins in *Gephyrocapsa huxleyi* exhibiting synchronised expression patterns with distinct peaks at both 12:00 and 18:00 across day-night transitions.

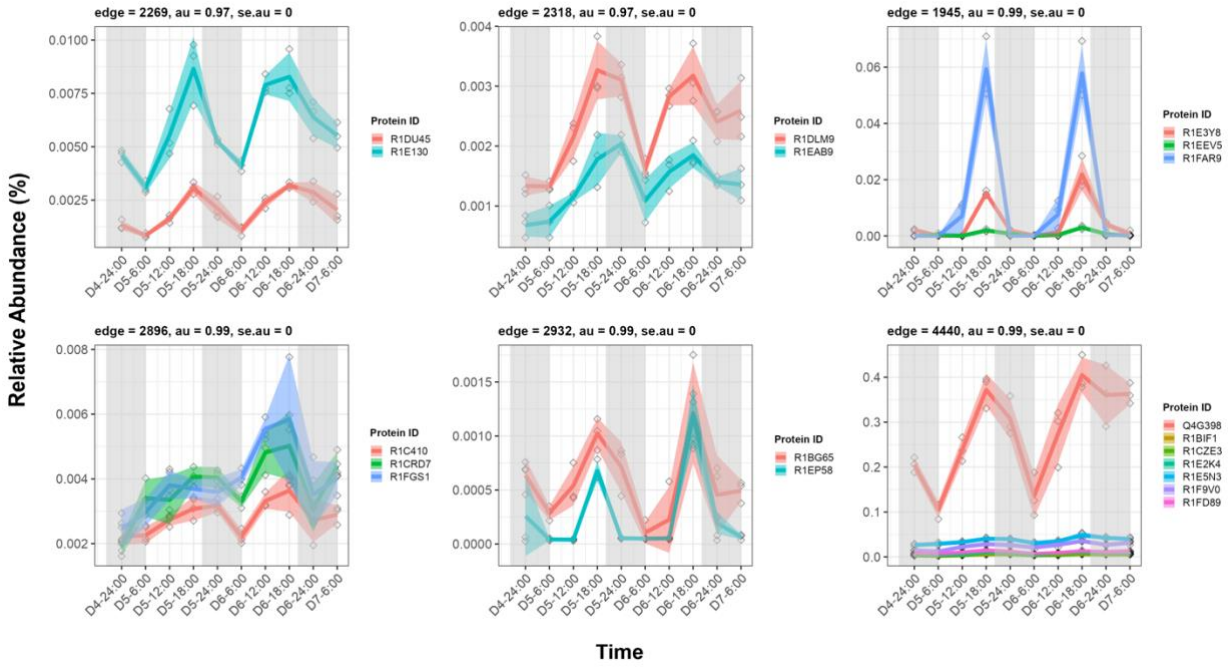

Figure A1. 12: Selected co-expression clusters of proteins in *Gephyrocapsa huxleyi* exhibiting synchronised expression patterns with distinct peaks at 18:00 across day-night transitions.

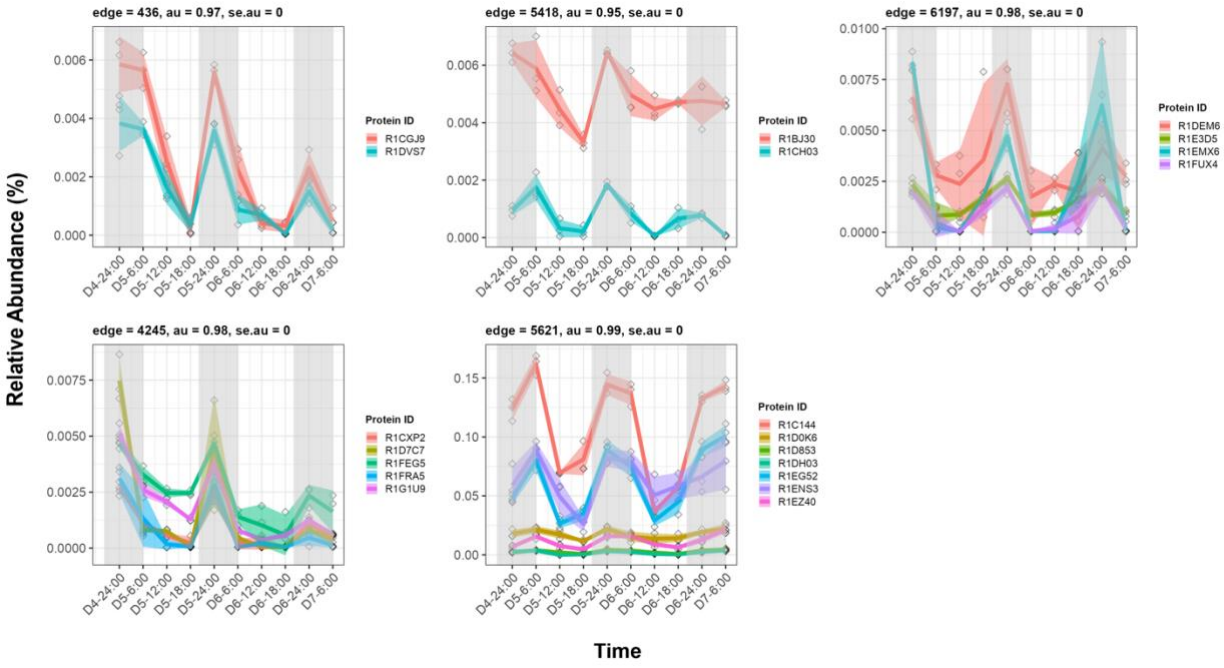

Figure A1. 13: Selected co-expression clusters of proteins in *Gephyrocapsa huxleyi* exhibiting synchronised expression patterns with distinct peaks at 24:00 across day-night transitions and distinct peaks at both 24:00 and 6:00 across day-night transitions.

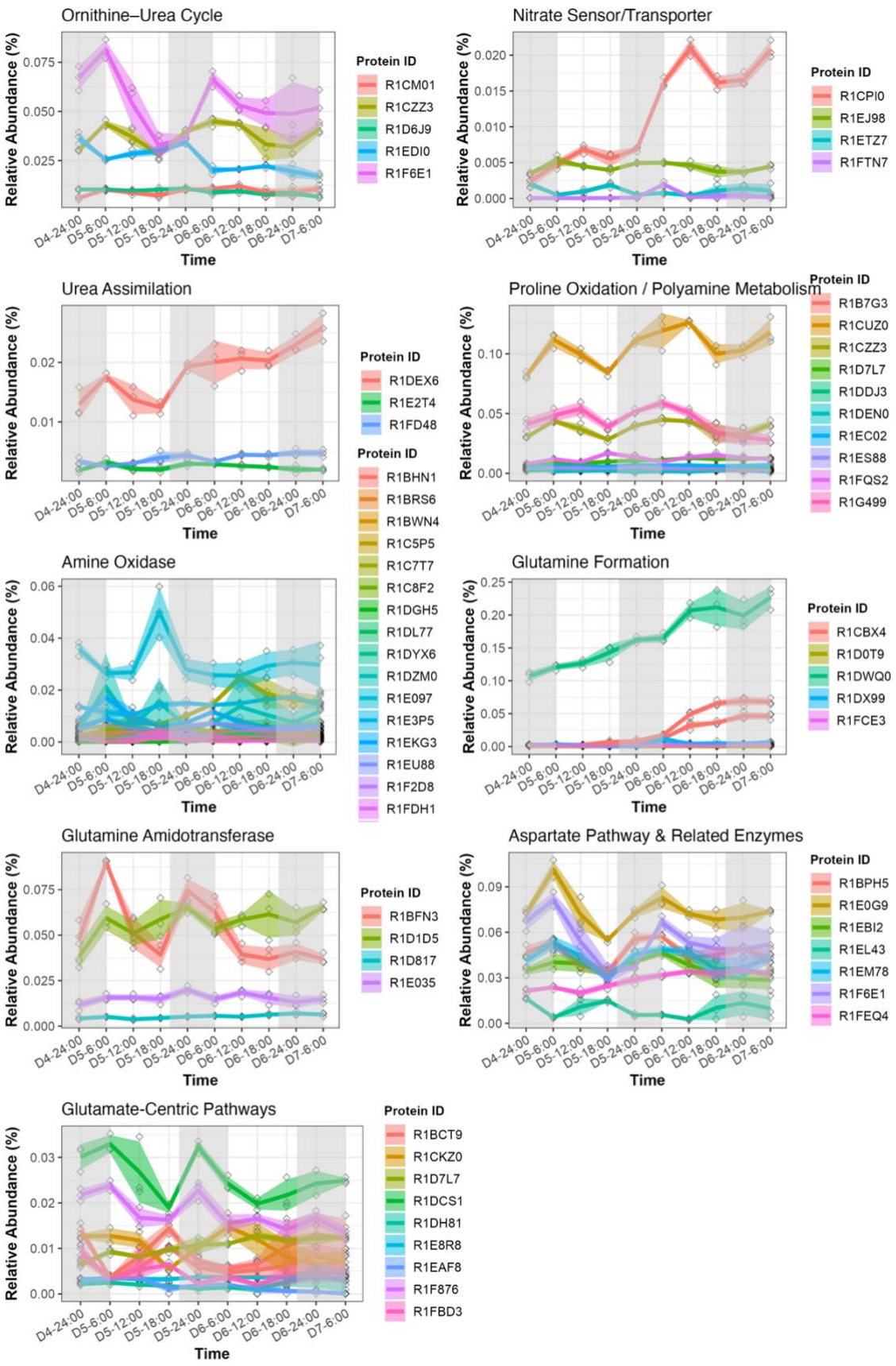

Figure A1. 14: Nitrogen- regulation pathways and protein expression dynamics in *Gephyrocapsa huxleyi* across day-night cycles.

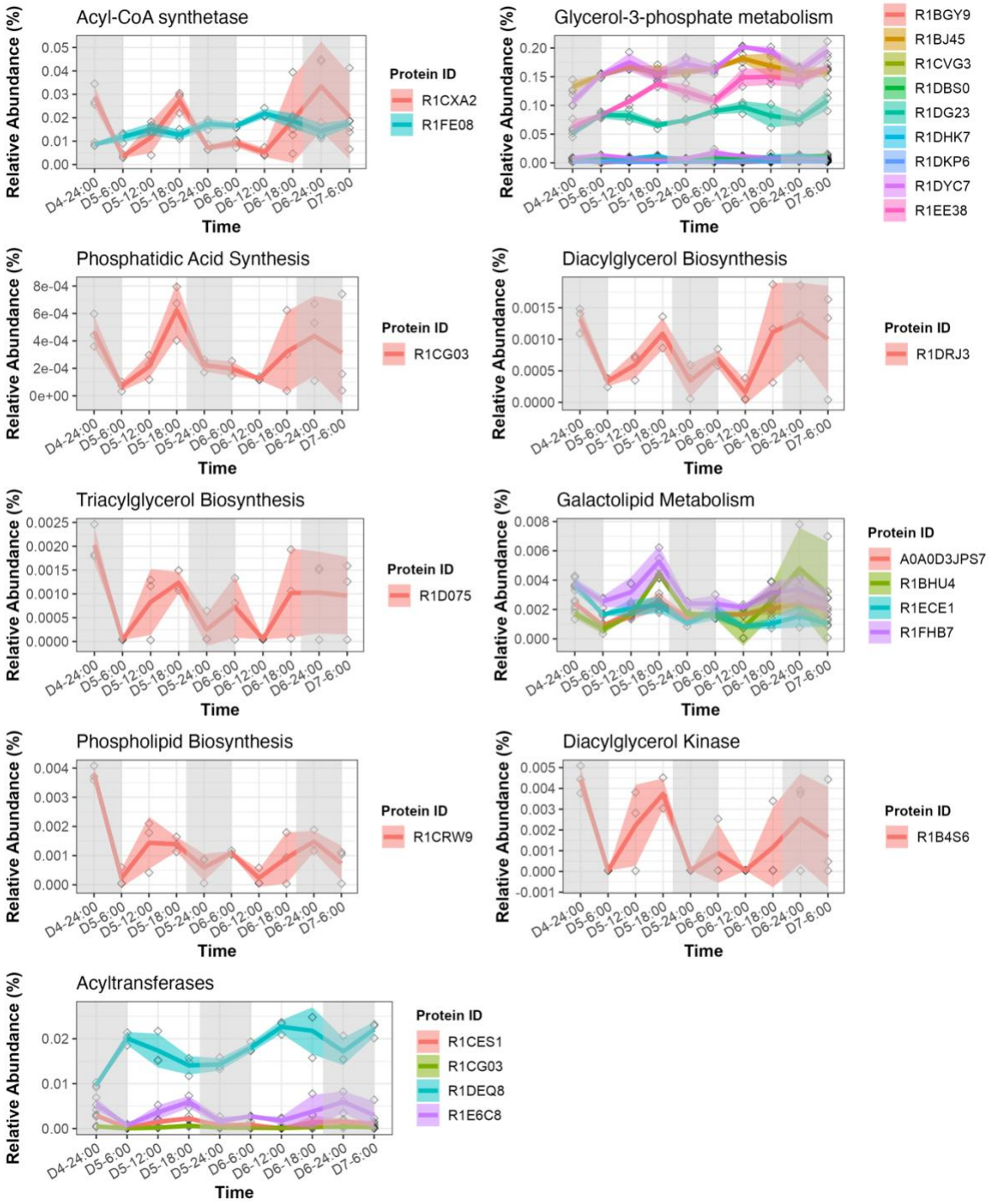

Figure A1. 15: Expression dynamics of proteins related to glycerolipid metabolism, encompassing the synthesis and modification of triacylglycerols (TAGs), phospholipids, and galactolipids in *Gephyrocapsa huxleyi* across day-night cycles.

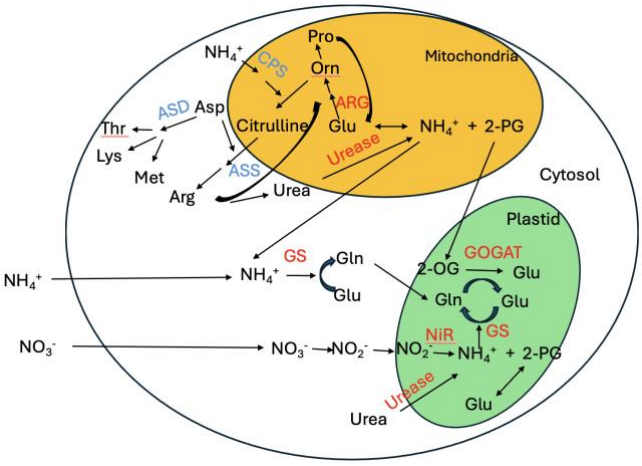

Figure A1. 16: Nitrogen assimilation in *Gephyrocapsa huxleyi* shifts between growth stages, transitioning from Day 5 (late exponential phase) to Day 6 (early stationary phase). On Day 6, nitrite reductase (NiR) is upregulated to convert nitrite to ammonium, which is then incorporated into glutamine (Gln) and glutamate (Glu) via the GS/GOGAT cycle (glutamine synthetase and glutamate synthase). Additional ammonium is provided by urease through the hydrolysis of urea and likewise enters this cycle. Increased levels of acetylglutamate kinase (ARG) may further promote ornithine (Orn) production. In contrast, aspartate-semialdehyde dehydrogenase (ASD), Carbamoyl phosphate synthetase (CPS) and argininosuccinate synthase (ASS) are downregulated, presumably reducing the energy-intensive steps of the urea cycle and limiting the biosynthesis of certain amino acids, such as threonine (Thr), lysine (Lys), and methionine (Met).

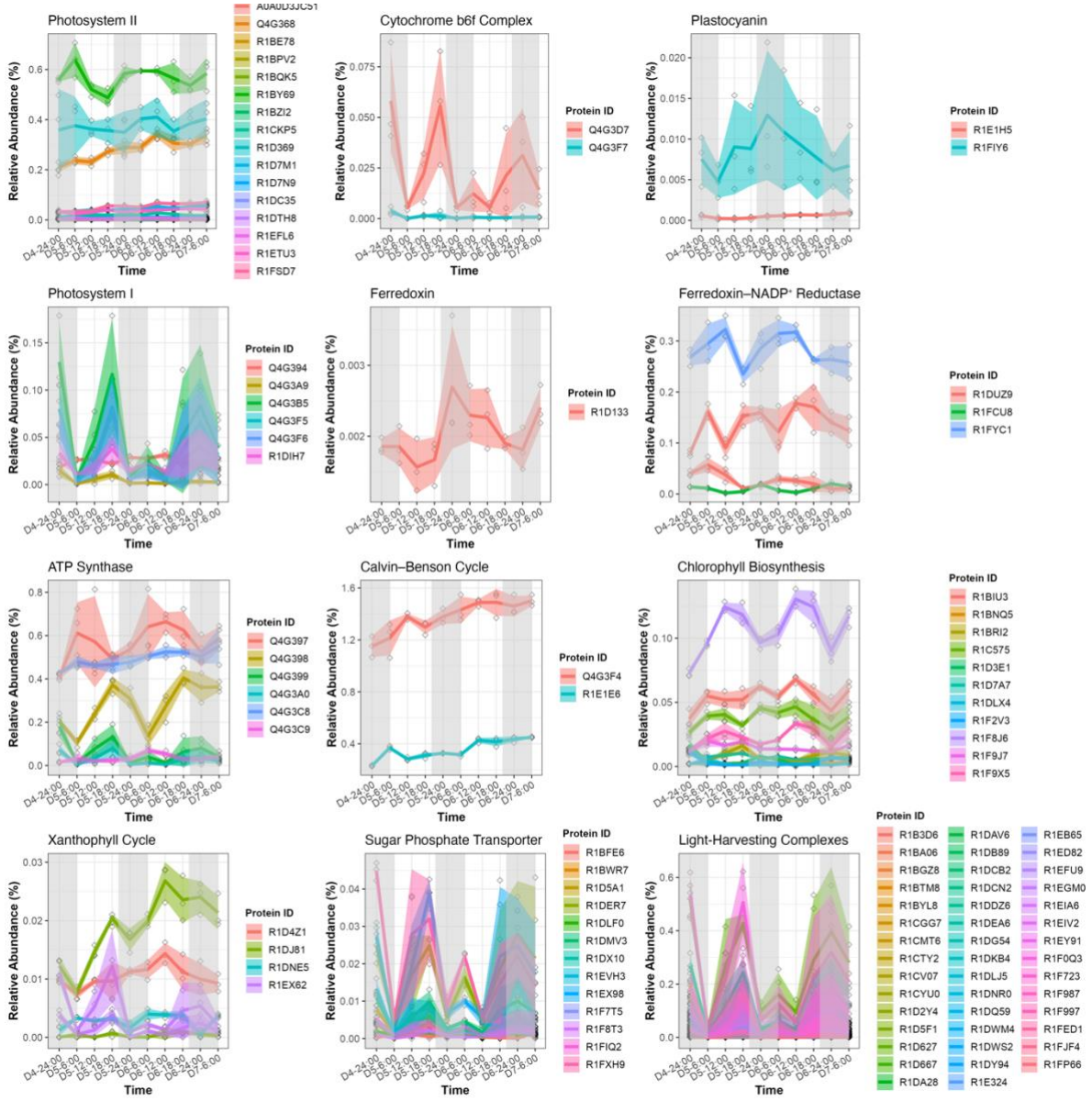

Figure A1. 17: Expression dynamics of proteins involved in photosynthesis, Calvin-Benson cycle and pigment (xanthophyll and chlorophyll) biosynthesis in *Gephyrocapsa huxleyi* across day-night cycles.

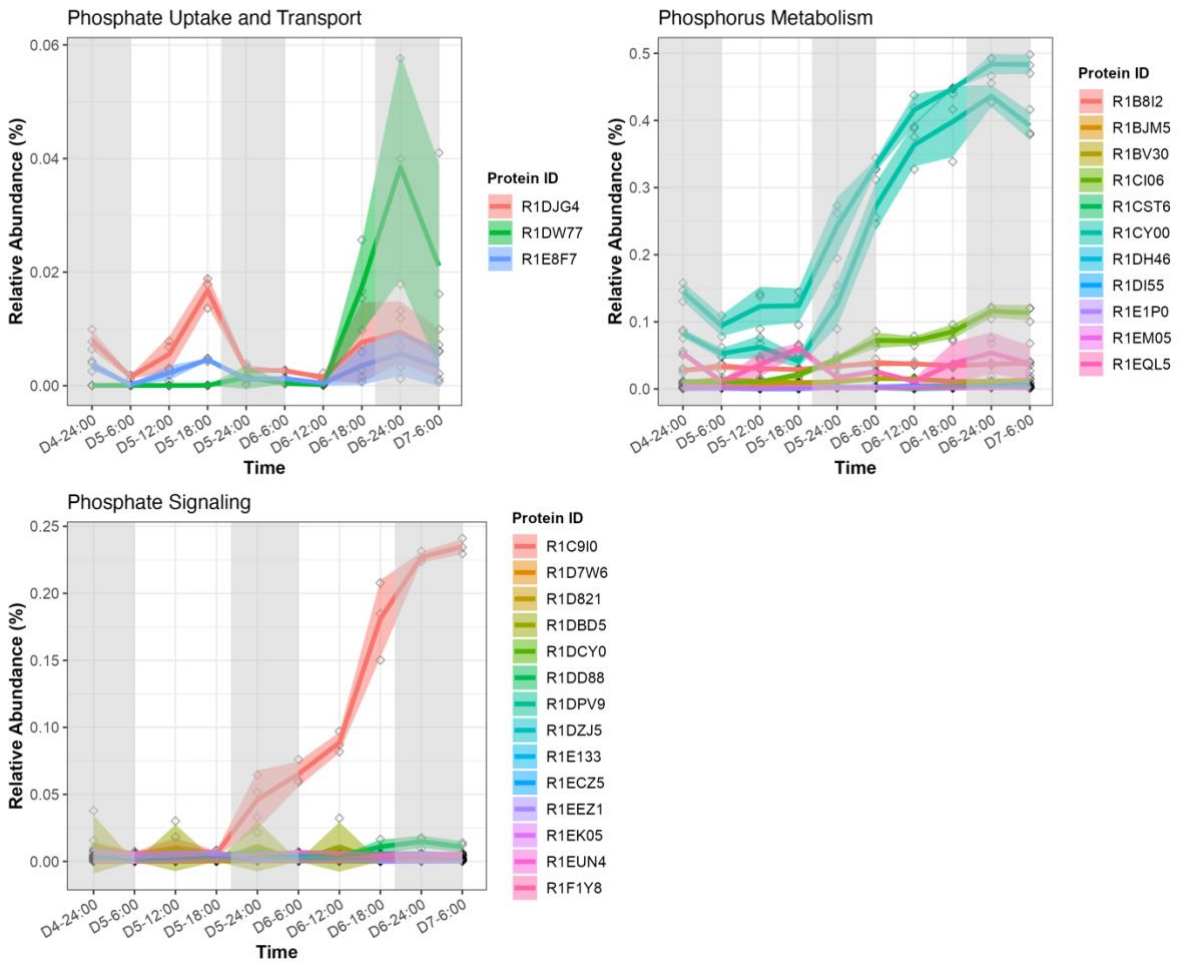

Figure A1. 18: Phosphate- assimilation pathways and protein expression dynamics in *Gephyrocapsa huxleyi* across day-night cycles.

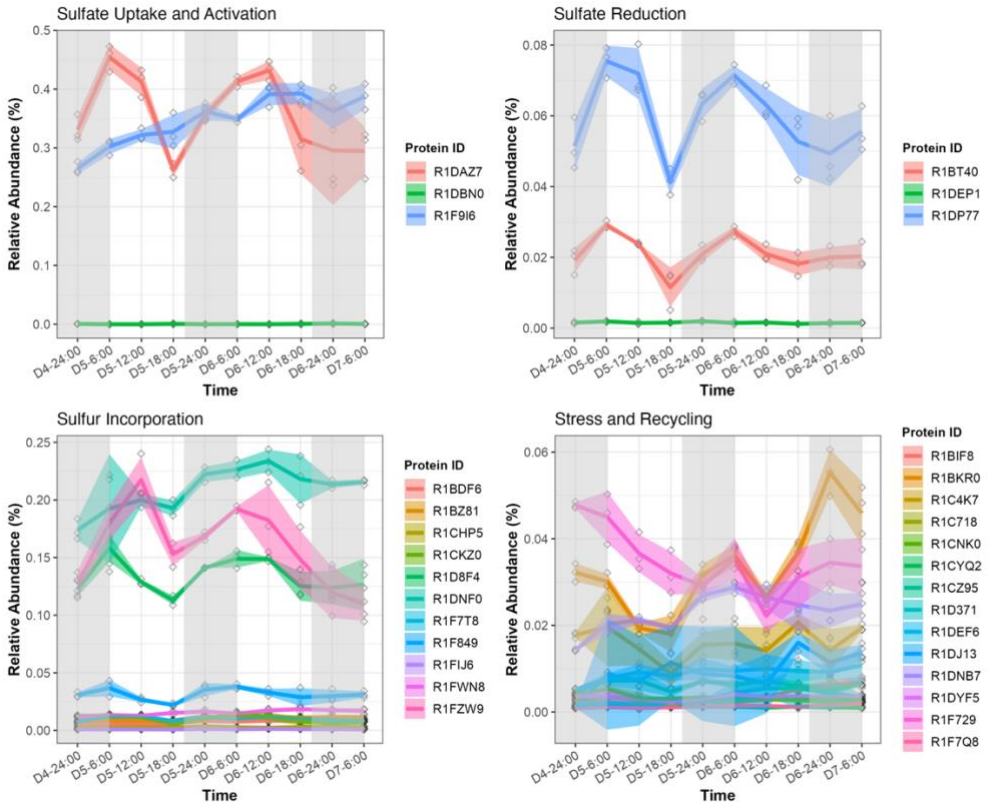

Figure A1. 19: Sulfur- assimilation pathways and protein expression dynamics in *Gephyrocapsa huxleyi* across day-night cycles.

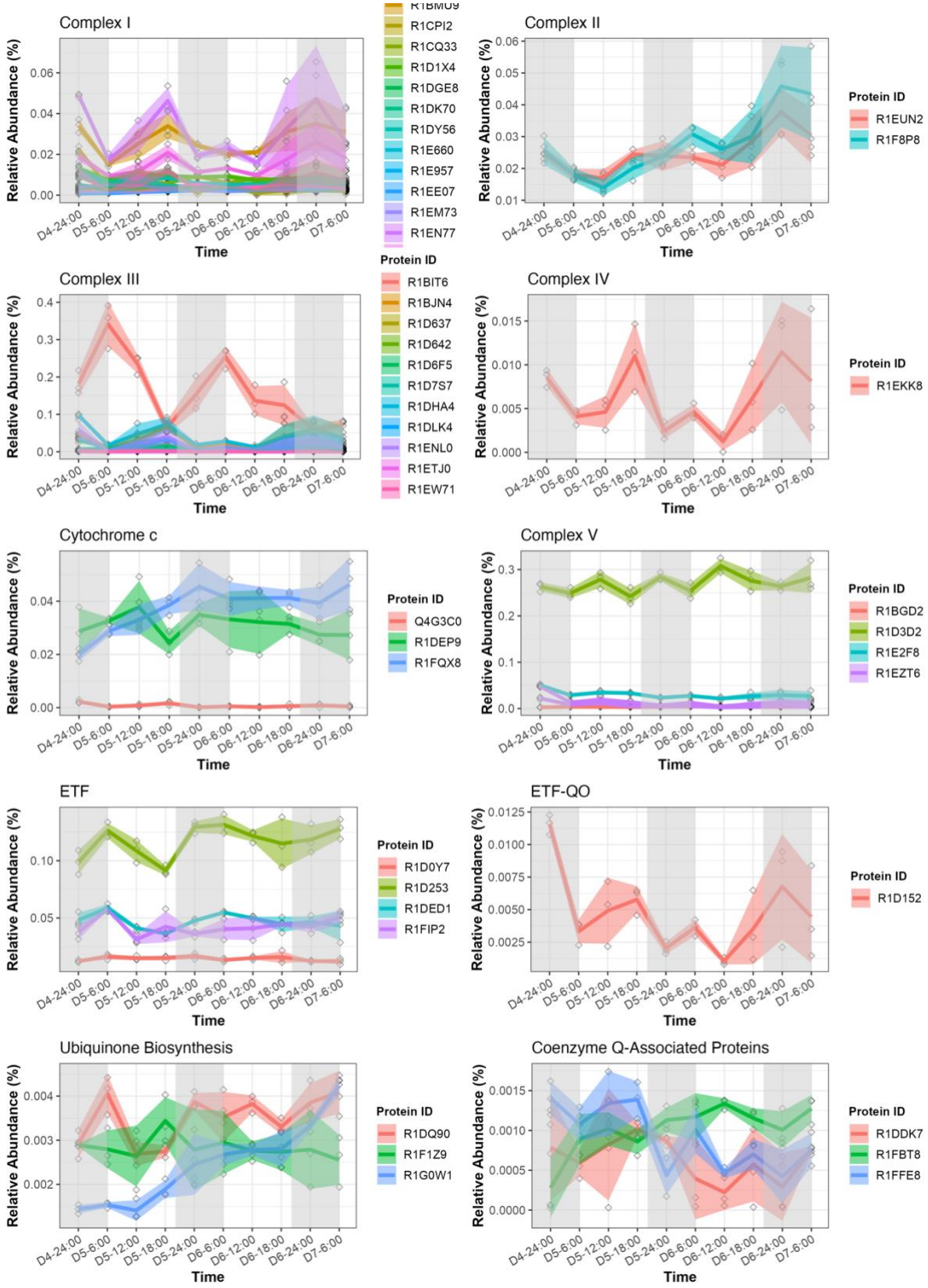

Figure A1. 20: Expression dynamics of proteins involved in the respiratory electron transport chain, ubiquinone biosynthesis, and related systems in *Gephyrocapsa huxleyi* across day-night cycles.

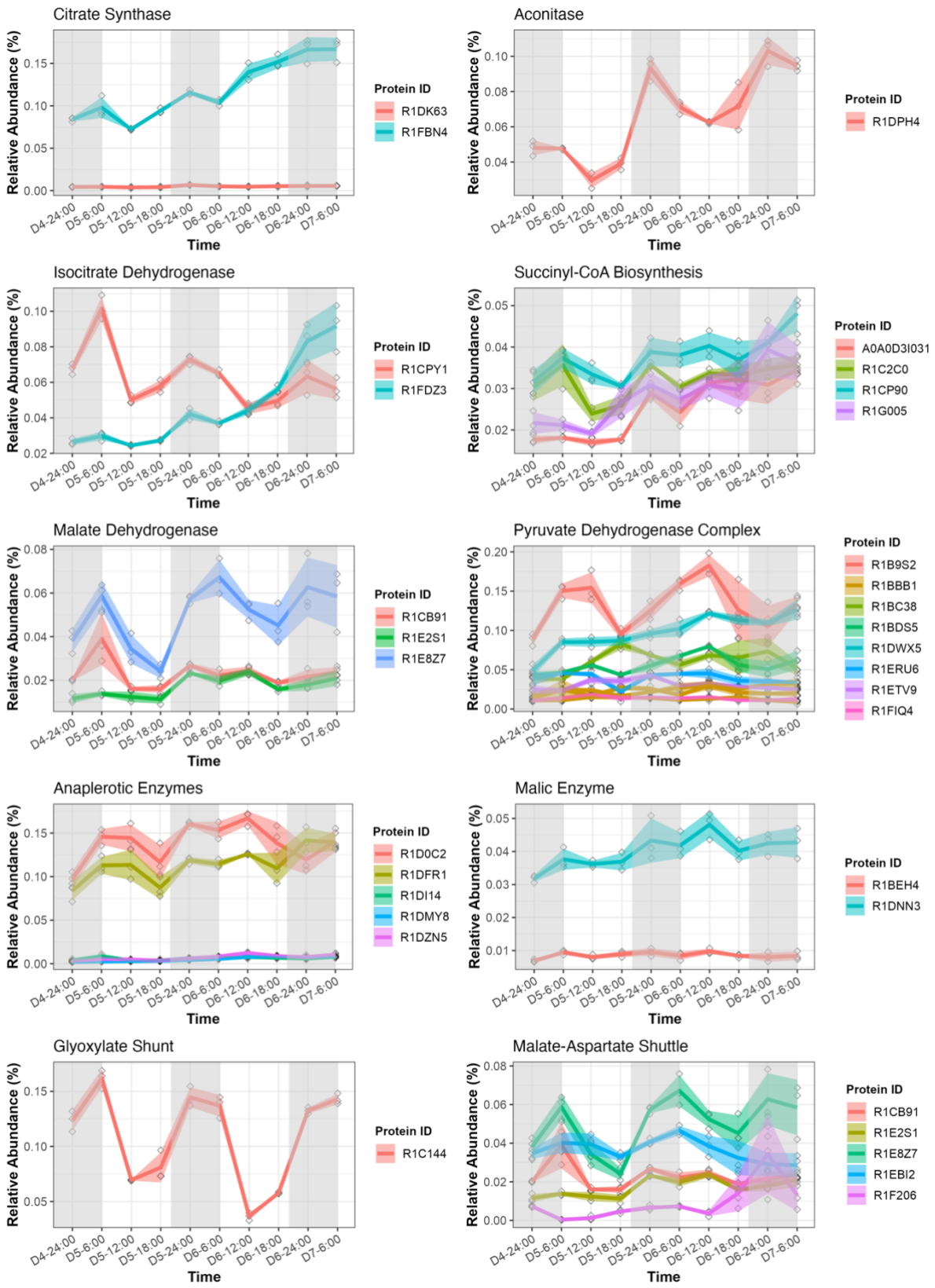

Figure A1. 21: Expression dynamics of proteins involved in the tricarboxylic acid cycle, its bypass pathways, and supplementary metabolite biosynthesis in *Gephyrocapsa huxleyi* across day-night cycles.

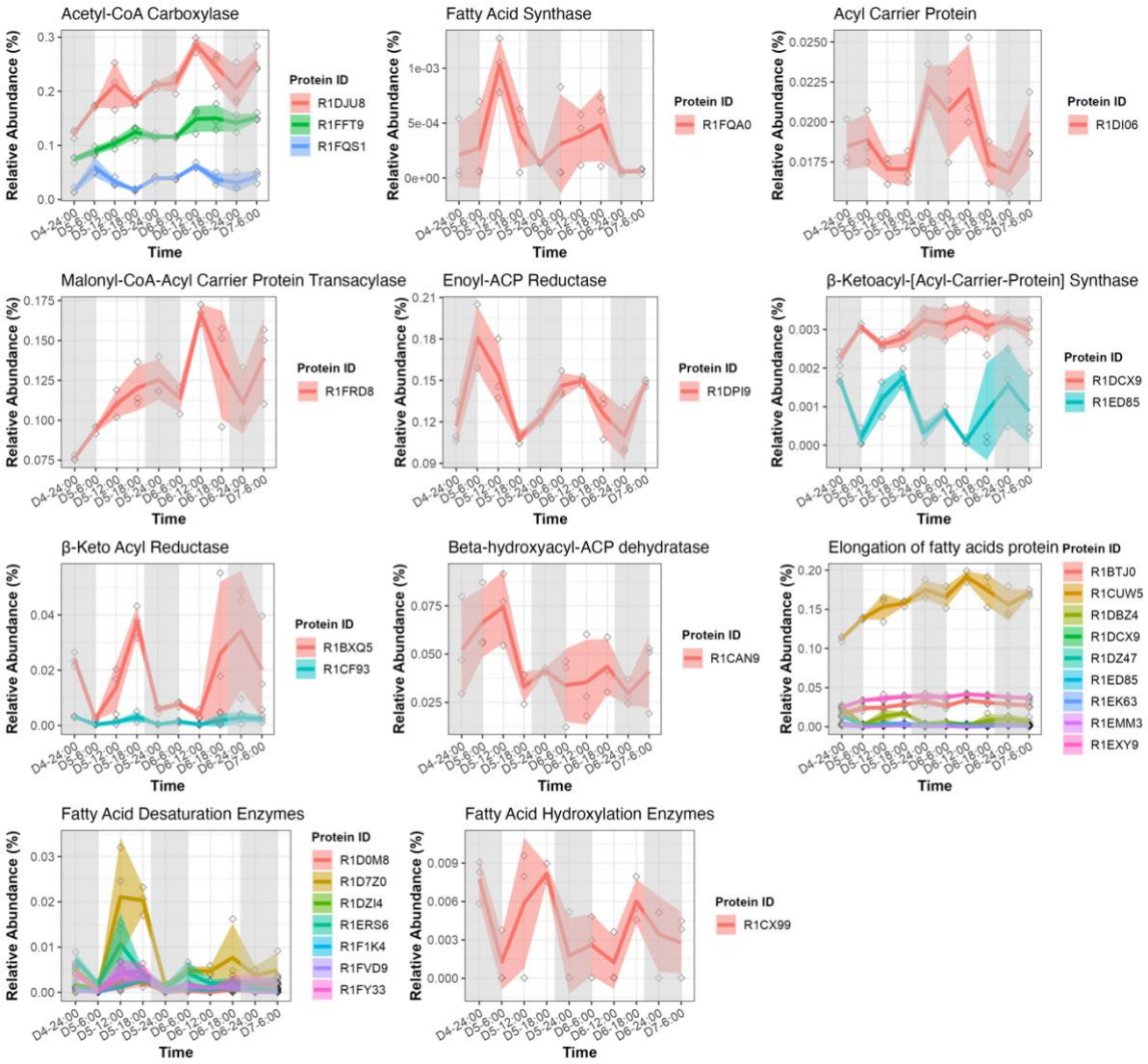

Figure A1. 22: Expression dynamics of proteins involved in the de novo fatty acid biosynthesis and its elongation, desaturation, and hydroxylation in *Gephyrocapsa huxleyi* across day-night cycles.

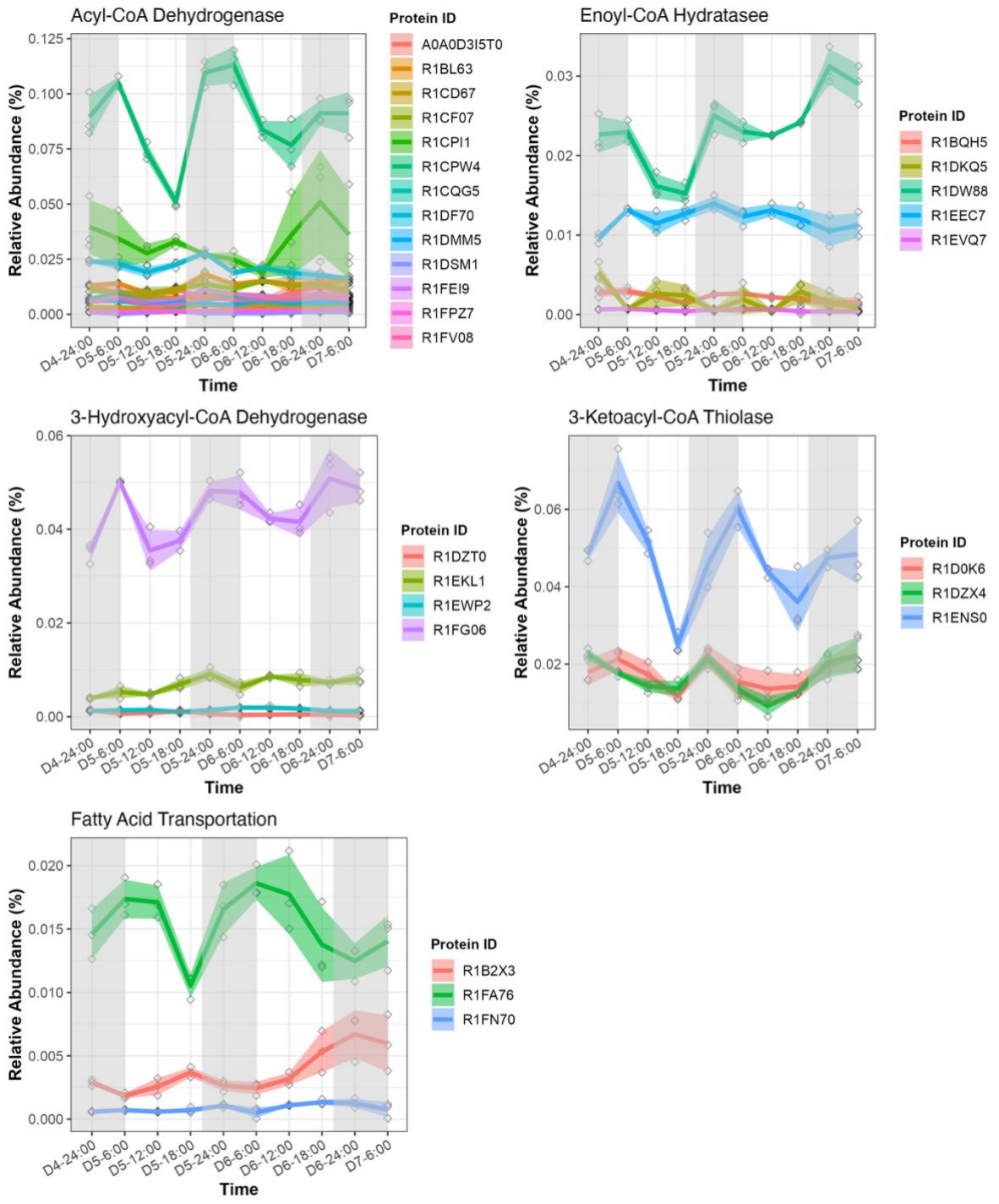

Figure A1. 23: Expression dynamics of proteins involved in β-oxidation in *Gephyrocapsa huxleyi* across day-night cycles.

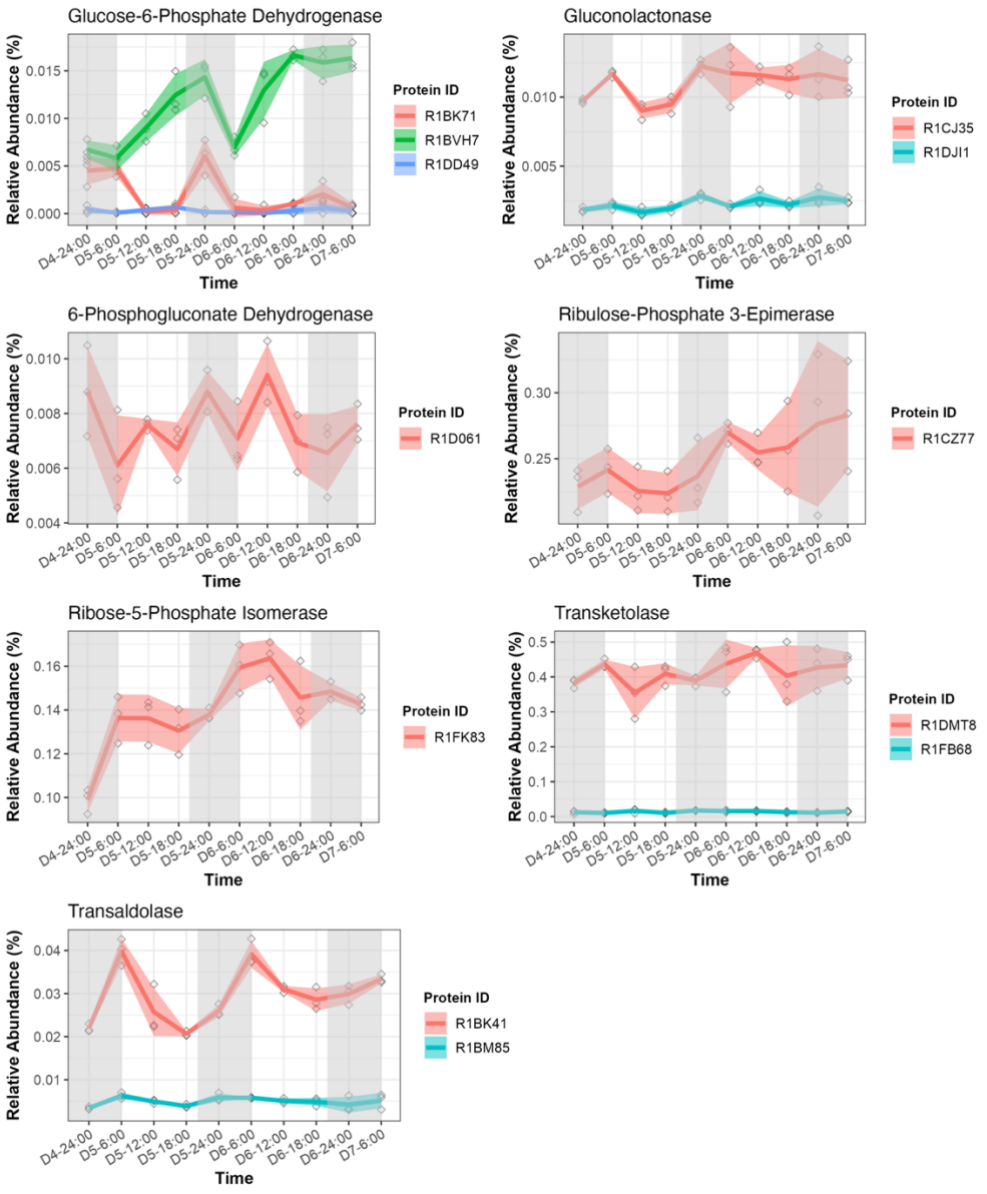

Figure A1. 24: Expression dynamics of proteins involved in pentose phosphate pathway in *Gephyrocapsa huxleyi* across day-night cycles.

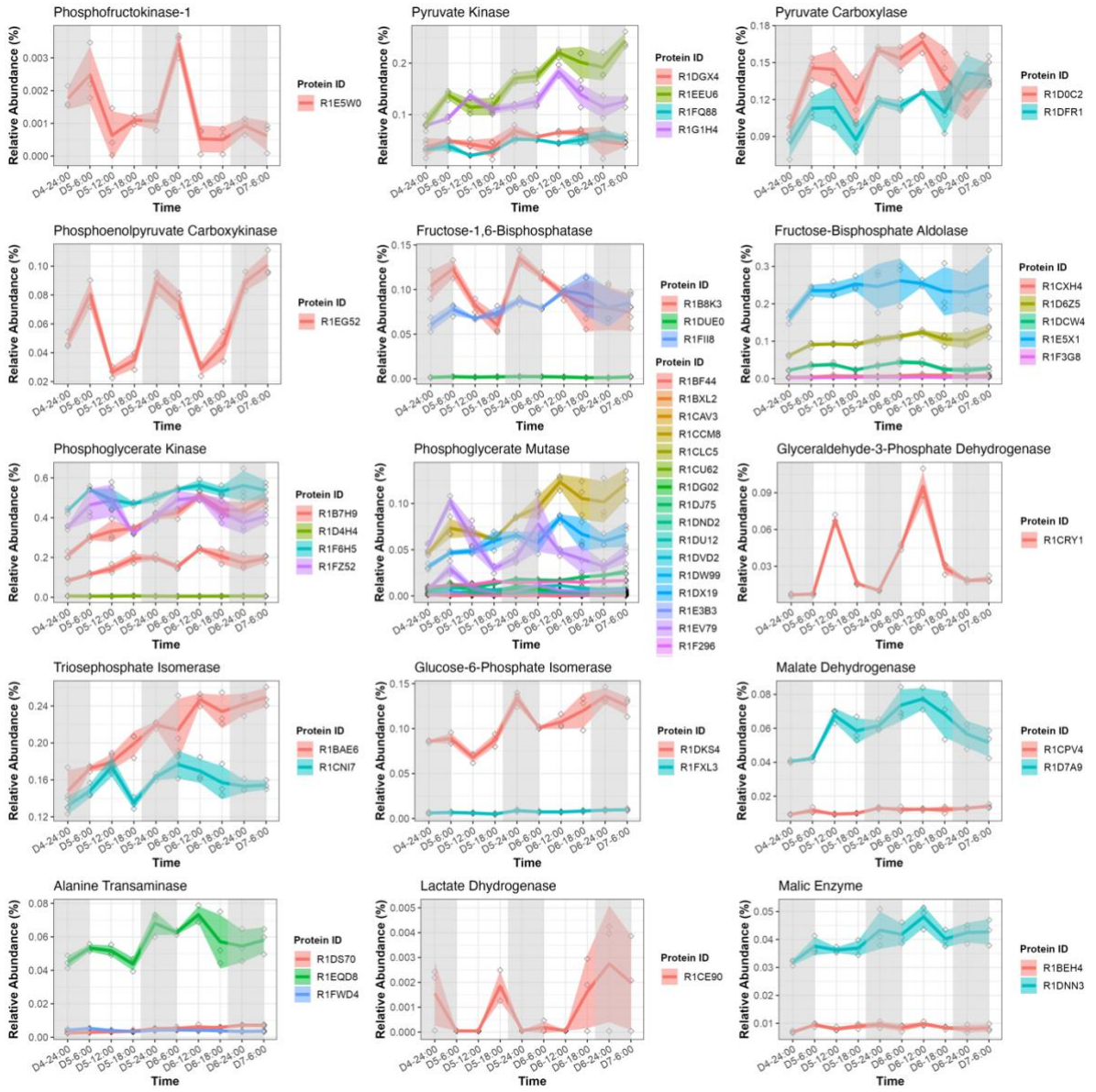

Figure A1. 25: Expression dynamics of proteins involved in glycolysis, gluconeogenesis, and pyruvate metabolism in *Gephyrocapsa huxleyi* across day-night cycles.

Figure A1. 26: Expression dynamics of proteins involved in cell cycle regulation and related chromosomal and mitotic processes in *Gephyrocapsa huxleyi* across day-night cycles.

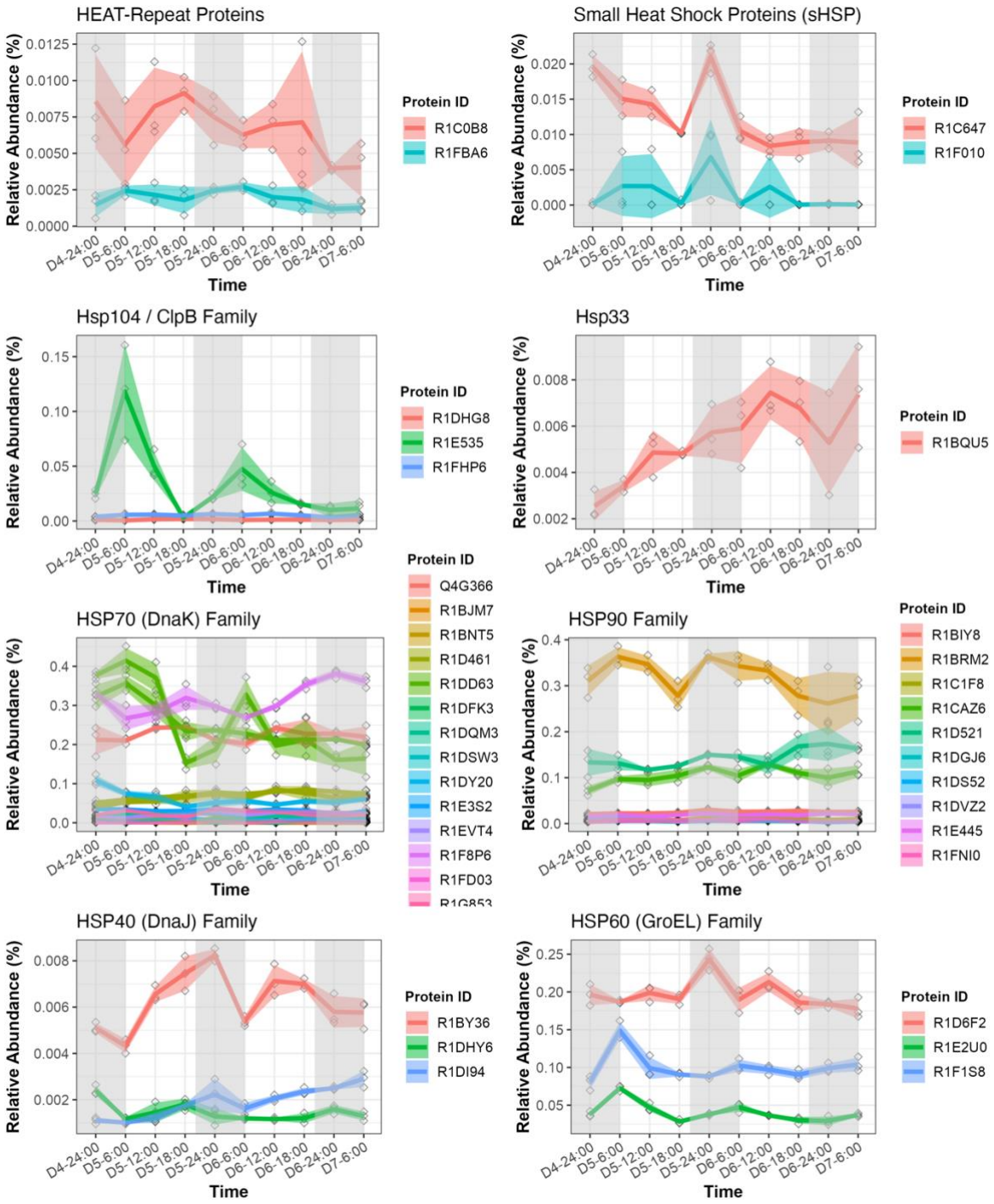

Figure A1. 27: Expression dynamics of heat shock and chaperone proteins in *Gephyrocapsa huxleyi* across day-night cycles.

Appendix 2: Supporting information for Chapter 3

MethodA2. 1 Photosynthetic efficiency (Fv/Fm) measurement

The maximum efficiency of PSII, determined by Fv/Fm, was measured daily from the exponential to stationary phase for three growth curves. Each triplicate sample was dark-adapted for > 1 h before measurement with the Fluorescence Induction and Relaxation system (FIRe, Satlantic). The maximum Fv/Fm value for each condition as selected for performance comparison.

MethodA2. 2 Carbon isotope measurement

Upon reaching the late exponential phase of growth, a 300ml sub-sample from each triplicate culture was collected and centrifuged at 4500 rpm for 20 minutes. The cell pellets were pre-washed with alkaline water (pH ~10) to remove seawater residue. The removal of cellular organic matter was achieved using a mixture of 0.625% (v/v) TritonX-100 and 4.5% NaOCl in 0.05 M $NaHCO_3$. Thorough rinsing was performed to remove any chemical residues. The resuspended pellets were filtered onto polycarbonate filters (0.2 µm), followed by drying on a hotplate, sealing, and storing at room temperature for further isotopic measurement. Clean coccolith powder was weighed and analysed by a Delta V Advantage isotope mass spectrometer fitted with a Gas Bench II in the Department of Earth Sciences at the University of Oxford. Samples were calibrated to PeeDee Belemnite via the international NBS-19 standard. All measurements are expressed relative to the Vienna PeeDee Belemnite standard.

MethodA2. 3 Measuring the short-term metabolic thermal response curves

To improve the signal to noise ratio, all biological replicate samples were concentrated by centrifugation at 500 rpm, 17 °C, for 5 minutes and re-suspended in 5ml of fresh seawater medium. A 10-minute dark adaptation period was applied to the cultures in the incubator at the growth temperature of 17 °C before data collection.

For each experimental treatment measurement, the respective sterile growth medium (with treatment Mg concentrations) was used to obtain 36 measurements of background oxygen deletion, which served to correct the oxygen flux measurements of the biological samples.

The sample was placed in the chamber for an additional 5-minute dark adaptation period with the stirrer on to maintain balanced O_2 concentration. Respiration was measured as oxygen consumption in the dark for 5-minute period directly after dark adaptation, and again for a 5-minuate period after the photosynthesis light response measurement. The light intensity for the following photosynthesis light response measurement after the initial 5-minute dark respiration measurement was set to 45 µmol m^{-2} s^{-1} and 75 µmol m^{-2} s^{-1} for 10 minutes each, covering the light intensity range in the incubator.

This was followed by 150 µmol m^{-2} s^{-1}, 300 µmol m^{-2} s^{-1}, 600 µmol m^{-2} s^{-1} and 1200 µmol m^{-2} s^{-1} with a 3-minute interval. This range of light intensities was chosen to characterise the algal photosynthesis response across different conditions and identify the light saturation point. The rates of net photosynthesis and respiration were calculated using the slope of the linear model between O_2 concentration and time.

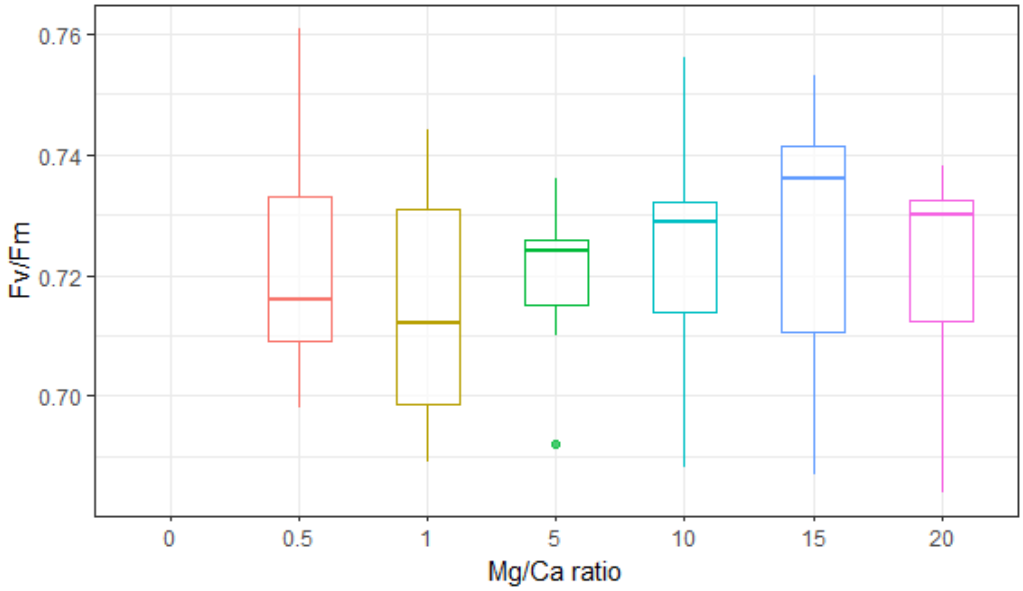

Figure A2. 1: Fv/Fm measurements of *Gephyrocapsa huxleyi* under different Mg/Ca ratios.

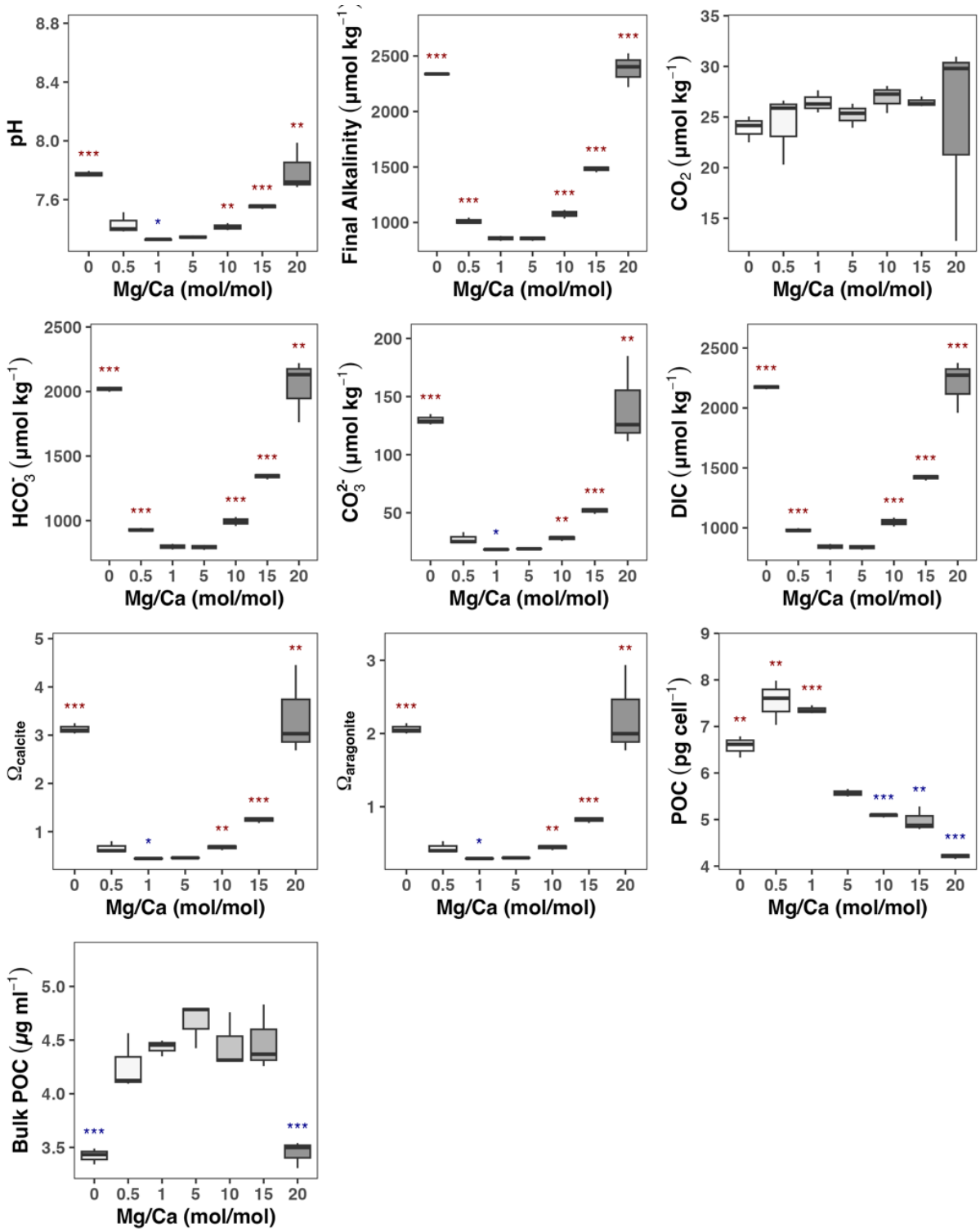

Figure A2. 2: Final carbonate species composition in medium after *Gephyrocapsa huxleyi* reached stationary phase under different seawater Mg/Ca ratios, alongside calculated cellular particulate organic carbon (POC) concentration and POC yield.

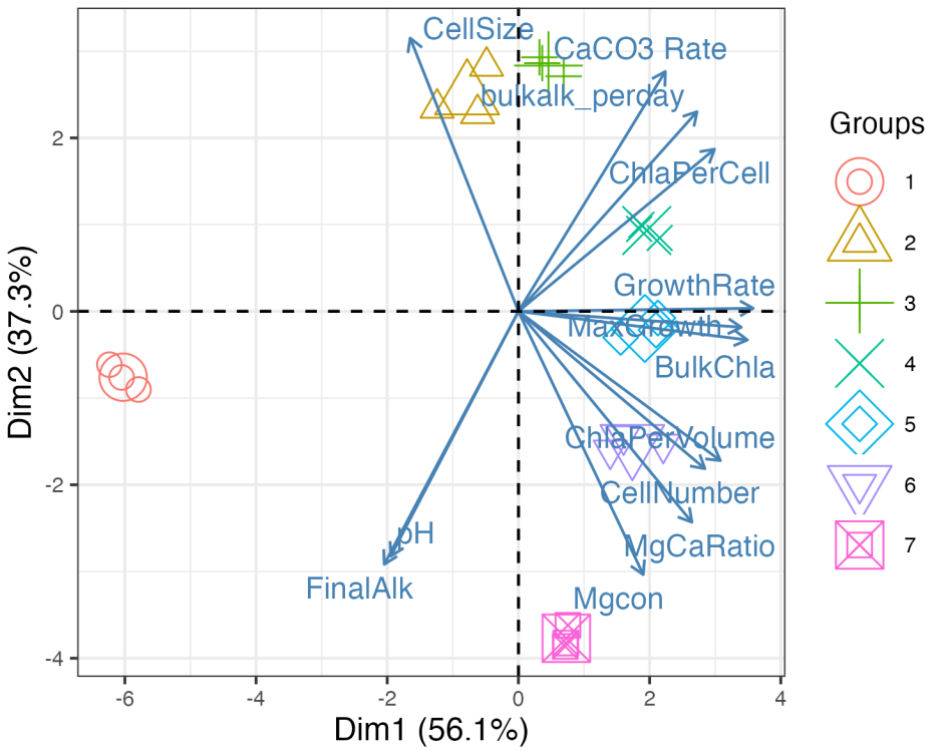

Figure A2. 3: Principal component analysis of physiological traits across Mg treatments for all the physiological parameters collected.

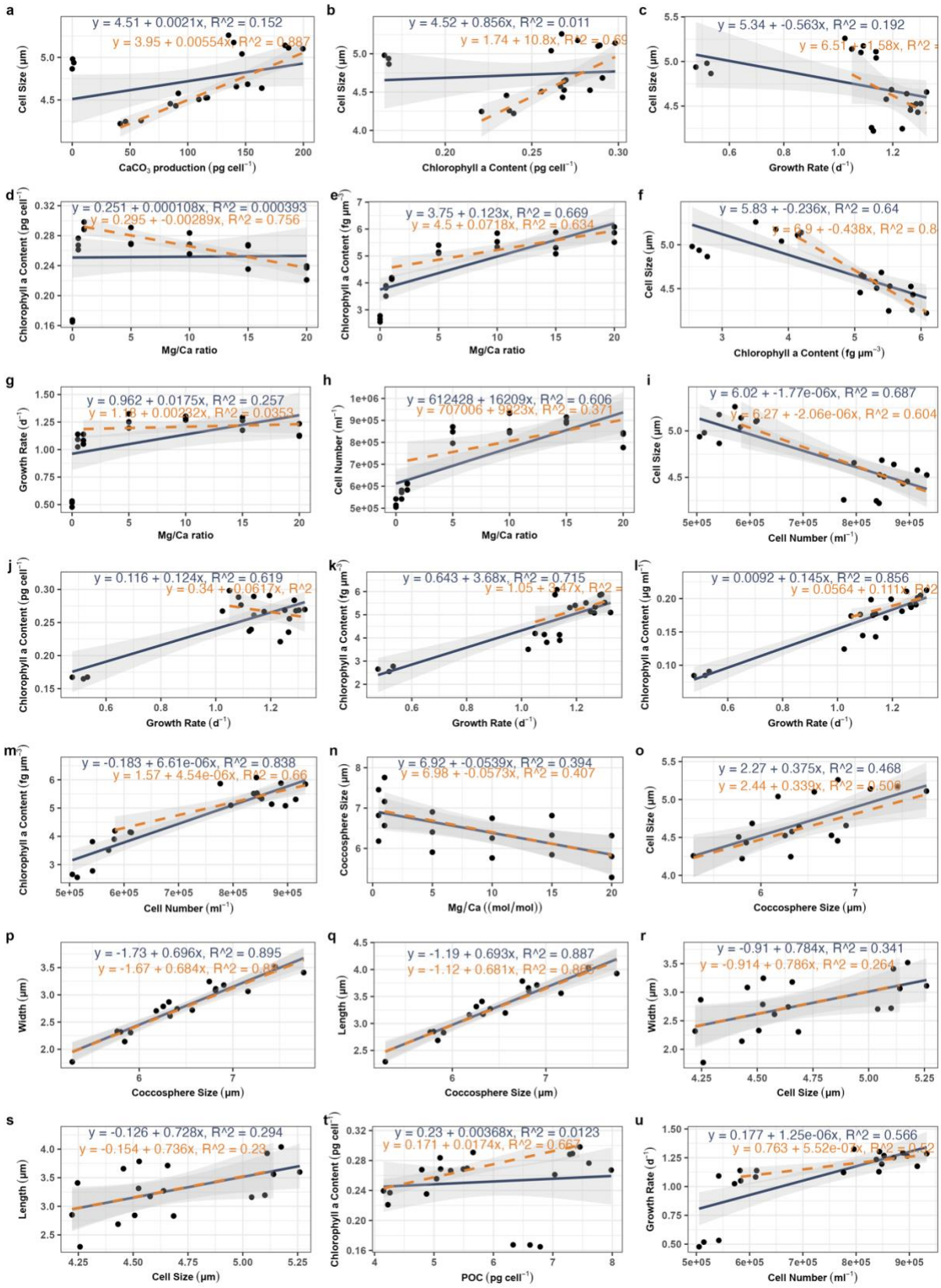

Figure A2. 4: Linear relationship between seawater Mg availability and physiological traits in *Gephyrocapsa huxleyi*.

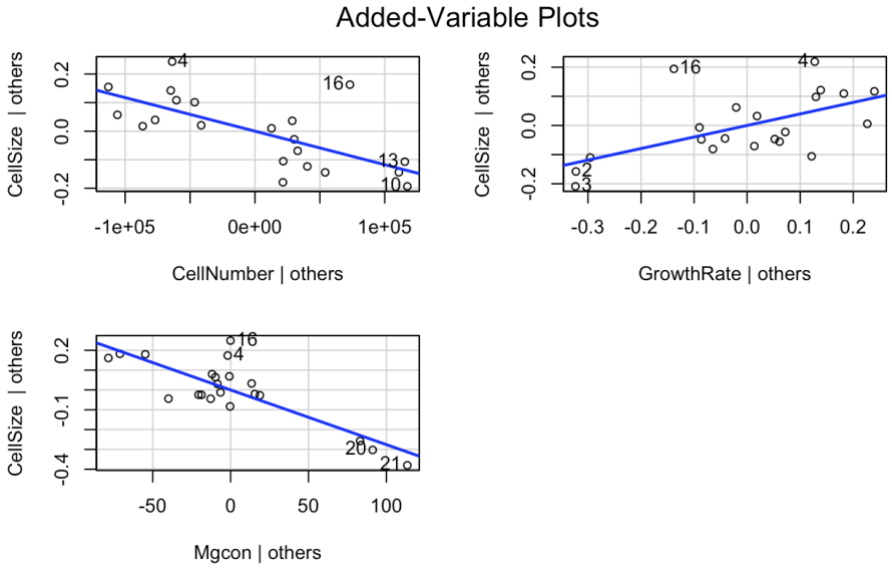

Figure A2. 5: The added-variable plot for the multiple linear regression model identifies the interrelationship between cell density, Mg concentration, and growth rate on cell size in *Gephyrocapsa huxleyi*.

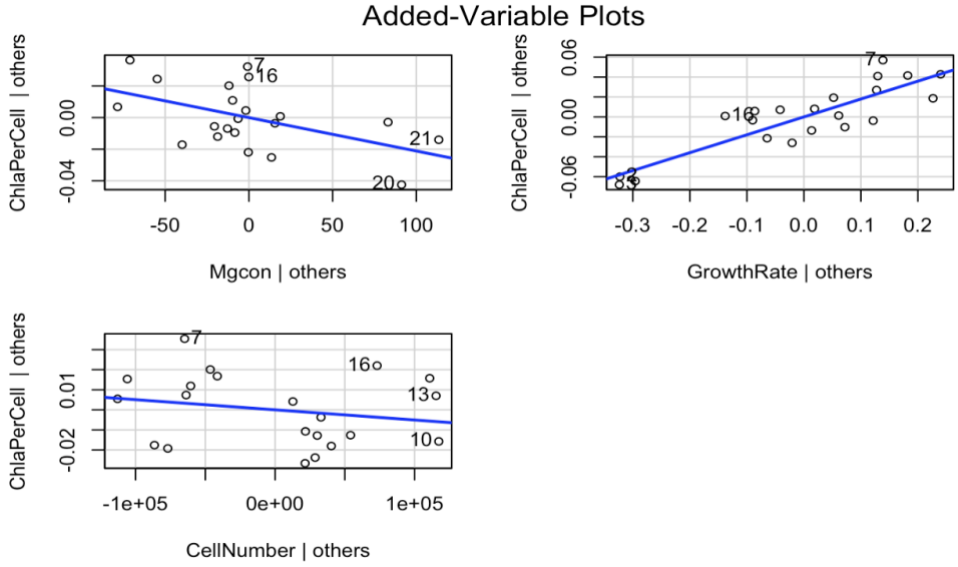

Figure A2. 6: The added-variable plot for the multiple linear regression model identifies the interrelationship between cell density, Mg concentration, and growth rate on cellular chlorophyll-a content in *Gephyrocapsa huxleyi*.

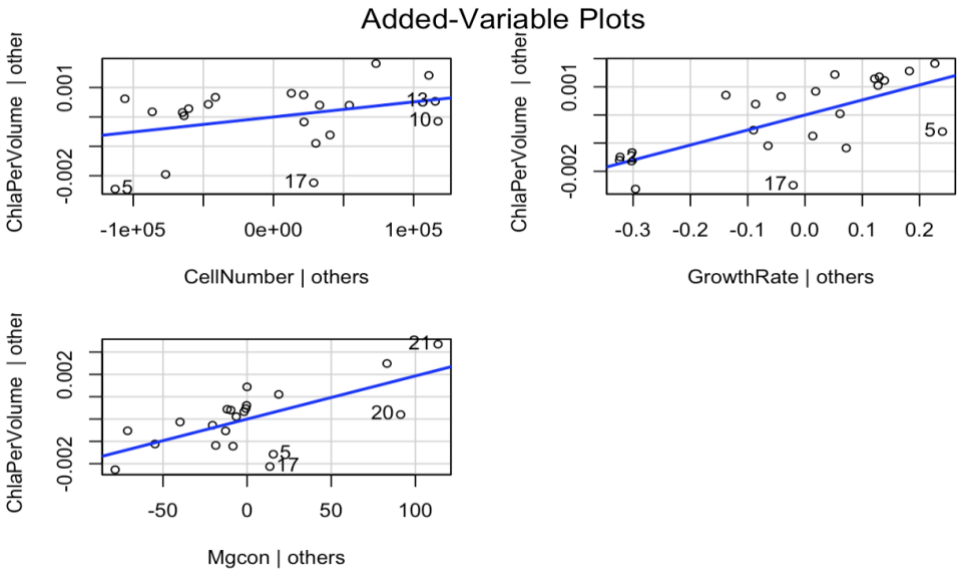

Figure A2. 7: The added-variable plot for the multiple linear regression model identifies the interrelationship between cell density, Mg concentration, and growth rate on chlorophyll-a content per unit volume in *Gephyrocapsa huxleyi*.

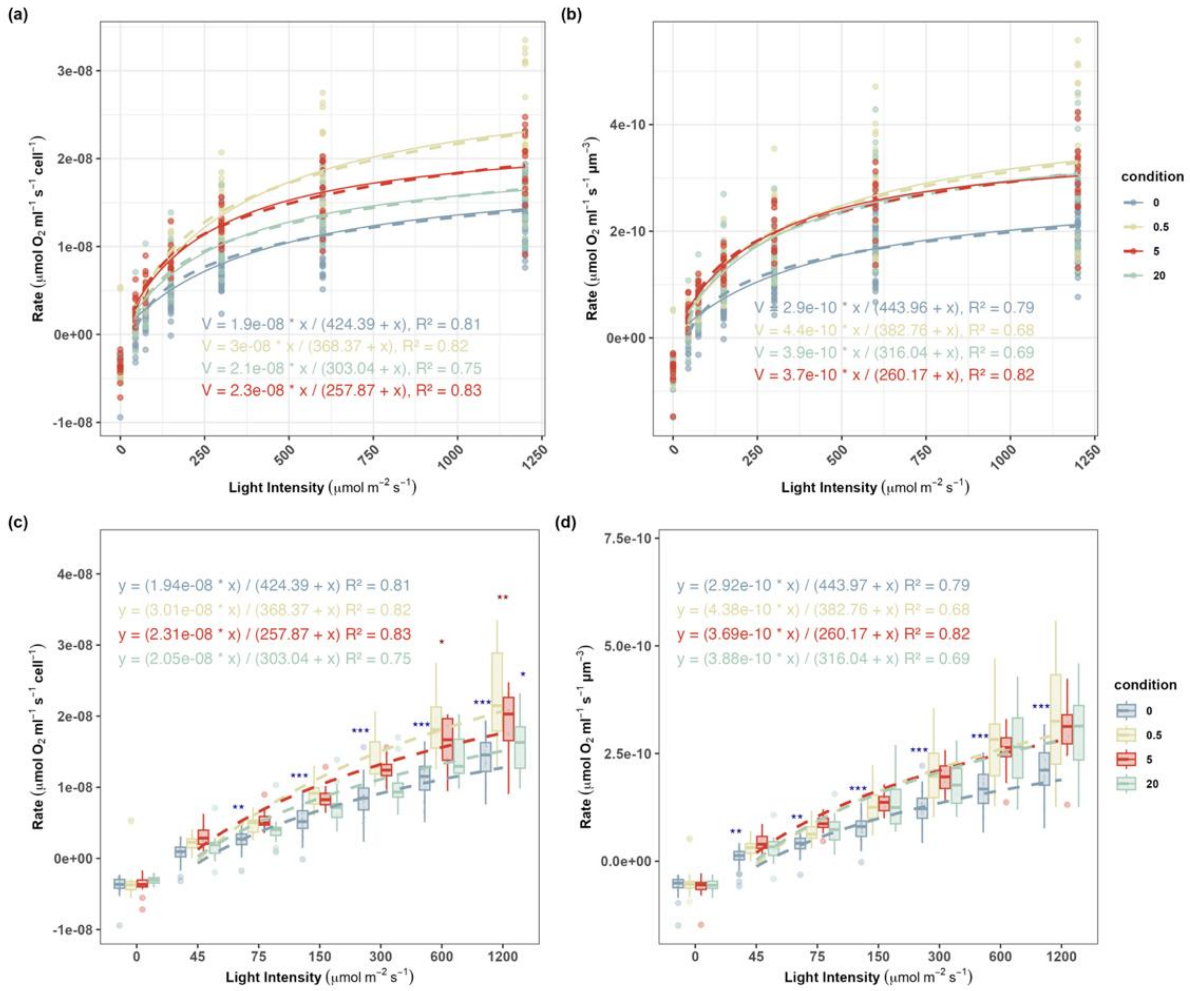

Figure A2. 8: Photosynthetic light-response curves of *Gephyrocapsa huxleyi* under varying magnesium conditions: Mg-0, Mg-0.5, Mg-5 and Mg-20. (a) cellular metabolic rate; (b) Metabolite rate per unit cell volume. Rates at 0 µmol photons m^{-2} s^{-1} represent respiration, while rates from 45 to 1200 µmol photons m^{-2} s^{-1} represent net photosynthesis. Saturation points and equations are derived from Michaelis- Menten model with trendlines showing a linear fit. Asterisks indicate significant differences from control (red indicates higher values, blue indicates lower values; the number of asterisks corresponds to the significance level, with 'ns' denoting non-significant differences).

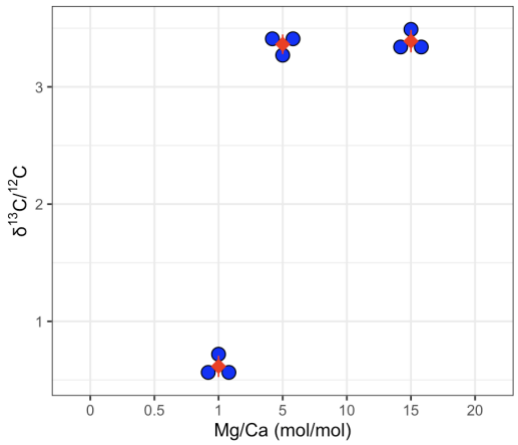

Figure A2. 9: Coccolith carbon isotope ratios in different seawater Mg/Ca ratios.

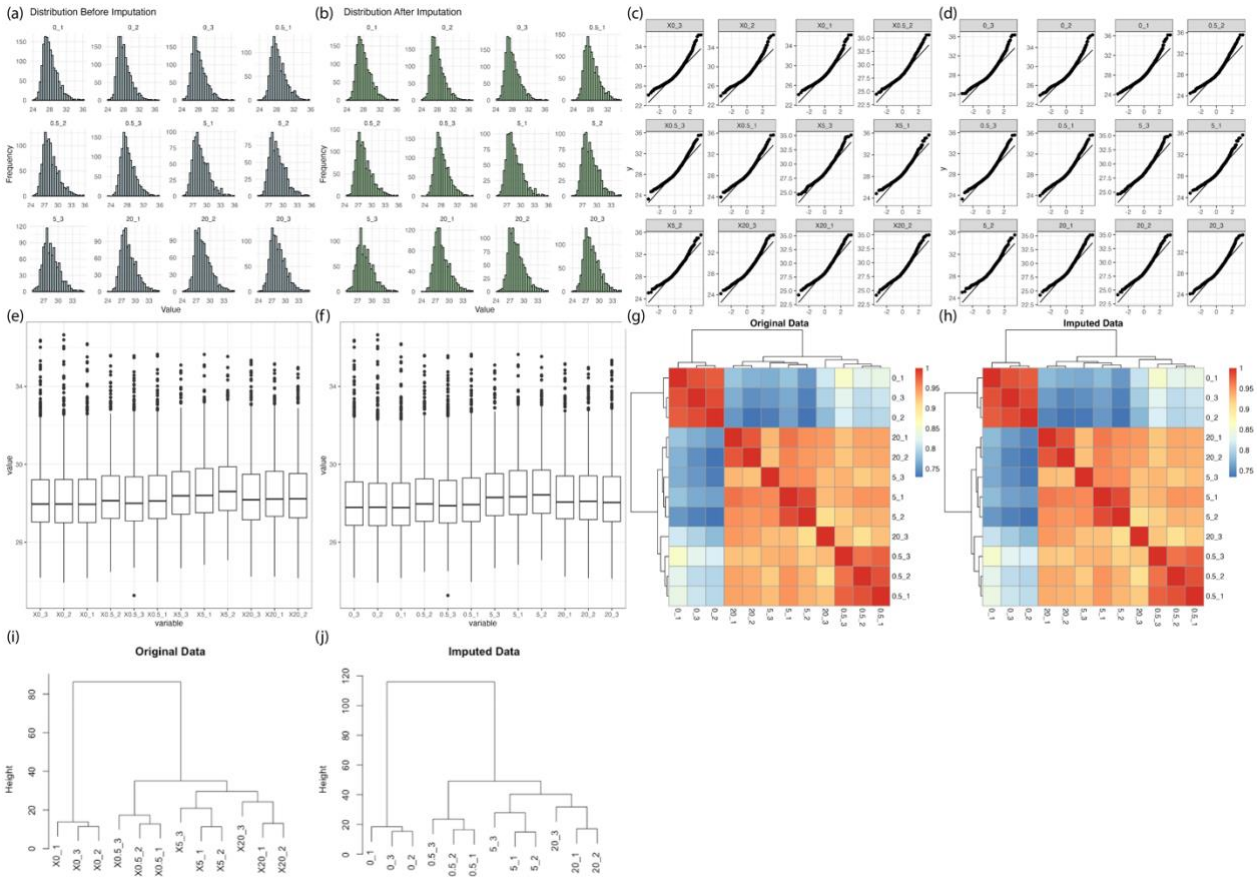

Figure A2. 10: Comprehensive quality control of proteomics data comparing raw (left panels) and imputed (right panels) datasets for *Gephyrocapsa huxleyi* under different Mg/Ca ratios. shown are: (a-b) distribution plots, (c-d) quantile-quantile (Q-Q) plots, (e-f) box plots, (g-h) correlation heatmaps, and (i-j) hierarchical clustering dendrograms.

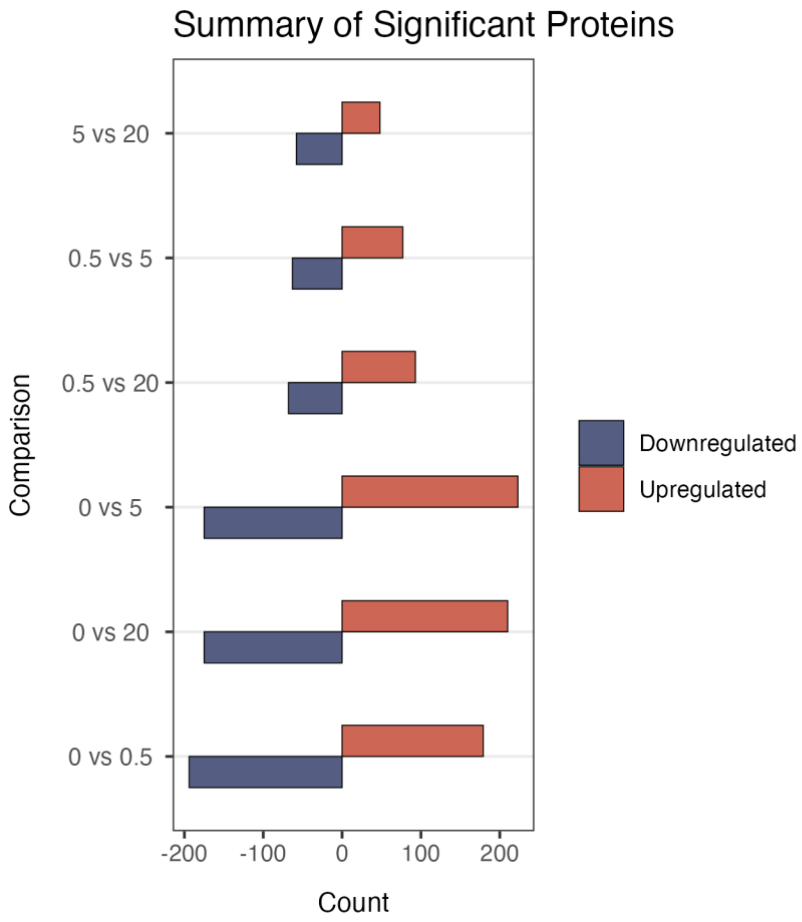

Figure A2. 11: Total number of upregulated and downregulated proteins identified between each treatment condition.

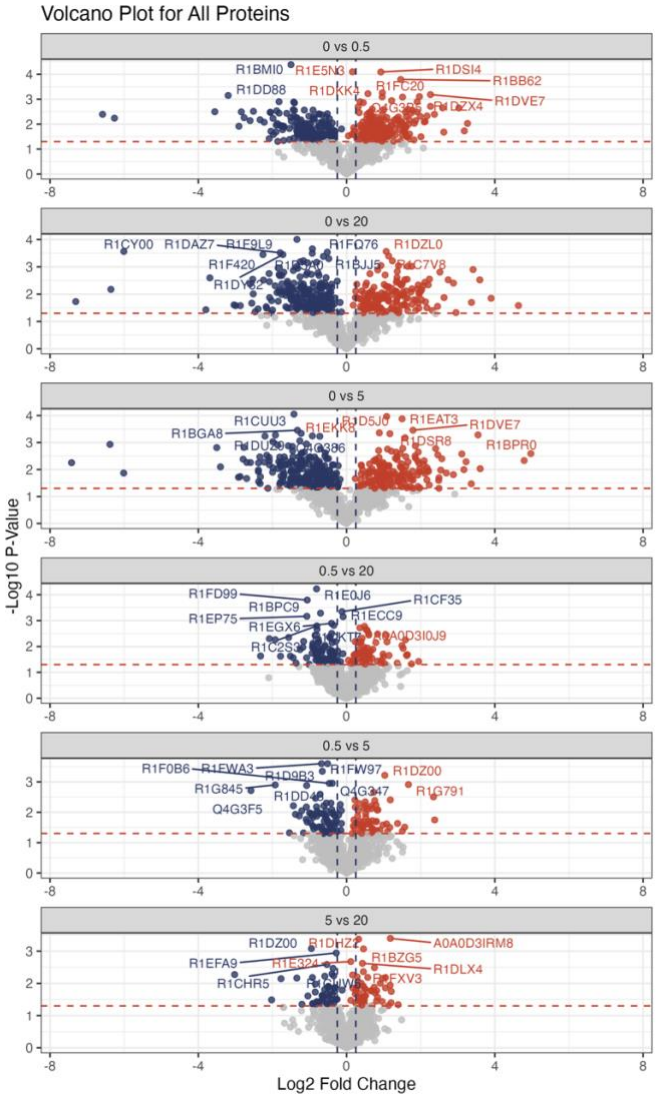

Figure A2. 12: Volcano plot of differentially expressed proteins between conditions. Red points indicate upregulated proteins, and blue points indicate downregulated proteins relative to the control (Mg-5).

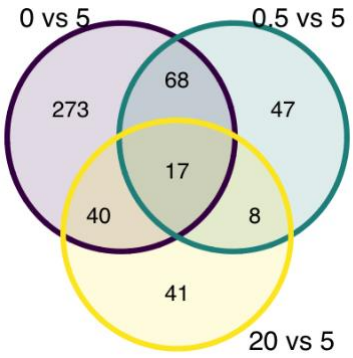

Figure A2. 13: Venn diagram showing significantly expressed proteins in *Gephyrocapsa huxleyi* under varying Mg availabilities compared to the control (Mg-5).

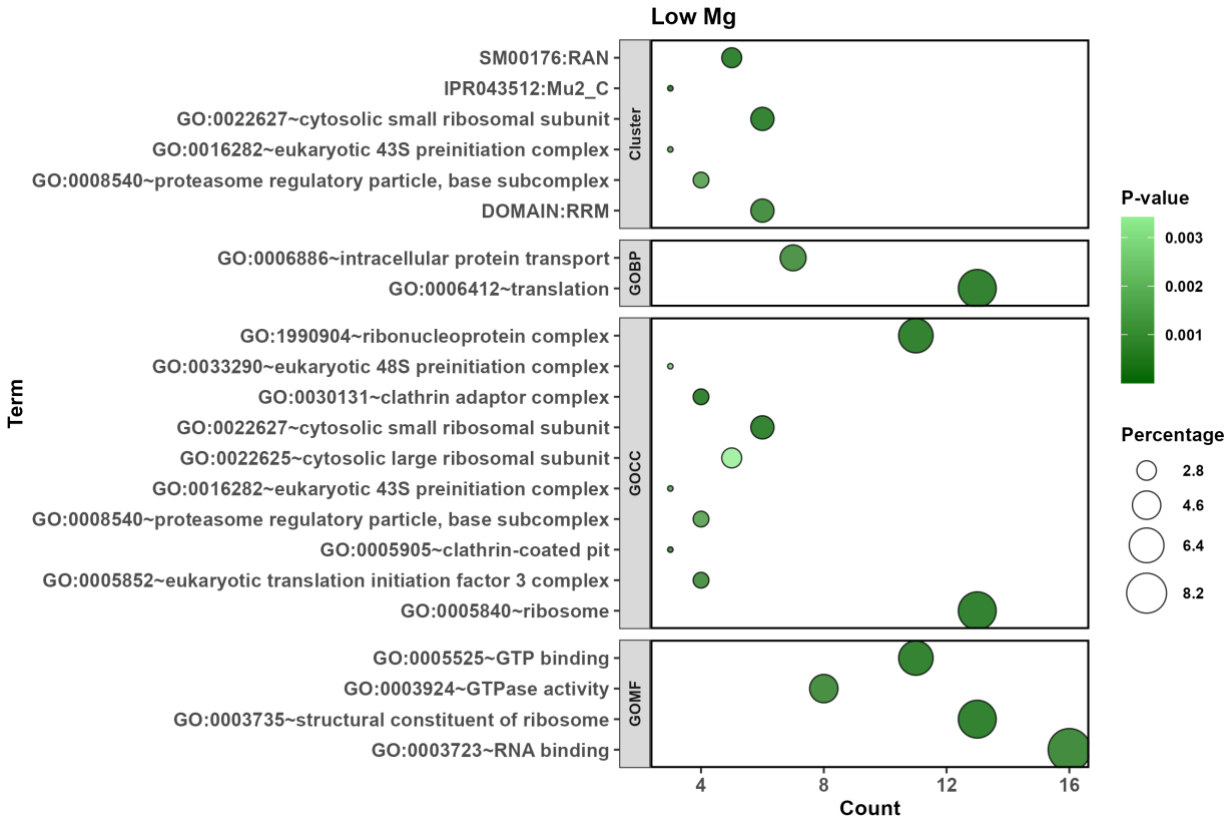

Figure A2. 14: Protein functional group enrichment in *Gephyrocapsa huxleyi* under Mg-0 and Mg-0.5 conditions. The y-axis shows functional group names, while the x-axis represents the count of proteins in each group. Colour indicates the p-value of enrichment, and point size represents the proportion of identified proteins associated with each functional group.

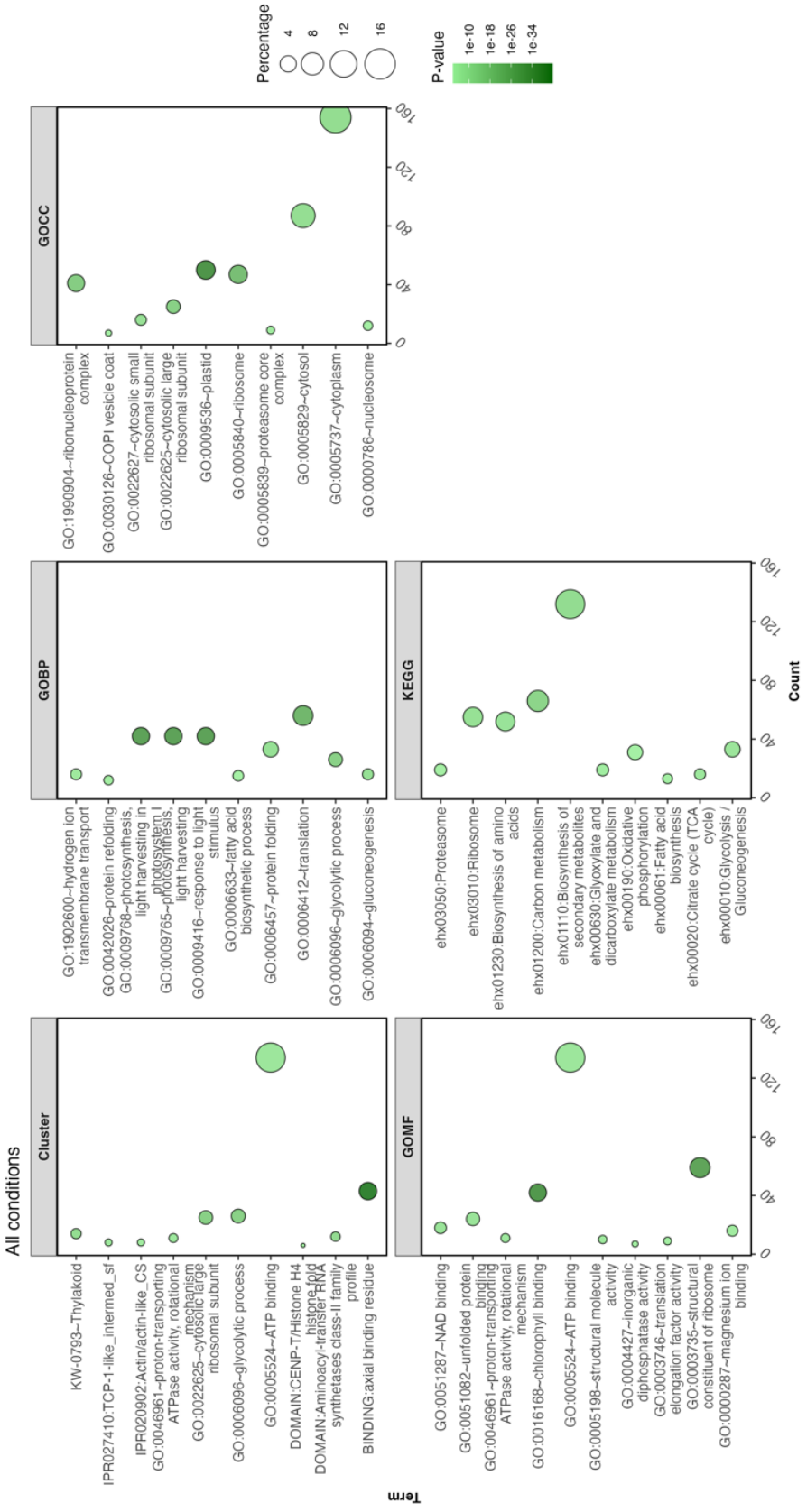

Figure A2. 15: Protein functional group enrichment in *Gephyrocapsa huxleyi* detected across all conditions. The y-axis shows functional group names, while the x-axis represents the count of proteins in each group. Colour indicates p-value, and point size represents the percentage of identified proteins in each functional group.

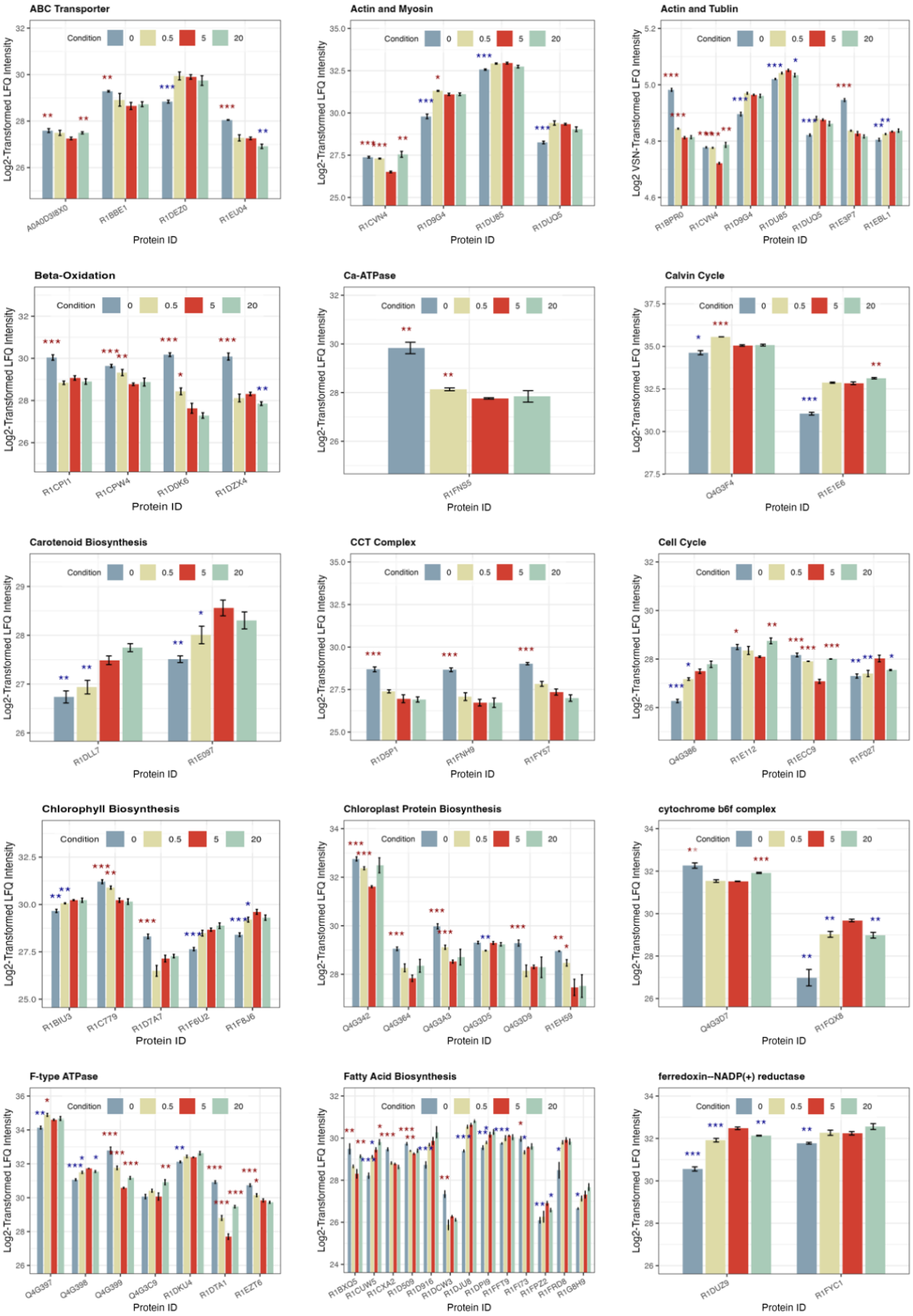
ABC Transporter
Actin and Myosin
Actin and Tublin
Beta-Oxidation
Ca-ATPase
Calvin Cycle
Carotenoid Biosynthesis
CCT Complex
Cell Cycle
Chlorophyll Biosynthesis
Chloroplast Protein Biosynthesis
cytochrome b6f complex
F-type ATPase
Fatty Acid Biosynthesis
ferredoxin--NADP(+) reductase
Condition 0 0.5 5 20
Log2-Transformed LFQ Intensity
Log2 VSN-Transformed LFQ Intensity
Protein ID

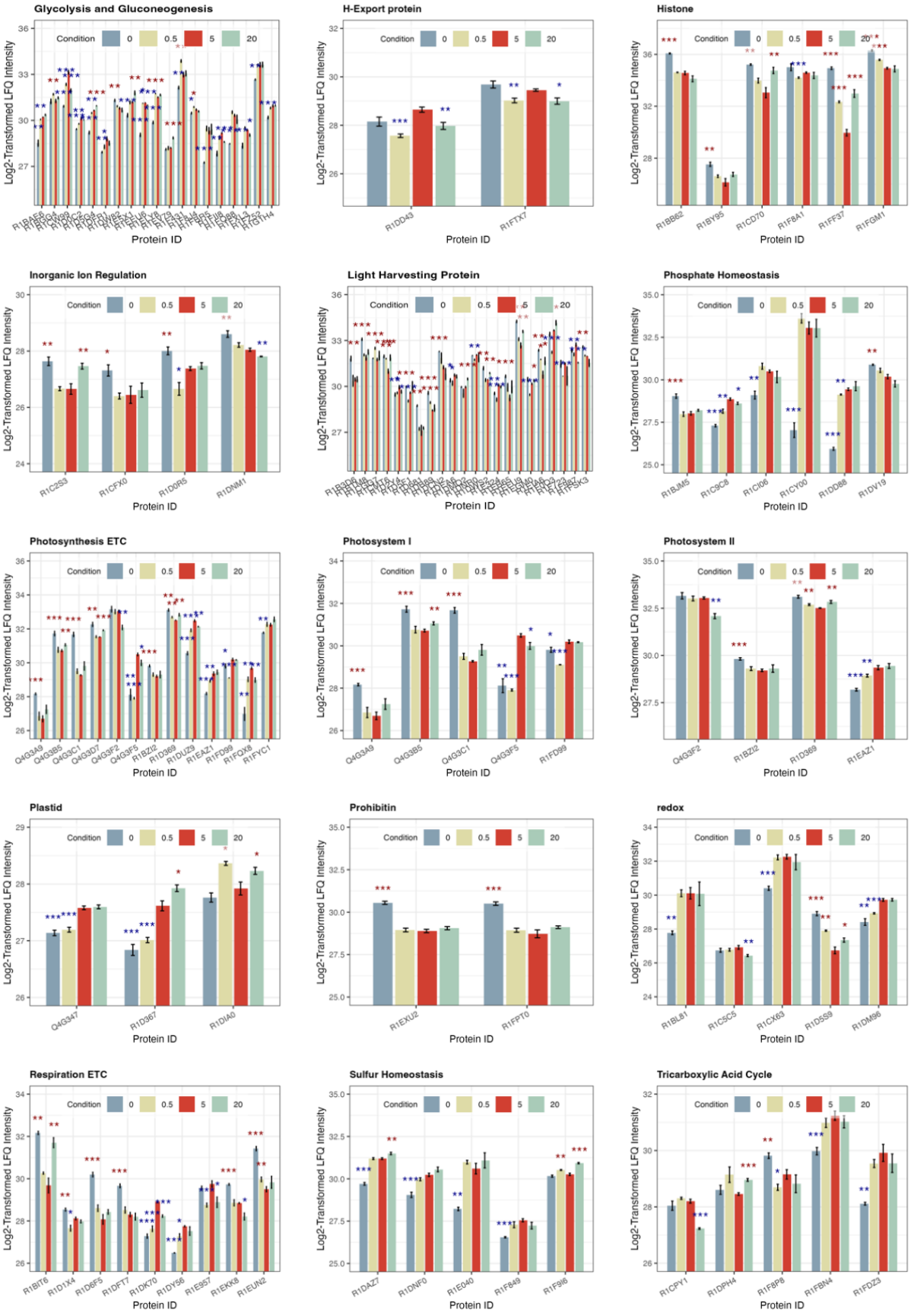
Glycolysis and Gluconeogenesis
H-Export protein
Histone
Inorganic Ion Regulation
Light Harvesting Protein
Phosphate Homeostasis
Photosynthesis ETC
Photosystem I
Photosystem II
Plastidin
Prohibitin
redox
Respiration ETC
Sulfur Homeostasis
Tricarboxylic Acid Cycle
Condition 0 0.5 5 20
Log2-Transformed LFQ Intensity
Protein ID

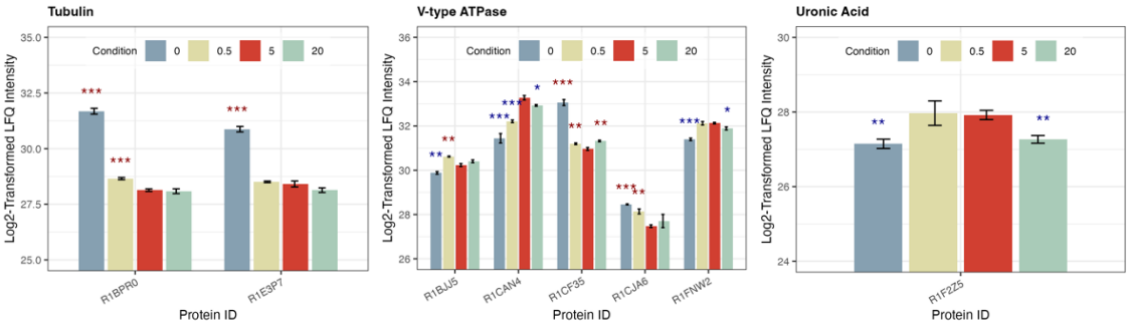

Figure A2. 16: Log2-transformed protein intensities for proteins associated with specific metabolic pathways. Asterisks indicate statistical significance based on t-tests (red: upregulated, blue: downregulated), with the number of asterisks corresponding to the significance level.

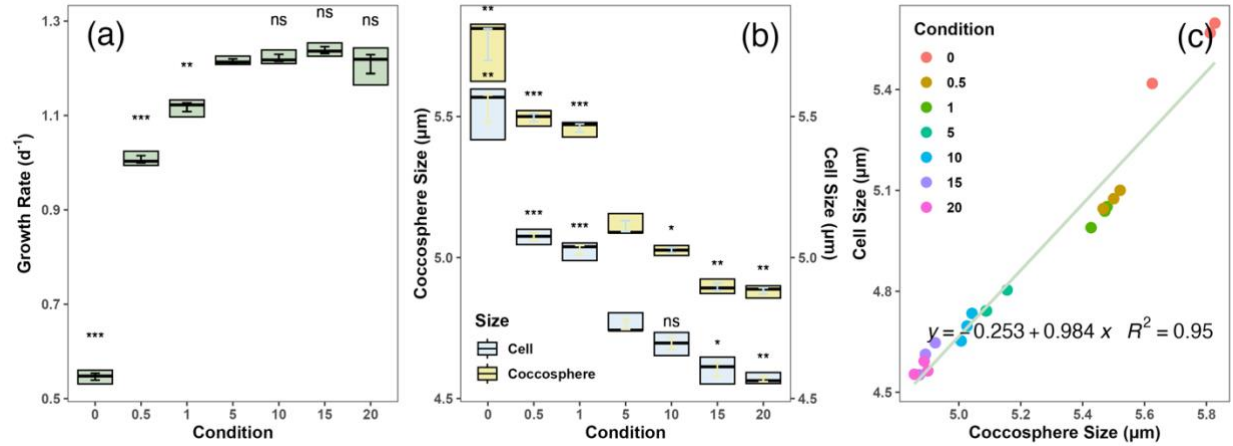

Figure A2. 17: Physiological responses of *Gephyrocapsa huxleyi* to varying seawater Mg availabilities. (a) Growth rate; (b) Coccosphere and naked cell sizes; (c) Linear relationship between coccosphere and naked cell sizes. Data were collected from the same batch used for metabolism measurements, demonstrating consistency in physiological behaviour across measurements and stable adaptation. Experimental conditions (Mg/Ca ratios of 0, 0.5, 1, 10, 15, 20) were compared to the control condition (Mg/Ca ratio of 5) using paired t-tests. Asterisks indicate significant differences from the control: red for significantly higher values and blue for significantly lower values. The number of asterisks represents the level of significance (*p < 0.05, **p < 0.01, ***p < 0.001).

MgCon (mM)	CaCO3 Content (pg cell-1)	(± s.e.m)	Growth Rate	(± s.e.m)	Cell Size (µm)	(± s.e.m)	Chlorophyll a Content (pg cell-1)	(± s.e.m)	Strain
0.00	0.58	0.73	0.51	0.03	4.93	0.06	0.17	0.00	OA1
5.46	140.63	5.84	1.09	0.06	5.16	0.11	0.27	0.00	OA1
10.50	190.33	8.18	1.09	0.04	5.12	0.02	0.29	0.00	OA1
54.60	152.61	11.01	1.26	0.06	4.66	0.02	0.28	0.00	OA1
105.00	114.08	3.96	1.29	0.02	4.52	0.01	0.27	0.00	OA1
157.50	88.79	3.55	1.24	0.06	4.49	0.08	0.26	0.00	OA1
210.00	49.11	9.40	1.16	0.06	4.24	0.02	0.23	0.00	OA1

Table A2. 1: Physiological traits of *Gephyrocapsa huxleyi* in response to varying seawater Mg availability.

Multiple Linear Model: Cell Size ~ Cell Number + Growth Rate + Mg concentration					
Coefficients	Estimate	Std. Error	t value	Pr (>|t|)	VIF
(Intercept)	5.37e+00	1.43e-01	37.58	< 2e-16	
CellNumber	-1.18e-06	3.04e-07	-3.87	1.23e-03	4.55
GrowthRate	3.96e-01	1.33e-01	2.99	8.30e-03	2.39
Mgcon	-2.76e-04	4.62e-04	-5.97	1.51e-05	2.67
Summary	Multiple R-squared	F-statistics	p		
	0.92	69.18	9.85e-10		

Table A2. 2: Multiple linear regression analysis of cell size in relation to cell number, growth rate, and Mg concentration, with variance inflation factor (VIF) assessment in *Gephyrocapsa huxleyi* under varying Mg availability.

Multiple Linear Model: ChlPerCell ~ Cell Number + Growth Rate + Mg concentration					
Coefficients	Estimate	Std. Error	t value	Pr (>|t|)	VIF
(Intercept)	1.09e-01	2.69e-02	4.06	8.17e-04	
CellNumber	-5.08e-08	5.72e-08	-0.89	0.39	4.55
GrowthRate	1.80e-01	2.50e-02	7.20	1.49e-06	2.39
Mgcon	-2.12e-04	8.70e-05	-2.43	0.03	2.67
Summary	Multiple R-squared	F-statistics	p		
	0.82	26.07	1.38e-06		

Table A2. 3: Multiple linear regression analysis of cellular chlorophyll-a content in relation to cell number, growth rate, and Mg concentration, with variance inflation factor (VIF) assessment in *Gephyrocapsa huxleyi* under varying Mg availability.

Multiple Linear Model: ChlPerVol ~ Cell Number + Growth Rate + Mg concentration					
Coefficients	Estimate	Std. Error	t value	Pr (>|t|)	VIF
(Intercept)	3.11e-03	1.63e-03	1.91	0.07	
CellNumber	5.11e-09	3.45e-09	1.48	0.16	4.55
GrowthRate	5.34e-03	1.51e-03	3.55	2.48e-03	2.39
Mgcon	1.93e-05	5.25e-06	3.68	1.86e-03	2.67
Summary	Multiple R-squared	F-statistics	p		
	0.91	55.17	5.68e-09		

Table A2. 4: Multiple linear regression analysis of chlorophyll-a content per unit cell volume in relation to cell number, growth rate, and Mg concentration, including variance inflation factor (VIF) assessment, in *Gephyrocapsa huxleyi* under varying Mg availability.

condition	**model_type**	**equation**	**r_squared**
0	Linear	y=1.065e-11 * x + 2.909e-09	0.695
0	Logarithmic	y=4.108e-09 * ln(x) + -1.501e-08	0.816
0	Exponential	y=1.605e-08 * e^ (5.108e-04 * x) + -1.318e-08	0.65
0	Michaelis-Menten	y= (1.936e-08 * x) / (4.244e+02 + x)	0.807
0.5	Linear	y=1.665e-11 * x + 5.328e-09	0.689
0.5	Logarithmic	y=6.448e-09 * ln(x) + -2.283e-08	0.82
0.5	Exponential	y=1.527e-08 * e^ (7.389e-04 * x) + -9.988e-09	0.654
0.5	Michaelis-Menten	y= (3.011e-08 * x) / (3.684e+02 + x)	0.818
5	Linear	y=1.278e-11 * x + 5.722e-09	0.688
5	Logarithmic	y=4.988e-09 * ln(x) + -1.610e-08	0.831
5	Exponential	y=1.488e-08 * e^ (6.237e-04 * x) + -9.237e-09	0.633
5	Michaelis-Menten	y= (2.313e-08 * x) / (2.579e+02 + x)	0.83
20	Linear	y=1.144e-11 * x + 4.297e-09	0.614
20	Logarithmic	y=4.508e-09 * ln(x) + -1.542e-08	0.755
20	Exponential	y=1.612e-08 * e^ (5.404e-04 * x) + -1.198e-08	0.586
20	Michaelis-Menten	y= (2.055e-08 * x) / (3.030e+02 + x)	0.752

Table A2. 5: Comparison of linear fit model for cellular photosynthesis-irradiance response in *Gephyrocapsa huxleyi* under varying Mg availability.

condition	model_type	equation	r_squared
0	Linear	y=1.598e-13 * x + 4.156e-11	0.679
0	Logarithmic	y=6.154e-11 * ln(x) + -2.267e-10	0.795
0	Exponential	y=1.010e-08 * e^ (1.569e-05 * x) + -1.006e-08	0.678
0	Michaelis-Menten	y= (2.915e-10 * x) / (4.440e+02 + x)	0.786
0.5	Linear	y=2.415e-13 * x + 7.481e-11	0.579
0.5	Logarithmic	y=9.312e-11 * ln(x) + -3.315e-10	0.683
0.5	Exponential	y=1.007e-08 * e^ (2.363e-05 * x) + -1.000e-08	0.58
0.5	Michaelis-Menten	y= (4.381e-10 * x) / (3.828e+02 + x)	0.682
20	Linear	y=2.162e-13 * x + 7.831e-11	0.567
20	Logarithmic	y=8.480e-11 * ln(x) + -2.921e-10	0.692
20	Exponential	y=1.012e-08 * e^ (2.111e-05 * x) + -1.004e-08	0.567
20	Michaelis-Menten	y= (3.884e-10 * x) / (3.160e+02 + x)	0.689
5	Linear	y=2.044e-13 * x + 9.067e-11	0.684
5	Logarithmic	y=7.971e-11 * ln(x) + -2.580e-10	0.825
5	Exponential	y=1.008e-08 * e^ (2.006e-05 * x) + -9.990e-09	0.683
5	Michaelis-Menten	y= (3.695e-10 * x) / (2.602e+02 + x)	0.824

Table A2. 6: Comparison of linear fit models describing the relationship between photosynthesis and irradiance on a per-cell-volume basis in *Gephyrocapsa huxleyi* under varying Mg availability.

Variable	*Mean*	*Median*	*Variance*	*Skewness*	*Kurtosis*
Original	28.38619	28.0671	3.045756	0.8864599	0.9778787
Imputed	28.32702	28.00002	3.024367	0.9115945	1.0335698

Table A2. 7: Summary statistics for protein expression data before and after MissForest imputation. The variance includes mean, median, variance, skewness and kurtosis, providing an overview of the data's central tendency, dispersion, and distribution characteristics.

Condition	Pmax (µmol O_2 ml^{-1} s^{-1} $cell^{-1}$)	Ek (µmol photons m^{-2} s^{-1})	R^2 (M-M fit)	Respiration (mean, µmol O_2 ml^{-1} s^{-1} $cell^{-1}$)	SD (R)
Mg-0	1.94×10^{-8}	424.4	0.807	-3.68×10^{-9}	1.06e-9
Mg-0.5	3.01×10^{-8}	368.4	0.818	-3.18×10^{-9}	2.78e-9
Mg-5	2.31×10^{-8}	257.9	0.830	-3.77×10^{-9}	1.40e-9
Mg-20	2.06×10^{-8}	303.0	0.752	-3.06×10^{-9}	6.38e-10

Table A2. 8: Maximum photosynthetic rates (Pmax), half-saturation irradiance (Ek), model fit quality (R^2), and mean dark respiration rates across Mg treatments in *Gephyrocapsa huxleyi*.

Appendix 3: Supporting information for Chapter 4

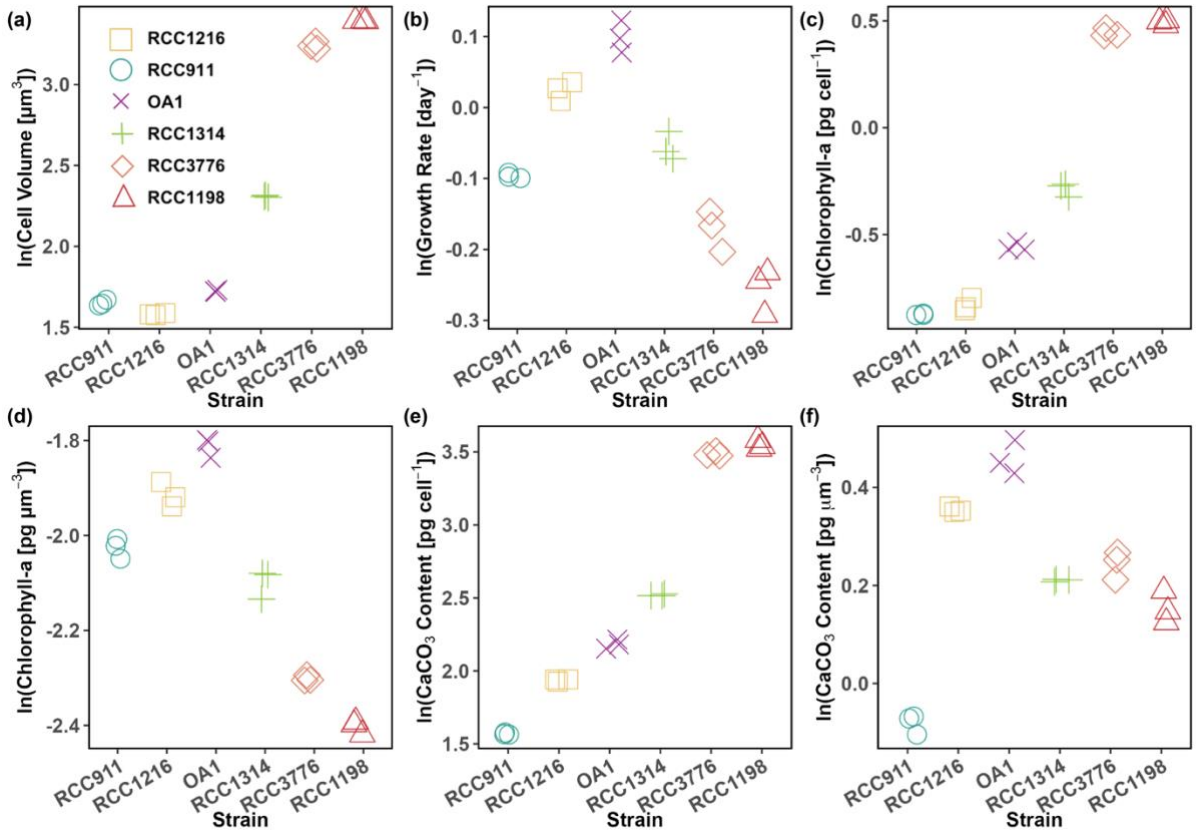

Figure A3. 1: Log-transformed key physiological traits in four coccolithophore species (*Gephyrocapsa huxleyi* (RCC911, RCC1216), *Gephyrocapsa oceanica* (RCC1314), *Coccolithus braarudii* (RCC1198), and *Coccolithus pelagicus* (RCC3776)). Panels are (a) cell volume, (b) growth rate, (c) cellular chlorophyll-a content, (d) chlorophyll-a content per unit volume, (e) cellular $CaCO_3$ content, and (f) $CaCO_3$ content per unit volume.

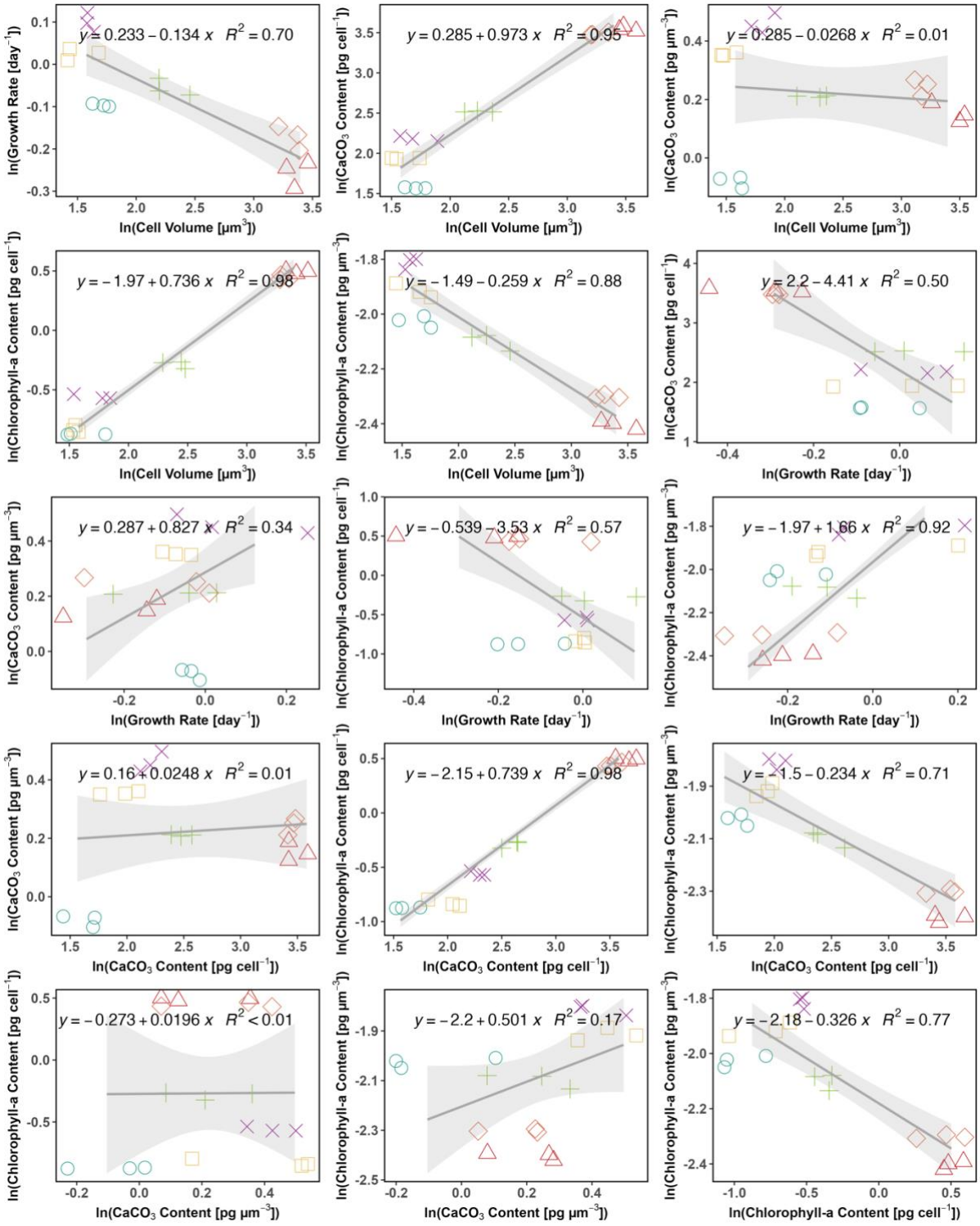

Figure A3. 2: Log-log relationships among key physiological traits in four coccolithophore species (Gephyrocapsa huxleyi (OA1, RCC911, RCC1216), *Gephyrocapsa oceanica* (RCC1314), *Coccolithus braarudii* (RCC1198), and *Coccolithus pelagicus* (RCC3776)).

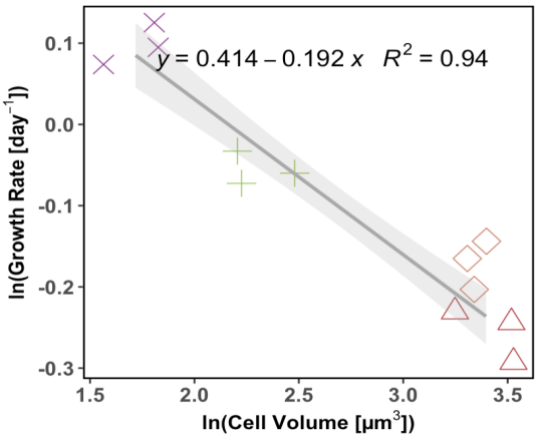

Figure A3. 3: Log-log relationships among growth rate and cell volume in four coccolithophore species (*Gephyrocapsa huxleyi* (OA1), *Gephyrocapsa oceanica* (RCC1314), *Coccolithus braarudii* (RCC1198), and *Coccolithus pelagicus* (RCC3776)).

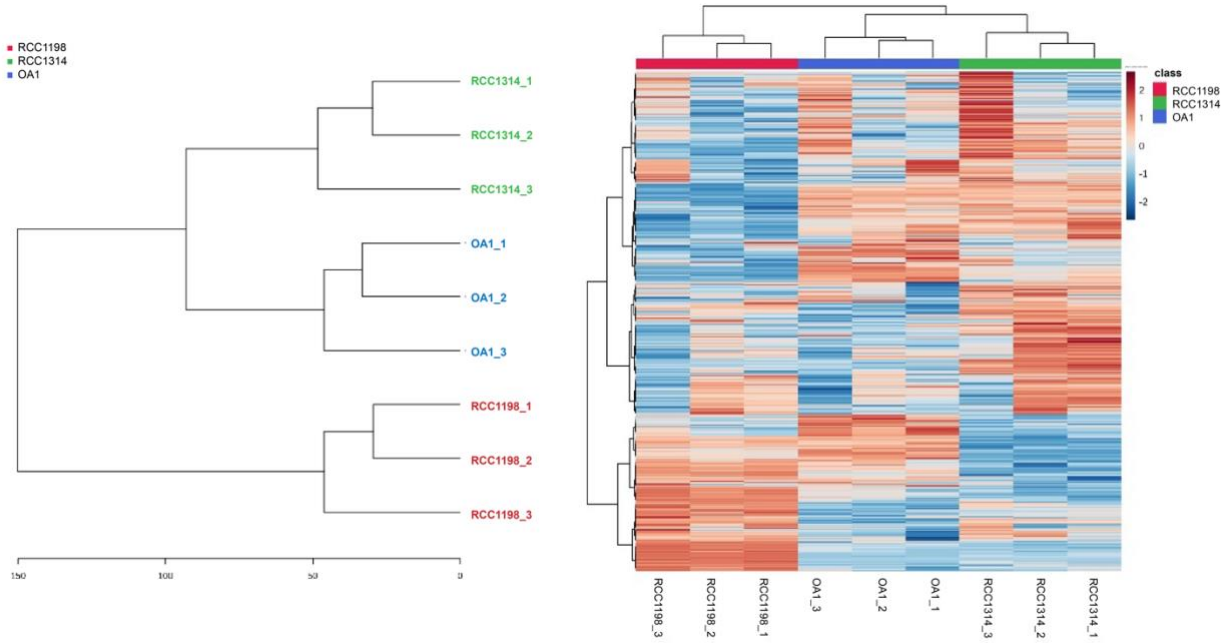

Figure A3. 4: Dendrogram (left) and hierarchical clustering heatmap (right) of non-targeted metabolomics data from three coccolithophore species: *Gephyrocapsa huxleyi* (OA1), *Gephyrocapsa oceanica* (RCC1314), and *Coccolithus braarudii* (RCC1198). Each column in the heatmap represents a replicate sample, and each row corresponds to a detected metabolite. Colours indicate relative metabolite abundance (scaled from low (blue) to high (red)), and the clustering reveals distinct metabolic profiles that group by species.

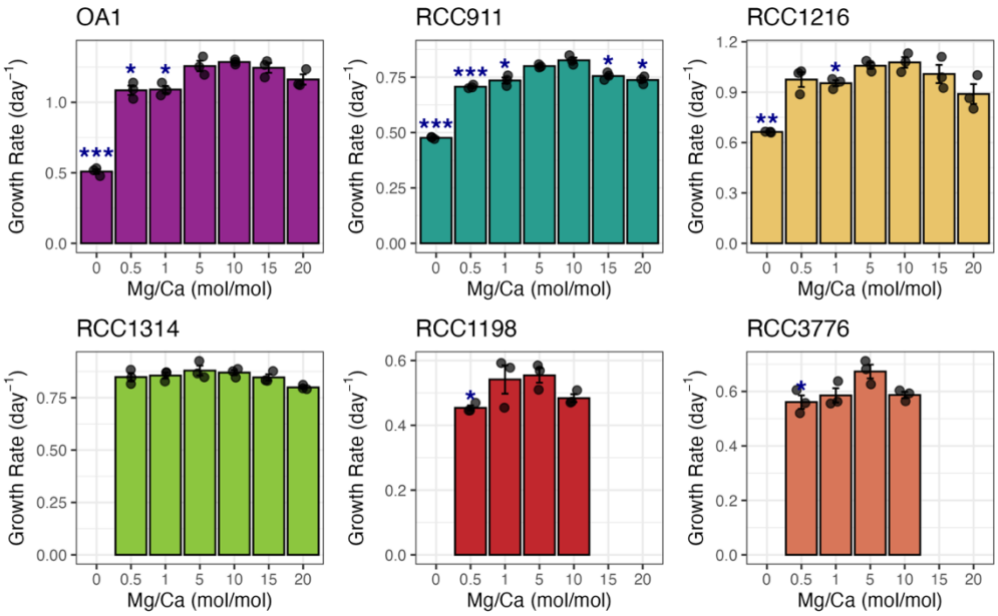

Figure A3. 5: Responses of growth rate in four coccolithophore species (*Gephyrocapsa huxleyi* (RCC911, RCC1216), *Gephyrocapsa oceanica* (RCC1314), *Coccolithus braarudii* (RCC1198), and *Coccolithus pelagicus* (RCC3776)) to varying seawater Mg availability. Asterisks indicate significant differences from the control (Mg-5), with red indicating significantly higher and blue indicating significantly lower values. Significance levels: * p<0.05, ** p<0.01, *** p<0.001.

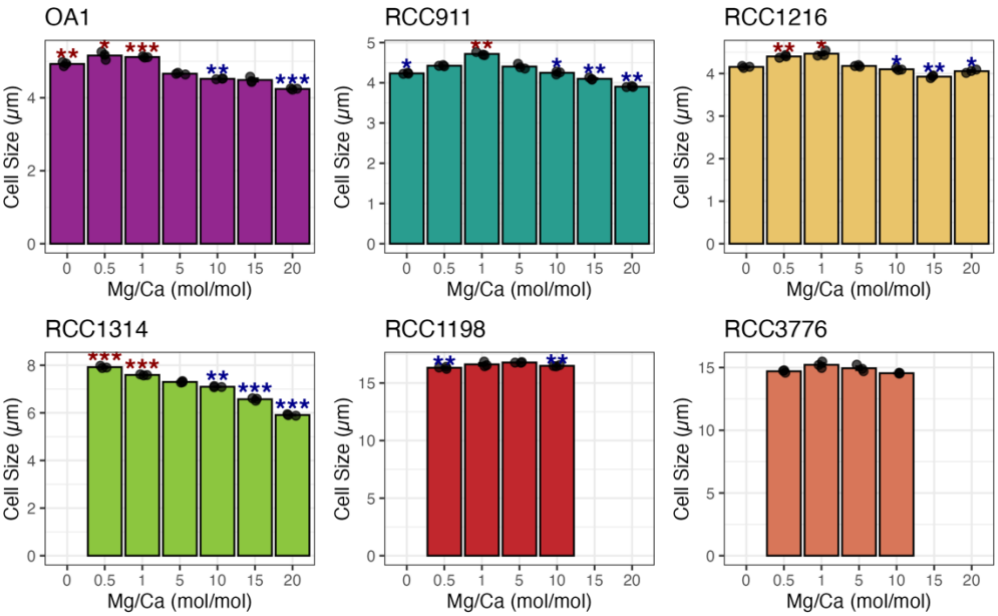

Figure A3. 6: Responses of cell size in four coccolithophore species (*Gephyrocapsa huxleyi* (RCC911, RCC1216), *Gephyrocapsa oceanica* (RCC1314), *Coccolithus braarudii* (RCC1198), and *Coccolithus pelagicus* (RCC3776)) to varying seawater Mg availability. Asterisks indicate significant differences from the control (Mg-5), with red indicating significantly higher and blue indicating significantly lower values. Significance levels: * p<0.05, ** p<0.01, *** p<0.001.

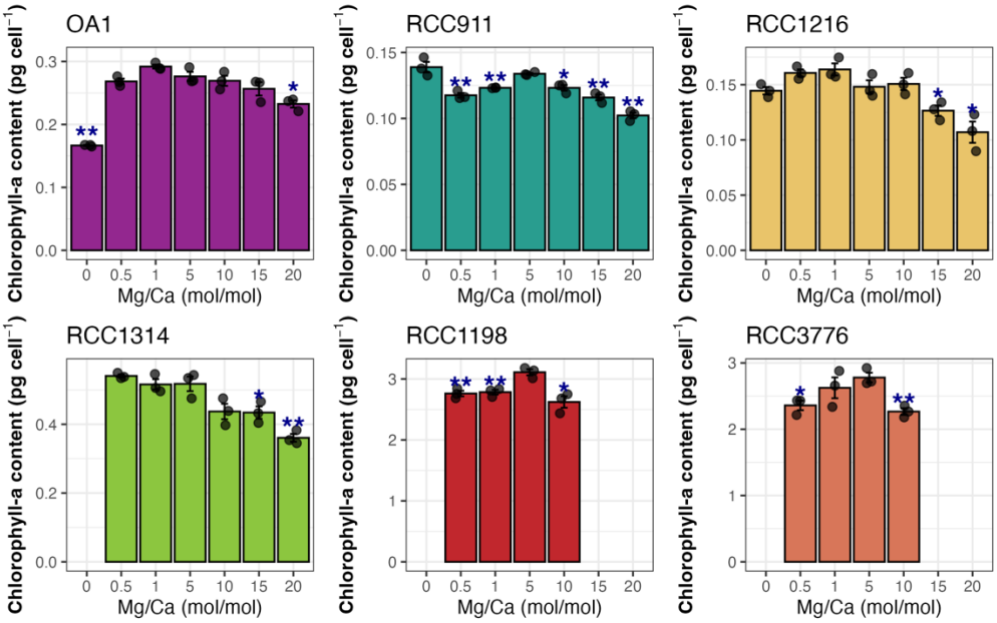

Figure A3. 7: Responses of cellular chlorophyll-a content in four coccolithophore species (*Gephyrocapsa huxleyi* (RCC911, RCC1216), *Gephyrocapsa oceanica* (RCC1314), *Coccolithus braarudii* (RCC1198), and *Coccolithus pelagicus* (RCC3776)) to varying seawater Mg availability.Asterisks indicate significant differences from the control (Mg-5), with red indicating significantly higher and blue indicating significantly lower values. Significance levels: * p<0.05, ** p<0.01, *** p<0.001.

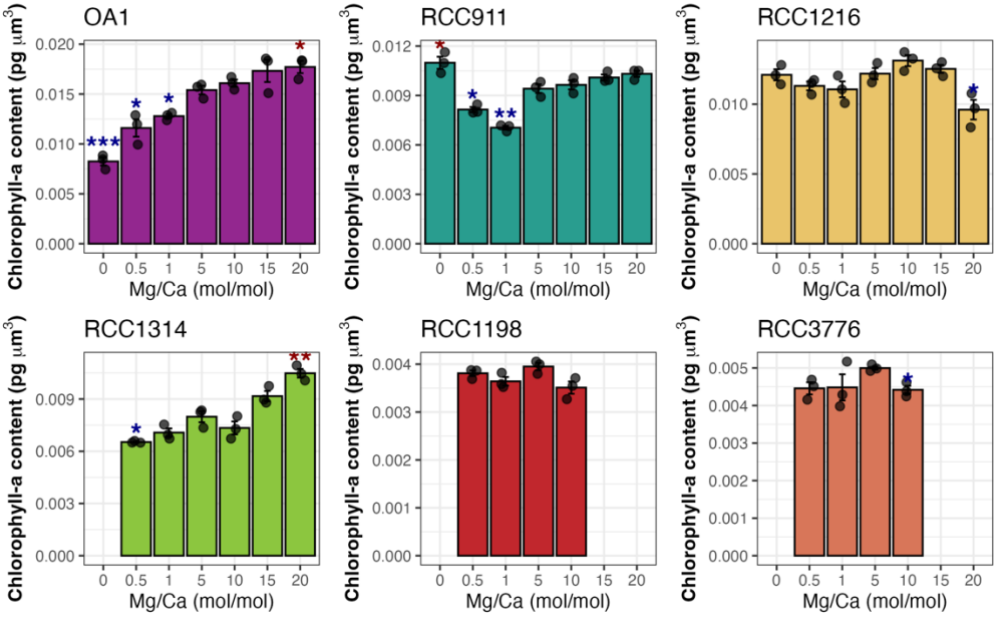

Figure A3. 8: Responses of chlorophyll-a content per unit volume in four coccolithophore species (*Gephyrocapsa huxleyi* (RCC911, RCC1216), *Gephyrocapsa oceanica* (RCC1314), *Coccolithus braarudii* (RCC1198), and *Coccolithus pelagicus* (RCC3776)) to varying seawater Mg availability.Asterisks indicate significant differences from the control (Mg-5), with red indicating significantly higher and blue indicating significantly lower values. Significance levels: * p<0.05, ** p<0.01, *** p<0.001.

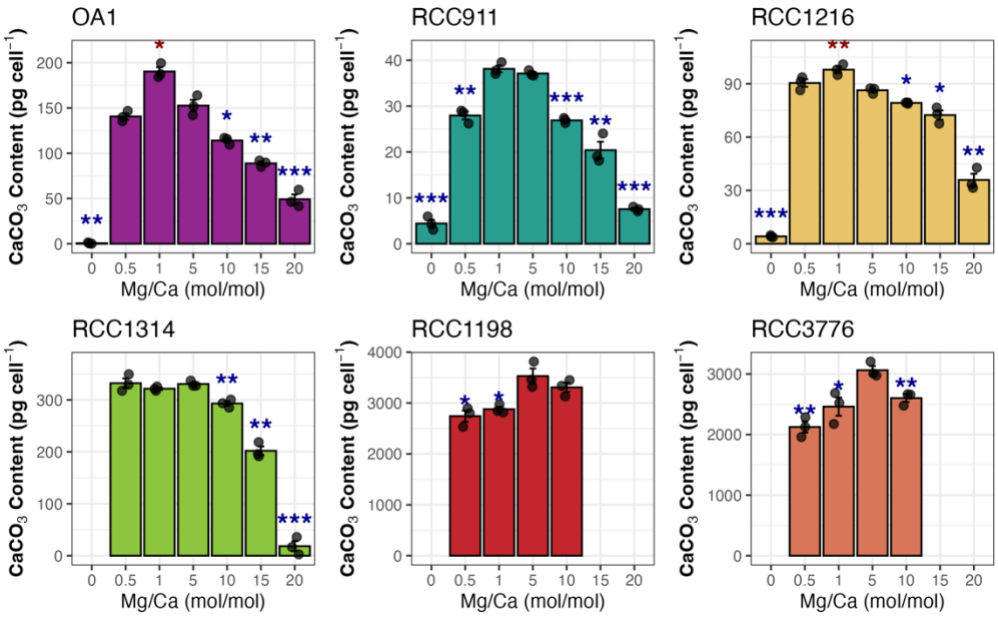

Figure A3. 9: Responses of cellular $CaCO_3$ content in four coccolithophore species (*Gephyrocapsa huxleyi* (RCC911, RCC1216), *Gephyrocapsa oceanica* (RCC1314), *Coccolithus braarudii* (RCC1198), and *Coccolithus pelagicus* (RCC3776)) to varying seawater Mg availability.Asterisks indicate significant differences from the control (Mg- 5), with red indicating significantly higher and blue indicating significantly lower values. Significance levels: * p<0.05, ** p<0.01, *** p<0.001.

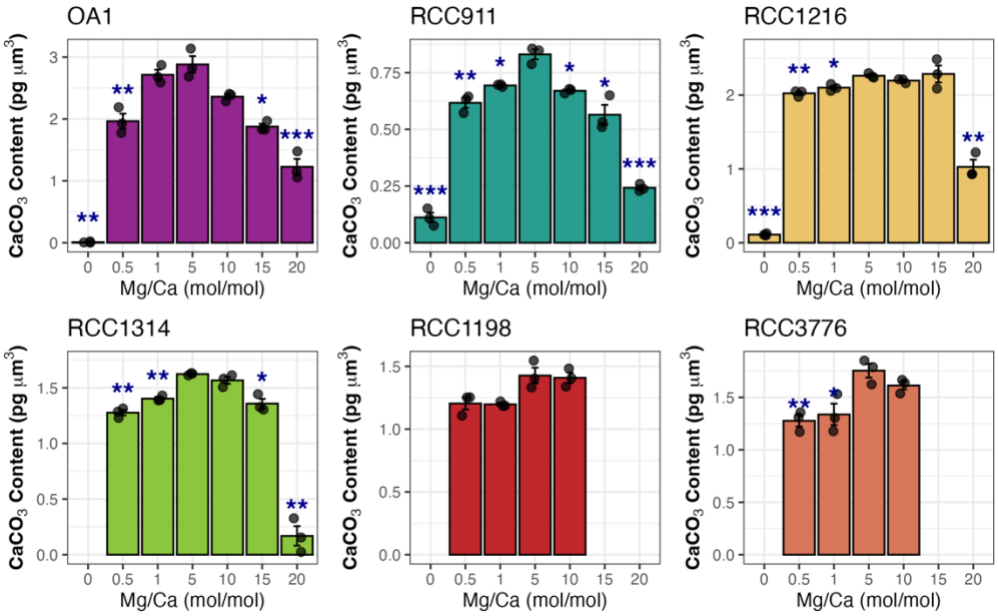

Figure A3. 10: Responses of $CaCO_3$ content per unit volume in four coccolithophore species (*Gephyrocapsa huxleyi* (RCC911, RCC1216), *Gephyrocapsa oceanica* (RCC1314), *Coccolithus braarudii* (RCC1198), and *Coccolithus pelagicus* (RCC3776) to varying seawater Mg availability.Asterisks indicate significant differences from the control (Mg-5), with red indicating significantly higher and blue indicating significantly lower values. Significance levels: * p<0.05, ** p<0.01, *** p<0.001.

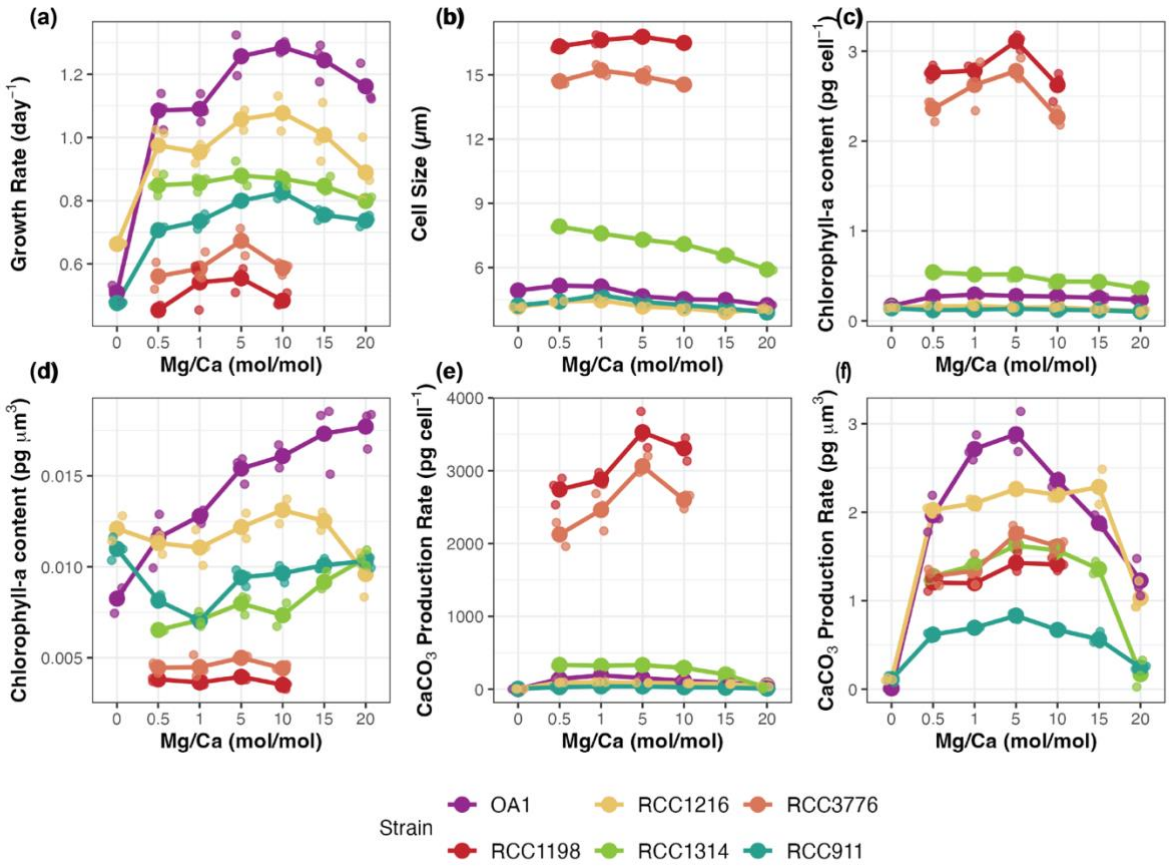

Figure A3. 11: Physiological traits in response to varying seawater Mg availability for four coccolithophore species: *Gephyrocapsa huxleyi* (RCC911, RCC1216), *Gephyrocapsa oceanica* (RCC1314), *Coccolithus braarudii* (RCC1198), and *Coccolithus pelagicus* (RCC3776). The traits include (a) growth rate, (b) cell size, (c) cellular chlorophyll-a content, (d) chlorophyll-a content per unit cell volume, (e) $CaCO_3$ production rate, and (f) $CaCO_3$ production per unit cell volume.

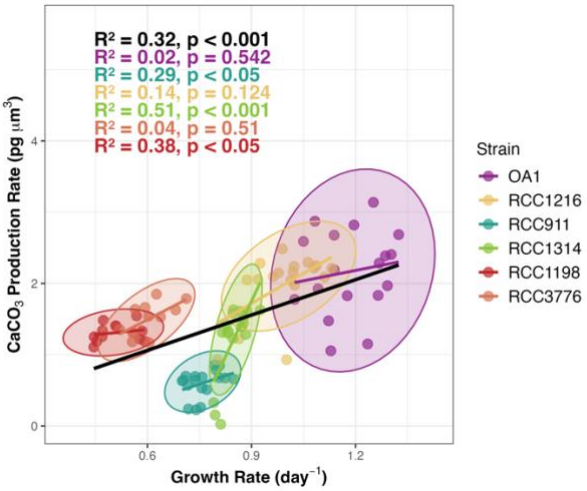

Figure A3. 12: Linear correlation between $CaCO_3$ production per unit cell volume and growth rate across a gradient of seawater Mg concentrations for four coccolithophore species: *Gephyrocapsa huxleyi* (RCC911, RCC1216), *Gephyrocapsa oceanica* (RCC1314), *Coccolithus braarudii* (RCC1198), and *Coccolithus pelagicus* (RCC3776).

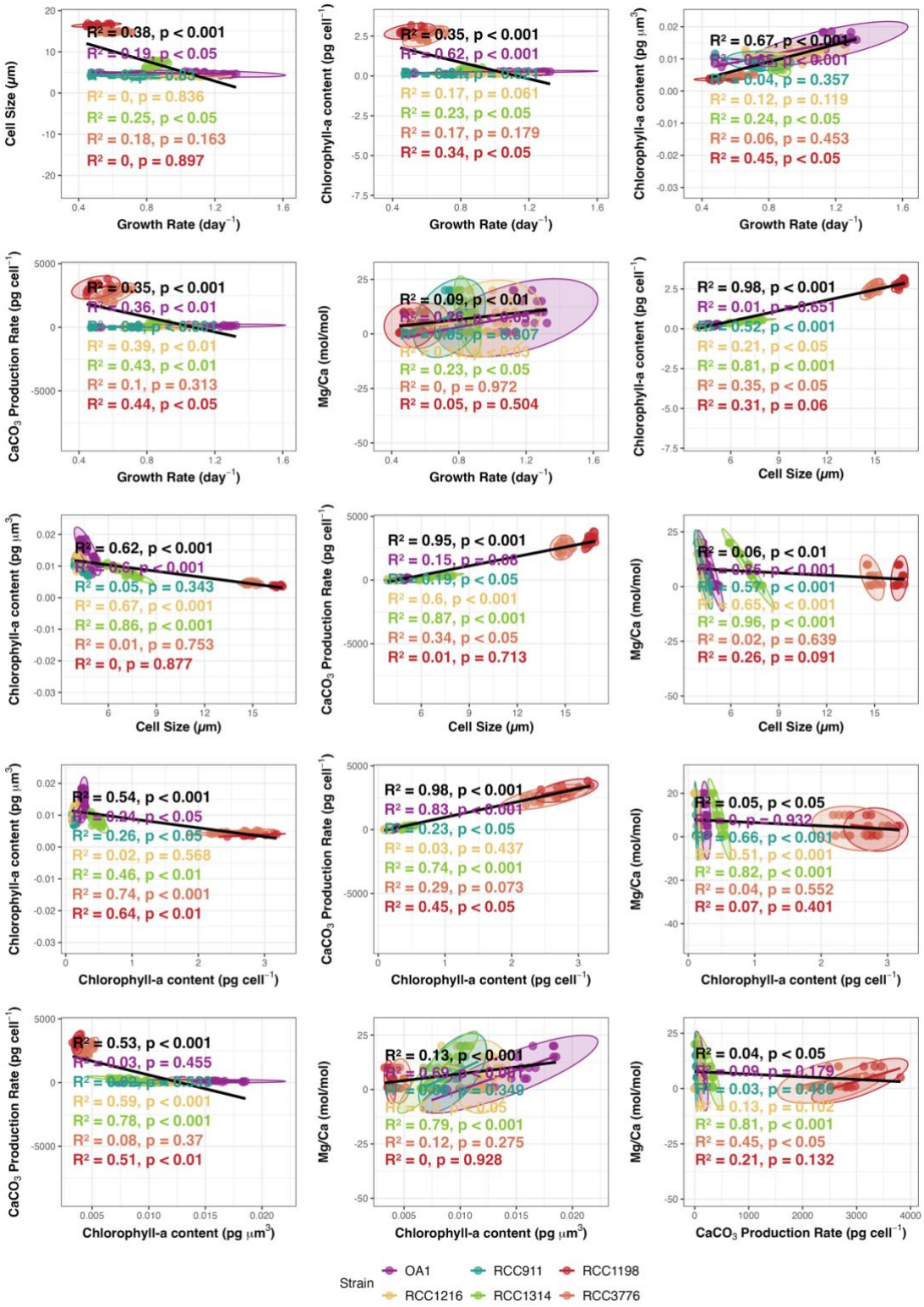

Figure A3. 13: Linear correlation of physiological traits in response to varying seawater Mg availability for four coccolithophore species: *Gephyrocapsa huxleyi* (RCC911, RCC1216), *Gephyrocapsa oceanica* (RCC1314), *Coccolithus braarudii* (RCC1198), and *Coccolithus pelagicus* (RCC3776).The left panel displays multiple regression analyses with overall linear regression equations and R^2 values for all strains under all Mg conditions, while the right panel presents strain-specific regression analyses showing responses to corresponding Mg availability.

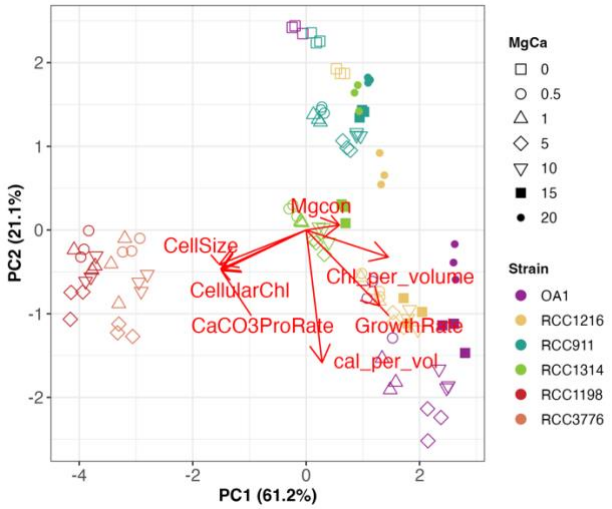

Figure A3. 14: Principal component analysis (PCA) of physiological traits, including $CaCO_3$ production per unit cell volume (cal_per_vol), in response to varying seawater Mg availability for four coccolithophore species: *Gephyrocapsa huxleyi* (RCC911, RCC1216), *Gephyrocapsa oceanica* (RCC1314), *Coccolithus braarudii* (RCC1198), and *Coccolithus pelagicus* (RCC3776).

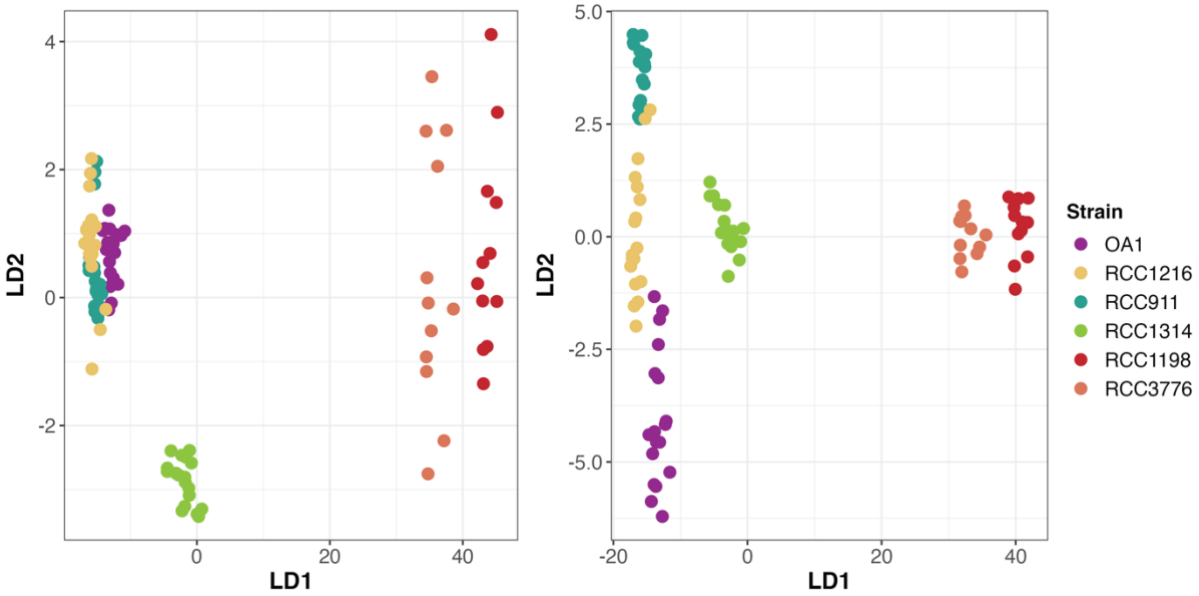

Figure A3. 15: Linear Discriminant Analysis (LDA) illustrating strain-based separation of physiological traits in response to seawater Mg availability in coccolithophores, including *Gephyrocapsa huxleyi* (RCC911, RCC1216), *Gephyrocapsa oceanica* (RCC1314), *Coccolithus braarudii* (RCC1198), and *Coccolithus pelagicus* (RCC3776). The left panel represents results based on the full dataset, and the right panel excludes data from the Mg-0 treatment.

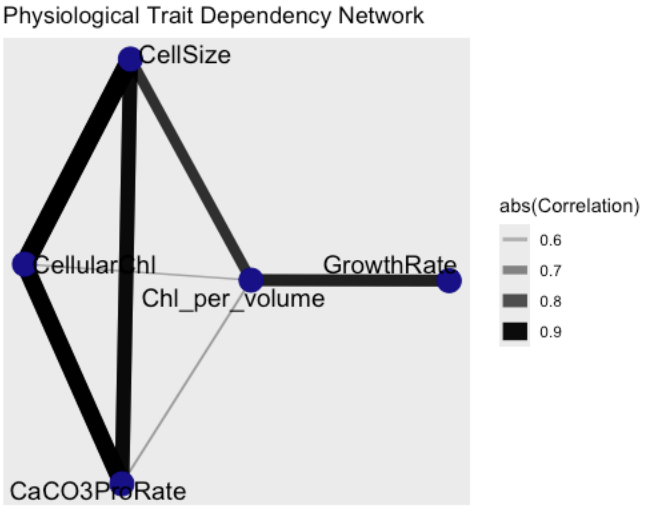

Figure A3. 16: Physiological trait dependency network illustrating correlation strengths among physiological traits in response to varying seawater Mg availability for four coccolithophore Species: *Gephyrocapsa huxleyi* (RCC911, RCC1216), *Gephyrocapsa oceanica* (RCC1314), *Coccolithus braarudii* (RCC1198), and *Coccolithus pelagicus* (RCC3776).Nodes represent individual physiological traits, while edges (lines) indicate the magnitude of their correlation. The width and darkness of the edges correspond to the absolute strength of the correlation, with thicker and darker edges representing stronger relationships.

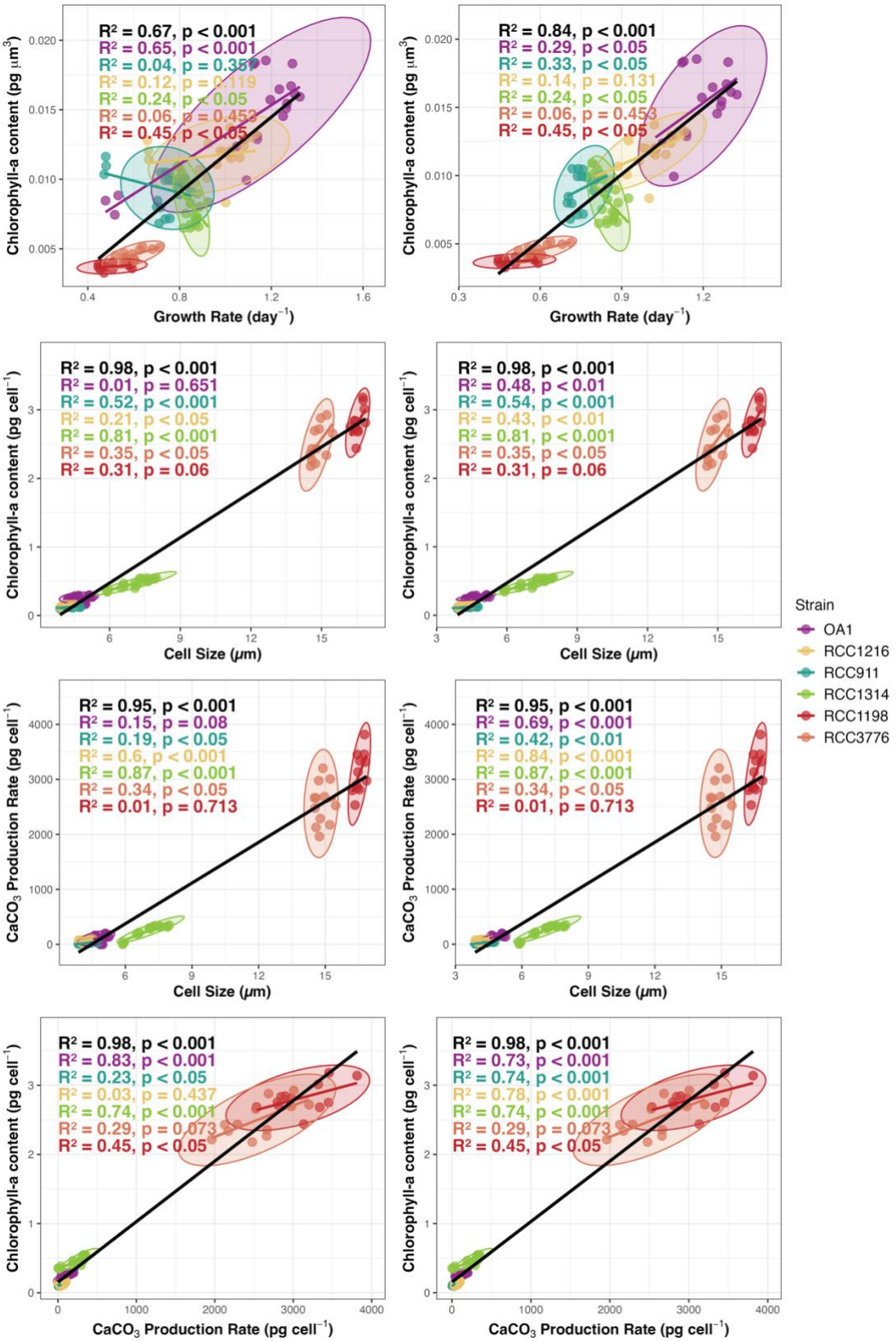

Figure A3. 17: Linear regression analyses of physiological traits across four coccolithophore species: *Gephyrocapsa huxleyi* (RCC911, RCC1216), *Gephyrocapsa oceanica* (RCC1314), *Coccolithus braarudii* (RCC1198), and *Coccolithus pelagicus* (RCC3776), in response to varying seawater Mg availability. Left panels include all data, while right panels exclude M-0 treatment.

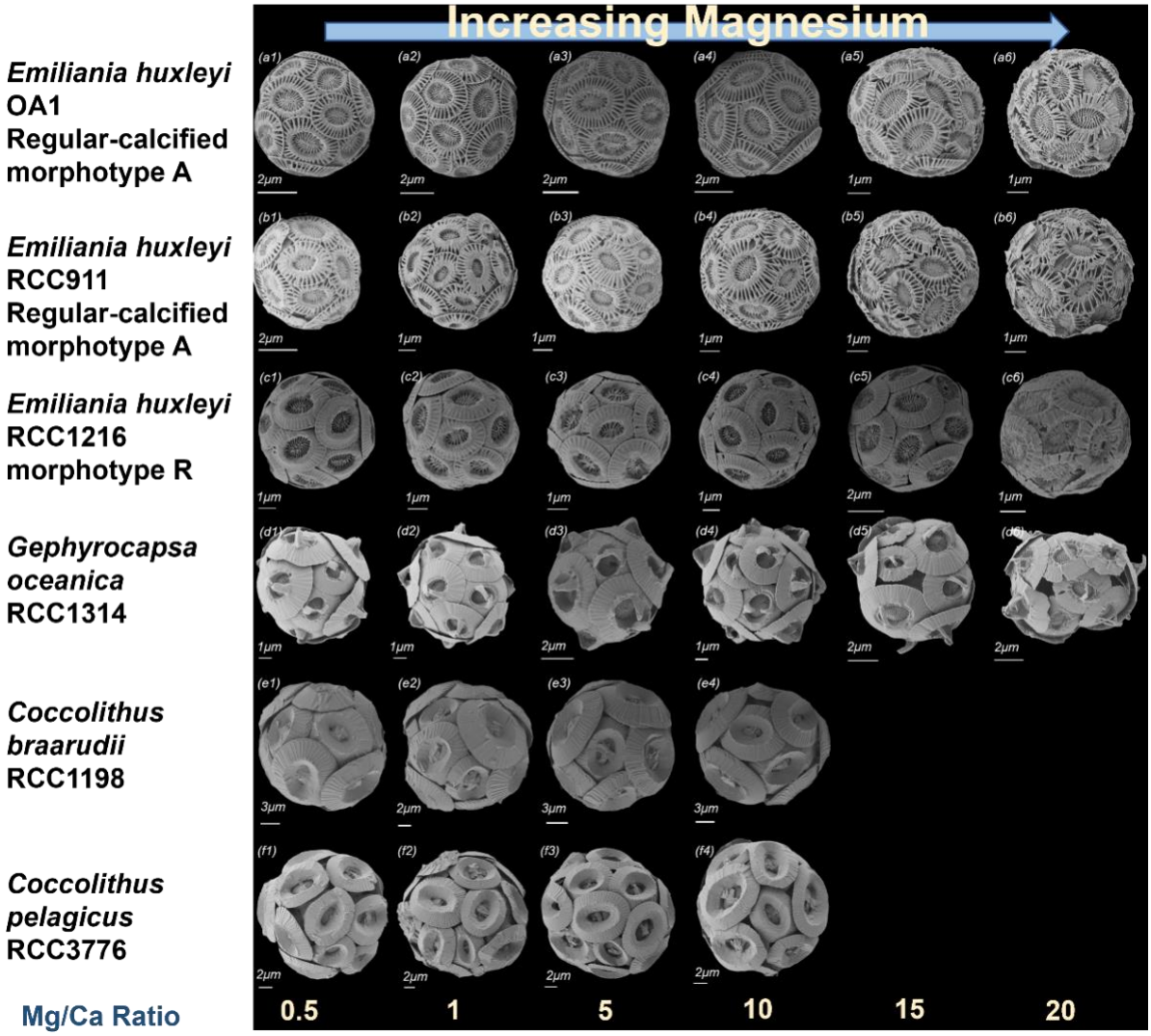

Figure A3. 18: SEM images of coccospheres from four coccolithophore species: *Gephyrocapsa huxleyi* (RCC911, RCC1216), *Gephyrocapsa oceanica* (RCC1314), *Coccolithus braarudii* (RCC1198), and *Coccolithus pelagicus* (RCC3776) grown under varying seawater Mg availability.

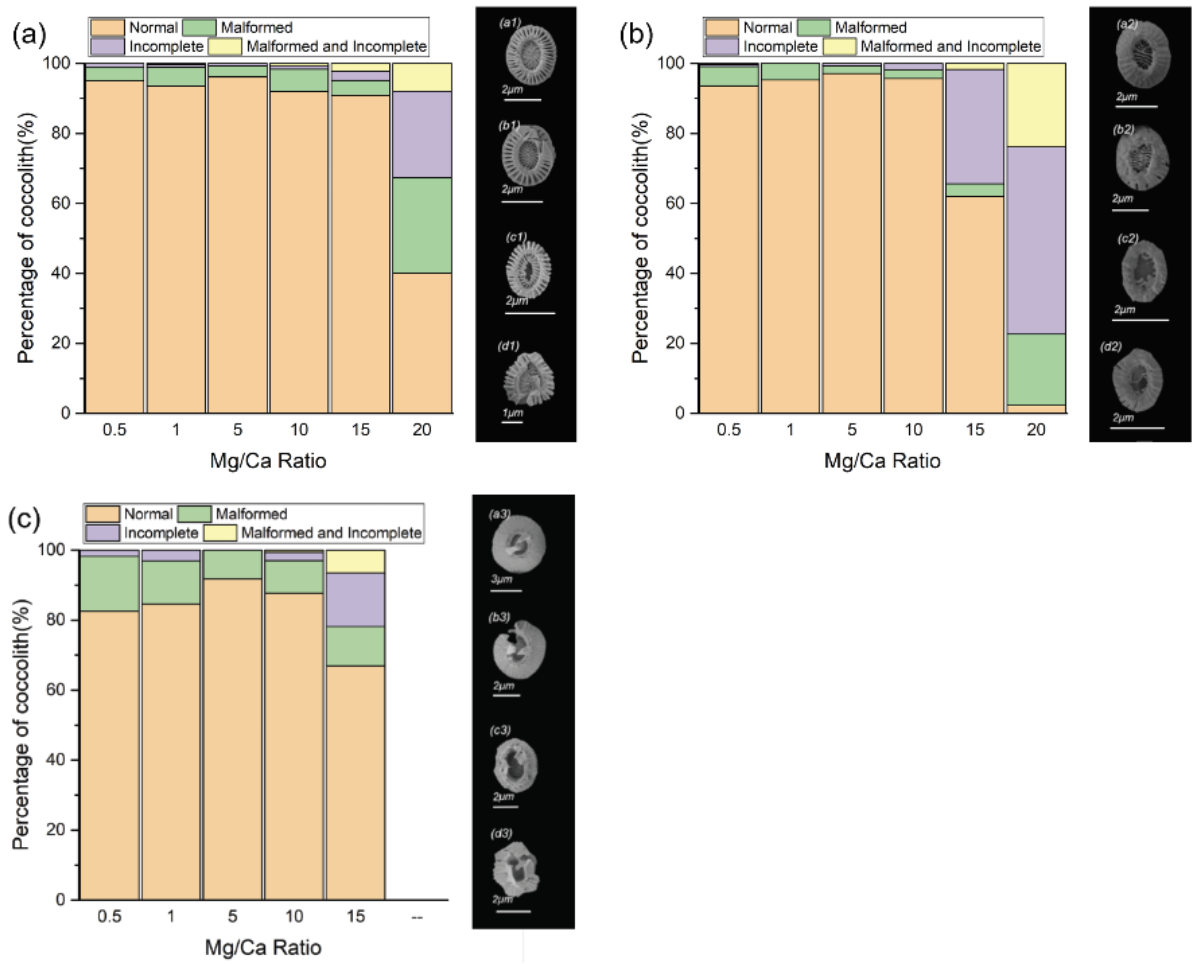

Figure A3. 19: Percentage of normal, malformed, incomplete, and both malformed and incomplete coccoliths in coccolithophore species *Gephyrocapsa huxleyi* (OA1, RCC1216) and *Gephyrocapsa oceanica* (RCC1314) grown under varying seawater Mg availability. Over 150 coccoliths were examined per condition for each strain.

MgCon (mM)	$CaCO_3$ Content (pg cell^{-1})	(± s.e.m)	Growth Rate	(± s.e.m)	Cell Size (µm)	(± s.e.m)	Chlorophyll a Content (pg cell^{-1})	(± s.e.m)	Strain
0.00	4.41	1.44	0.48	0.00	4.23	0.01	0.14	0.00	RCC911
5.46	27.95	1.51	0.71	0.01	4.42	0.01	0.12	0.00	RCC911
10.50	38.12	1.30	0.74	0.02	4.72	0.04	0.12	0.00	RCC911
54.60	37.11	0.61	0.80	0.01	4.40	0.06	0.13	0.00	RCC911
105.00	26.89	0.56	0.83	0.02	4.25	0.04	0.12	0.00	RCC911
157.50	20.40	3.18	0.76	0.02	4.10	0.03	0.12	0.00	RCC911
210.00	7.54	0.50	0.74	0.02	3.90	0.01	0.10	0.00	RCC911
0.00	4.14	0.55	0.66	0.00	4.15	0.02	0.14	0.00	RCC1216
5.46	90.43	3.72	0.97	0.08	4.40	0.03	0.16	0.00	RCC1216
10.50	97.94	3.02	0.95	0.03	4.47	0.07	0.16	0.00	RCC1216
54.60	86.35	1.70	1.06	0.03	4.18	0.02	0.15	0.00	RCC1216
105.00	79.21	0.43	1.08	0.06	4.10	0.02	0.15	0.00	RCC1216
157.50	72.38	4.55	1.01	0.09	3.93	0.03	0.13	0.00	RCC1216
210.00	35.88	6.07	0.89	0.10	4.06	0.04	0.11	0.00	RCC1216
5.46	332.09	16.12	0.85	0.03	7.92	0.05	0.54	0.00	RCC1314
10.50	321.50	4.07	0.86	0.02	7.59	0.02	0.52	0.00	RCC1314
54.60	330.54	5.55	0.88	0.04	7.30	0.03	0.52	0.00	RCC1314
105.00	293.03	7.71	0.87	0.02	7.10	0.03	0.44	0.00	RCC1314
157.50	201.97	14.54	0.85	0.03	6.57	0.06	0.43	0.00	RCC1314
210.00	18.42	16.76	0.80	0.01	5.91	0.03	0.36	0.00	RCC1314
5.46	2742.15	188.35	0.45	0.01	16.32	0.09	2.76	0.00	RCC1198
10.50	2878.26	84.76	0.54	0.08	16.62	0.21	2.78	0.00	RCC1198
54.60	3529.40	256.13	0.55	0.04	16.78	0.03	3.11	0.00	RCC1198
105.00	3306.84	160.78	0.48	0.02	16.49	0.06	2.62	0.00	RCC1198
5.46	2124.67	163.36	0.56	0.04	14.70	0.10	2.36	0.00	RCC3776
10.50	2460.71	261.75	0.59	0.05	15.21	0.26	2.62	0.00	RCC3776
54.60	3061.79	122.12	0.67	0.04	14.94	0.26	2.78	0.00	RCC3776
105.00	2600.85	106.99	0.59	0.02	14.55	0.03	2.27	0.00	RCC3776

Table A3. 1: Physiological traits of four coccolithophore species: *Gephyrocapsa huxleyi* (RCC911, RCC1216), *Gephyrocapsa oceanica* (RCC1314), *Coccolithus braarudii* (RCC1198), and *Coccolithus pelagicus* (RCC3776), in response to varying seawater Mg concentrations.

Multiple Linear Model: $CaCO_3$ content per unit volume ~ Cell volume +Growth Rate					
Coefficients	Estimate	Std. Error	t value	Pr (>|t|)	VIF
(Intercept)	-2.15	0.45	-4.78	***	
CellVolume	0.00	0.00	5.65	***	2.68
GrowthRate	4.02	0.44	9.21	***	2.68
Summary	Multiple R-squared	F-statistics	p		
	0.86	46.3	3.97e-07		

Table A3. 2: Summary of multiple linear regression assessing the relationship between $CaCO_3$ content per unit volume, cell volume, and growth rate.

Model: aov (growth rate ~ strain * Mg/Ca)					
Two-Way ANOVA for all strains					
Summary	Df	Sum Sq	Mean Sq	F value	Pr (>F)
Strain	5	3.84	0.77	388.53	<2e-16
Mg/Ca	6	1.59	0.27	134.36	<2e-16
Strain: Mg/Ca	23	0.35	0.02	7.73	1.38e-11
residuals	70	0.14	0.00		
Two-Way ANOVA for strain OA1, RCC911, RCC1216					
Summary	Df	Sum Sq	Mean Sq	F value	Pr (>F)
Strain	2	1.47	0.73	306.50	<2e-16
Mg/Ca	6	1.61	0.27	111.91	<2e-16
Strain: Mg/Ca	12	0.28	0.02	9.76	1.11e-08
residuals	42	0.10	0.00		
Two-Way ANOVA for strain RCC1314, RCC1198, RCC3776					
Summary	Df	Sum Sq	Mean Sq	F value	Pr (>F)
Strain	2	0.95	0.47	352.77	<2e-16
Mg/Ca	5	0.04	0.01	6.13	5.91e-04
Strain: Mg/Ca	6	0.01	0.00	1.57	0.19
residuals	28	0.04	0.00		
Two-Way ANOVA for strain RCC1198, RCC3776					
Summary	Df	Sum Sq	Mean Sq	F value	Pr (>F)
Strain	1	0.05	0.05	29.43	5.62e-05
Mg/Ca	3	0.04	0.01	6.97	3.26e-03
Strain: Mg/Ca	3	0.01	0.00	0.95	0.44
residuals	16	0.03	0.00		

Table A3. 3: Summary of two-way ANOVA models evaluating the effects of strain, Mg/Ca ratio, and their interaction on growth rate across all strains and in separate strain subsets.

Model: aov (CellSize ~ strain * Mg/Ca)					
Two-Way ANOVA for all strains					
Summary	Df	Sum Sq	Mean Sq	F value	Pr (>F)
Strain	5	2243.50	448.70	62114.52	<2e-16
Mg/Ca	6	8.50	1.40	196.28	<2e-16
Strain: Mg/Ca	23	4.50	0.20	27.38	<2e-16
residuals	70	0.50	0.00		
Two-Way ANOVA for strain OA1, RCC911, RCC1216					
Summary	Df	Sum Sq	Mean Sq	F value	Pr (>F)
Strain	2	3.54	1.77	905.07	<2e-16
Mg/Ca	6	3.42	0.57	291.86	<2e-16
Strain: Mg/Ca	12	0.60	0.05	25.59	1.74e-15
residuals	42	0.08	0.00		
Two-Way ANOVA for strain RCC1314, RCC1198, RCC3776					
Summary	Df	Sum Sq	Mean Sq	F value	Pr (>F)
Strain	2	784.60	392.30	25931.26	<2e-16
Mg/Ca	5	7.70	1.50	101.19	<2e-16
Strain: Mg/Ca	6	1.40	0.20	15.22	1.13e-07
residuals	28	0.40	0.00		
Two-Way ANOVA for strain RCC1198, RCC3776					
Summary	Df	Sum Sq	Mean Sq	F value	Pr (>F)
Strain	1	17.37	17.37	685.53	1.45e-14
Mg/Ca	3	0.85	0.28	11.16	3.38e-04
Strain: Mg/Ca	3	0.26	0.09	3.37	0.05
residuals	16	0.41	0.03		

Table A3. 4: Summary of two-way ANOVA models evaluating the effects of strain, Mg/Ca ratio, and their interaction on cell size across all strains and in separate strain subsets.

Model: aov (CellularChlorophyllContent ~ strain * Mg/Ca)					
Two-Way ANOVA for all strains					
Summary	Df	Sum Sq	Mean Sq	F value	Pr (>F)
Strain	5	110.96	22.19	4688.07	<2e-16
Mg/Ca	6	0.37	0.06	13.11	6.96e-10
Strain: Mg/Ca	23	0.63	0.03	5.75	6.62e-09
residuals	70	0.33	0.01		
Two-Way ANOVA for strain OA1, RCC911, RCC1216					
Summary	Df	Sum Sq	Mean Sq	F value	Pr (>F)
Strain	2	0.20	0.10	1270.39	<2e-16
Mg/Ca	6	0.02	0.00	36.66	3.67e-15
Strain: Mg/Ca	12	0.02	0.00	24.72	3.46e-15
residuals	42	0.00	0.00		
Two-Way ANOVA for strain RCC1314, RCC1198, RCC3776					
Summary	Df	Sum Sq	Mean Sq	F value	Pr (>F)
Strain	2	50.19	25.10	2142.32	<2e-16
Mg/Ca	5	0.68	0.14	11.55	4.06e-06
Strain: Mg/Ca	6	0.28	0.05	4.00	5.17e-03
residuals	28	0.33	0.01		
Two-Way ANOVA for strain RCC1198, RCC3776					
Summary	Df	Sum Sq	Mean Sq	F value	Pr (>F)
Strain	1	0.59	0.59	29.46	5.58e-05
Mg/Ca	3	0.84	0.28	14.02	9.64e-05
Strain: Mg/Ca	3	0.05	0.02	0.85	0.49
residuals	16	0.32	0.02		

Table A3. 5: Summary of two-way ANOVA models evaluating the effects of strain, Mg/Ca ratio, and their interaction on cellular chlorophyll-a content across all strains and in separate strain subsets.

Model: aov (ChlorophyllPerUnitVolume ~ strain * Mg/Ca)					
Two-Way ANOVA for all strains					
Summary	Df	Sum Sq	Mean Sq	F value	Pr (>F)
Strain	5	1.28e-03	2.56e-04	549.91	<2e-16
Mg/Ca	6	9.87e-05	1.64e-05	35.26	<2e-16
Strain: Mg/Ca	23	2.10e-04	8.95e-06	19.20	<2e-16
residuals	70	3.26e-05	4.70e-07		
Two-Way ANOVA for strain OA1, RCC911, RCC1216					
Summary	Df	Sum Sq	Mean Sq	F value	Pr (>F)
Strain	2	2.41e-04	1.20e-04	175.61	<2e-16
Mg/Ca	6	9.56e-05	1.59e-05	23.24	6.94e-12
Strain: Mg/Ca	12	1.75e-04	1.46e-05	21.30	4.42e-14
residuals	42	2.88e-05	6.90e-07		
Two-Way ANOVA for strain RCC1314, RCC1198, RCC3776					
Summary	Df	Sum Sq	Mean Sq	F value	Pr (>F)
Strain	2	1.64e-04	8.19e-05	595.87	<2e-16
Mg/Ca	5	3.22e-05	6.43e-06	46.80	9.7e-13
Strain: Mg/Ca	6	1.62e-06	2.70e-07	1.96	0.105
residuals	28	3.85e-06	1.40e-07		
Two-Way ANOVA for strain RCC1198, RCC3776					
Summary	Df	Sum Sq	Mean Sq	F value	Pr (>F)
Strain	1	0.59	0.59	29.46	5.58e-05
Mg/Ca	3	0.84	0.28	14.02	9.64e-05
Strain: Mg/Ca	3	0.05	0.02	0.85	0.49
residuals	16	0.32	0.02		

Table A3. 6: Summary of two-way ANOVA models evaluating the effects of strain, Mg/Ca ratio, and their interaction on chlorophyll-a content per unit cell volume across all strains and in separate strain subsets.

Model: aov ($CaCO_3$ProductionRate ~ strain * Mg/Ca)					
Two-Way ANOVA for all strains					
Summary	Df	Sum Sq	Mean Sq	F value	Pr (>F)
Strain	5	1.41e+08	2.81e+07	3829.19	<2e-16
Mg/Ca	6	9.97e+05	166168	22.63	1.21e-14
Strain: Mg/Ca	23	1.90e+06	82619	11.25	1.77e-15
residuals	70	513946	7342		
Two-Way ANOVA for strain OA1, RCC911, RCC1216					
Summary	Df	Sum Sq	Mean Sq	F value	Pr (>F)
Strain	2	70614	35307	1683.7	<2e-16
Mg/Ca	6	73794	12299	586.5	<2e-16
Strain: Mg/Ca	12	25883	2157	102.9	<2e-16
residuals	42	881	21		
Two-Way ANOVA for strain RCC1314, RCC1198, RCC3776					
Summary	Df	Sum Sq	Mean Sq	F value	Pr (>F)
Strain	2	7.08e+07	3.54e-07	1930.46	<2e-16
Mg/Ca	5	1.87e+06	3.75e-05	20.44	1.45e-08
Strain: Mg/Ca	6	9.25e-05	1.54e-05	8.42	2.88e-05
residuals	28	5.13e-05	18324		
Two-Way ANOVA for strain RCC1198, RCC3776					
Summary	Df	Sum Sq	Mean Sq	F value	Pr (>F)
Strain	1	1.83e+06	1.83e+06	57.24	1.14e-06
Mg/Ca	3	2.49e+06	8.30e+5	25.96	2.19e-06
Strain: Mg/Ca	3	7.98e+04	2.66e+04	0.83	0.50
residuals	16	5.11e+05	3.20e+04		

Table A3. 7: Summary of two-way ANOVA models evaluating the effects of strain, Mg/Ca ratio, and their interaction on cellular $CaCO_3$ content across all strains and in separate strain subsets.

Model: aov ($CaCO_3$ProductionPerUnitVolume ~ strain * Mg/Ca)					
Two-Way ANOVA for all strains					
Summary	Df	Sum Sq	Mean Sq	F value	Pr (>F)
Strain	5	22.85	4.57	421.08	<2e-16
Mg/Ca	6	29.29	4.88	449.83	<2e-16
Strain: Mg/Ca	23	6.87	0.30	27.54	<2e-16
residuals	70	0.76	0.01		
Two-Way ANOVA for strain OA1, RCC911, RCC1216					
Summary	Df	Sum Sq	Mean Sq	F value	Pr (>F)
Strain	2	22.30	11.15	890.3	<2e-16
Mg/Ca	6	25.00	4.16	332.0	<2e-16
Strain: Mg/Ca	12	6.28	0.52	41.8	<2e-16
residuals	42	0.53	0.01		
Two-Way ANOVA for strain RCC1314, RCC1198, RCC3776					
Summary	Df	Sum Sq	Mean Sq	F value	Pr (>F)
Strain	2	0.51	0.25	30.33	9.83e-08
Mg/Ca	5	4.86	0.97	116.61	<2e-16
Strain: Mg/Ca	6	0.07	0.01	1.34	0.27
residuals	28	0.23	0.01		

Table A3. 8: Summary of two-way ANOVA models evaluating the effects of strain, Mg/Ca ratio, and their interaction on $CaCO_3$ content per unit volume across all strains and in separate strain subsets.

	PC1	PC2	PC3	PC4	PC5	PC6
Growth Rate	0.38	-0.22	0.69	-0.57	-0.05	-0.03
Cell Size	-0.47	-0.19	0.22	-0.06	0.68	0.49
Cellular Chlorophyll-a Content	-0.46	-0.23	0.28	0.15	0.11	-0.79
Chlorophyll-a Content per Unit Volume	0.43	-0.15	0.37	0.79	0.13	0.09
$CaCO_3$ Content	-0.46	-0.25	0.26	0.16	-0.71	0.35
Mg concentration	0.18	-0.88	-0.43	-0.07	0.02	-0.01

Table A3. 9: Principal component loadings for each physiological trait included in the analysis.

	Df	Sum Sq	Mean Sq	F value	Pr(>F)
aov (PC1 ~ Strain, data = pca_scores)					
	5	416.8	83.36	314.9	<2e-16
aov (PC2 ~ Strain, data = pca_scores)					
	5	9.15	1.83	1.98	0.08
aov (PC1 ~ MgCa, data = pca_scores)					
	6	84.7	14.12	3.86	1.68e-3
aov (PC2 ~ MgCa, data = pca_scores)					
	6	81.8	13.63	71.28	<2e-16

Table A3. 10: ANOVA results testing the effects of strain and Mg availability on principal component scores.

Multiple Linear Model: $CaCO_3$ content per unit volume ~ Cell volume +Growth Rate					
Coefficients	Estimate	Std. Error	t value	Pr (>|t|)	VIF
(Intercept)	-1.76	0.21	-8.36	3.35e-13	
CellVolume	6.17e-04	6.28e-05	9.82	<2e-16	1.64
GrowthRate	3.38	0.23	15.15	<2e-16	1.64
Summary	Multiple R-squared	F-statistics	p		
	0.86	46.3	3.97e-07		

Table A3. 11: Summary of the multiple linear regression model testing the combined effects of cell volume and growth rate on $CaCO_3$ content per unit volume across all Mg concentrations. The model assesses how structural (cell size) and physiological (division rate) traits jointly contribute to variation in volume-specific calcification.

Two-way MANOVA Model: GrowthRate, CellSize, CellularChl, Chl_per_volume, CaCO3ProRate, cal_per_vol) ~ Strain * MgCa						
	Df	Pillai	approx F	num Df	den Df	Pr(>F)
Strains	5	4.01	46.79	30	345	< 2.2e-16
MgCa	6	3.32	14.42	36	420	< 2.2e-16
Strain*MgCa	23	4.20	7.08	138	420	< 2.2e-16

Table A3. 12: Two-way MANOVA using Pillai's trace statistic to assess the multivariate effects of species (strain) on physiological traits.

Bibliography

Aloisi G. **2015**. Covariation of metabolic rates and cell size in coccolithophores. *Biogeosciences* **12**: 4665–4692.

Álvarez E, Nogueira E, López-Urrutia Á. **2017**. In Vivo Single-Cell Fluorescence and Size Scaling of Phytoplankton Chlorophyll Content. *Applied and Environmental Microbiology* **83**: e03317-16.

Ambrosio S, Di Palo G, Napolitano G, Amente S, Dellino GI, Faretta M, Pelicci PG, Lania L, Majello B. **2015**. Cell cycle-dependent resolution of DNA double-strand breaks. *Oncotarget* **7**: 4949–4960.

Amponsah PS, Yahya G, Zimmermann J, Mai M, Mergel S, Mühlhaus T, Storchova Z, Morgan B. **2021**. Peroxiredoxins couple metabolism and cell division in an ultradian cycle. *Nature Chemical Biology* **17**: 477–484.

Anderson SI, Barton AD, Clayton S, Dutkiewicz S, Rynearson TA. **2021**. Marine phytoplankton functional types exhibit diverse responses to thermal change. *Nature Communications* **12**: 6413.

Andersson I, Backlund A. **2008**. Structure and function of Rubisco. *Plant physiology and biochemistry: PPB* **46**: 275–291.

Anning T, Nimer N, Merrett MJ, Brownlee C. **1996**. Costs and benefits of calcification in coccolithophorids. *Journal of Marine Systems* **9**: 45–56.

Armstrong E, Law CS. **2023**. Resilience of Emiliania huxleyi to future changes in subantarctic waters. *PLOS ONE* **18**: e0284415.

Armstrong RA, Lee C, Hedges JI, Honjo S, Wakeham SG. **2001**. A new, mechanistic model for organic carbon fluxes in the ocean based on the quantitative association of POC with ballast minerals. *Deep Sea Research Part II: Topical Studies in Oceanography* **49**: 219–236.

Arnold S, Kadenbach B. **1997**. Cell respiration is controlled by ATP, an allosteric inhibitor of cytochrome-c oxidase. *European Journal of Biochemistry* **249**: 350–354.

Asada K. **2006**. Production and Scavenging of Reactive Oxygen Species in Chloroplasts and Their Functions. *Plant Physiology* **141**: 391–396.

Asahina M, Okazaki M. **2004**. Inhibition of Crystal Growth in Coccolith Formation of Pleurochrysis Carterae by a potent Scale Inhibitor, (1-Hydroxyethylidene) Bisphosphonic Acid (HEBP). *Thalassas: An international journal of marine sciences, ISSN 0212-5919, Vol. 20, Nº. 1, 2004, pags. 51-58*.

Ashworth J, Coesel S, Lee A, Armbrust EV, Orellana MV, Baliga NS. **2013**. Genome-wide diel growth state transitions in the diatom Thalassiosira pseudonana. *Proceedings of the National Academy of Sciences* **110**: 7518–7523.

Atkins KC, Cross FR. **2018**. Interregulation of CDKA/CDK1 and the Plant-Specific Cyclin-Dependent Kinase CDKB in Control of the Chlamydomonas Cell Cycle. *The Plant Cell* **30**: 429–446.

Avrahami EM, Eyal Z, Varsano N, Zagoriy I, Mahamid J, Gal A. **2024**. Transport-Limited Growth of Coccolith Crystals. *Advanced Materials* **36**: 2309547.

Aylward FO, Eppley JM, Smith JM, Chavez FP, Scholin CA, DeLong EF. **2015**. Microbial community transcriptional networks are conserved in three domains at ocean basin scales. *Proceedings of the National Academy of Sciences* **112**: 5443–5448.

Bach LT, Bauke C, Meier KJS, Riebesell U, Schulz KG. **2012**. Influence of changing carbonate chemistry on morphology and weight of coccoliths formed by *Emiliania huxleyi*. *Biogeosciences* **9**: 3449–3463.

Bach LT, Mackinder LCM, Schulz KG, Wheeler G, Schroeder DC, Brownlee C, Riebesell U. **2013**. Dissecting the impact of CO2 and pH on the mechanisms of photosynthesis and calcification in the coccolithophore Emiliania huxleyi. *New Phytologist* **199**: 121–134.

Bach LT, Riebesell U, Gutowska MA, Federwisch L, Schulz KG. **2015**. A unifying concept of coccolithophore sensitivity to changing carbonate chemistry embedded in an ecological framework. *Progress in Oceanography* **135**: 125–138.

Bach LT, Riebesell U, Schulz KG. **2011**. Distinguishing between the effects of ocean acidification and ocean carbonation in the coccolithophore Emiliania huxleyi. *Limnology and Oceanography* **56**: 2040–2050.

Balaguer J, Koch F, Hassler C, Trimborn S. **2022**. Iron and manganese co-limit the growth of two phytoplankton groups dominant at two locations of the Drake Passage. *Communications Biology* **5**: 207.

Balch WM. **2018**. The Ecology, Biogeochemistry, and Optical Properties of Coccolithophores. *Annual Review of Marine Science* **10**: 71–98.

Balch W, Fritz J, Fernández E. **1996**. Decoupling of calcification and photosynthesis in the coccolithophore Emiliania huxleyi under steady-state light-limited growth. *Marine Ecology Progress Series* **142**: 87.

Balch WM, Holligan PM, Kilpatrick KA. **1992**. Calcification, photosynthesis and growth of the bloom-forming coccolithophore, *Emiliania huxleyi*. *Continental Shelf Research* **12**: 1353–1374.

Balch WM, Kilpatrick K, Holligan PM, Cucci T. **1993**. Coccolith Production and Detachment by Emiliania Huxleyi (prymnesiophyceae). *Journal of Phycology* **29**: 566–575.

Balotf S, Kavoosi G, Kholdebarin B. **2016**. Nitrate reductase, nitrite reductase, glutamine synthetase, and glutamate synthase expression and activity in response to different nitrogen sources in nitrogen-starved wheat seedlings. *Biotechnology and Applied Biochemistry* **63**: 220–229.

Barnum KJ, O'Connell MJ. **2014**. Cell Cycle Regulation by Checkpoints. *Methods in molecular biology (Clifton, N.J.)* **1170**: 29–40.

Barton S, Jenkins J, Buckling A, Schaum C-E, Smirnoff N, Raven JA, Yvon-Durocher G. **2020**. Evolutionary temperature compensation of carbon fixation in marine phytoplankton. *Ecology Letters* **23**: 722–733.

Barton S, Yvon-Durocher G. **2019**. Quantifying the temperature dependence of growth rate in marine phytoplankton within and across species. *Limnology and Oceanography* **64**: 2081–2091.

Beaufort L, Bolton CT, Sarr A-C, Suchéras-Marx B, Rosenthal Y, Donnadieu Y, Barbarin N, Bova S, Cornuault P, Gally Y, *et al*. 2022. Cyclic evolution of phytoplankton forced by changes in tropical seasonality. *Nature* **601**: 79–84.

Bec Bé, Collos Y, Vaquer A, Mouillot D, Souchu P. **2008**. Growth rate peaks at intermediate cell size in marine photosynthetic picoeukaryotes. *Limnology and Oceanography* **53**: 863–867.

Becker KW, Harke MJ, Mende DR, Muratore D, Weitz JS, DeLong EF, Dyhrman ST, Van Mooy BAS. **2021**. Combined pigment and metatranscriptomic analysis reveals highly synchronized diel patterns of phenotypic light response across domains in the open oligotrophic ocean. *The ISME Journal* **15**: 520–533.

Bendif EM, Nevado B, Wong ELY, Hagino K, Probert I, Young JR, Rickaby REM, Filatov DA. **2019**. Repeated species radiations in the recent evolution of the key marine phytoplankton lineage Gephyrocapsa. *Nature Communications* **10**: 4234.

Bendif EM, Probert I, Archontikis OA, Young JR, Beaufort L, Rickaby RE, Filatov D. **2023**. Rapid diversification underlying the global dominance of a cosmopolitan phytoplankton. *The ISME Journal* **17**: 630–640.

Ben-Joseph O, de Haan D, Rechav K, Shimoni E, Levin-Zaidman S, Langer G, Probert I, Wheeler GL, Gal A. **2023**. Crystallization of Coccolith Calcite at Different Life-Cycle Phases Exhibits Distinct Degrees of Cellular Confinement. *Small Structures* **4**: 2200353.

Benner I, Diner RE, Lefebvre SC, Li D, Komada T, Carpenter EJ, Stillman JH. **2013**. Emiliania huxleyi increases calcification but not expression of calcification-related genes in long-term exposure to elevated temperature and pCO2. *Philosophical Transactions of the Royal Society B: Biological Sciences* **368**: 20130049.

Bergstrom JD. **2023**. The lipogenic enzyme acetoacetyl-CoA synthetase and ketone body utilization for denovo lipid synthesis, a review. *Journal of Lipid Research* **64**: 100407.

Beyenbach KW. **1990**. Transport of magnesium across biological membranes. *Magnesium and Trace Elements* **9**: 233–254.

Bianco S, Bordiga M, Langer G, Ziveri P, Cerino F, Di Giulio AS, Lupi C. **2024**. Low sensitivity of a heavily-calcified coccolithophore under increasing CO_2: the case study of Helicosphaera carteri. *EGUsphere*: 1–25.

Bilcke G, Osuna-Cruz CM, Santana Silva M, Poulsen N, D'hondt S, Bulankova P, Vyverman W, De Veylder L, Vandepoele K. **2021**. Diurnal transcript profiling of the diatom Seminavis robusta reveals adaptations to a benthic lifestyle. *The Plant Journal* **107**: 315–336.

Bino E, Aram L, Paul D, Kadan Y, Clare D, Gilchrist JB, Elad N, Gal A. **2025**. The Role of Macromolecular Condensates in the Regulation of Intracellular Calcium Transport for Coccolith Formation. *Advanced Functional Materials* **35**: 2415344.

Björklund M. **2019**. Cell size homeostasis: Metabolic control of growth and cell division. *Biochimica et Biophysica Acta (BBA) - Molecular Cell Research* **1866**: 409–417.

Blanco-Ameijeiras S, Lebrato M, Stoll HM, Iglesias-Rodriguez MD, Méndez-Vicente A, Sett S, Müller MN, Oschlies A, Schulz KG. **2012**. Removal of organic magnesium in coccolithophore calcite. *Geochimica et Cosmochimica Acta* **89**: 226–239.

Blankenship ML, Wilbur KM. **1975**. Cobalt Effects on Cell Division and Calcium Uptake in the Coccolithophorid Cricosphaera Carterae (haptophyceae). *Journal of Phycology* **11**: 211–219.

van Bleijswijk JDL, Kempers RS, Veldhuis MJ, Westbroek P. **1994**. Cell and Growth Characteristics of Types a and B of Emiliania Huxleyi (prymnesiophyceae) as Determined by Flow Cytometry and Chemical Analyses. *Journal of Phycology* **30**: 230–241.

Bligny R, Gout E. **2017**. Regulation of Respiration by Cellular Key Parameters: Energy Demand, ADP, and Mg2+. In: Tcherkez G, Ghashghaie J, eds. Plant Respiration: Metabolic Fluxes and Carbon Balance. Cham: Springer International Publishing, 19–41.

Bloom AJ, Lancaster KM. **2018**. Manganese binding to Rubisco could drive a photorespiratory pathway that increases the energy efficiency of photosynthesis. *Nature Plants* **4**: 414–422.

Bolton CT, Hernández-Sánchez MT, Fuertes M-Á, González-Lemos S, Abrevaya L, Mendez-Vicente A, Flores J-A, Probert I, Giosan L, Johnson J, *et al*. 2016. Decrease in coccolithophore calcification and CO2 since the middle Miocene. *Nature Communications* **7**: 10284.

Bolton CT, Stoll HM. **2024**. Coccoliths as Recorders of Paleoceanography and Paleoclimate over the Past 66 Million Years.

Boon M, Rickard WDA, Rohl AL, Jones F. **2020**. Stabilization of Aragonite: Role of Mg2+ and Other Impurity Ions. *Crystal Growth & Design* **20**: 5006–5017.

Borah KD, Bhuyan J. **2017**. Magnesium porphyrins with relevance to chlorophylls. *Dalton Transactions* **46**: 6497–6509.

Bousquet L, Fainsod S, Decelle J, Murik O, Chevalier F, Gallet B, Templin R, Schwab Y, Avrahami Y, Koplovitz G, *et al.* 2025. Life cycle and morphogenetic differentiation in heteromorphic cell types of a cosmopolitan marine microalga. *New Phytologist* **245**: 1969–1984.

Bown PR. **2005**. Calcareous nannoplankton evolution: a tale of two oceans. *Micropaleontology* **51**: 299–308.

Bown PR, Lees JA, Young JR. **2004**. Calcareous nannoplankton evolution and diversity through time. In: Thierstein HR, Young JR, eds. Coccolithophores: From Molecular Processes to Global Impact. Berlin, Heidelberg: Springer, 481–508.

Boysen AK, Carlson LT, Durham BP, Groussman RD, Aylward FO, Ribalet F, Heal KR, White AE, DeLong EF, Armbrust EV, *et al.* 2021. Particulate Metabolites and Transcripts Reflect Diel Oscillations of Microbial Activity in the Surface Ocean. *mSystems* **6**: 10.1128/msystems.00896-20.

Bracher A, Whitney SM, Hartl FU, Hayer-Hartl M. **2017**. Biogenesis and Metabolic Maintenance of Rubisco. *Annual Review of Plant Biology* **68**: 29–60.

Bradford MM. **1976**. A rapid and sensitive method for the quantitation of microgram quantities of protein utilizing the principle of protein-dye binding. *Analytical Biochemistry* **72**: 248–254.

Bradley JP, Laws EA. **2024**. Interactive Effects of CO2, Temperature, and Nutrient Limitation on the Growth and Physiology of the Marine Coccolithophore Emiliania huxleyi (Prymnesiophyceae). *Water* **16**: 3184.

Brand LE. **1982**. Persistent diel rhythms in the chlorophyll fluorescence of marine phytoplankton species. *Marine Biology* **69**: 253–262.

Broecker W, Clark E. **2009**. Ratio of coccolith CaCO3 to foraminifera CaCO3 in late Holocene deep sea sediments. *Paleoceanography* **24**.

Broecker W, Yu J. **2011**. What do we know about the evolution of Mg to Ca ratios in seawater? *Paleoceanography* **26**.

Browning TJ, Moore CM. **2023**. Global analysis of ocean phytoplankton nutrient limitation reveals high prevalence of co-limitation. *Nature Communications* **14**: 5014.

Brownlee C, Davies M. **1995**. Calcification, photosynthesis and intracellular regulation in Emiliania huxleyi. Bulletin de l'Institute Océanographique.

Brownlee C, Langer G, Wheeler GL. **2021**. Coccolithophore calcification: Changing paradigms in changing oceans. *Acta Biomaterialia* **120**: 4–11.

Buitenhuis ET, De Baar HJW, Veldhuis MJW. **1999**. Photosynthesis and Calcification by Emiliania Huxleyi (prymnesiophyceae) as a Function of Inorganic Carbon Species. *Journal of Phycology* **35**: 949–959.

Buitenhuis ET, Pangerc T, Franklin DJ, Le Quéré C, Malin G. **2008**. Growth rates of six coccolithophorid strains as a function of temperature. *Limnology and Oceanography* **53**: 1181–1185.

Burlacot A. **2023**. Quantifying the roles of algal photosynthetic electron pathways: a milestone towards photosynthetic robustness. *New Phytologist* **240**: 2197–2203.

Burlacot A, Dao O, Auroy P, Cuiné S, Li-Beisson Y, Peltier G. **2022**. Alternative photosynthesis pathways drive the algal CO2-concentrating mechanism. *Nature* **605**: 366–371.

Calvo AM, Dabholkar A, Wyman EM, Lohmar JM, Cary JW. **2024**. Regulatory functions of homeobox domain transcription factors in fungi. *Applied and Environmental Microbiology* **90**: e02208-23.

Carlton JG, Jones H, Eggert US. **2020**. Membrane and organelle dynamics during cell division. *Nature Reviews Molecular Cell Biology* **21**: 151–166.

Chaudhry AH, Nayab S, Hussain SB, Ali M, Pan Z. **2021**. Current Understandings on Magnesium Deficiency and Future Outlooks for Sustainable Agriculture. *International Journal of Molecular Sciences* **22**: 1819.

Chauton MS, Winge P, Brembu T, Vadstein O, Bones AM. **2013**. Gene Regulation of Carbon Fixation, Storage, and Utilization in the Diatom Phaeodactylum tricornutum Acclimated to Light/Dark Cycles. *Plant Physiology* **161**: 1034–1048.

Chichkova S, Arellano J, Vance CP, Hernández G. **2001**. Transgenic tobacco plants that overexpress alfalfa NADH-glutamate synthase have higher carbon and nitrogen content. *Journal of Experimental Botany* **52**: 2079–2087.

Chisholm SW, Brand LE. **1981**. Persistence of cell division phasing in marine phytoplankton in continuous light after entrainment to light: Dark cycles. *Journal of Experimental Marine Biology and Ecology* **51**: 107–118.

Cho YB, Boyd RA, Ren Y, Lee M-S, Jones SI, Ruiz-Vera UM, McGrath JM, Masters MD, Ort DR. **2024**. Reducing chlorophyll levels in seed-filling stages results in higher seed nitrogen without impacting canopy carbon assimilation. *Plant, Cell & Environment* **47**: 278–293.

Coesel SN, Durham BP, Groussman RD, Hu SK, Caron DA, Morales RL, Ribalet F, Armbrust EV. **2021**. Diel transcriptional oscillations of light-sensitive regulatory elements in open-ocean eukaryotic plankton communities. *Proceedings of the National Academy of Sciences* **118**: e2011038118.

Colin A, Micali G, Faure L, Cosentino Lagomarsino M, van Teeffelen S. **2021**. Two different cell-cycle processes determine the timing of cell division in Escherichia coli. *eLife* **10**: e67495.

Corstjens PLAM, Araki Y, González EL. **2001**. A COCCOLITHOPHORID CALCIFYING VESICLE WITH A VACUOLAR-TYPE ATPASE PROTON PUMP: CLONING AND IMMUNOLOCALIZATION OF THE V0 SUBUNIT c. *Journal of Phycology* **37**: 71–78.

Corstjens PLAM, Van Der Kooij A, Linschooten C, Brouwers G-J, Westbroek P, Jong EW de V. **1998**. Gpa, a Calcium-Binding Protein in the Coccolithophorid Emiliania Huxleyi (prymnesiophyceae). *Journal of Phycology* **34**: 622–630.

Costa A, Resentini F, Buratti S, Bonza MC. **2023**. Plant Ca2+-ATPases: From biochemistry to signalling. *Biochimica et Biophysica Acta (BBA) - Molecular Cell Research* **1870**: 119508.

Cox J, Hein MY, Luber CA, Paron I, Nagaraj N, Mann M. **2014**. Accurate Proteome-wide Label-free Quantification by Delayed Normalization and Maximal Peptide Ratio Extraction, Termed MaxLFQ. *Molecular & Cellular Proteomics : MCP* **13**: 2513–2526.

Cox J, Mann M. **2008**. MaxQuant enables high peptide identification rates, individualized p.p.b.-range mass accuracies and proteome-wide protein quantification. *Nature Biotechnology* **26**: 1367–1372.

Cros L, Kleijne A, Zeltner A, Billard C, Young JR. **2000**. New examples of holococcolith–heterococcolith combination coccospheres and their implications for coccolithophorid biology. *Marine Micropaleontology* **39**: 1–34.

Cross FR. **2020**. Regulation of Multiple Fission and Cell-Cycle-Dependent Gene Expression by CDKA1 and the Rb-E2F Pathway in Chlamydomonas. *Current Biology* **30**: 1855-1865.e4.

Cross FR, Umen JG. **2015**. The Chlamydomonas cell cycle. *The Plant Journal* **82**: 370–392.

Crudeli D, Young JR, Erba E, Geisen M, Ziveri P, de Lange GJ, Slomp CP. **2006**. Fossil record of holococcoliths and selected hetero-holococcolith associations from the Mediterranean (Holocene–late Pleistocene): Evaluation of carbonate diagenesis and palaeoecological–palaeocenographic implications. *Palaeogeography, Palaeoclimatology, Palaeoecology* **237**: 191–212.

Csikász-Nagy A. **2009**. Computational systems biology of the cell cycle. *Briefings in Bioinformatics* **10**: 424–434.

D'Amario B, Pérez C, Grelaud M, Pitta P, Krasakopoulou E, Ziveri P. **2020**. Coccolithophore community response to ocean acidification and warming in the Eastern Mediterranean Sea: results from a mesocosm experiment. *Scientific Reports* **10**: 12637.

D'Amario B, Ziveri P, Grelaud M, Oviedo A, Kralj M. **2017**. Coccolithophore haploid and diploid distribution patterns in the Mediterranean Sea: can a haplo-diploid life cycle be advantageous under climate change? *Journal of Plankton Research* **39**: 781–794.

Daniels CJ, Poulton AJ, Young JR, Esposito M, Humphreys MP, Ribas-Ribas M, Tynan E, Tyrrell T. **2016**. Species-specific calcite production reveals Coccolithus pelagicus as the key calcifier in the Arctic Ocean. *Marine Ecology Progress Series* **555**: 29–47.

Daniels CJ, Sheward RM, Poulton AJ. **2014**. Biogeochemical implications of comparative growth rates of *Emiliania huxleyi* and *Coccolithus* species. *Biogeosciences* **11**: 6915–6925.

Dao O, Bertrand M, Alseekh S, Veillet F, Auroy P, Nguyen P-C, Légeret B, Epting V, Morin A, Cuiné S, *et al*. 2025. The green algae CO2 concentrating mechanism and photorespiration jointly operate during acclimation to low CO2. *Nature Communications* **16**: 5296.

Das K, Roychoudhury A. **2014**. Reactive oxygen species (ROS) and response of antioxidants as ROS-scavengers during environmental stress in plants. *Frontiers in Environmental Science* **2**.

von Dassow P, Montresor M. **2011**. Unveiling the mysteries of phytoplankton life cycles: patterns and opportunities behind complexity. *Journal of Plankton Research* **33**: 3–12.

von Dassow P, Muñoz Farías PV, Pinon S, Velasco-Senovilla E, Anguita-Salinas S. **2021**. Do Differences in Latitudinal Distributions of Species and Organelle Haplotypes Reflect Thermal Reaction Norms Within the Emiliania/Gephyrocapsa Complex? *Frontiers in Marine Science* **8**.

von Dassow P, Ogata H, Probert I, Wincker P, Da Silva C, Audic S, Claverie J-M, de Vargas C. **2009**. Transcriptome analysis of functional differentiation between haploid and diploid cells of Emiliania huxleyi, a globally significant photosynthetic calcifying cell. *Genome Biology* **10**: R114.

Davis KJ, Dove PM, De Yoreo JJ. **2000**. The Role of Mg2+ as an Impurity in Calcite Growth. *Science* **290**: 1134–1137.

Dedman CJ, Barton S, Fournier M, Rickaby REM. **2023**. The cellular response to ocean warming in Emiliania huxleyi. *Frontiers in Microbiology* **14**.

DeLong JP, Okie JG, Moses ME, Sibly RM, Brown JH. **2010**. Shifts in metabolic scaling, production, and efficiency across major evolutionary transitions of life. *Proceedings of the National Academy of Sciences* **107**: 12941–12945.

Devi Borah K, Bhuyan J. **2017**. Magnesium porphyrins with relevance to chlorophylls. *Dalton Transactions* **46**: 6497–6509.

Diaz BP, Zelzion E, Halsey K, Gaube P, Behrenfeld M, Bidle KD. **2023**. Marine phytoplankton downregulate core photosynthesis and carbon storage genes upon rapid mixed layer shallowing. *The ISME Journal* **17**: 1074–1088.

Diner RE, Benner I, Passow U, Komada T, Carpenter EJ, Stillman JH. **2015**. Negative effects of ocean acidification on calcification vary within the coccolithophore genus Calcidiscus. *Marine Biology* **162**: 1287–1305.

Dodd AN, Belbin FE, Frank A, Webb AAR. **2015**. Interactions between circadian clocks and photosynthesis for the temporal and spatial coordination of metabolism. *Frontiers in Plant Science* **6**.

Dolch L-J, Lupette J, Tourcier G, Bedhomme M, Collin S, Magneschi L, Conte M, Seddiki K, Richard C, Corre E, *et al*. 2017. Nitric Oxide Mediates Nitrite-Sensing and Acclimation and Triggers a Remodeling of Lipids. *Plant Physiology* **175**: 1407–1423.

Driver T, Trivedi DK, McIntosh OA, Dean AP, Goodacre R, Pittman JK. **2017**. Two Glycerol-3-Phosphate Dehydrogenases from Chlamydomonas Have Distinct Roles in Lipid Metabolism1[CC-BY]. *Plant Physiology* **174**: 2083–2097.

Durak GM, Brownlee C, Wheeler GL. **2017**. The role of the cytoskeleton in biomineralisation in haptophyte algae. *Scientific Reports* **7**: 15409.

Durak GM, Taylor AR, Walker CE, Probert I, de Vargas C, Audic S, Schroeder D, Brownlee C, Wheeler GL. **2016**. A role for diatom-like silicon transporters in calcifying coccolithophores. *Nature Communications* **7**: 10543.

Eyal Z, Krounbi L, Ben Joseph O, Avrahami EM, Pinkas I, Peled-Zehavi H, Gal A. **2022**. The variability in the structural and functional properties of coccolith base plates. *Acta Biomaterialia* **148**: 336–344.

Ezard THG, Aze T, Pearson PN, Purvis A. **2011**. Interplay Between Changing Climate and Species' Ecology Drives Macroevolutionary Dynamics. *Science* **332**: 349–351.

Falkowski PG, Katz ME, Knoll AH, Quigg A, Raven JA, Schofield O, Taylor FJR. **2004**. The Evolution of Modern Eukaryotic Phytoplankton. *Science* **305**: 354–360.

Fan X, Batchelor-McAuley C, Yang M, Barton S, Rickaby REM, Bouman HA, Compton RG. **2022**. Quantifying the Extent of Calcification of a Coccolithophore Using a Coulter Counter. *Analytical Chemistry* **94**: 12664–12672.

Fanesi A, Wagner H, Wilhelm C. **2017**. Phytoplankton growth rate modelling: can spectroscopic cell chemotyping be superior to physiological predictors? *Proceedings of the Royal Society B: Biological Sciences* **284**: 20161956.

Fantle MS, DePaolo DJ. **2006**. Sr isotopes and pore fluid chemistry in carbonate sediment of the Ontong Java Plateau: Calcite recrystallization rates and evidence for a rapid rise in seawater Mg over the last 10 million years. *Geochimica et Cosmochimica Acta* **70**: 3883–3904.

Faucher G, Hoffmann L, Bach LT, Bottini C, Erba E, Riebesell U. **2017**. Impact of trace metal concentrations on coccolithophore growth and morphology: laboratory simulations of Cretaceous stress. *Biogeosciences* **14**: 3603–3613.

Faucher G, Riebesell U, Bach LT. **2020**. Can morphological features of coccolithophores serve as a reliable proxy to reconstruct environmental conditions of the past? *Climate of the Past* **16**: 1007–1025.

Feeney KA, Hansen LL, Putker M, Olivares-Yañez C, Day J, Eades LJ, Larrondo LF, Hoyle NP, O'Neill JS, van Ooijen G. **2016**. Daily magnesium fluxes regulate cellular timekeeping and energy balance. *Nature* **532**: 375–379.

Fenech M. **2012**. Folate (vitamin B9) and vitamin B12 and their function in the maintenance of nuclear and mitochondrial genome integrity. *Mutation Research/Fundamental and Molecular Mechanisms of Mutagenesis* **733**: 21–33.

Feng Y, Roleda MY, Armstrong E, Boyd PW, Hurd CL. **2017**. Environmental controls on the growth, photosynthetic and calcification rates of a Southern Hemisphere strain of the coccolithophore Emiliania huxleyi. *Limnology and Oceanography* **62**: 519–540.

Feng Y, Roleda MY, Armstrong E, Summerfield TC, Law CS, Hurd CL, Boyd PW. **2020**. Effects of multiple drivers of ocean global change on the physiology and functional gene expression of the coccolithophore Emiliania huxleyi. *Global Change Biology* **26**: 5630–5645.

Feng Y, Warner ME, Zhang Y, Sun J, Fu F-X, Rose JM, Hutchins DA. **2008**. Interactive effects of increased pCO2, temperature and irradiance on the marine coccolithophore Emiliania huxleyi (Prymnesiophyceae). *European Journal of Phycology* **43**: 87–98.

Ferrari C, Proost S, Janowski M, Becker J, Nikoloski Z, Bhattacharya D, Price D, Tohge T, Bar-Even A, Fernie A, *et al*. 2019. Kingdom-wide comparison reveals the evolution of diurnal gene expression in Archaeplastida. *Nature Communications* **10**: 737.

Fichtinger-Schepman AMJ, Kamerling JP, Versluis C, Vliegenthart JFG. **1981**. Structural studies of the methylated, acidic polysaccharide associated with coccoliths of *Emiliania huxleyi* (lohmann) kamptner. *Carbohydrate Research* **93**: 105–123.

Finkel ZV. **2001**. Light absorption and size scaling of light-limited metabolism in marine diatoms. *Limnology and Oceanography* **46**: 86–94.

Finkel ZV, Beardall J, Flynn KJ, Quigg A, Rees TAV, Raven JA. **2010**. Phytoplankton in a changing world: cell size and elemental stoichiometry. *Journal of Plankton Research* **32**: 119–137.

Finkel ZV, Irwin AJ, Schofield O. **2004**. Resource limitation alters the 3/4 size scaling of metabolic rates in phytoplankton. *Marine Ecology Progress Series* **273**: 269–279.

Fiorini S, Middelburg JJ, Gattuso J-P. **2011**. Testing the Effects of Elevated Pco2 on Coccolithophores (prymnesiophyceae): Comparison Between Haploid and Diploid Life Stages. *Journal of Phycology* **47**: 1281–1291.

Flynn KJ, Raven JA, Rees TAV, Finkel Z, Quigg A, Beardall J. **2010**. Is the Growth Rate Hypothesis Applicable to Microalgae? *Journal of Phycology* **46**: 1–12.

Frada MJ, Bendif EM, Keuter S, Probert I. **2019**. The private life of coccolithophores. *Perspectives in Phycology*: 11–30.

Frada MJ, Bidle KD, Probert I, de Vargas C. **2012**. In situ survey of life cycle phases of the coccolithophore Emiliania huxleyi (Haptophyta). *Environmental Microbiology* **14**: 1558–1569.

Frada M, Probert I, Allen MJ, Wilson WH, de Vargas C. **2008**. The "Cheshire Cat" escape strategy of the coccolithophore Emiliania huxleyi in response to viral infection. *Proceedings of the National Academy of Sciences* **105**: 15944–15949.

Fuentes SI, Allen DJ, Ortiz-Lopez A, Hernández G. **2001**. Over-expression of cytosolic glutamine synthetase increases photosynthesis and growth at low nitrogen concentrations. *Journal of Experimental Botany* **52**: 1071–1081.

Fujiwara T, Hirooka S, Ohbayashi R, Onuma R, Miyagishima S. **2020**. Relationship between Cell Cycle and Diel Transcriptomic Changes in Metabolism in a Unicellular Red Alga. *Plant Physiology* **183**: 1484–1501.

Fukuda S, Suzuki Y, Shiraiwa Y. **2014**. Difference in physiological responses of growth, photosynthesis and calcification of the coccolithophore Emiliania huxleyi to acidification by acid and CO2 enrichment. *Photosynthesis Research* **121**: 299–309.

Gafar NA, Eyre BD, Schulz KG. **2019**. A comparison of species specific sensitivities to changing light and carbonate chemistry in calcifying marine phytoplankton. *Scientific Reports* **9**: 2486.

Gafar NA, Schulz KG. **2018**. A three-dimensional niche comparison of *Emiliania huxleyi* and *Gephyrocapsa oceanica*: reconciling observations with projections. *Biogeosciences* **15**: 3541–3560.

Gal A, Sorrentino A, Kahil K, Pereiro E, Faivre D, Scheffel A. **2018**. Native-state imaging of calcifying and noncalcifying microalgae reveals similarities in their calcium storage organelles. *Proceedings of the National Academy of Sciences* **115**: 11000–11005.

Gal A, Wirth R, Kopka J, Fratzl P, Faivre D, Scheffel A. **2016**. Macromolecular recognition directs calcium ions to coccolith mineralization sites. *Science* **353**: 590–593.

Gao K, Ruan Z, Villafañe VE, Gattuso J-P, Helbling EW. **2009**. Ocean acidification exacerbates the effect of UV radiation on the calcifying phytoplankter Emiliania huxleyi. *Limnology and Oceanography* **54**: 1855–1862.

Gao Y, Smith GJ, Alberte RS. **1992**. Light regulation of nitrate reductase in Ulya fenestrata (Chlorophyceae). *Marine Biology* **112**: 691–696.

Garrido JL, Brunet C, Rodríguez F. **2016**. Pigment variations in Emiliania huxleyi (CCMP370) as a response to changes in light intensity or quality. *Environmental Microbiology* **18**: 4412–4425.

Gattuso J-P, Epitalon J-M, Heloise L, Orr J, Gentili B, Hagens M, Hofmann A, Mueller J-D, Proye A, Rae J, *et al*. 2024. seacarb: Seawater Carbonate Chemistry.

Gebühr C, Sheward RM, Herrle JO, Bollmann J. **2021**. Strain-specific morphological response of the dominant calcifying phytoplankton species Emiliania huxleyi to salinity change. *PloS One* **16**: e0246745.

Geigenberger P, Riewe D, Fernie AR. **2010**. The central regulation of plant physiology by adenylates. *Trends in Plant Science* **15**: 98–105.

Gerecht AC, Šupraha L, Edvardsen B, Probert I, Henderiks J. **2014**. High temperature decreases the PIC / POC ratio and increases phosphorus requirements in *Coccolithus pelagicus* (Haptophyta). *Biogeosciences* **11**: 3531–3545.

Gerecht AC, Šupraha L, Langer G, Henderiks J. **2018**. Phosphorus limitation and heat stress decrease calcification in *Emiliania huxleyi*. *Biogeosciences* **15**: 833–845.

Gibbs SJ, Poulton AJ, Bown PR, Daniels CJ, Hopkins J, Young JR, Jones HL, Thiemann GJ, O'Dea SA, Newsam C. **2013**. Species-specific growth response of coccolithophores to Palaeocene–Eocene environmental change. *Nature Geoscience* **6**: 218–222.

Gibbs SJ, Sheward RM, Bown PR, Poulton AJ, Alvarez SA. **2018**. Warm plankton soup and red herrings: calcareous nannoplankton cellular communities and the Palaeocene–Eocene Thermal Maximum. *Philosophical Transactions of the Royal Society A: Mathematical, Physical and Engineering Sciences* **376**: 20170075.

Giordano M, Palmucci M, Raven JA. **2015**. Growth rate hypothesis and efficiency of protein synthesis under different sulphate concentrations in two green algae. *Plant, Cell & Environment* **38**: 2313–2317.

Glazier DS. **2022**. How Metabolic Rate Relates to Cell Size. *Biology* **11**: 1106.

Godrijan J, Drapeau DT, Balch WM. **2022**. Osmotrophy of dissolved organic carbon by coccolithophores in darkness. *New Phytologist* **233**: 781–794.

Gore S, Renforth P, Perkins R. **2019**. The potential environmental response to increasing oceanalkalinity for negative emissions. *Mitigation and Adaptation Strategies for Global Change* **24**: 1191–1211.

Gregg WW, Casey NW. **2007**. Modeling coccolithophores in the global oceans. *Deep Sea Research Part II: Topical Studies in Oceanography* **54**: 447–477.

Grettenberger CL, Abou-Shanab R, Hamilton TL. **2024**. Limiting factors in the operation of photosystems I and II in cyanobacteria. *Microbial Biotechnology* **17**: e14519.

Grubb AR, Johns CT, Hayden MG, Subhas AV, Thamatrakoln K, Bidle KD. **2024**. Calcification increases carbon supply, photosynthesis, and growth in a globally distributed coccolithophore. *Limnology and Oceanography* **69**: 2152–2166.

Guerreiro CV, Baumann K-H, Brummer G-JA, Fischer G, Korte LF, Merkel U, Sá C, de Stigter H, Stuut J-BW. **2017**. Coccolithophore fluxes in the open tropical North Atlantic: influence of thermocline depth, Amazon water, and Saharan dust. *Biogeosciences* **14**: 4577–4599.

Guerreiro CV, Baumann K-H, Brummer G-JA, Valente A, Fischer G, Ziveri P, Brotas V, Stuut J-BW. **2021**. Carbonate fluxes by coccolithophore species between NW Africa and the Caribbean: Implications for the biological carbon pump. *Limnology and Oceanography* **66**: 3190–3208.

Guitián J, Dunkley Jones T, Hernández-Almeida I, Löffel T, Stoll HM. **2020**. Adaptations of Coccolithophore Size to Selective Pressures During the Oligocene to Early Miocene High CO2 World. *Paleoceanography and Paleoclimatology* **35**: e2020PA003918.

Guitián J, Fuertes MÁ, Flores J-A, Hernández-Almeida I, Stoll H. **2022**. Variation in calcification of *Reticulofenestra* coccoliths over the Oligocene–Early Miocene. *Biogeosciences* **19**: 5007–5019.

Guo X, Chen L. **2024**. From G1 to M: a comparative study of methods for identifying cell cycle phases. *Briefings in Bioinformatics* **25**: bbad517.

Guo T, Herman JK. **2022**. Magnesium Modulates Bacillus subtilis Cell Division Frequency. *Journal of Bacteriology* **205**: e00375-22.

Guo W, Nazim H, Liang Z, Yang D. **2016**. Magnesium deficiency in plants: An urgent problem. *The Crop Journal* **4**: 83–91.

Hannisdal B, Henderiks J, Liow LH. **2012**. Long-term evolutionary and ecological responses of calcifying phytoplankton to changes in atmospheric 2. *Global Change Biology* **18**: 3504–3516.

Hardie LA. **1996**. Secular variation in seawater chemistry: An explanation for the coupled secular variation in the mineralogies of marine limestones and potash evaporites over the past 600 m.y. *Geology* **24**: 279–283.

Harding LW, Meeson BW, Prézelin BB, Sweeney BM. **1981**. Diel periodicity of photosynthesis in marine phytoplankton. *Marine Biology* **61**: 95–105.

Harding LW, Prézelin BB, Sweeney BM, Cox JL. **1982**. Diel oscillations of the photosynthesis-irradiance (P-I) relationship in natural assemblages of phytoplankton. *Marine Biology* **67**: 167–178.

Hawco NJ, Tagliabue A, Twining BS. **2022**. Manganese Limitation of Phytoplankton Physiology and Productivity in the Southern Ocean. *Global Biogeochemical Cycles* **36**: e2022GB007382.

Haydon MJ, Román Á, Arshad W. **2015**. Nutrient homeostasis within the plant circadian network. *Frontiers in Plant Science* **6**: 299.

Haythorne E, Lloyd M, Walsby-Tickle J, Tarasov AI, Sandbrink J, Portillo I, Exposito RT, Sachse G, Cyranka M, Rohm M, *et al.* 2022. Altered glycolysis triggers impaired mitochondrial metabolism and mTORC1 activation in diabetic β-cells. *Nature Communications* **13**: 6754.

Heidenreich E, Wördenweber R, Kirschhöfer F, Nusser M, Friedrich F, Fahl K, Kruse O, Rost B, Franzreb M, Brenner-Weiß G, *et al.* 2019. Ocean acidification has little effect on the biochemical composition of the coccolithophore Emiliania huxleyi. *PLOS ONE* **14**: e0218564.

Heinrichs AL, Hardorp OJ, Hillebrand H, Schott T, Striebel M. **2024**. Direct and indirect cumulative effects of temperature, nutrients, and light on phytoplankton growth. *Ecology and Evolution* **14**: e70073.

Henderiks J. **2008**. Coccolithophore size rules — Reconstructing ancient cell geometry and cellular calcite quota from fossil coccoliths. *Marine Micropaleontology* **67**: 143–154.

Henderiks J, Bartol M, Pige N, Karatsolis B-Th, Lougheed BC. **2020**. Shifts in Phytoplankton Composition and Stepwise Climate Change During the Middle Miocene. *Paleoceanography and Paleoclimatology* **35**: e2020PA003915.

Hennessey TL, Field CB. **1991**. Circadian Rhythms in Photosynthesis : Oscillations in Carbon Assimilation and Stomatal Conductance under Constant Conditions. *Plant Physiology* **96**: 831–836.

Hennessey TL, Freeden AL, Field CB. **1993**. Environmental effects on circadian rhythms in photosynthesis and stomatal opening. *Planta* **189**: 369–376.

Herfort L, Loste E, Meldrum F, Thake B. **2004**. Structural and physiological effects of calcium and magnesium in *Emiliania huxleyi* (Lohmann) Hay and Mohler. *Journal of Structural Biology* **148**: 307–314.

Herfort L, Thake B, Roberts J. **2002**. Acquisition and use of bicarbonate by Emiliania huxleyi. *The New Phytologist* **156**: 427–436.

Hermans C, Conn SJ, Chen J, Xiao Q, Verbruggen N. **2013**. An update on magnesium homeostasis mechanisms in plants. *Metallomics: Integrated Biometal Science* **5**: 1170–1183.

Hermans C, Vuylsteke M, Coppens F, Craciun A, Inzé D, Verbruggen N. **2010**. Early transcriptomic changes induced by magnesium deficiency in Arabidopsis thaliana reveal

the alteration of circadian clock gene expression in roots and the triggering of abscisic acid-responsive genes. *New Phytologist* **187**: 119–131.

Hermoso M, Lefeuvre B, Minoletti F, Rafélis M de. **2017**. Extreme strontium concentrations reveal specific biomineralization pathways in certain coccolithophores with implications for the Sr/Ca paleoproductivity proxy. *PLOS ONE* **12**: e0185655.

Hernández Limón MD, Hennon GMM, Harke MJ, Frischkorn KR, Haley ST, Dyhrman ST. **2020**. Transcriptional patterns of Emiliania huxleyi in the North Pacific Subtropical Gyre reveal the daily rhythms of its metabolic potential. *Environmental Microbiology* **22**: 381–396.

Hersey RL, Swift E. **1976**. Nitrate Reductase Activity of Amphidinium Carteri and Cachonina Niei (dinophyceae) in Batch Culture: Diel Periodicity and Effects of Light Intensity and Ammonia. *Journal of Phycology* **12**: 36–44.

Higgins JA, Schrag DP. **2015**. The Mg isotopic composition of Cenozoic seawater – evidence for a link between Mg-clays, seawater Mg/Ca, and climate. *Earth and Planetary Science Letters* **416**: 73–81.

Hillebrand H, Acevedo-Trejos E, Moorthi SD, Ryabov A, Striebel M, Thomas PK, Schneider M-L. **2022**. Cell size as driver and sentinel of phytoplankton community structure and functioning. *Functional Ecology* **36**: 276–293.

Hirayama T, Shinozaki K. **2010**. Research on plant abiotic stress responses in the post-genome era: past, present and future. *The Plant Journal* **61**: 1041–1052.

Ho T-Y, Quigg A, Finkel ZV, Milligan AJ, Wyman K, Falkowski PG, Morel FMM. **2003**. The Elemental Composition of Some Marine Phytoplankton. *Journal of Phycology* **39**: 1145–1159.

Hofmann P, Chatzinotas A, Harpole WS, Dunker S. **2019**. Temperature and stoichiometric dependence of phytoplankton traits. *Ecology* **100**: e02875.

Holligan PM, Fernández E, Aiken J, Balch WM, Boyd P, Burkill PH, Finch M, Groom SB, Malin G, Muller K, *et al.* 1993. A biogeochemical study of the coccolithophore, Emiliania huxleyi, in the North Atlantic. *Global Biogeochemical Cycles* **7**: 879–900.

Holtz L-M, Thoms S, Langer G, Wolf-Gladrow DA. **2013**. Substrate supply for calcite precipitation in Emiliania huxleyi: assessment of different model approaches. *Journal of Phycology* **49**: 417–426.

Holtz L-M, Wolf-Gladrow D, Thoms S. **2015a**. Numerical cell model investigating cellular carbon fluxes in *Emiliania huxleyi*. *Journal of Theoretical Biology* **364**: 305–315.

Holtz L-M, Wolf-Gladrow D, Thoms S. **2015b**. Simulating the effects of light intensity and carbonate system composition on particulate organic and inorganic carbon production in *Emiliania huxleyi*. *Journal of Theoretical Biology* **372**: 192–204.

Holtz L-M, Wolf-Gladrow D, Thoms S. **2017**. Stable carbon isotope signals in particulate organic and inorganic carbon of coccolithophores – A numerical model study for *Emiliania huxleyi*. *Journal of Theoretical Biology* **420**: 117–127.

Hopkins J, Henson SA, Painter SC, Tyrrell T, Poulton AJ. **2015**. Phenological characteristics of global coccolithophore blooms. *Global Biogeochemical Cycles* **29**: 239–253.

Hopkins J, Henson SA, Poulton AJ, Balch WM. **2019**. Regional Characteristics of the Temporal Variability in the Global Particulate Inorganic Carbon Inventory. *Global Biogeochemical Cycles* **33**: 1328–1338.

Hoppe CJM, Langer G, Rost B. **2011**. *Emiliania huxleyi* shows identical responses to elevated pCO2 in TA and DIC manipulations. *Journal of Experimental Marine Biology and Ecology* **406**: 54–62.

Horita J, Zimmermann H, Holland HD. **2002**. Chemical evolution of seawater during the Phanerozoic: Implications from the record of marine evaporites. *Geochimica et Cosmochimica Acta* **66**: 3733–3756.

Houdan A, Probert I, Lenning KV, Lefebvre S. **2005**. Comparison of photosynthetic responses in diploid and haploid life-cycle phases of Emiliania huxleyi (Prymnesiophyceae). *Marine Ecology Progress Series* **292**: 139–146.

Houdan A, Probert I, Zatylny C, Véron B, Billard C. **2006**. Ecology of oceanic coccolithophores. I. Nutritional preferences of the two stages in the life cycle of Coccolithus braarudii and Calcidiscus leptoporus. *Aquatic Microbial Ecology* **44**: 291–301.

Hughes ME, Hogenesch JB, Kornacker K. **2010**. JTK_CYCLE: An Efficient Nonparametric Algorithm for Detecting Rhythmic Components in Genome-Scale Data Sets. *Journal of Biological Rhythms* **25**: 372–380.

Huysman MJJ, Vyverman W, De Veylder L. **2014**. Molecular regulation of the diatom cell cycle. *Journal of Experimental Botany* **65**: 2573–2584.

Iglesias-Rodriguez MD, Halloran PR, Rickaby REM, Hall IR, Colmenero-Hidalgo E, Gittins JR, Green DRH, Tyrrell T, Gibbs SJ, von Dassow P, *et al*. 2008. Phytoplankton Calcification in a High-CO2 World. *Science* **320**: 336–340.

Iglesias-Rodriguez MD, Jones BM, Blanco-Ameijeiras S, Greaves M, Huete-Ortega M, Lebrato M. **2017**. Physiological responses of coccolithophores to abrupt exposure of naturally low pH deep seawater. *PLOS ONE* **12**: e0181713.

Ilsley JL, Sudol M, Winder SJ. **2002**. The WW domain: Linking cell signalling to the membrane cytoskeleton. *Cellular Signalling* **14**: 183–189.

Imai R, Farida M, Sato T, Iryu Y. **2015**. Evidence for eutrophication in the northwestern Pacific and eastern Indian oceans during the Miocene to Pleistocene based on the

nannofossil accumulation rate, *Discoaster* abundance, and coccolith size distribution of *Reticulofenestra*. *Marine Micropaleontology* **116**: 15–27.

Inomura K, Omta AW, Talmy D, Bragg J, Deutsch C, Follows MJ. **2020**. A Mechanistic Model of Macromolecular Allocation, Elemental Stoichiometry, and Growth Rate in Phytoplankton. *Frontiers in Microbiology* **11**.

Jamali Jaghdani S, Jahns P, Tränkner M. **2021**. The impact of magnesium deficiency on photosynthesis and photoprotection in *Spinacia oleracea*. *Plant Stress* **2**: 100040.

Jiang X, Zhang Y, Hutchins DA, Gao K. **2022**. Nitrogen-limitation exacerbates the impact of ultraviolet radiation on the coccolithophore *Gephyrocapsa oceanica*. *Journal of Photochemistry and Photobiology B: Biology* **226**: 112368.

Jin P, Ding J, Xing T, Riebesell U, Gao K. **2017**. High levels of solar radiation offset impacts of ocean acidification on calcifying and non-calcifying strains of Emiliania huxleyi. *Marine Ecology Progress Series* **568**: 47–58.

Jochem FJ, Meyerdierks D. **1999**. Cytometric measurement of the DNA cell cycle in the presence of chlorophyll autofluorescence in marine eukaryotic phytoplankton by the blue-light excited dye YOYO-1. *Marine Ecology Progress Series* **185**: 301–307.

Johnsen SAL, Bollmann J, Gebuehr C, Herrle JO. **2019**. Relationship between coccolith length and thickness in the coccolithophore species Emiliania huxleyi and Gephyrocapsa oceanica. *PLOS ONE* **14**: e0220725.

Jones EM, Fenton M, Meredith MP, Clargo NM, Ossebaar S, Ducklow HW, Venables HJ, de Baar HJW. **2017**. Ocean acidification and calcium carbonate saturation states in the coastal zone of the West Antarctic Peninsula. *Deep Sea Research Part II: Topical Studies in Oceanography* **139**: 181–194.

Jones BM, Iglesias-Rodriguez MD, Skipp PJ, Edwards RJ, Greaves MJ, Young JR, Elderfield H, O'Connor CD. **2013**. Responses of the Emiliania huxleyi Proteome to Ocean Acidification. *PLOS ONE* **8**: e61868.

de Jong EW, Bosch L, Westbroek P. **1976**. Isolation and characterization of a Ca2+ - binding polysaccharide associated with coccoliths of Emiliania huxleyi (Lohmann) Kamptner. *European Journal of Biochemistry* **70**: 611–621.

Joseph L, Villareal TA. **1998**. Nitrate reductase activity as a measure of nitrogen incorporation in *Rhizosolenia formosa* (H. Peragallo): Internal nitrate and diel effects. *Journal of Experimental Marine Biology and Ecology* **229**: 159–176.

Kadan Y, Aram L, Shimoni E, Levin-Zaidman S, Rosenwasser S, Gal A. **2020**. In situ electron microscopy characterization of intracellular ion pools in mineral forming microalgae. *Journal of Structural Biology* **210**: 107465.

Kadan Y, Tollervey F, Varsano N, Mahamid J, Gal A. **2021**. Intracellular nanoscale architecture as a master regulator of calcium carbonate crystallization in marine microalgae. *Proceedings of the National Academy of Sciences* **118**: e2025670118.

Kaffes A, Thoms S, Trimborn S, Rost B, Langer G, Richter K-U, Köhler A, Norici A, Giordano M. **2010**. Carbon and nitrogen fluxes in the marine coccolithophore *Emiliania huxleyi* grown under different nitrate concentrations. *Journal of Experimental Marine Biology and Ecology* **393**: 1–8.

Kampinga HH, Andreasson C, Barducci A, Cheetham ME, Cyr D, Emanuelsson C, Genevaux P, Gestwicki JE, Goloubinoff P, Huerta-Cepas J, *et al.* 2019. Function, evolution, and structure of J-domain proteins. *Cell Stress & Chaperones* **24**: 7–15.

Kanai F, Marignani PA, Sarbassova D, Yagi R, Hall RA, Donowitz M, Hisaminato A, Fujiwara T, Ito Y, Cantley LC, *et al.* 2000. TAZ: a novel transcriptional co-activator regulated by interactions with 14-3-3 and PDZ domain proteins. *The EMBO Journal* **19**: 6778–6791.

Kawaguchi Y, Kovacs JJ, McLaurin A, Vance JM, Ito A, Yao T-P. **2003**. The Deacetylase HDAC6 Regulates Aggresome Formation and Cell Viability in Response to Misfolded Protein Stress. *Cell* **115**: 727–738.

Kayano K, Saruwatari K, Kogure T, Shiraiwa Y. **2011**. Effect of coccolith polysaccharides isolated from the coccolithophorid, Emiliania huxleyi, on calcite crystal formation in in vitro CaCO3 crystallization. *Marine Biotechnology (New York, N.Y.)* **13**: 83–92.

Kayano K, Shiraiwa Y. **2009**. Physiological Regulation of Coccolith Polysaccharide Production by Phosphate Availability in the Coccolithophorid Emiliania huxleyi. *Plant and Cell Physiology* **50**: 1522–1531.

Keller MD, Selvin RC, Claus W, Guillard RRL. **1987**. Media for the Culture of Oceanic Ultraphytoplankton. *Journal of Phycology* **23**: 633–638.

Keuter S, Young JR, Frada MJ. **2019**. Life cycle association of the coccolithophore *Syracosphaera gaarderae* comb. nov. (ex *Alveosphaera bimurata*): Taxonomy, ecology and evolutionary implications. *Marine Micropaleontology* **148**: 58–64.

Key T, McCarthy A, Campbell DA, Six C, Roy S, Finkel ZV. **2010**. Cell size trade-offs govern light exploitation strategies in marine phytoplankton. *Environmental Microbiology* **12**: 95–104.

Kharwar S, Mishra AK. **2020**. Unraveling the complexities underlying sulfur deficiency and starvation in the cyanobacterium *Anabaena* sp. PCC 7120. *Environmental and Experimental Botany* **172**: 103966.

Klaas C, Archer DE. **2002**. Association of sinking organic matter with various types of mineral ballast in the deep sea: Implications for the rain ratio. *Global Biogeochemical Cycles* **16**: 63-1-63–14.

Kleczkowski LA, Igamberdiev AU. **2021**. Magnesium Signaling in Plants. *International Journal of Molecular Sciences* **22**: 1159.

Knappertsbusch M. **2000**. Morphologic evolution of the coccolithophorid Calcidiscus leptoporus from the Early Miocene to Recent. *Journal of Paleontology* **74**: 712–730.

Knies D, Wittmüß P, Appel S, Sawodny O, Ederer M, Feuer R. **2015**. Modeling and Simulation of Optimal Resource Management during the Diurnal Cycle in Emiliania huxleyi by Genome-Scale Reconstruction and an Extended Flux Balance Analysis Approach. *Metabolites* **5**: 659–676.

Kobayashi NI, Tanoi K. **2015**. Critical Issues in the Study of Magnesium Transport Systems and Magnesium Deficiency Symptoms in Plants. *International Journal of Molecular Sciences* **16**: 23076–23093.

Kolberg L, Raudvere U, Kuzmin I, Vilo J, Peterson H. **2020**. gprofiler2 -- an R package for gene list functional enrichment analysis and namespace conversion toolset g:Profiler. *F1000Research* **9**: ELIXIR-709.

Kondrik DV, Pozdnyakov DV, Johannessen OM. **2018**. Satellite Evidence that Phytoplankton Blooms Weaken Marine Carbon Sinks. *Geophysical Research Letters* **45**: 846–854.

Kottmeier DM, Chrachri A, Langer G, Helliwell KE, Wheeler GL, Brownlee C. **2022**. Reduced H+ channel activity disrupts pH homeostasis and calcification in coccolithophores at low ocean pH. *Proceedings of the National Academy of Sciences* **119**: e2118009119.

Kottmeier D, Chrachri A, Langer G, Wheeler G, Brownlee C. **2020a**. Differences in acid-base regulation of haploid and diploid life-cycle stages of Coccolithus braarudii and their consequences for the sensitivity towards ocean acidification. *Access Microbiology* **2**: 863.

Kottmeier DM, Rokitta SD, Rost B. **2016a**. H+-driven increase in CO2 uptake and decrease in uptake explain coccolithophores' acclimation responses to ocean acidification. *Limnology and Oceanography* **61**: 2045–2057.

Kottmeier DM, Rokitta SD, Rost B. **2016b**. Acidification, not carbonation, is the major regulator of carbon fluxes in the coccolithophore miliania huxleyi. *New Phytologist* **211**: 126–137.

Kottmeier DM, Rokitta SD, Tortell PD, Rost B. **2014**. Strong shift from HCO3− to CO2 uptake in Emiliania huxleyi with acidification: new approach unravels acclimation versus short-term pH effects. *Photosynthesis Research* **121**: 265–275.

Kottmeier DM, Terbrüggen A, Wolf-Gladrow DA, Thoms S. **2020b**. Diel variations in cell division and biomass production of Emiliania huxleyi—Consequences for the calculation of physiological cell parameters. *Limnology and Oceanography* **65**: 1781–1800.

Krinos AI, Shapiro SK, Li W, Haley ST, Dyhrman ST, Dutkiewicz S, Follows MJ, Alexander H. **2025**. Intraspecific Diversity in Thermal Performance Determines Phytoplankton Ecological Niche. *Ecology Letters* **28**: e70055.

Krug SA, Schulz KG, Riebesell U. **2011**. Effects of changes in carbonate chemistry speciation on *Coccolithus braarudii*: a discussion of coccolithophorid sensitivities. *Biogeosciences* **8**: 771–777.

Krumhardt KM, Lovenduski NS, Freeman NM, Bates NR. **2016**. Apparent increase in coccolithophore abundance in the subtropical North Atlantic from 1990 to 2014. *Biogeosciences* **13**: 1163–1177.

Krumhardt KM, Lovenduski NS, Iglesias-Rodriguez MD, Kleypas JA. **2017**. Coccolithophore growth and calcification in a changing ocean. *Progress in Oceanography* **159**: 276–295.

Krumhardt KM, Lovenduski NS, Long MC, Levy M, Lindsay K, Moore JK, Nissen C. **2019**. Coccolithophore Growth and Calcification in an Acidified Ocean: Insights From Community Earth System Model Simulations. *Journal of Advances in Modeling Earth Systems* **11**: 1418–1437.

Langer G, Geisen M, Baumann K-H, Kläs J, Riebesell U, Thoms S, Young JR. **2006**. Species-specific responses of calcifying algae to changing seawater carbonate chemistry. *Geochemistry, Geophysics, Geosystems* **7**.

Langer G, Jie VW, Kottmeier D, Flori S, Sturm D, de Vries J, Harper GM, Brownlee C, Wheeler G. **2023**. Distinct physiological responses of Coccolithus braarudii life cycle phases to light intensity and nutrient availability. *European Journal of Phycology* **58**: 58–71.

Langer G, Nehrke G, Probert I, Ly J, Ziveri P. **2009**. Strain-specific responses of *Emiliania huxleyi* to changing seawater carbonate chemistry. *Biogeosciences* **6**: 2637–2646.

Langer G, Taylor AR, Walker CE, Meyer EM, Ben Joseph O, Gal A, Harper GM, Probert I, Brownlee C, Wheeler GL. **2021**. Role of silicon in the development of complex crystal shapes in coccolithophores. *New Phytologist* **231**: 1845–1857.

Larsen SH, and Beardall J. **2023**. The effect of temperature and salinity on DMSP production in Gephyrocapsa oceanica (Isochrysidales, Coccolithophyceae). *Phycologia* **62**: 152–163.

Lasa B, Frechilla S, Aleu M, González-Moro B, Lamsfus C, Aparicio-Tejo PM. **2000**. Effects of low and high levels of magnesium on the response of sunflower plants grown with ammonium and nitrate. *Plant and Soil* **225**: 167–174.

Lebrato M, Garbe-Schönberg D, Müller MN, Blanco-Ameijeiras S, Feely RA, Lorenzoni L, Molinero J-C, Bremer K, Jones DOB, Iglesias-Rodriguez D, *et al*. 2020. Global variability in seawater Mg:Ca and Sr:Ca ratios in the modern ocean. *Proceedings of the National Academy of Sciences* **117**: 22281–22292.

Lecourt M, Muggli DL, Harrison PJ. **1996**. Comparison of Growth and Sinking Rates of Non-Coccolith- and Coccolith-Forming Strains of Emiliania Huxleyi(prymnesiophyceae) Grown Under Different Irradiances and Nitrogen Sources. *Journal of Phycology* **32**: 17–21.

Lee RBY, Mavridou DAI, Papadakos G, McClelland HLO, Rickaby REM. **2016**. The uronic acid content of coccolith-associated polysaccharides provides insight into coccolithogenesis and past climate. *Nature Communications* **7**: 13144.

Lefebvre SC, Benner I, Stillman JH, Parker AE, Drake MK, Rossignol PE, Okimura KM, Komada T, Carpenter EJ. **2012**. Nitrogen source and p synergistically affect carbon allocation, growth and morphology of the coccolithophore miliania huxleyi: potential implications of ocean acidification for the carbon cycle. *Global Change Biology* **18**: 493–503.

Leonardos N, Harris GN. **2006**. Comparative Effects of Light on Pigments of Two Strains of Emiliania Huxleyi (haptophyta). *Journal of Phycology* **42**: 1217–1224.

Leonardos N, Read B, Thake B, Young JR. **2009**. NO MECHANISTIC DEPENDENCE OF PHOTOSYNTHESIS ON CALCIFICATION IN THE COCCOLITHOPHORID EMILIANIA HUXLEYI (HAPTOPHYTA)(1). *Journal of Phycology* **45**: 1046–1051.

Li Y, Liu D, López-Paz C, Olson BJ, Umen JG. **2016**. A new class of cyclin dependent kinase in Chlamydomonas is required for coupling cell size to cell division (DC Bergmann, Ed.). *eLife* **5**: e10767.

Li J, Zhang K, Li L, Wang Y, Wang C, Lin S. **2023**. Two-sided effects of the organic phosphorus phytate on a globally important marine coccolithophorid phytoplankton. *Microbiology Spectrum* **11**: e01255-23.

Lin S, Carpenter EJ. **1995**. Growth Characteristics of Marine Phytoplankton Determined by Cell Cycle Proteins: The Cell Cycle of Ethmodiscus Rex (bacillariophyceae) in the Southwestern North Atlantic Ocean and Caribbean Sea. *Journal of Phycology* **31**: 778–785.

Linschooten C, van Bleijswijk JDL, van Emburg PR, de Vrind JPM, Kempers ES, Westbroek P, de Vrind-de Jong EW. **1991**. Role of the Light-Dark Cycle and Medium Composition on the Production of Coccoliths by Emiliania Huxleyi (haptophyceae). *Journal of Phycology* **27**: 82–86.

Litchman E, Klausmeier CA, Schofield OM, Falkowski PG. **2007**. The role of functional traits and trade-offs in structuring phytoplankton communities: scaling from cellular to ecosystem level. *Ecology Letters* **10**: 1170–1181.

Liu Y-W, Eagle RA, Aciego SM, Gilmore RE, Ries JB. **2018**. A coastal coccolithophore maintains pH homeostasis and switches carbon sources in response to ocean acidification. *Nature Communications* **9**: 2857.

Liu X-L, Yu H-D, Guan Y, Li J-K, Guo F-Q. **2012**. Carbonylation and Loss-of-Function Analyses of SBPase Reveal Its Metabolic Interface Role in Oxidative Stress, Carbon

Assimilation, and Multiple Aspects of Growth and Development in *Arabidopsis*. *Molecular Plant* **5**: 1082–1099.

Loebl M, Cockshutt AM, Campbell DA, Finkel, and Zoe V. 2010. Physiological basis for high resistance to photoinhibition under nitrogen depletion in Emiliania huxleyi. *Limnology and Oceanography* **55**: 2150–2160.

Lorenzo MR, Neale PJ, Sobrino C, León P, Vázquez V, Bresnan E, Segovia M. **2019**. Effects of elevated CO2 on growth, calcification, and spectral dependence of photoinhibition in the coccolithophore Emiliania huxleyi (Prymnesiophyceae)1. *Journal of Phycology* **55**: 775–788.

Lu J, Wu T, Zhang B, Liu S, Song W, Qiao J, Ruan H. **2021**. Types of nuclear localization signals and mechanisms of protein import into the nucleus. *Cell Communication and Signaling* **19**: 60.

Ma Z, Hu L, Jiang W. **2024**. Understanding AP2/ERF Transcription Factor Responses and Tolerance to Various Abiotic Stresses in Plants: A Comprehensive Review. *International Journal of Molecular Sciences* **25**: 893.

Ma R, Jin X, Liu C. **2023**. High-Resolution Coccolithophore Morphological Changes in Response to Orbital Forcings During the Early Oligocene. *Geochemistry, Geophysics, Geosystems* **24**: e2022GC010746.

Mackinder L, Wheeler G, Schroeder D, von Dassow P, Riebesell U, Brownlee C. **2011**. Expression of biomineralization-related ion transport genes in Emiliania huxleyi. *Environmental Microbiology* **13**: 3250–3265.

Maier JA. **2013**. Magnesium and Cell Cycle. In: Kretsinger RH, Uversky VN, Permyakov EA, eds. Encyclopedia of Metalloproteins. New York, NY: Springer, 1227–1232.

Malerba ME, Palacios MM, Palacios Delgado YM, Beardall J, Marshall DJ. **2018**. Cell size, photosynthesis and the package effect: an artificial selection approach. *New Phytologist* **219**: 449–461.

Malerba ME, White CR, Marshall DJ. **2017**. Phytoplankton size-scaling of net-energy flux across light and biomass gradients. *Ecology* **98**: 3106–3115.

Manton I, Leedale GF. **1969**. Observations on the Microanatomy of Coccolithus Pelagicus and Cricosphaera Carterae, With Special Reference to the Origin and Nature of Coccoliths and Scales. *Journal of the Marine Biological Association of the United Kingdom* **49**: 1–16.

Manton I, Peterfi LS. **1969**. Observations on the tine structure of coccoliths, scales and the protoplast of a freshwater coccolithophorid, Hymenomonas roseola Stein, with supplementary observations on the protoplast of Cricosphaera carterae. *Proceedings of the Royal Society of London. Series B. Biological Sciences* **172**: 1–15.

Marañón E. 2008. Inter-specific scaling of phytoplankton production and cell size in the field. *Journal of Plankton Research* **30**: 157–163.

Marañón E. 2015. Cell Size as a Key Determinant of Phytoplankton Metabolism and Community Structure. *Annual Review of Marine Science* **7**: 241–264.

Marañón E, Cermeño P, López-Sandoval DC, Rodríguez-Ramos T, Sobrino C, Huete-Ortega M, Blanco JM, Rodríguez J. 2013. Unimodal size scaling of phytoplankton growth and the size dependence of nutrient uptake and use. *Ecology Letters* **16**: 371–379.

Marañón E, Cermeño P, Rodríguez J, Zubkov MV, Harris RP. 2007. Scaling of phytoplankton photosynthesis and cell size in the ocean. *Limnology and Oceanography* **52**: 2190–2198.

Marsh ME. 1994. Polyanion-mediated mineralization — assembly and reorganization of acidic polysaccharides in the Golgi system of a coccolithophorid alga during mineral deposition. *Protoplasma* **177**: 108–122.

Marsh ME. 2003. Regulation of CaCO3 formation in coccolithophores. *Comparative Biochemistry and Physiology Part B: Biochemistry and Molecular Biology* **136**: 743–754.

Marsh ME, Chang DK, King GC. 1992. Isolation and characterization of a novel acidic polysaccharide containing tartrate and glyoxylate residues from the mineralized scales of a unicellular coccolithophorid alga Pleurochrysis carterae. *Journal of Biological Chemistry* **267**: 20507–20512.

Marsh ME, Dickinson DP. 1997. Polyanion-mediated mineralization — mineralization in coccolithophore (Pleurochrysis carterae) variants which do not express PS2, the most abundant and acidic mineral-associated polyanion in wild-type cells. *Protoplasma* **199**: 9–17.

Marshall WF, Young KD, Swaffer M, Wood E, Nurse P, Kimura A, Frankel J, Wallingford J, Walbot V, Qu X, *et al.* 2012. What determines cell size? *BMC Biology* **10**: 101.

Martinez R, Packard TT, Blasco D. 1987. Light effects and diel variations of nitrate reductase activity in phytoplankton from the northwest Africa upwelling region. *Deep Sea Research Part A. Oceanographic Research Papers* **34**: 741–753.

Marzec B, Walker JM, Panagopoulou M, Jhons Y, Clare D, Wheeler A, Shaver MP, Nudelman F. 2019. Three-dimensional architecture and surface functionality of coccolith base plates. *Journal of Structural Biology* **208**: 127–136.

Matson PG, Ladd TM, Halewood ER, Sangodkar RP, Chmelka BF, Iglesias-Rodriguez MD. 2016. Intraspecific Differences in Biogeochemical Responses to Thermal Change in the Coccolithophore Emiliania huxleyi. *PLOS ONE* **11**: e0162313.

Matson PG, Washburn L, Fields EA, Gotschalk C, Ladd TM, Siegel DA, Welch ZS, Iglesias-Rodriguez MD. 2019. Formation, Development, and Propagation of a Rare

Coastal Coccolithophore Bloom. *Journal of Geophysical Research: Oceans* **124**: 3298–3316.

McCarthy A, Rogers SP, Duffy SJ, Campbell DA. **2012**. ELEVATED CARBON DIOXIDE DIFFERENTIALLY ALTERS THE PHOTOPHYSIOLOGY OF THALASSIOSIRA PSEUDONANA (BACILLARIOPHYCEAE) AND EMILIANIA HUXLEYI (HAPTOPHYTA)(1). *Journal of Phycology* **48**: 635–646.

McClelland HLO, Bruggeman J, Hermoso M, Rickaby REM. **2017**. The origin of carbon isotope vital effects in coccolith calcite. *Nature Communications* **8**: 14511.

McKew BA, Lefebvre SC, Achterberg EP, Metodieva G, Raines CA, Metodiev MV, Geider RJ. **2013**. Plasticity in the proteome of Emiliania huxleyi CCMP 1516 to extremes of light is highly targeted. *New Phytologist* **200**: 61–73.

McKew BA, Metodieva G, Raines CA, Metodiev MV, Geider RJ. **2015**. Acclimation of miliania huxleyi (1516) to nutrient limitation involves precise modification of the proteome to scavenge alternative sources of N and P. *Environmental Microbiology* **17**: 4050–4062.

Mei Z-P, Finkel ZV, Irwin AJ. **2011**. Phytoplankton growth allometry and size dependent C:N stoichiometry revealed by a variable quota model. *Marine Ecology Progress Series* **434**: 29–43.

Mellott A, Rockwood J, Zhelay T, Luu CT, Kaitsuka T, Kozak JA. **2020**. TRPM7 channel activity in Jurkat T lymphocytes during magnesium depletion and loading: implications for divalent metal entry and cytotoxicity. *Pflugers Archiv : European journal of physiology* **472**: 1589–1606.

Meyer J, Riebesell U. **2015**. Reviews and Syntheses: Responses of coccolithophores to ocean acidification: a meta-analysis. *Biogeosciences* **12**: 1671–1682.

Meyer RC, Steinfath M, Lisec J, Becher M, Witucka-Wall H, Törjék O, Fiehn O, Eckardt Ä, Willmitzer L, Selbig J, *et al.* 2007. The metabolic signature related to high plant growth rate in Arabidopsis thaliana. *Proceedings of the National Academy of Sciences* **104**: 4759–4764.

Meyer EM, Taylor AR. **2025**. A comparison of calcification mechanisms in haploid and diploid cells of the coccolithophore Calcidiscus leptoporus (Murray & Blackman 1898). *Journal of Phycology*.

Milner S, Langer G, Grelaud M, Ziveri P. **2016**. Ocean warming modulates the effects of acidification on Emiliania huxleyi calcification and sinking. *Limnology and Oceanography* **61**: 1322–1336.

Mizukawa Y, Miyashita Y, Satoh M, Shiraiwa Y, Iwasaka M. **2015**. Light intensity modulation by coccoliths of Emiliania huxleyi as a micro-photo-regulator. *Scientific Reports* **5**: 13577.

Moheimani NR, Borowitzka MA. **2011**. Increased CO2 and the effect of pH on growth and calcification of Pleurochrysis carterae and Emiliania huxleyi (Haptophyta) in semicontinuous cultures. *Applied Microbiology and Biotechnology* **90**: 1399–1407.

Moheimani NR, Webb JP, Borowitzka MA. **2012**. Bioremediation and other potential applications of coccolithophorid algae: A review. *Algal Research* **1**: 120–133.

Monnier A, Liverani S, Bouvet R, Jesson B, Smith JQ, Mosser J, Corellou F, Bouget F-Y. **2010**. Orchestrated transcription of biological processes in the marine picoeukaryote Ostreococcus exposed to light/dark cycles. *BMC Genomics* **11**: 192.

Montagnes DJS, Berges JA, Harrison PJ, Taylor FJR. **1994**. Estimating carbon, nitrogen, protein, and chlorophyll a from volume in marine phytoplankton. *Limnology and Oceanography* **39**: 1044–1060.

Monteiro FM, Bach LT, Brownlee C, Bown P, Rickaby REM, Poulton AJ, Tyrrell T, Beaufort L, Dutkiewicz S, Gibbs S, *et al.* 2016. Why marine phytoplankton calcify. *Science Advances* **2**: e1501822.

Moore TS, Dowell MD, Franz BA. **2012**. Detection of coccolithophore blooms in ocean color satellite imagery: A generalized approach for use with multiple sensors. *Remote Sensing of Environment* **117**: 249–263.

Moore CM, Mills MM, Arrigo KR, Berman-Frank I, Bopp L, Boyd PW, Galbraith ED, Geider RJ, Guieu C, Jaccard SL, *et al.* 2013. Processes and patterns of oceanic nutrient limitation. *Nature Geoscience* **6**: 701–710.

Morse JW, Wang Q, Tsio MY. **1997**. Influences of temperature and Mg:Ca ratio on CaCO3 precipitates from seawater. *Geology* **25**: 85–87.

Muggli D, Lecourt M, Harrison P. **1996**. Effects of iron and nitrogen source on the sinking rate, physiology and metal composition of an oceanic diatom from the subarctic Pacific. *Marine Ecology Progress Series* **132**: 215–227.

Müller MN, Antia AN, LaRoche J. **2008**. Influence of cell cycle phase on calcification in the coccolithophore Emiliania huxleyi. *Limnology and Oceanography* **53**: 506–512.

Müller MN, Barcelos e Ramos J, Schulz KG, Riebesell U, Kaźmierczak J, Gallo F, Mackinder L, Li Y, Nesterenko PN, Trull TW, *et al.* 2015a. Phytoplankton calcification as an effective mechanism to alleviate cellular calcium poisoning. *Biogeosciences* **12**: 6493–6501.

Müller MN, Blanco-Ameijeiras S, Stoll HM, Mendez-Vicente A, Lebrato M. **2021a**. Temperature Induced Physiological Reaction Norms of the Coccolithophore Gephyrocapsa oceanica and Resulting Coccolith Sr/Ca and Mg/Ca Ratios. *Frontiers in Earth Science* **9**.

Müller MN, Brandini FP, Trull TW, Hallegraeff GM. **2021b**. Coccolith volume of the Southern Ocean coccolithophore Emiliania huxleyi as a possible indicator for palaeo-cell volume. *Geobiology* **19**: 63–74.

Müller MN, Kısakürek B, Buhl D, Gutperlet R, Kolevica A, Riebesell U, Stoll H, Eisenhauer A. **2011**. Response of the coccolithophores *Emiliania huxleyi* and *Coccolithus braarudii* to changing seawater Mg2+ and Ca2+ concentrations: Mg/Ca, Sr/Ca ratios and δ44/40Ca, δ26/24Mg of coccolith calcite. *Geochimica et Cosmochimica Acta* **75**: 2088–2102.

Müller MN, Lebrato M, Riebesell U, Barcelos e Ramos J, Schulz KG, Blanco-Ameijeiras S, Sett S, Eisenhauer A, Stoll HM. **2014**. Influence of temperature and CO_2 on the strontium and magnesium composition of coccolithophore calcite. *Biogeosciences* **11**: 1065–1075.

Müller MN, Trull TW, Hallegraeff GM. **2015b**. Differing responses of three Southern Ocean Emiliania huxleyi ecotypes to changing seawater carbonate chemistry. *Marine Ecology Progress Series* **531**: 81–90.

Müller MN, Trull TW, Hallegraeff GM. **2017**. Independence of nutrient limitation and carbon dioxide impacts on the Southern Ocean coccolithophore Emiliania huxleyi. *The ISME Journal* **11**: 1777–1787.

Muratore D, Boysen AK, Harke MJ, Becker KW, Casey JR, Coesel SN, Mende DR, Wilson ST, Aylward FO, Eppley JM, *et al*. 2022. Complex marine microbial communities partition metabolism of scarce resources over the diel cycle. *Nature Ecology & Evolution* **6**: 218–229.

Nam O, Park J-M, Lee H, Jin E. **2019**. De novo transcriptome profile of coccolithophorid alga Emiliania huxleyi CCMP371 at different calcium concentrations with proteome analysis. *PLOS ONE* **14**: e0221938.

Napoléon C, Raimbault V, Claquin P. **2013**. Influence of Nutrient Stress on the Relationships between PAM Measurements and Carbon Incorporation in Four Phytoplankton Species. *PLOS ONE* **8**: e66423.

Nelson DM, Brand LE. **1979**. Cell Division Periodicity in 13 Species of Marine Phytoplankton on a Light: Dark Cycle1. *Journal of Phycology* **15**: 67–75.

Nielsen MV. **1995**. Photosynthetic Characteristics of the Coccolithophorid Emiliania Huxleyi (prymnesiophyceae) Exposed to Elevated Concentrations of Dissolved Inorganic Carbon. *Journal of Phycology* **31**: 715–719.

Nielsen MV. **1997**. Growth, Dark Respiration and Photosynthetic Parameters of the Coccolithophorid Emiliania Huxleyi (prymnesiophyceae) Acclimated to Different Day Length-Irradiance Combinations. *Journal of Phycology* **33**: 818–822.

Nissen C, Vogt M, Münnich M, Gruber N, Haumann FA. **2018**. Factors controlling coccolithophore biogeography in the Southern Ocean. *Biogeosciences* **15**: 6997–7024.

Nowak CM, Quarton T, Bleris L. **2023**. Impact of variability in cell cycle periodicity on cell population dynamics. *PLOS Computational Biology* **19**: e1011080.

Nyberg KA, Michelson RJ, Putnam CW, Weinert TA. **2002**. Toward maintaining the genome: DNA damage and replication checkpoints. *Annual Review of Genetics* **36**: 617–656.

O'Brien CJ, Peloquin JA, Vogt M, Heinle M, Gruber N, Ajani P, Andruleit H, Arístegui J, Beaufort L, Estrada M, *et al*. 2013. Global marine plankton functional type biomass distributions: coccolithophores. *Earth System Science Data* **5**: 259–276.

O'Dea SA, Gibbs SJ, Bown PR, Young JR, Poulton AJ, Newsam C, Wilson PA. **2014**. Coccolithophore calcification response to past ocean acidification and climate change. *Nature Communications* **5**: 5363.

Oliver H, Krumhardt KM, McGillicuddy Jr. DJ, Mitchell C, Balch WM. **2024**. Mechanisms Regulating Coccolithophore Dynamics in the Great Calcite Belt in the Southern Ocean in the Community Earth System Model. *Journal of Geophysical Research: Oceans* **129**: e2024JC021371.

Oliver H, McGillicuddy Jr. DJ, Krumhardt KM, Long MC, Bates NR, Bowler BC, Drapeau DT, Balch WM. **2023**. Environmental Drivers of Coccolithophore Growth in the Pacific Sector of the Southern Ocean. *Global Biogeochemical Cycles* **37**: e2023GB007751.

Olofsson M, Ferrer-González FX, Uchimiya M, Schreier JE, Holderman NR, Smith CB, Edison AS, Moran MA. **2022**. Growth-stage-related shifts in diatom endometabolome composition set the stage for bacterial heterotrophy. *ISME Communications* **2**: 1–9.

Olson RJ, Vaulot D, Chisholm SW. **1986**. Effects of Environmental Stresses on the Cell Cycle of Two Marine Phytoplankton Species. *Plant Physiology* **80**: 918.

Ottesen EA, Young CR, Eppley JM, Ryan JP, Chavez FP, Scholin CA, DeLong EF. **2013**. Pattern and synchrony of gene expression among sympatric marine microbial populations. *Proceedings of the National Academy of Sciences* **110**: E488–E497.

Outka DE, Williams DC. **1971**. Sequential Coccolith Morphogenesis in Hymenomonas carterae. *The Journal of Protozoology* **18**: 285–297.

Oviedo AM, Langer G, Ziveri P. **2014**. Effect of phosphorus limitation on coccolith morphology and element ratios in Mediterranean strains of the coccolithophore *Emiliania huxleyi*. *Journal of Experimental Marine Biology and Ecology* **459**: 105–113.

Ozaki N, Okazaki M, Sakuda S, Kogure T, Nagasawa H. **2004**. Structural and Functional Diversity of Acidic Polysaccharides from Various Species of Coocolithophorid Algae). *Thalassas: an International Journal of Marine Sciences*.

Ozaki N, Sakuda S, Nagasawa H. **2007**. A novel highly acidic polysaccharide with inhibitory activity on calcification from the calcified scale "coccolith" of a

coccolithophorid alga, *Pleurochrysis haptonemofera*. *Biochemical and Biophysical Research Communications* **357**: 1172–1176.

Paasche E. **1967**. Marine Plankton Algae Grown with Light-Dark Cycles. I. Coccolithus huxleyi. *Physiologia Plantarum* **20**: 946–956.

Paasche E. **1969**. Light-dependent coccolith formation in the two forms of Coccolithus pelagicus. *Archiv für Mikrobiologie* **67**: 199–208.

Paasche E. **2001**. A review of the coccolithophorid Emiliania huxleyi (Prymnesiophyceae), with particular reference to growth, coccolith formation, and calcification-photosynthesis interactions. *Phycologia* **40**: 503–529.

Paasche E, Brubak S, Skattebøl S, Young JR, Green JC. **1996**. Growth and calcification in the coccolithophorid Emiliania huxleyi (Haptophyceae) at low salinities. *Phycologia* **35**: 394–403.

Paasche E, Klaveness D. **1970**. A physiological comparison of coccolith-forming and naked cells of Coccolithus huxleyi. *Archiv für Mikrobiologie* **73**: 143–152.

Pan Y, Li Y, Ma Q, He H, Wang S, Sun Z, Cai W-J, Dong B, Di Y, Fu W, *et al*. 2021. The role of Mg2+ in inhibiting CaCO3 precipitation from seawater. *Marine Chemistry* **237**: 104036.

Pantorno A, Holland DP, Stojkovic S, Beardall J. **2013**. Impacts of nitrogen limitation on the sinking rate of the coccolithophorid Emiliania huxleyi (Prymnesiophyceae). *Phycologia* **52**: 288–294.

Papadakis IE, Antonopoulou C, Sotiropoulos T, Chatzissavvidis C, Therios I. **2023**. Effect of Magnesium on Mineral Nutrition, Chlorophyll, Proline and Carbohydrate Concentrations of Sweet Orange (Citrus sinensis cv. Newhall) Plants. *Applied Sciences* **13**: 7995.

Pareek A, Mishra D, Rathi D, Verma JK, Chakraborty S, Chakraborty N. **2021**. The small heat shock proteins, chaperonin 10, in plants: An evolutionary view and emerging functional diversity. *Environmental and Experimental Botany* **182**: 104323.

Parry MAJ, Keys AJ, Madgwick PJ, Carmo-Silva AE, Andralojc PJ. **2008**. Rubisco regulation: a role for inhibitors. *Journal of Experimental Botany* **59**: 1569–1580.

Pascual M, Caswell H. **1997**. From the Cell Cycle to Population Cycles in Phytoplankton–Nutrient Interactions. *Ecology* **78**: 897–912.

Patterson JC, Joughin BA, van de Kooij B, Lim DC, Lauffenburger DA, Yaffe MB. **2019**. ROS and Oxidative Stress are Elevated in Mitosis During Asynchronous Cell Cycle Progression and are Exacerbated by Mitotic Arrest. *Cell systems* **8**: 163-167.e2.

Pei J, Pan X, Wei G, Hua Y. **2023**. Research progress of glutathione peroxidase family (GPX) in redoxidation. *Frontiers in Pharmacology* **14**: 1147414.

Perkins DM, Perna A, Adrian R, Cermeño P, Gaedke U, Huete-Ortega M, White EP, Yvon-Durocher G. **2019**. Energetic equivalence underpins the size structure of tree and phytoplankton communities. *Nature Communications* **10**: 255.

Perrin L, Probert I, Langer G, Aloisi G. **2016**. Growth of the coccolithophore *Emiliania huxleyi* in light- and nutrient-limited batch reactors: relevance for the BIOSOPE deep ecological niche of coccolithophores. *Biogeosciences* **13**: 5983–6001.

Pitsawong W, Pádua RAP, Grant T, Hoemberger M, Otten R, Bradshaw N, Grigorieff N, Kern D. **2023**. From primordial clocks to circadian oscillators. *Nature* **616**: 183–189.

Pivato M, Ballottari M. **2021**. Chlamydomonas reinhardtii cellular compartments and their contribution to intracellular calcium signalling. *Journal of Experimental Botany* **72**: 5312–5335.

Poliner E, Panchy N, Newton L, Wu G, Lapinsky A, Bullard B, Zienkiewicz A, Benning C, Shiu S-H, Farré EM. **2015**. Transcriptional coordination of physiological responses in annochloropsis oceanica CCMP1779 under light/dark cycles. *The Plant Journal* **83**: 1097–1113.

van de Poll WH, Visser RJW, Buma AGJ. **2007**. Acclimation to a dynamic irradiance regime changes excessive irradiance sensitivity of Emiliania huxleyi and Thalassiosira weissflogii. *Limnology and Oceanography* **52**: 1430–1438.

Pontes MH, Yeom J, Groisman EA. **2016**. Reducing Ribosome Biosynthesis Promotes Translation during Low Mg2+ Stress. *Molecular Cell* **64**: 480–492.

Poulson-Ellestad KL, Harvey EL, Johnson MD, Mincer TJ. **2016**. Evidence for Strain-Specific Exometabolomic Responses of the Coccolithophore Emiliania huxleyi to Grazing by the Dinoflagellate Oxyrrhis marina. *Frontiers in Marine Science* **3**.

Poulton AJ, Adey TR, Balch WM, Holligan PM. **2007**. Relating coccolithophore calcification rates to phytoplankton community dynamics: Regional differences and implications for carbon export. *Deep Sea Research Part II: Topical Studies in Oceanography* **54**: 538–557.

Poulton AJ, Charalampopoulou A, Young JR, Tarran GA, Lucas MI, Quartlya GD. **2010**. Coccolithophore dynamics in non-bloom conditions during late summer in the central Iceland Basin (July-August 2007). *Limnology and Oceanography* **55**: 1601–1613.

Poulton AJ, Holligan PM, Charalampopoulou A, Adey TR. **2017**. Coccolithophore ecology in the tropical and subtropical Atlantic Ocean: New perspectives from the Atlantic meridional transect (AMT) programme. *Progress in Oceanography* **158**: 150–170.

Poulton AJ, Painter SC, Young JR, Bates NR, Bowler B, Drapeau D, Lyczsckowski E, Balch WM. **2013**. The 2008 Emiliania huxleyi bloom along the Patagonian Shelf: Ecology, biogeochemistry, and cellular calcification. *Global Biogeochemical Cycles* **27**: 1023–1033.

Poulton AJ, Stinchcombe MC, Achterberg EP, Bakker DCE, Dumousseaud C, Lawson HE, Lee GA, Richier S, Suggett DJ, Young JR. **2014**. Coccolithophores on the north-west European shelf: calcification rates and environmental controls. *Biogeosciences* **11**: 3919–3940.

Poulton AJ, Young JR, Bates NR, Balch WM. **2011**. Biometry of detached Emiliania huxleyi coccoliths along the Patagonian Shelf. *Marine Ecology Progress Series* **443**: 1–17.

Prasad M, Kataria P, Ningaraju S, Buddidathi R, Bankapalli K, Swetha C, Susarla G, Venkatesan R, D'Silva P, Shivaprasad PV. **2022**. Double DJ-1 domain containing Arabidopsis DJ-1D is a robust macromolecule deglycase. *New Phytologist* **236**: 1061–1074.

Price LL, Yin K, Harrison PJ. **1998**. Influence of continuous light and L:D cycles on the growth and chemical composition of Prymnesiophyceae including coccolithophores. *Journal of Experimental Marine Biology and Ecology* **223**: 223–234.

Probert I, Fresnel J, Young J. **2014**. The Life Cycle and Taxonomic Affinity of the Coccolithophore Jomonlithus littoralis (Prymnesiophyceae). *Cryptogamie, Algologie* **35**: 389–405.

Quinn P, Bowers RM, Zhang X, Wahlund TM, Fanelli MA, Olszova D, Read BA. **2006**. cDNA Microarrays as a Tool for Identification of Biomineralization Proteins in the Coccolithophorid Emiliania huxleyi (Haptophyta). *Applied and Environmental Microbiology* **72**: 5512–5526.

Ra K, Kitagawa H, Shiraiwa Y. **2010a**. Mg isotopes in chlorophyll-a and coccoliths of cultured coccolithophores (*Emiliania huxleyi*) by MC-ICP-MS. *Marine Chemistry* **122**: 130–137.

Ra K, Kitagawa H, Shiraiwa Y. **2010b**. Mg isotopes and Mg/Ca values of coccoliths from cultured specimens of the species *Emiliania huxleyi* and *Gephyrocapsa oceanica*. *Marine Micropaleontology* **77**: 119–124.

Ramos JB e, Schulz KG, Febiri S, Riebesell U. **2012**. Photoacclimation to abrupt changes in light intensity by Phaeodactylum tricornutum and Emiliania huxleyi: the role of calcification. *Marine Ecology Progress Series* **452**: 11–26.

Raven JA, Beardall J. **2016**. The ins and outs of CO2. *Journal of Experimental Botany* **67**: 1–13.

Raven JA, Crawfurd K. **2012**. Environmental controls on coccolithophore calcification. *Marine Ecology Progress Series* **470**: 137–166.

Raven JA, Johnston AM. **1991**. Mechanisms of inorganic-carbon acquisition in marine phytoplankton and their implications for the use of other resources. *Limnology and Oceanography* **36**: 1701–1714.

Read BA, Kegel J, Klute MJ, Kuo A, Lefebvre SC, Maumus F, Mayer C, Miller J, Monier A, Salamov A, *et al.* 2013. Pan genome of the phytoplankton Emiliania underpins its global distribution. *Nature* **499**: 209–213.

Rees T a. V, Raven JA. **2021**. The maximum growth rate hypothesis is correct for eukaryotic photosynthetic organisms, but not cyanobacteria. *New Phytologist* **230**: 601–611.

Rengefors K, Kremp A, Reusch TBH, Wood AM. **2017**. Genetic diversity and evolution in eukaryotic phytoplankton: revelations from population genetic studies. *Journal of Plankton Research* **39**: 165–179.

Renger G, Renger G (Eds). **2007**. *Primary Processes of Photosynthesis, Part 1: Principles and Apparatus*. The Royal Society of Chemistry.

Rhind N. **2021**. Cell-size control. *Current Biology* **31**: R1414–R1420.

Riba A, Oravecz A, Durik M, Jiménez S, Alunni V, Cerciat M, Jung M, Keime C, Keyes WM, Molina N. **2022**. Cell cycle gene regulation dynamics revealed by RNA velocity and deep-learning. *Nature Communications* **13**: 2865.

Richier S, Fiorini S, Kerros M-E, von Dassow P, Gattuso J-P. **2011**. Response of the calcifying coccolithophore Emiliania huxleyi to low pH/high pCO2: from physiology to molecular level. *Marine Biology* **158**: 551–560.

Richts B, Rosenberg J, Commichau FM. **2019**. A Survey of Pyridoxal 5'-Phosphate-Dependent Proteins in the Gram-Positive Model Bacterium Bacillus subtilis. *Frontiers in Molecular Biosciences* **6**.

Rickaby REM, Hermoso M, Lee RBY, Rae BD, Heureux AMC, Balestreri C, Chakravarti L, Schroeder DC, Brownlee C. **2016**. Environmental carbonate chemistry selects for phenotype of recently isolated strains of *Emiliania huxleyi*. *Deep Sea Research Part II: Topical Studies in Oceanography* **127**: 28–40.

Ridgwell A, Schmidt DN, Turley C, Brownlee C, Maldonado MT, Tortell P, Young JR. **2009**. From laboratory manipulations to Earth system models: scaling calcification impacts of ocean acidification. *Biogeosciences* **6**: 2611–2623.

Ridgwell A, Zeebe RE. **2005**. The role of the global carbonate cycle in the regulation and evolution of the Earth system. *Earth and Planetary Science Letters* **234**: 299–315.

Ridgwell A, Zondervan I, Hargreaves JC, Bijma J, Lenton TM. **2007**. Assessing the potential long-term increase of oceanic fossil fuel CO_2 uptake due to CO_2-calcification feedback. *Biogeosciences* **4**: 481–492.

Riebesell U, Zondervan I, Rost B, Tortell PD, Zeebe RE, Morel FMM. **2000**. Reduced calcification of marine plankton in response to increased atmospheric CO2. *Nature* **407**: 364–367.

Riegman R, Stolte W, Noordeloos AAM, Slezak D. **2000**. Nutrient uptake and alkaline phosphatase (ec 3:1:3:1) activity of emiliania huxleyi (PRYMNESIOPHYCEAE) during growth under n and p limitation in continuous cultures. *Journal of Phycology* **36**: 87–96.

Ries JB. **2010**. Review: geological and experimental evidence for secular variation in seawater Mg/Ca (calcite-aragonite seas) and its effects on marine biological calcification. *Biogeosciences* **7**: 2795–2849.

Rigual Hernández AS, Trull TW, Nodder SD, Flores JA, Bostock H, Abrantes F, Eriksen RS, Sierro FJ, Davies DM, Ballegeer A-M, *et al.* 2020. Coccolithophore biodiversity controls carbonate export in the Southern Ocean. *Biogeosciences* **17**: 245–263.

Ritchie RJ. **2006**. Consistent sets of spectrophotometric chlorophyll equations for acetone, methanol and ethanol solvents. *Photosynthesis Research* **89**: 27–41.

Ritchie RJ. **2008**. Fitting light saturation curves measured using modulated fluorometry. *Photosynthesis Research* **96**: 201–215.

Rivero-Calle S, Gnanadesikan A, Del Castillo CE, Balch WM, Guikema SD. **2015**. Multidecadal increase in North Atlantic coccolithophores and the potential role of rising CO2. *Science* **350**: 1533–1537.

Rochaix J-D. **2011**. Regulation of photosynthetic electron transport. *Biochimica et biophysica acta* **1807**: 375–383.

Rockholm DC, Yamamoto HY. **1996**. Violaxanthin de-epoxidase. *Plant Physiology* **110**: 697–703.

Rokitta SD, von Dassow P, Rost B, John U. **2016**. P- and N-Depletion Trigger Similar Cellular Responses to Promote Senescence in Eukaryotic Phytoplankton. *Frontiers in Marine Science* **3**.

Rokitta SD, Rost B. **2012**. Effects of CO2 and their modulation by light in the life-cycle stages of the coccolithophore Emiliania huxleyi. *Limnology and Oceanography* **57**: 607–618.

Rokitta SD, Von Dassow P, Rost B, John U. **2014**. Emiliania huxleyi endures N-limitation with an efficient metabolic budgeting and effective ATP synthesis. *BMC Genomics* **15**: 1051.

Romani AMP. **2011**. CELLULAR MAGNESIUM HOMEOSTASIS. *Archives of biochemistry and biophysics* **512**: 1–23.

Rosario Lorenzo M, Iñiguez C, Egge JK, Larsen A, Berger SA, García-Gómez C, Segovia M. **2018**. Increased CO2 and iron availability effects on carbon assimilation and calcification on the formation of *Emiliania huxleyi* blooms in a coastal phytoplankton community. *Environmental and Experimental Botany* **148**: 47–58.

Rosas-Navarro A, Langer G, Ziveri P. **2016**. Temperature affects the morphology and calcification of *Emiliania huxleyi* strains. *Biogeosciences* **13**: 2913–2926.

Rost B, Riebesell U. **2004**. Coccolithophores and the biological pump: responses to environmental changes. In: Thierstein HR, Young JR, eds. Coccolithophores: From Molecular Processes to Global Impact. Berlin, Heidelberg: Springer, 99–125.

Rouco M, Branson O, Lebrato M, Iglesias-Rodriguez MD. **2013**. The effect of nitrate and phosphate availability on Emiliania huxleyi (NZEH) physiology under different CO2 scenarios. *Frontiers in Microbiology* **4**.

Ruan Z, Lu M, Lin H, Chen S, Li P, Chen W, Xu H, Qiu D. **2023**. Different photosynthetic responses of haploid and diploid Emiliania huxleyi (Prymnesiophyceae) to high light and ultraviolet radiation. *Bioresources and Bioprocessing* **10**: 40.

Sakurai H, Enoki Y. **2010**. Novel aspects of heat shock factors: DNA recognition, chromatin modulation and gene expression. *The FEBS Journal* **277**: 4140–4149.

Salomon E, Bar-Eyal L, Sharon S, Keren N. **2013**. Balancing photosynthetic electron flow is critical for cyanobacterial acclimation to nitrogen limitation. *Biochimica et Biophysica Acta (BBA) - Bioenergetics* **1827**: 340–347.

Santomauro G, Sun W-L, Brümmer F, Bill J. **2016**. Incorporation of zinc into the coccoliths of the microalga Emiliania huxleyi. *BioMetals* **29**: 225–234.

Sarthou G, Timmermans KR, Blain S, Tréguer P. **2005**. Growth physiology and fate of diatoms in the ocean: a review. *Journal of Sea Research* **53**: 25–42.

Saruwatari K, Satoh M, Harada N, Suzuki I, Shiraiwa Y. **2016**. Change in coccolith size and morphology due to response to temperature and salinity in coccolithophore *Emiliania huxleyi* (Haptophyta) isolated from the Bering and Chukchi seas. *Biogeosciences* **13**: 2743–2755.

Satoh M, Iwamoto K, Suzuki I, Shiraiwa Y. **2009**. Cold stress stimulates intracellular calcification by the coccolithophore, Emiliania huxleyi (Haptophyceae) under phosphate-deficient conditions. *Marine Biotechnology (New York, N.Y.)* **11**: 327–333.

Schlüter L, Lohbeck KT, Gröger JP, Riebesell U, Reusch TBH. **2016**. Long-term dynamics of adaptive evolution in a globally important phytoplankton species to ocean acidification. *Science Advances* **2**: e1501660.

Schlüter L, Lohbeck KT, Gutowska MA, Gröger JP, Riebesell U, Reusch TBH. **2014**. Adaptation of a globally important coccolithophore to ocean warming and acidification. *Nature Climate Change* **4**: 1024–1030.

Schneider LJ, Bralower TJ, Kump LR, Patzkowsky ME. **2013**. Calcareous nannoplankton ecology and community change across the Paleocene-Eocene Thermal Maximum. *Paleobiology* **39**: 628–647.

Schroeder DC, Biggi GF, Hall M, Davy J, Martínez JM, Richardson AJ, Malin G, Wilson WH. **2005**. A Genetic Marker to Separate Emiliania Huxleyi (prymnesiophyceae) Morphotypes. *Journal of Phycology* **41**: 874–879.

Schulz KG, Rost B, Burkhardt S, Riebesell U, Thoms S, Wolf-Gladrow DA. **2007**. The effect of iron availability on the regulation of inorganic carbon acquisition in the coccolithophore *Emiliania huxleyi* and the significance of cellular compartmentation for stable carbon isotope fractionation. *Geochimica et Cosmochimica Acta* **71**: 5301–5312.

Sclafani RA, Holzen TM. **2007**. Cell Cycle Regulation of DNA Replication. *Annual review of genetics* **41**: 237–280.

Seaver LC, Imlay JA. **2001**. Alkyl Hydroperoxide Reductase Is the Primary Scavenger of Endogenous Hydrogen Peroxide in Escherichia coli. *Journal of Bacteriology* **183**: 7173–7181.

Selan OTE, Hawu HN, Poy L, Cunha TD, Darmakusuma D. **2021**. The substitution of Mg^{2+} with $Mn^{2+/4+}$ metal ions in chlorophyll structure isolated from Gliricidia sepium leaves. *Journal of Physics: Conference Series* **2017**: 012002.

Sett S, Bach LT, Schulz KG, Koch-Klavsen S, Lebrato M, Riebesell U. **2014**. Temperature Modulates Coccolithophorid Sensitivity of Growth, Photosynthesis and Calcification to Increasing Seawater pCO2. *PLOS ONE* **9**: e88308.

Shemi A, Schatz D, Fredricks HF, Van Mooy BAS, Porat Z, Vardi A. **2016**. Phosphorus starvation induces membrane remodeling and recycling in Emiliania huxleyi. *New Phytologist* **211**: 886–898.

Sheward RM, Gebühr C, Bollmann J, Herrle JO. **2024**. Short-term response of *Emiliania huxleyi* growth and morphology to abrupt salinity stress. *Biogeosciences* **21**: 3121–3141.

Sheward RM, Liefer JD, Irwin AJ, Finkel ZV. **2023**. Elemental stoichiometry of the key calcifying marine phytoplankton Emiliania huxleyi under ocean climate change: A meta-analysis. *Global Change Biology* **29**: 4259–4278.

Sheward RM, Poulton AJ, Gibbs SJ, Daniels CJ, Bown PR. **2017**. Physiology regulates the relationship between coccosphere geometry and growth phase in coccolithophores. *Biogeosciences* **14**: 1493–1509.

Shiraiwa Y. **2003**. Physiological regulation of carbon fixation in the photosynthesis and calcification of coccolithophorids. *Comparative Biochemistry and Physiology. Part B, Biochemistry & Molecular Biology* **136**: 775–783.

Shire DM, Kustka AB. **2022**. Proteomic responses of the coccolithophore Emiliania huxleyi to zinc limitation and trace metal substitution. *Environmental Microbiology* **24**: 819–834.

Shkolnik D, Nuriel R, Bonza MC, Costa A, Fromm H. **2018**. MIZ1 regulates ECA1 to generate a slow, long-distance phloem-transmitted Ca2+ signal essential for root water

tracking in Arabidopsis. *Proceedings of the National Academy of Sciences* **115**: 8031–8036.

Sikes CS, Roer RD, Wilbur KM. **1980**. Photosynthesis and coccolith formation: Inorganic carbon sources and net inorganic reaction of deposition. *Limnology and Oceanography* **25**: 248–261.

Skeffington A, Fischer A, Sviben S, Brzezinka M, Górka M, Bertinetti L, Woehle C, Huettel B, Graf A, Scheffel A. **2023**. A joint proteomic and genomic investigation provides insights into the mechanism of calcification in coccolithophores. *Nature Communications* **14**: 3749.

Smith SV, Key GS. **1975**. Carbon dioxide and metabolism in marine environments. *Limnology and Oceanography* **20**: 493–495.

Smith HEK, Tyrrell T, Charalampopoulou A, Dumousseaud C, Legge OJ, Birchenough S, Pettit LR, Garley R, Hartman SE, Hartman MC, *et al*. 2012. Predominance of heavily calcified coccolithophores at low CaCO3 saturation during winter in the Bay of Biscay. *Proceedings of the National Academy of Sciences* **109**: 8845–8849.

Sorrosa JM, Satoh M, Shiraiwa Y. **2005**. Low Temperature Stimulates Cell Enlargement and Intracellular Calcification of Coccolithophorids. *Marine Biotechnology* **7**: 128–133.

Soto AR, Zheng H, Shoemaker D, Rodriguez J, Read BA, Wahlund TM. **2006**. Identification and preliminary characterization of two cDNAs encoding unique carbonic anhydrases from the marine alga Emiliania huxleyi. *Applied and Environmental Microbiology* **72**: 5500–5511.

Stanley SM, Hardie LA. **1998**. Secular oscillations in the carbonate mineralogy of reef-building and sediment-producing organisms driven by tectonically forced shifts in seawater chemistry. *Palaeogeography, Palaeoclimatology, Palaeoecology* **144**: 3–19.

Stoll HM, Ziveri P. **2004**. Coccolithophorid-based geochemical paleoproxies. In: Thierstein HR, Young JR, eds. Coccolithophores: From Molecular Processes to Global Impact. Berlin, Heidelberg: Springer, 529–562.

Stuchell-Brereton MD, Siglin A, Li J, Moore JK, Ahmed S, Williams JC, Cooper JA. **2011**. Functional interaction between dynein light chain and intermediate chain is required for mitotic spindle positioning. *Molecular Biology of the Cell* **22**: 2690–2701.

Sturm D, Wheeler G, Brownlee C, Tyrell T. **2022**. Examining Phosphate Physiology in Coccolithophore Life Cycle Stages. *Access Microbiology* **4**: po0190.

Su Y, Hu J, Xia M, Chen J, Meng W, Qian C, Shu Y, Wang C, Wang X, Salehi-Ashtiani K, *et al*. 2024. An undiscovered circadian clock to regulate phytoplankton photosynthesis. *PNAS Nexus* **3**: pgae497.

Suchéras-Marx B, Henderiks J. **2014**. Downsizing the pelagic carbonate factory: Impacts of calcareous nannoplankton evolution on carbonate burial over the past 17 million years. *Global and Planetary Change* **123**: 97–109.

Suchéras-Marx B, Viseur S, Walker CE, Beaufort L, Probert I, Bolton C. **2022**. Coccolith size rules – What controls the size of coccoliths during coccolithogenesis? *Marine Micropaleontology* **170**: 102080.

Suffrian K, Schulz KG, Gutowska MA, Riebesell U, Bleich M. **2011**. Cellular pH measurements in Emiliania huxleyi reveal pronounced membrane proton permeability. *New Phytologist* **190**: 595–608.

Sulpice R, Pyl E-T, Ishihara H, Trenkamp S, Steinfath M, Witucka-Wall H, Gibon Y, Usadel B, Poree F, Piques MC, *et al.* 2009. Starch as a major integrator in the regulation of plant growth. *Proceedings of the National Academy of Sciences* **106**: 10348–10353.

Sun S, Liu M, Nie X, Dong F, Hu W, Tan D, Huo T. **2018**. A synergetic biomineralization strategy for immobilizing strontium during calcification of the coccolithophore Emiliania huxleyi. *Environmental Science and Pollution Research International* **25**: 22446–22454.

Sunda WG, Huntsman SA. **1998**. Processes regulating cellular metal accumulation and physiological effects: Phytoplankton as model systems. *Science of The Total Environment* **219**: 165–181.

Šupraha L, Henderiks J. **2020**. A 15-million-year-long record of phenotypic evolution in the heavily calcified coccolithophore *Helicosphaera* and its biogeochemical implications. *Biogeosciences* **17**: 2955–2969.

Šupraha L, Ljubešić Z, Mihanović H, Henderiks J. **2016**. Coccolithophore life-cycle dynamics in a coastal Mediterranean ecosystem: seasonality and species-specific patterns. *Journal of Plankton Research* **38**: 1178–1193.

Suykens K, Delille B, Chou L, De Bodt C, Harlay J, Borges AV. **2010**. Dissolved inorganic carbon dynamics and air-sea carbon dioxide fluxes during coccolithophore blooms in the northwest European continental margin (northern Bay of Biscay). *Global Biogeochemical Cycles* **24**.

Suzuki R, Shimodaira H. **2006**. Pvclust: an R package for assessing the uncertainty in hierarchical clustering. *Bioinformatics (Oxford, England)* **22**: 1540–1542.

Suzuki R, Terada Y, Shimodaira H. **2019**. pvclust: Hierarchical Clustering with P-Values via Multiscale Bootstrap Resampling. : 2.2–0.

Sviben S, Gal A, Hood MA, Bertinetti L, Politi Y, Bennet M, Krishnamoorthy P, Schertel A, Wirth R, Sorrentino A, *et al.* 2016. A vacuole-like compartment concentrates a disordered calcium phase in a key coccolithophorid alga. *Nature Communications* **7**: 11228.

Taylor AR, Brownlee C. **2003**. A Novel Cl− Inward-Rectifying Current in the Plasma Membrane of the Calcifying Marine Phytoplankton Coccolithus pelagicus. *Plant Physiology* **131**: 1391–1400.

Taylor AR, Russell ,Mark A., Harper ,Glenn M., Collins ,Toby f. T., and Brownlee C. **2007**. Dynamics of formation and secretion of heterococcoliths by Coccolithus pelagicus ssp. braarudii. *European Journal of Phycology* **42**: 125–136.

Taylor AR, Chrachri A, Wheeler G, Goddard H, Brownlee C. **2011**. A Voltage-Gated H+ Channel Underlying pH Homeostasis in Calcifying Coccolithophores. *PLOS Biology* **9**: e1001085.

Thaben PF, Westermark PO. **2014**. Detecting rhythms in time series with RAIN. *Journal of Biological Rhythms* **29**: 391–400.

Thyberg J, Moskalewski S. **1998**. Partitioning of cytoplasmic organelles during mitosis with special reference to the Golgi complex. *Microscopy Research and Technique* **40**: 354–368.

Tong S, Hutchins DA, Fu F, Gao K. **2016**. Effects of varying growth irradiance and nitrogen sources on calcification and physiological performance of the coccolithophore Gephyrocapsa oceanica grown under nitrogen limitation. *Limnology and Oceanography* **61**: 2234–2242.

Tong S, Hutchins DA, Gao K. **2019**. Physiological and biochemical responses of *Emiliania huxleyi* to ocean acidification and warming are modulated by UV radiation. *Biogeosciences* **16**: 561–572.

Tong T, Li Q, Jiang W, Chen G, Xue D, Deng F, Zeng F, Chen Z-H. **2021**. Molecular Evolution of Calcium Signaling and Transport in Plant Adaptation to Abiotic Stress. *International Journal of Molecular Sciences* **22**: 12308.

Torres-Delgado A, Kotamarthi HC, Sauer RT, Baker TA. **2020**. The Intrinsically Disordered N-terminal Extension of the ClpS Adaptor Reprograms Its Partner AAA + ClpAP Protease. *Journal of Molecular Biology* **432**: 4908–4921.

Tränkner M, Jákli B, Tavakol E, Geilfus C-M, Cakmak I, Dittert K, Senbayram M. **2016**. Magnesium deficiency decreases biomass water-use efficiency and increases leaf water-use efficiency and oxidative stress in barley plants. *Plant and Soil* **406**: 409–423.

Trimborn S, Langer G, Rost B rn. **2007**. Effect of varying calcium concentrations and light intensities on calcification and photosynthesis in Emiliania huxleyi. *Limnology and Oceanography* **52**: 2285–2293.

Tsakalakis I, Follows MJ, Dutkiewicz S, Follett CL, Vallino JJ. **2022**. Diel light cycles affect phytoplankton competition in the global ocean. *Global Ecology and Biogeography* **31**: 1838–1849.

Turner JJ, Ewald JC, Skotheim JM. **2012**. Cell size control in yeast. *Current Biology* **22**: R350–R359.

Uchimiya M, Schroer W, Olofsson M, Edison AS, Moran MA. **2022**. Diel investments in metabolite production and consumption in a model microbial system. *The ISME Journal* **16**: 1306–1317.

UniProt Consortium. **2021**. UniProt: the universal protein knowledgebase in 2021. *Nucleic Acids Research* **49**: D480–D489.

Vadia S, Levin PA. **2015**. Growth rate and cell size: A re-examination of the growth law. *Current opinion in microbiology* **24**: 96–103.

Vaish S, Gupta D, Mehrotra R, Mehrotra S, Basantani MK. **2020**. Glutathione S-transferase: a versatile protein family. *3 Biotech* **10**: 321.

Vaulot D, Olson RJ, Chisholm SW. **1986**. Light and dark control of the cell cycle in two marine phytoplankton species. *Experimental Cell Research* **167**: 38–52.

Verbruggen N, Hermans C. **2013**. Physiological and molecular responses to magnesium nutritional imbalance in plants. *Plant and Soil* **368**: 87–99.

Villiot N, Poulton AJ, Butcher ET, Daniels LR, Coggins A. **2021**. Allometry of carbon and nitrogen content and growth rate in a diverse range of coccolithophores. *Journal of Plankton Research* **43**: 511–526.

de Vries J, Monteiro F, Langer G, Brownlee C, Wheeler G. **2024**. A critical trade-off between nitrogen quota and growth allows *Coccolithus braarudii* life cycle phases to exploit varying environment. *Biogeosciences* **21**: 1707–1727.

van der Wal P, de Jong EW, Westbroek P, de Bruijn WC, Mulder-Stapel AA. **1983a**. Ultrastructural polysaccharide localization in calcifying and naked cells of the coccolithophoridEmiliania huxleyi. *Protoplasma* **118**: 157–168.

van der Wal P, de Jong EW, Westbroek P, de Bruijn WC, Mulder-Stapel AA. **1983b**. Polysaccharide localization, coccolith formation, and golgi dynamics in the coccolithophorid *Hymenomonas carterae*. *Journal of Ultrastructure Research* **85**: 139–158.

van der Wal. P, de Vrind JPM, de Vrind-de Jong EW, Borman AH. **1987**. Incompleteness of the Coccosphere as a Possible Stimulus for Coccolith Formation in Pleurochrysis Carterae(prymnesiophyceae). *Journal of Phycology* **23**: 218–221.

Walker GM. **1986**. Magnesium and cell cycle control: an update. *Magnesium* **5**: 9–23.

Walker CE, Heath S, Salmon DL, Smirnoff N, Langer G, Taylor AR, Brownlee C, Wheeler GL. **2018a**. An Extracellular Polysaccharide-Rich Organic Layer Contributes to Organization of the Coccosphere in Coccolithophores. *Frontiers in Marine Science* **5**.

Walker JM, Marzec B, Ozaki N, Clare D, Nudelman F. **2020**. Morphological development of *Pleurochrysis carterae* coccoliths examined by cryo-electron tomography. *Journal of Structural Biology* **210**: 107476.

Walker CE, Taylor AR, Langer G, Durak GM, Heath S, Probert I, Tyrrell T, Brownlee C, Wheeler GL. **2018b**. The requirement for calcification differs between ecologically important coccolithophore species. *New Phytologist* **220**: 147–162.

Wang Y, Branicky R, Noë A, Hekimi S. **2018**. Superoxide dismutases: Dual roles in controlling ROS damage and regulating ROS signaling. *Journal of Cell Biology* **217**: 1915–1928.

Wang X, Fu F, Qu P, Kling JD, Jiang H, Gao Y, Hutchins DA. **2019**. How will the key marine calcifier *Emiliania huxleyi* respond to a warmer and more thermally variable ocean? *Biogeosciences* **16**: 4393–4409.

Wang Y, Li Z, Wang X, Zhao Z, Jiao L, Liu R, Wang K, Ma R, Yang Y, Chen G, *et al*. 2023. Insights into membrane association of the SMP domain of extended synaptotagmin. *Nature Communications* **14**: 1504.

Wang Z, Tong S, Xu D, Huang X, Sun Y, Wang B, Sun H, Zhang X, Fan X, Wang W, *et al*. 2024. Effects of temperature and nitrogen sources on physiological performance of the coccolithophore *Emiliania huxleyi*. *Marine Environmental Research* **196**: 106405.

Weart RB, Lee AH, Chien A-C, Haeusser DP, Hill NS, Levin PA. **2007**. A Metabolic Sensor Governing Cell Size in Bacteria. *Cell* **130**: 335–347.

Weissbach H, Etienne F, Hoshi T, Heinemann SH, Lowther WT, Matthews B, St John G, Nathan C, Brot N. **2002**. Peptide methionine sulfoxide reductase: structure, mechanism of action, and biological function. *Archives of Biochemistry and Biophysics* **397**: 172–178.

Wendel AA, Lewin TM, Coleman RA. **2009**. Glycerol-3-phosphate acyltransferases: Rate limiting enzymes of triacylglycerol biosynthesis. *Biochimica et biophysica acta* **1791**: 501–506.

White MM, Drapeau DT, Lubelczyk LC, Abel VC, Bowler BC, Balch WM. **2018**. Calcification of an estuarine coccolithophore increases with ocean acidification when subjected to diurnally fluctuating carbonate chemistry. *Marine Ecology Progress Series* **601**: 59–76.

van Wijk SJL, Timmers HTM. **2010**. The family of ubiquitin-conjugating enzymes (E2s): deciding between life and death of proteins. *FASEB journal: official publication of the Federation of American Societies for Experimental Biology* **24**: 981–993.

Winter A, Henderiks J, Beaufort L, Rickaby REM, Brown CW. **2014**. Poleward expansion of the coccolithophore Emiliania huxleyi. *Journal of Plankton Research* **36**: 316–325.

Wirtz W, Stitt M, Heldt HW. **1982**. Light activation of calvin cycle enzymes as measured in pea leaves. *FEBS Letters* **142**: 223–226.

Witte C-P. **2011**. Urea metabolism in plants. *Plant Science* **180**: 431–438.

Wolf FI, Cittadini A. **1999**. Magnesium in cell proliferation and differentiation. *Frontiers in Bioscience-Landmark* **4**: 607–617.

Woodrow IE, Murphy DJ, Latzko E. **1984**. Regulation of stromal sedoheptulose 1,7-bisphosphatase activity by pH and Mg2+ concentration. *Journal of Biological Chemistry* **259**: 3791–3795.

Wu F, Guo J, Duan H, Li T, Wang Y, Wang Y, Wang S, Feng Y. **2023**. Ocean Acidification Affects the Response of the Coastal Coccolithophore Pleurochrysis carterae to Irradiance. *Biology* **12**: 1249.

Wykoff DD, Davies JP, Melis A, Grossman AR. **1998**. The regulation of photosynthetic electron transport during nutrient deprivation in Chlamydomonas reinhardtii. *Plant Physiology* **117**: 129–139.

Xie E, Xu K, Li Z, Li W, Yi X, Li H, Han Y, Zhang H, Zhang Y. **2021**. Disentangling the Effects of Ocean Carbonation and Acidification on Elemental Contents and Macromolecules of the Coccolithophore Emiliania huxleyi. *Frontiers in Microbiology* **12**.

Xing J, Gumerov VM, Zhulin IB. **2023**. Origin and functional diversification of PAS domain, a ubiquitous intracellular sensor. *Science Advances* **9**: eadi4517.

Xu J, Sun J, Beardall J, Gao K. **2020**. Lower Salinity Leads to Improved Physiological Performance in the Coccolithophorid Emiliania huxleyi, Which Partly Ameliorates the Effects of Ocean Acidification. *Frontiers in Marine Science* **7**.

Xue L, Cai W-J, Jiang L-Q, Wei Q. **2021**. Why are Surface Ocean pH and CaCO3 Saturation State Often out of Phase in Spatial Patterns and Seasonal Cycles? *Global Biogeochemical Cycles* **35**: e2021GB006949.

Yan Y-W, Mao D-D, Yang L, Qi J-L, Zhang X-X, Tang Q-L, Li Y-P, Tang R-J, Luan S. **2018**. Magnesium Transporter MGT6 Plays an Essential Role in Maintaining Magnesium Homeostasis and Regulating High Magnesium Tolerance in Arabidopsis. *Frontiers in Plant Science* **9**.

Young JR, Davis SA, Bown PR, Mann S. **1999**. Coccolith Ultrastructure and Biomineralisation. *Journal of Structural Biology* **126**: 195–215.

Young J, Geisen M, Cros L, Kleijne A, Sprengel C, Probert I, Østergaard J. **2003**. A guide to extant coccolithophore taxonomy. *J. Nannoplankton Res.*: 1–125.

Young JR, Geisen M, Probert I. **2005**. A Review of Selected Aspects of Coccolithophore Biology with Implications for Paleobiodiversity Estimation. *Micropaleontology* **51**: 267–288.

Young JR, Ziveri P. **2000**. Calculation of coccolith volume and it use in calibration of carbonate flux estimates. *Deep Sea Research Part II: Topical Studies in Oceanography* **47**: 1679–1700.

Yu L, Fan J, Xu C. **2019**. Peroxisomal fatty acid β-oxidation negatively impacts plant survival under salt stress. *Plant Signaling & Behavior* **14**: 1561121.

Zhang Y, Bach LT, Lohbeck KT, Schulz KG, Listmann L, Klapper R, Riebesell U. **2018**. Population-specific responses in physiological rates of *Emiliania huxleyi* to a broad CO_2 range. *Biogeosciences* **15**: 3691–3701.

Zhang Y, Bach LT, Schulz KG, Riebesell U. **2015**. The modulating effect of light intensity on the response of the coccolithophore ephyrocapsa oceanica to ocean acidification. *Limnology and Oceanography* **60**: 2145–2157.

Zhang Y, Collins S, Gao K. **2020**. Reduced growth with increased quotas of particulate organic and inorganic carbon in the coccolithophore *Emiliania huxleyi* under future ocean climate change conditions. *Biogeosciences* **17**: 6357–6375.

Zhang Y, Fu F-X, Hutchins D, Gao K. **2019**. Combined effects of CO2 level, light intensity, and nutrient availability on the coccolithophore Emiliania huxleyi. *Hydrobiologia* **842**.

Zhang Y, Gao K. **2021**. Photosynthesis and calcification of the coccolithophore *Emiliania huxleyi* are more sensitive to changed levels of light and CO2 under nutrient limitation. *Journal of Photochemistry and Photobiology B: Biology* **217**: 112145.

Zhang Y, Ma S, Chen H, Li J, Li Z, Xu K, Huang R, Zhang H, Han Y, Sun J. **2023**. Reallocation of elemental content and macromolecules in the coccolithophore *Emiliania huxleyi* to acclimate to climate change. *Biogeosciences* **20**: 1299–1312.

Zhao Y, Wang Y, Quigg A. **2015**. Comparison of population growth and photosynthetic apparatus changes in response to different nutrient status in a diatom and a coccolithophore. *Journal of Phycology* **51**: 872–884.

Zhu J, Thompson CB. **2019**. Metabolic regulation of cell growth and proliferation. *Nature Reviews Molecular Cell Biology* **20**: 436–450.

Ziveri P, de Bernardi B, Baumann K-H, Stoll HM, Mortyn PG. **2007**. Sinking of coccolith carbonate and potential contribution to organic carbon ballasting in the deep ocean. *Deep Sea Research Part II: Topical Studies in Oceanography* **54**: 659–675.

Ziveri P, Gray WR, Anglada-Ortiz G, Manno C, Grelaud M, Incarbona A, Rae JWB, Subhas AV, Pallacks S, White A, *et al*. 2023. Pelagic calcium carbonate production and shallow dissolution in the North Pacific Ocean. *Nature Communications* **14**: 805.

Zondervan I. **2007**. The effects of light, macronutrients, trace metals and CO2 on the production of calcium carbonate and organic carbon in coccolithophores—A review. *Deep Sea Research Part II: Topical Studies in Oceanography* **54**: 521–537.

Zondervan I, Rost B, Riebesell U. **2002**. Effect of CO2 concentration on the PIC/POC ratio in the coccolithophore *Emiliania huxleyi* grown under light-limiting conditions and different daylengths. *Journal of Experimental Marine Biology and Ecology* **272**: 55–70.

Zones JM, Blaby IK, Merchant SS, Umen JG. **2015**. High-Resolution Profiling of a Synchronized Diurnal Transcriptome from Chlamydomonas reinhardtii Reveals Continuous Cell and Metabolic Differentiation. *The Plant Cell* **27**: 2743–2769.